Dissertation

submitted to the
Combined Faculty of Mathematics, Engineering and Natural Sciences
of
Heidelberg University, Germany
for the degree of
Doctor of Natural Sciences

Put forward by

Charlotte Maria König

born in: Port Huron (USA)

Oral examination: April 15, 2025

High-Precision Measurements of Single Molecular Hydrogen Ions at ALPHATRAP

Referees:

Prof. Dr. Klaus Blaum
Prof. Dr. Jeroen Koelemeij

Abstract

The work of this thesis demonstrates single-ion nondestructive spectroscopy of molecules in Penning traps. Due to their rovibrational level structure and the close proximity of at least two nuclei, molecular ions exhibit unique sensitivities for tests of the Standard Model of particle physics. In particular, a high-precision comparison of rovibrational transition energies of H_2^+ and its antimatter counterpart $\overline{H}_2^-$ promises to stringently test for violations of the fundamental charge-parity-time reversal symmetry [1, 2]. Here, a new method for nondestructive readout of the internal quantum state of a single molecular hydrogen ion (MHI) was demonstrated, along with external production and several month-long confinement in a Penning trap, which are among the requirements for future measurements of $\overline{H}_2^-$. The internal quantum state - vibrational, rotational, hyperfine, Zeeman - of the MHI was determined via millimeter wave-induced resonant electron spin flips (eSF) employing the continuous Stern-Gerlach effect [3]. This was applied for spectroscopy of all six eSF transitions in the rovibrational ground state of HD^+, resulting in the determination of the bound-electron $g_e(0,0)$ factor to 0.20 ppb and the spin-spin interaction coefficients of the hyperfine structure (HFS), $E_4(0,0)$ and $E_5(0,0)$, to 44 ppb and 151 ppb, respectively. The experimental precision of $g_e(0,0)$ exceeds the precision of the current theoretical prediction by almost three orders of magnitude [4]. Our value also shows agreement with a new, still unpublished calculation, which surpasses the experimental precision. Precise values of g_e factors allow the unambiguous internal quantum state detection of MHI. $E_4(0,0)$ and $E_5(0,0)$ probe HFS theory below the ppm level, which enters the prediction of rovibrational transition frequencies. The near-agreement of the values does not explain deviations observed in rovibrational measurements [5]. Furthermore, efforts towards applying the developed methods to high-precision rovibrational spectroscopy in Penning traps are presented.

Zusammenfassung

In dieser Arbeit wird nichtdestruktive Einzelionenspektroskopie von Molekülen in Penning-Fallen demonstriert. Aufgrund ihrer Rovibrationszuständen und der unmittelbaren Nähe von mindestens zwei Atomkernen weisen Molekülionen eine einzigartige Sensitivität für Tests des Standardmodells der Teilchenphysik auf. Insbesondere verspricht ein hochpräziser Vergleich der Rovibrationsübergangsenergien von H_2^+ und seinem Antimaterie-Gegenstück $\overline{H}_2^-$ einen stringenten Test auf Verletzungen der fundamentalen Ladungs-Paritäts-Zeit-Umkehrsymmetrie [1, 2]. Hier wurde eine neue Methode zur nichtdestruktiven Bestimmung des internen Quantenzustands eines einzelnen molekularen Wasserstoffions (MHI) demonstriert, zusammen mit der externen Produktion und dem mehrmonatigen Speichern in einer Penning-Falle, die zu den Voraussetzungen für zukünftige Messungen von $\overline{H}_2^-$ gehören. Der interne Quantenzustand - Vibration, Rotation, Hyperfein, Zeeman - des MHI wurde über Millimeterwellen-induzierte resonante Elektronenspinflips (eSF) unter Verwendung mit dem kontinuierlichen Stern-Gerlach-Effekt [3] bestimmt. Dies wurde für Spektroskopie aller sechs eSF-Übergänge im rovibratorischen Grundzustand von HD^+ angewandt, was zur Bestimmung des $g_e(0,0)$ Faktors des gebundenen Elektrons auf 0,20 ppb und der Spin-Spin-Wechselwirkungskoeffizienten der Hyperfeinstruktur (HFS), $E_4(0,0)$ und $E_5(0,0)$, auf 44 ppb bzw. 151 ppb führte. Die experimentelle Genauigkeit von $g_e(0,0)$ übertrifft die Genauigkeit der aktuellen theoretischen Vorhersage um fast drei Größenordnungen. Unser Wert zeigt auch eine Übereinstimmung mit einer neuen, noch unveröffentlichten Berechnung, welche die experimentelle Genauigkeit übertrifft. Genaue Werte der g_e-Faktoren erlauben den eindeutigen Nachweis des internen Quantenzustands von MHI. $E_4(0,0)$ und $E_5(0,0)$ prüfen die HFS-Theorie unterhalb des ppm-Niveaus, die in die Vorhersage der Rovibrationsübergangsfrequenzen eingeht. Die annähernde Übereinstimmung der Werte erklärt nicht die Abweichungen, die bei Rovibrationsmessungen beobachtet wurden [5]. Darüber hinaus werden die Bemühungen um die Anwendung der entwickelten Methoden auf die hochpräzise Rovibrationsspektroskopie in Penning-Fallen vorgestellt.

Contents

List of Figures

List of Tables

1 Introduction

First, I would like to begin by explaining the general idea of why it is worthwhile to carry out high-precision measurements of atomic and molecular systems. A question, I have been asked by many non-physicists as well as by physicists working in other fields. I will then explain why molecules, especially molecular hydrogen ions (MHI), are great systems for such measurements with the potential to probe and push the limits of our current understanding of physics. After, I will introduce the structure of this thesis, from the techniques we are developing to what was measured in the course of this thesis work at ALPHATRAP and why.

1.1 Testing the Standard Model of Particle Physics

The Standard Model of particle physics (SM) [6] is so far the theoretical framework that comes closest to a theory explaining all observations and classifying all elementary particles. In short, while it is not 'the theory of everything', it successfully predicts and describes observations and interactions in the universe to a large extent, from the minute sub-atomic scale up to large scales such as stars. The SM incorporates three of the four known fundamental interactions. These three fundamental interactions are the electromagnetic interaction described by the quantum field theory of quantum electrodynamics (QED), the strong force described by quantum chromodynamics (QCD) and the weak interaction. The weak and electromagnetic interaction can be unified by the description of the electroweak interaction [6]. There are dedicated charges for each interaction that the elementary particles, the quarks and leptons and the force-exchange particles, can carry: electric charge (QED), color charge (QCD), and weak isospin and weak charge (weak interaction). Furthermore, almost all types of elementary particle have an intrinsic angular momentum, the spin. The force-exchange particle mediating the interactions are the photon in QED, the gluons in QCD, and the Z and W bosons in the weak force.

While today, the SM is the most successful theory of particle physics, some big questions about the universe remain unanswered. A major shortcoming is that the SM does not contain gravity which is described by general relativity and so far cannot be included in a quantum field theory framework. Further, the SM assumed neutrinos (a class of fundamental particles) to be massless. However, the observation of neutrino oscillations, is evidence for a nonzero neutrino mass [6]. Astrophysical and cosmological observations indicate that there is far more to the universe than the observed matter, resulting in the open question of dark matter and dark energy, beyond the description of the SM, in the universe [7, 8]. Moreover, the asymmetry in the abundance of matter and antimatter with respect to the photon density of the Cosmic Microwave Background Radiation in the universe does not

align with the SM prediction either [7].

As these open questions cannot be answered by the SM today, this motivates to probe further for a better understanding of our universe and to uncover the limitations of the SM and possibly find extensions to it. This can be carried out in vastly different ways. Progress in astrophysics and cosmology, can address open questions at large-scale systems and high-energy particle accelerators can give access to tests of the SM in unchartered high-energy regimes. Alternatively, extensions to the SM would slightly shift the energy levels of atomic and molecular systems. Therefore, the complementary high-precision and low-energy approach of atomic-molecular-optics (AMO) physics aims to measure atomic and molecular properties, such as transition energies, to compare experimentally determined values to theoretical SM predictions in unchartered precision regimes. This approach can mostly be carried out in small-scale or even table-top experiments, compared to particle accelerators.

QED, describing the interaction of light and matter, is most accessible experimentally as well as the best computed interaction theoretically and is thus the so far best tested quantum field theory of the SM. For example, it successfully predicts the Lamb shift in the fine structure of atomic systems [9]. Moreover, its prediction of the magnitude of the magnetic moment of the electron (g_e factor) agrees at the 1 ppt level with the experimental determination, allowing to determine the fine structure constant α to 0.11 ppb relative precision [10]. However, different experimental determinations of this value have resulted in so far unresolved tension of up to 5 σ [10]. This coupling constant describes the strength of the interaction between charged particles and photons in QED. The recent measurement of the muon anomalous magnetic moment ((g_μ-2)/2) to 0.2 ppm initially showed a 5 σ deviation to the SM prediction [11, 12]. Potentially, such deviations can be a hint at new physics beyond the SM, however an updated theoretical prediction including new large-scale lattice QCD simulations lead to agreement of the experimental result and theory, validating the SM [13].

When specifically addressing the open question about the observed imbalance of matter and antimatter in the universe there are three criteria postulated by Sakharov that would allow such an imbalance under the conditions of baryon violation, charge-parity (CP) symmetry violation and departure from thermal equilibrium [7, 14]. For example, breaking of CP symmetry induces an electric dipole moment of the electron, the size of which depends on the strength of the violation of this symmetry. Upper limits for this quantity have been set by high-precision experiments with neutral molecules [15, 16, 17] or trapped molecular ions [18].

Alternatively, the imbalance of matter and antimatter could be explained by a violation of charge-parity-time (CPT) reversal symmetry, manifesting itself as a slight difference between properties, such as mass, charge, and transition energies, of matter and antimatter particle pairs. This would have consequences for all quantum field theories and thus the SM. So far, AMO-type antimatter experiments for limits of CPT reversal symmetry violation have either been carried out on single particles in Penning traps, comparing the electron e^- and the positron e^+ [19, 6] or the proton p and the antiproton $\bar{p}$ [20, 21], on short-lived, composite matter-antimatter systems such as antiprotonic helium [22] or positronium (e^-e^+) [23], or by comparing properties of the hydrogen H and the antihydrogen atom $\overline{\mathrm{H}}$ [24, 25, 26, 27].

Additionally, accelerator-based observations can set limits on CPT symmetry violation by observing neutral kaon decays [6], comparing muon and antimuon lifetimes [28] and their

anomalous magnetic moments [29, 30] and detecting evidence of antineutrons and light antineutron-containing nuclei [31].

While they are produced in high-energy collisions along-side antiprotons, as of now, it is not feasible to slow down and trap antineutrons or antineutron-containing nuclei for high-precision AMO-type measurements. What options does this leave on stable systems for antimatter experiments besides using H and $\overline{\mathrm{H}}$? As electrically neutral particles, H/$\overline{\mathrm{H}}$ are difficult to confine and different measurement techniques are used in the matter and antimatter experiments. There are two other options to form stable ions made solely from the accessible $\overline{p}$ and e^+. One option is one $\overline{p}$ and two e^+, so $\overline{\mathrm{H}}^+$, however this ion does not have bound excited states for spectroscopic measurements [32]. The second option is two $\overline{p}$ and one e^+, so $\overline{\mathrm{H}}_2^-$, a molecular hydrogen ion (MHI) with many bound excited states which I will introduce in the following.

1.2 A Prime Candidate: Molecular Hydrogen Ions

In my slightly biased opinion: MHI are amazing systems and they have great properties for tests of the SM. I will discuss their level structure and details on what has been probed in Ch. 2, so here I will state the main points only.

Diatomic MHI are single-electron and therefore simple systems allowing high precision in theoretical QED calculations of their properties such as transition energies between bound excited states. As molecules, MHI have more than one nucleus and thus exhibit additional internal quantum states compared to atomic systems. Namely, they feature excited rotational and vibrational states of the nuclei with respect to each other. Many transitions between these rovibrational states lie in the laser-accessible infrared (IR) regime, allowing high-precision measurements on the experimental side. The potential for high precision on both the theoretical and experimental side makes them great candidates for tests of fundamental physics and of limits of the SM, analogous to the hydrogen atom. Note that since the theoretical prediction of these rovibrational transition frequencies are correlated, a specific selection of transitions and dedicated analysis are necessary, to gain in precision from measuring more than one such transition [33].

Given agreement between the experimental and the theoretical results, they can be combined to extract fundamental constants, as fundamental constants are input parameters for the theoretical prediction of the transition energies, or to set upper bounds on beyond SM effects, both with different sensitivities than by using transitions in purely atomic systems [34, 33, 35, 36]. For example, the rovibrational transitions in MHI are up to three orders of magnitude more sensitive to the proton-to-electron mass ratio than electronic transitions in H and molecules feature unique sensitivity to nuclear-nuclear interaction compared to atoms [1, 2, 37]. Exploring MHI is an active field of research, for example, it has been proposed to use MHI as optical molecular clocks and thereby set limits on the variation of fundamental constants [38, 39]. A viable path to higher precision on the experimental side, is to move towards single ion measurements, thus mitigating systematic effects of ion-ion interaction. This can be followed either in Paul traps [40, 41, 42] or our approach in Penning traps.

Now, after establishing the beneficial features of MHI for test of QED, let's come back to the antimatter $\overline{\mathrm{H}}_2^-$ case. As mentioned above, it features laser-accessible rovibrational

transitions that are sensitive to fundamental constants and particle properties. Furthermore, as a charged particle the same ion trapping techniques can be applied to both the matter and antimatter counterpart, reducing the effect of possible systematics in the comparison. This makes $H_2^+/\overline{H}_2^-$ a promising system to push the precision in tests of CPT symmetry violation.

In the measurements of this thesis work, not only steps towards a measurement technique for rovibrational spectroscopy of a single MHI are demonstrated, but also high-precision spectroscopy of the hyperfine structure (HFS) and Zeeman splitting of the rovibrational ground state of HD^+. A description of the HFS and Zeeman splitting and the respective Hamiltonians of this substructure for H_2^+ and HD^+ are given in Ch. 2, Sec. 2.1.2. The HFS includes spin-spin and spin-rotation interactions and the strength of each interaction is given by HFS coefficients. The Zeeman splitting is due to the interaction of the magnetic moments of the molecule with an external magnetic field. The magnitude of the magnetic moments, arising from the spins of the particles and the rotation of the molecule, are characterized by their g factors.

Generally, HFS and g factors are of interest for fundamental physics, as both can be described by QED theory. For example, high-precision measurements combined with high-precision QED calculations of the free and bound electron g factor have been used for stringent tests of QED and thus of the SM in general [10, 43]. Similarly, HFS theory has been tested to high precision in the hydrogen atom, muonium (μ^+e^-), and positronium (e^+e^-) [44] as well as in $^3He^+$ [45] and $^9Be^{3}+$ [46]. Furthermore, the HFS of ^{133}Cs is used as the definition of the second in the International System of Units (SI) [47].

Specifically in MHI, both HFS coefficients and g factors are important for multiple reasons. First, high-precision measurements of frequencies between HFS and Zeeman substates can be compared to theoretical predictions of spin-spin interaction and g factor theory for tests of QED. Furthermore, for high-precision measurements of rovibrational transition frequencies of MHI, precise values of the energies of the HFS and Zeeman substates are needed to extract the rovibrational transition frequency averaged over the HFS sub-splitting ('spin-averaged frequency') from the experimental data. This then allows a comparison to a QED prediction of this spin-averaged frequency for the above mentioned SM tests and determination of fundamental constants. This is especially interesting as discrepancies have been seen between experimental data and the theoretical prediction in the HFS of HD^+ [5]. Moreover, since transition frequencies between HFS and Zeeman substates depend on the rovibrational state, resonantly driving such a transition can be used in single-ion measurements to detect which rovibrational and hyperfine state the ion is in for nondestructive state detection. This is demonstrated in this thesis work for HD^+ and is applicable to any other light molecular ion with nonzero electron spin, such as $\overline{H}_2^-$ for future tests of CPT symmetry violation.

1.3 Structure of this Thesis

In the first chapter (Ch. 2), I will give an introduction to MHI, their quantum levels and the transitions that can be probed. Following this, I will introduce the main features of the Penning trap, the tool with which I have measured properties of MHI in single-ion experiments, in Ch. 3. Then, I will describe the experimental setup of ALPHATRAP in

Ch. 4. Since this has been done in previous theses and in a review paper [48], this chapter will focus on the parts relevant for the MHI measurements and on the upgrades we integrated throughout my time at ALPHATRAP.

After these introductory chapters, I will describe the measurements of the HFS and Zeeman splitting of HD^+ in the rovibrational ground state in Ch. 5. These measurements demonstrate experimental techniques, such as nondestructive internal quantum state detection, for future rovibrational spectroscopy of single MHI in a Penning trap, as well as allow the determination of HFS coefficients and the bound electron g factor for comparison with their respective theoretical prediction. In the following chapter (Ch. 6), I will then describe proposed measurement schemes for rovibrational spectroscopy of a single MHI in a Penning trap, the steps we have taken at ALPHATRAP towards this goal as well as the obstacles along the way, finishing with an outlook for future efforts towards rovibrational spectroscopy of $\overline{H_2^-}$. In the end, I will conclude with a comparison of the obtained experimental results and their theoretical prediction as well as a summary of the efforts towards nondestructive single-ion spectroscopy of molecular ions in Penning traps.

2 Molecular Hydrogen Ions

Molecular hydrogen ions (MHI) can be used to probe our understanding of fundamental physics, for example by comparing matter (H_2^+) and antimatter ($\overline{H}_2^+$) for tests of CPT symmetry [1, 2], or by combining experimental and theoretical results to test the validity of the theory of quantum electrodynamics (QED) [34], to extract fundamental constants [34, 33], or to constrain beyond Standard Model physics [39, 38, 36, 35]. To make this possible, the level structure has to be well understood and in the latter cases even predicted to high precision.

To a large extent, the work of this thesis was aimed at developing Penning-trap techniques for comparisons of matter and antimatter using H_2^+ and $\overline{H}_2^+$. Once production of the antimatter molecular ion becomes possible, it will only be at very low production rates (see Sec. 6.5.2 and Refs. [2, 49, 50]). Thus, experimental techniques for spectroscopy based on long trapping times coupled with single-ion, nondestructive state detection are essential. With this goal in mind, the following chapter will focus on the homonuclear diatomic H_2^+ and its close heteronuclear diatomic relative HD^+, which has been used at ALPHATRAP so far. Nevertheless, to a large extent the topics discussed here are at least qualitatively true for the other diatomic MHI isotopologues D_2^+, T_2^+ and HT^+, DT^+.

In the following chapter, I will give an overview of the vast level structure of H_2^+ and HD^+ as well as an overview of the current *state-of-the-art* on the experimental side for various types of transitions.

2.1 Level Structure of Molecular Hydrogen Ions

Let us first consider the electronic states of MHI. For both H_2^+ and HD^+, only the ground electronic state ($1s\sigma_g$) exhibits a significant energy minimum, when considered as a function of the distance between the two nuclei (R). The first excited state ($2p\sigma_u$) exhibits only a very shallow energy minimum at a large value of $R \simeq 12.5\ a_0$, with $a_0 = \frac{4\pi\epsilon_0\hbar^2}{e^2 m_e} \sim 5{\cdot}10^{-11}$ m as the Bohr radius [51]. Here, ϵ_0 is the vacuum permittivity, $\hbar$ is the reduced Planck constant, m_e is the mass of the electron, and e is the elementary charge. Therefore, in the following only the $1s\sigma_g$ will be considered, as it is the only electronic state with a plethora of bound rovibrational sublevels. The energy of both electronic states as a function of R are displayed in Fig. 2.1 for HD^+. To the detail shown here, the energy of the electronic states for H_2^+ and HD^+ are identical [52].

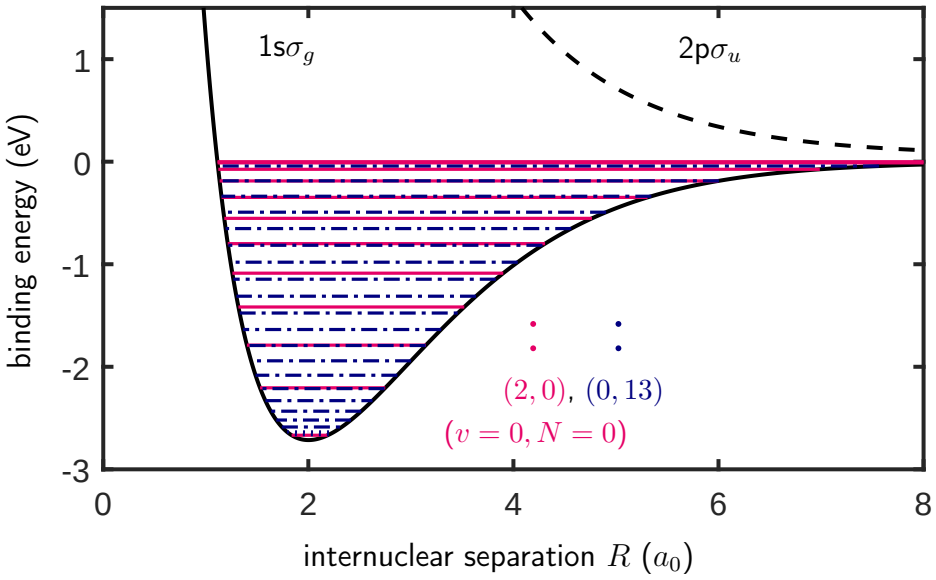

Figure 2.1: Potential curves for the electronic ground state, $1s\sigma_g$ (black solid line) of HD^+ and the first electronic excited state, $2p\sigma_u$ (black dashed line). Theoretical values for the potentials have been calculated in Ref. [53], explicit values are given in [52] and were obtained from Ref. [54]. A selection of bound rovibrational levels are marked in the electronic ground state. The red solid lines indicate the binding energy of vibrational states where the rotational quantum number $N = 0$, whereas the blue dot-dashed lines indicate the binding energy of rotational states where the vibrational quantum number $v = 0$. An example for both cases and the ground state are explicitly labeled. The values for the rovibrational binding energies are taken from Ref. [55]. To not overcrowd the plot only every second level is shown for both cases. The vibrational lines start from the rovibrational ground state $(v = 0, N = 0)$ and the rotational ones at the first excited state $(v = 0, N = 1)$.

2.1.1 Rovibrational Level Structure

In the case of HD^+, the electronic ground state has a substructure of 563 bound, quantized vibrational and rotational states [56], similarly also in the case of H_2^+ which has about 420 bound states [57]. A selection of these states is depicted in the energy minimum of the electronic ground state in Fig. 2.1. In the simplified description of a diatomic molecule as two nuclei connected by a spring, the rovibrational excitations can be understood rather pictorially. The two nuclei can vibrate with respect to each other (harmonic oscillation of the spring) and/or rotate around each other (rigid rotor). Note, these are approximations and both of these motions affect the distance between the nuclei in the molecule. Following the quantum-mechanical description, both the rotational and the vibrational excitations form discreet energy levels. For the rest of this thesis, the rovibrational levels will be denoted as (v, N), with the vibrational quantum number v and the rotational quantum number N.

The rotation of the molecule relates to an angular momentum, while the vibration does not. Therefore, transitions between rotational states follow multipole selection rules, such that $\Delta N = \pm 1$ transitions are electric-dipole transitions (E1) and $|\Delta N| > 1$ transitions are electric-quadrupole (E2) or higher-order transitions which have much smaller transition

strengths. Contrarily, there are no strict selection rules for transitions between vibrational states, so transitions with $|\Delta v| > 1$ are not strongly suppressed [58].

The energy spacing expressed as transition frequencies between the rotational and vibrational states (ν_{rot}, ν_{vib}), are approximately given by:

$$\nu_{rot} \approx R_\infty m_e \frac{1}{\mu}\,, \tag{2.1}$$

$$\nu_{vib} \approx R_\infty \sqrt{m_e \frac{1}{\mu}}\,, \tag{2.2}$$

where R_∞ is the Rydberg constant, m_e the mass of the electron and μ the reduced mass of the nuclei of the molecule, so $\mu^{\mathsf{H}_2^+} = \frac{m_p}{2}$ and $\mu^{\mathsf{HD}^+} = \left(\frac{1}{m_p} + \frac{1}{m_d}\right)^{-1}$, with m_p and m_d as the proton and deuteron mass, respectively. These approximate equations demonstrate the dependence of the rovibrational transitions frequencies on fundamental constants. Additionally, radiative and relativistic corrections for high-precision calculations depend on nuclear properties such as the radius of the proton and in the case of HD^+ the radius of the deuteron as well [34]. Consequently, combining a precise theoretical prediction with precise experimental data of the rovibrational transition frequencies allows to extract, for example, the mass ratios $\frac{m_e}{m_p}$, $\frac{m_e}{m_d}$, or $\frac{m_p}{m_d}$ [34]. Alternatively, when taking fundamental constants as input parameters from other sources [59], high-precision comparisons of theory and experimental results can be used to constrain new physics beyond the Standard Model (SM) [39, 38, 36, 35].

When comparing future measurements of H_2^+ and $\overline{\mathsf{H}}_2^-$, the strong dependence of the rovibrational transitions on the nuclear mass compared to electronic transitions in atomic (anti)hydrogen (H,$\overline{\mathsf{H}}$), can allow up to three orders of magnitude more stringent tests of CPT symmetry, with respect to the proton mass, at equal measurement precision [2]. Current state-of-the-art comparisons of matter and antimatter involving the antiproton mass ($m_{\bar{p}}$) are the 1s-2s transition in $\overline{\mathsf{H}}$ measured to $2{\cdot}10^{-12}$ precision [26] but with about three orders lower sensitivity to $m_{\bar{p}}$, antiprotonic helium spectroscopy determining $\frac{m_{\bar{p}}}{m_e}$ to $8{\cdot}10^{-10}$ [22], and cyclotron frequency measurements comparing the charge-to-mass ratio of protons and antiprotons to $1.6{\cdot}10^{-11}$ [21]. Rovibrational spectroscopy of H_2^+ has been estimated to have the potential for ultra-high precision at the level of 10^{-17} [37]. Furthermore, the molecular system allows to probe antiproton-antiproton interactions, requiring a system of at least two antiprotons, which is not the case in other antimatter experiments so far.

From the approximate equations for the rotational and vibrational transitions (Eq. 2.1) one can see that the energy spacing between the rovibrational levels of H_2^+ and HD^+ will be of the same order of magnitude but not identical. Although the energies of the rovibrational levels are fairly similar for both molecular ions, the transition strengths between states and thus the lifetimes of the excited levels are vastly different [57, 56]. Some exemplary values for transition energies and frequencies as well as state lifetimes for both MHI are listed in Tab. 2.1.

The main difference between the two is that H_2^+ is homonuclear and HD^+ is heteronulcear. Thus, electric dipole transitions in the rovibrational level structure ($\Delta N = \pm 1$) are allowed for HD^+ but forbidden for H_2^+. One approach to explain this is by considering the classical rigid-rotor model. The rotation of the rigid rotor is around the center of mass. For electric dipole transitions to occur, the molecular ion must exhibit an electric dipole

Table 2.1: An order of magnitude selection of rovibrational transition frequencies (top) and rovibrational state lifetimes (bottom) for H_2^+ and HD^+. The values for the state energies are taken from Ref. [52] and for the state lifetimes from Refs. [57, 56]. For the transitions the lowest possible single photon transition from the ground state was chosen. For both H_2^+ and HD^+ the $(0,2)$ and respectively $(0,1)$ state is the longest living state that decays, as the $(0,1)$ state of H_2^+ has basically infinite lifetime. For higher rovibrational states the lifetimes decrease to roughly the value of the $(5,1)$ state, for details see Refs. [57, 56].

transition frequencies	rotation		vibration	
	THz	μm	THz	μm
H_2^+ $(0,0)$-$(0,2)$, $(0,0)$-$(1,2)$	5.2	57.4	70.6	4.2
HD^+ $(0,0)$-$(0,1)$, $(0,0)$-$(1,1)$	1.3	228.0	58.6	5.1

lifetimes τ (s)	$(0,2)/(0,1)$	$(5,1)$
H_2^+	10^{11}	10^{6}
HD^+	10^{2}	10^{-2}

moment. For the symmetric H_2^+ molecule, the center of mass overlaps with the center of charge midway between both protons. For HD^+ on the other hand, the masses of the nuclei are not symmetric but the charges are, so the center of mass and center of charge do not overlap and HD^+ exhibits an electric dipole moment [58]. Furthermore, symmetry regarding the mean position of the electron with respect to the internuclear axis is given in H_2^+ (the mean position of the electron with respect to the internuclear axis is in the center between both nuclei), while in HD^+ the mean position of the electron is slightly off center [58].

More fundamentally, the lack of E1 transitions in H_2^+ can be argued for by the symmetry of the wavefunction. H_2^+ is a homonuclear diatomic molecule where both nuclei are protons, so fermions. Therefore, the total molecular wavefunction has to remain antisymmetric under exchange of the two nuclei. The electronic state is a g (gerade, symmetric) state, thus the combination of nuclear spin and rotational state have to be antisymmetric. For a total nuclear spin $I = 1$ the nuclear-spin contribution to the wavefunction is symmetric, therefore the rotational part has to be antisymmetric, hence N odd. Vice versa, for $I = 0$ the nuclear-spin part is antisymmetric, so only symmetric rotational states are allowed, hence N even. This essentially splits H_2^+ into two disjunct species: *para*-H_2^+, $I = 0$, N even and *ortho*-H_2^+, $I = 1$, N odd, between which transitions are highly forbidden. Therefore, only electric quadrupole (E2) transitions ($\Delta N = 0, \pm 2$) or higher-order even (E4,E8,..) transitions are allowed, thereby remaining in one species of *ortho* or *para*. Note, this is not a perfect symmetry and $\Delta N = \pm 1$ transitions can occur between high (v, N) states in H_2^+ [60]. In HD^+, the nuclei are not identical, so no symmetry arguments apply, and any N state can be populated irrespective of the spin configuration, thus allowing E1 transitions ($\Delta N = \pm 1$).

On the one hand, E2 transitions have very narrow natural line widths, potentially allowing ultra-high-precision rovibrational spectroscopy. On the other hand, finding and driving such transitions is more difficult. This is true not only for potential rovibrational spectroscopy of the transition of interest but especially also for state preparation. Due to these considerations, we had decided to perform first MHI measurements on HD^+ which rather quickly decays to and remains in the rovibrational ground state in a cryogenic environment.

In any case, to understand experimental data and extract the pure rovibrational transi-

tion frequencies from a measurement, a good understanding of the hyperfine substructure is essential.

2.1.2 Hyperfine Structure and g Factors

The hyperfine structure (HFS) is the substructural splitting of each rovibrational level. It is governed by the interactions of the magnetic dipole moments prevalent in the molecular ion. The magnetic dipole moments are given by the spins of the constituent particles and the rotation of the molecule. For H_2^+, these are the electron spin $\boldsymbol{s}_e = \frac{1}{2}$, the nuclear spin $\boldsymbol{I} = 0, 1$ which is the combination of the two proton spins $\boldsymbol{I}_p = \frac{1}{2}$, and the rotational quantum number $\boldsymbol{N} = 0, 1, 2, ...$ For HD^+, there are the electron spin $\boldsymbol{s}_e = \frac{1}{2}$, the proton spin $\boldsymbol{I}_p = \frac{1}{2}$, the deuteron spin $\boldsymbol{I}_d = 1$, and the rotational quantum number $\boldsymbol{N} = 0, 1, 2, ...$

In absence of an external magnetic field, the energy of the levels for H_2^+ and HD^+ can be described by the following effective hyperfine Hamiltonians: [61, 62]

$$\begin{aligned}\boldsymbol{H}_{HFS}^{H_2^+}(v,N) =& hb_F(\boldsymbol{I}\cdot\boldsymbol{s}_e) + hc_e(\boldsymbol{N}\cdot\boldsymbol{s}_e) + hc_I(\boldsymbol{N}\cdot\boldsymbol{I}) + \frac{hd_1}{(2N-1)(2N+3)} \\ &\times\left(\frac{2}{3}\boldsymbol{N}^2(\boldsymbol{I}\cdot\boldsymbol{s}_e) - [(\boldsymbol{N}\cdot\boldsymbol{I})(\boldsymbol{N}\cdot\boldsymbol{s}_e) + (\boldsymbol{N}\cdot\boldsymbol{s}_e)(\boldsymbol{N}\cdot\boldsymbol{I})]\right) \\ &+ \frac{hd_2}{(2N-1)(2N+3)}\left(\frac{1}{3}\boldsymbol{N}^2\boldsymbol{I}^2 - \frac{1}{2}(\boldsymbol{N}\cdot\boldsymbol{I}) - (\boldsymbol{N}\cdot\boldsymbol{I})^2\right)\end{aligned} \tag{2.3}$$

$$\begin{aligned}\boldsymbol{H}_{HFS}^{HD^+}(v,N) =& hE_1(\boldsymbol{N}\cdot\boldsymbol{s}_e) + hE_2(\boldsymbol{N}\cdot\boldsymbol{I}_p) + hE_3(\boldsymbol{N}\cdot\boldsymbol{I}_d) + hE_4(\boldsymbol{I}_p\cdot\boldsymbol{s}_e) \\ &+ hE_5(\boldsymbol{I}_d\cdot\boldsymbol{s}_e) + hE_6\{2\boldsymbol{N}^2(\boldsymbol{I}_p\cdot\boldsymbol{s}_e) - 3[(\boldsymbol{N}\cdot\boldsymbol{I}_p)(\boldsymbol{N}\cdot\boldsymbol{s}_e) \\ &+ (\boldsymbol{N}\cdot\boldsymbol{s}_e)(\boldsymbol{N}\cdot\boldsymbol{I}_p)]\} + hE_7\{2\boldsymbol{N}^2(\boldsymbol{I}_d\cdot\boldsymbol{s}_e) - 3[(\boldsymbol{N}\cdot\boldsymbol{I}_d)(\boldsymbol{N}\cdot\boldsymbol{s}_e) \\ &+ (\boldsymbol{N}\cdot\boldsymbol{s}_e)(\boldsymbol{N}\cdot\boldsymbol{I}_d)]\} + hE_8\{2\boldsymbol{N}^2(\boldsymbol{I}_p\cdot\boldsymbol{I}_d) - 3[(\boldsymbol{N}\cdot\boldsymbol{I}_p)(\boldsymbol{N}\cdot\boldsymbol{I}_d) \\ &+ (\boldsymbol{N}\cdot\boldsymbol{I}_d)(\boldsymbol{N}\cdot\boldsymbol{I}_p)]\} + hE_9[\boldsymbol{N}^2\boldsymbol{I}_d^2 - \frac{3}{2}(\boldsymbol{N}\cdot\boldsymbol{I}_d) - 3(\boldsymbol{N}\cdot\boldsymbol{I}_d)^2]\end{aligned} \tag{2.4}$$

where b_F, c_e, c_I, d_i, and E_i are spin interaction coefficients all of which depend on the rovibrational level (v, N) and h is the Planck constant. Theory values for these coefficients for some (v, N) have been computed and can be found in Refs [61, 62] with updated values for b_F and some E_i in Refs [63, 5].

As these are effective Hamiltonians, additional terms and corrections are possible. For example, the term related to the nuclear spin-spin interaction $\propto I_p \cdot I_d$, which is mediated by the electron spin, has been evaluated in Ref. [64]. There, the values for the $(v = 0, N = 1)$ state are given explicitly, where the individual HFS states are shifted by less than 27 Hz. Depending on the transition of interest, especially if the nuclear spin orientation is kept constant, the effect on the transition frequency is even smaller. For the electron spin transitions measured in this thesis ($m_{I,p}$, $m_{I,d}$ constant), this effect is below the measurement uncertainty of ~ 20 Hz.

Magnetic Field

The Zeeman splitting is due to the interaction of the magnetic moments of the molecule with an external magnetic field. The magnitude of the magnetic moments, arising from the

spins of the particles and the rotation of the molecule, are characterized by their g factors.

In the absence of external fields the hyperfine states are often described by a combined angular momentum basis. For example, for HD^+, $\boldsymbol{G}_1 = \boldsymbol{s}_e + \boldsymbol{I}_p$, $\boldsymbol{G}_2 = \boldsymbol{G}_1 + \boldsymbol{I}_d$, $\boldsymbol{F} = \boldsymbol{G}_2 + \boldsymbol{N}$ are used. An external magnetic field adds Zeeman splitting to the hyperfine levels, splitting them into their m_F states. In low magnetic fields smaller than about 5 mT the level splitting increases almost linearly. In this regime, HD^+ levels are thus often labeled by quantum numbers $|G_1, G_2, F, m_F\rangle$, from now on called the low-field basis. At strong fields above about 30 mT the level structure is in the Paschen–Back regime. Here, the levels can be more intuitively described by the orientation of the individual magnetic moments with respect to the strong external magnetic field. For HD^+, levels are labeled by quantum numbers $|m_s, m_{I,p}, m_{I,d}, m_N\rangle$, where $m_F = \sum_i m_i$ and m_i are the orientation of the electron spin, proton spin, deuteron spin, and rotational angular moment with respect to the external field. From now on, this is called the high-field basis. The level splitting at increasing magnetic field is shown for HD^+ in the rovibrational ground state in Fig. 2.2.

The energy of the Zeeman splitting can be described by the following Hamiltonians [65, 66]:

$$\begin{aligned}\boldsymbol{H}^{\mathsf{H}_2^+}_{Zeeman}(v,N) = &-\mu_B g_e(v,N)(\boldsymbol{B}\cdot\boldsymbol{s}_e) - \mu_B g_p(v,N)(\boldsymbol{B}\cdot\boldsymbol{I}) \\ &- \mu_B g_N(v,N)(\boldsymbol{B}\cdot\boldsymbol{N})\end{aligned} \tag{2.5}$$

$$\begin{aligned}\boldsymbol{H}^{\mathsf{HD}^+}_{Zeeman}(v,N) = &-\mu_B g_e(v,N)(\boldsymbol{B}\cdot\boldsymbol{s}_e) - \mu_B g_p(v,N)(\boldsymbol{B}\cdot\boldsymbol{I}_p) \\ &- \mu_B g_d(v,N)(\boldsymbol{B}\cdot\boldsymbol{I}_d) - \mu_B g_N(v,N)(\boldsymbol{B}\cdot\boldsymbol{N})\ ,\end{aligned} \tag{2.6}$$

where $\mu_B = 9.2740100657{\cdot}10^{-24}\ \frac{J}{T}$ [59] is the Bohr magneton and g_i are the g factors of the particles, which is a dimensionless proportionality constant describing the size of the magnetic moment associated with the spin of the particle. The total Hamiltonian is then given by $\boldsymbol{H}_{total}(v,N) = \boldsymbol{H}_{HFS}(v,N) + \boldsymbol{H}_{Zeeman}(v,N)$. See Appendix A.1 for the explicit Hamiltonian matrices in the high-field basis, for HD^+ in any $(v,0)$ state and for H_2^+ in any $(v,0)$ and $(v,2)$ state. For the low-field basis the explicit Hamiltonian matrices are given in the supplementary material of Ref. [58] for a selection of (v,N).

Electron Spin Transitions

In the work of this thesis, I measured the six electron spin transition frequencies in the rovibrational ground state of HD^+ at the trapping field of 4.02 T ($m_s \leftrightarrow -m_s$, m_p, m_d constant). In presence of an external magnetic field, the HFS Hamiltonian for the rovibrational ground state of HD^+ takes the form:

$$\begin{aligned}\boldsymbol{H}^{\mathsf{HD}^+}_{total}(0,0) = &hE_4(0,0)(\boldsymbol{I}_p\cdot\boldsymbol{s}_e) + hE_5(0,0)(\boldsymbol{I}_d\cdot\boldsymbol{s}_e) - \mu_B g_e(0,0)(\boldsymbol{B}\cdot\boldsymbol{s}_e) \\ &- \mu_B g_p(0,0)(\boldsymbol{B}\cdot\boldsymbol{I}_p) - \mu_B g_d(0,0)(\boldsymbol{B}\cdot\boldsymbol{I}_d)\end{aligned} \tag{2.7}$$

The electron spin transition frequencies can then be determined by solving for the eigenvalues of the Hamiltonian and subtracting the state energies of the two levels between which the transition occurs.

Higher-order effects due to the strong magnetic field have been calculated by Dimitar Bakalov [67]. Here, the hyperfine-assisted Zeeman shift known from atomic systems [68,

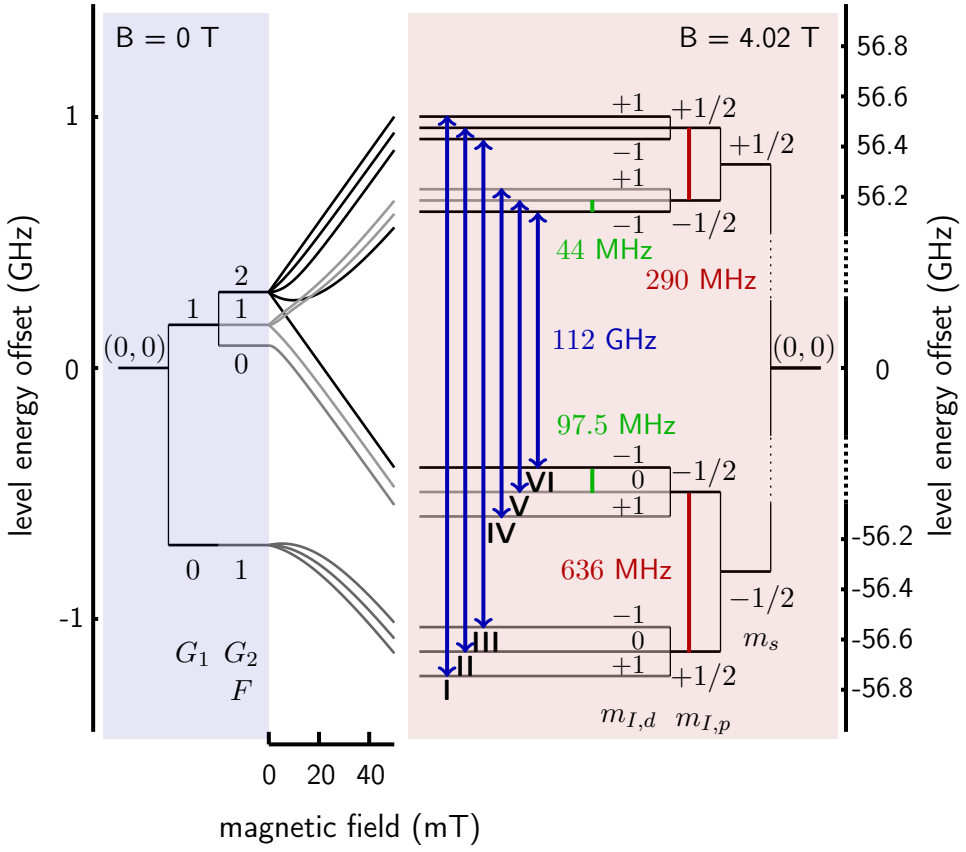

Figure 2.2: left: The hyperfine structure of HD^+ in the rovibrational ground state is shown at $B = 0$ T with the splitting labeled according to the low-field basis (G_1, G_2, and F). Note that for the rotational ground state $N = 0$ and therefore $G_2 = F$. **center:** This section shows the Zeeman splitting of the hyperfine structure at weak magnetic fields up to 50 mT. At ∼10 mT, the levels cross and the high magnetic field ordering of the level structure is reached. The different gray scales are for better visibility of the level crossing only. **right:** The hyperfine structure of HD^+ in the rovibrational ground state at the trapping field strength of 4.02 T is displayed, where the levels are labeled according to the particle-spin orientations m_s, $m_{I,p}$, $m_{I,d}$ (high-field basis). Note that $m_{I,d} = 0$ is always the center line in the groups of three level but is not marked in the upper half to not overcrowd the figure. The blue double arrows represent the six measured electron spin transitions I-VI ($m_{I,p}$, $m_{I,d}$ constant). The red and green lines mark proton and deuteron spin transitions. For the transitions, approximate frequencies are given in their respective color. Note, there are additional level crossings for the upper six states between 10 and 11 T, when the $\mu_B g_{p/d} B$ terms become larger than the E_i terms.

69], the dipole diamagnetic shift of the hyperfine structure coupling constants, also known from atomic systems [68], and a possible quadrupole diamagnetic shift arising from the electric quadrupole moment of the nuclei [68] were considered. For the electron spin transitions in the rovibrational ground state of HD^+ at our magnetic field strength of 4.02 T, the effects are orders of magnitude smaller than the measurement uncertainty.

Since the nuclear magnetic moments, and for excited (v, N) states also the rotational magnetic moments, are much smaller than the magnetic moment of the electron it is sufficient to know them to less precision than the bound-electron g factor. To compute electron spin transition frequencies to 10^{-10} precision (the experimental precision of this work), the free particle values for the nuclear magnetic moments or g factors can be used. With the magnetic moments in units of the Bohr magneton[1] the nuclear g factors are: $g_p = 3.04206440050{\cdot}10^{-3}$ and $g_d = 4.669754562{\cdot}10^{-4}$, both values are taken from CODATA22 [59]. For comparison, the order of magnitude of the rotational g factor of MHI is $g_N^{HD^+}(0,1) = 3.9886{\cdot}10^{-4}$ [66].

$E_4(0,0)$ and $E_5(0,0)$ were initially calculated in Ref. [62] and have been refined by improving the treatment of nuclear structure corrections and higher-order QED corrections in Ref. [63] to $925\,394.159(860)$ kHz and $142\,287.556(84)$, respectively [70], along with values for other rovibrational states to comparable precision. The Breit-Pauli Hamiltonian is used for these calculations. Nuclear structure effects are mostly independent of the rovibrational state and are derived from atomic hydrogen. Other corrections depend on the state and are calculated in that work, such as the relativistic Breit correction of order $(Z\alpha)^2 E_F$ and the vibrational state dependent higher-order non-recoil QED correction which is of order $\alpha(Z\alpha)^2 E_F$. Here, $Z\alpha$ is the expansion parameter for QED calculations with Z being the nuclear charge and α the fine structure constant, and E_F is the Fermi energy. The latter correction is of the order of the theoretical uncertainty and was computed as -2.9 kHz [63]. This effect is just above the theoretical uncertainty and can thus be probed by a measurement with a significantly smaller uncertainty, performed in the work of this thesis. In conclusion, the precision of the HFS theory of MHI is comparable to the precision of the HFS theory of atomic hydrogen, and thus it is worthwhile to experimentally probe the calculations of this fundamental interaction in MHI.

The bound-electron g factors of H_2^+ and HD^+ were calculated in the 1970s by Hegstrom to a precision of 0.1 ppm [4]. Here, calculations starting with the Breit formalism result in a g tensor that is accurate to order α^2. The numerical values for the g-tensor contributions depend on the internuclear distance, resulting in distinct values of the g-tensor components for each rovibrational state. The explicit values are computed in the coordinate frame of the internuclear axis, giving rise to two unique components: $g_\perp = g_{xx} = g_{yy}$ perpendicular and $g_\parallel = g_{zz}$ parallel to the internuclear axis. The scalar isotropic g factor of a rovibrational state is computed by:

$$g_{\mathrm{av}}(v, N) = \frac{1}{3}(2g_\perp(v, N) + g_\parallel(v, N)) \tag{2.8}$$

[1] All g factors, including the nuclear g factors, are given with the magnetic moments in units of the Bohr magneton μ_B, following the notation of previous work ([58]).

As an example, for the ground rovibrational state of HD^+, following values are listed [4]:

$$1 - \left(\frac{g_\perp}{g_\mathrm{e}}\right)_{0,0} = 20.817 \cdot 10^{-6} \tag{2.9}$$

$$1 - \left(\frac{g_\parallel}{g_\mathrm{e}}\right)_{0,0} = 19.562 \cdot 10^{-6}\ , \tag{2.10}$$

where g_e is the free-electron g factor.

Recently, leading-order relativistic corrections of order α^2 have been evaluated for $g_\mathrm{e}(H_2^+)$ [71]. Nevertheless, the uncertainty of the g_e factor remains at 0.1 ppm due to uncalculated radiative corrections of order α^3. Currently, efforts are being made to calculate these terms, allowing a theoretical prediction of the g_e factor of H_2^+ and HD^+ to better than the 10^{-10} level [72].

The contribution of the g_e term to the electron spin transition frequency ($\Delta m_s = 1$) is by far the largest: $\frac{\mu_B}{h} g_e(0,0)(B\Delta m_s) \approx 112\,660$ MHz versus $E_4(0,0)(\frac{1}{2}\Delta m_s) \approx 463$ MHz and $E_5(0,0)(1\Delta m_s) \approx 142$ MHz, which, on an order of magnitude scale, is true for excited rovibrational states as well. Therefore, the uncertainty of the $g_e(v,N)$ factor limits the precision with which the electron spin transition frequencies can be predicted.

As all hyperfine coefficients and bound g factors depend on the internuclear separation and thus on the rovibrational state, each such state has a unique electron spin transition frequency. By measuring this frequency, the rovibrational and hyperfine state can be determined nondestructively. This is an important prerequisite for future measurements of $\overline{H}_2^+$, for which this technique has been proposed [2] and which has been demonstrated in the work of this thesis for HD^+.

2.2 Overview of *state-of-the-art* Experiments on MHI

In this section, I will give an overview of the efforts and success of experimental groups working towards characterizing MHI and using them to probe our understanding of fundamental physics or for the extraction of fundamental constants. This is focused on results that either relate to the measurements performed in the course of this thesis or can be viewed as a step towards making a high-precision measurement of $\overline{H}_2^+$ feasible for CPT tests with MHI.

2.2.1 Rovibrational Transition Frequency Measurements

Several high-precision measurements of rovibrational transition frequencies have been performed on small ensembles of HD^+ in Paul traps using destructive measurement techniques [73, 74, 75, 35]. They all agree with the theoretical predictions of the respective rovibrational transition frequencies, thereby confirming QED calculations of rovibrational level energies at the 10^{-11} level. The results are used to extract $\frac{m_p m_d}{m_p+m_d}/m_e$ and combined with CODATA values then $\frac{m_p}{m_e}$ [70, 59] or probe for beyond Standard Model physics [36]. Note, to extract the final spin-average rovibrational transition frequency from the measurements, the effect of the hyperfine structure has to be known and corrected for.

Single-ion rovibrational measurements have been demonstrated for HD^+ as well, although, as for now, only with in-trap production, co-trapping with a Be^+ ions and a destructive state detection technique [40], all of which would not be feasible for an antimatter experiment using $\overline{H}_2^+$.

Recently, the measurement of rovibrational transition frequencies of H_2^+ has been achieved on ion ensembles [76, 37]. One approach uses highly excited Rydberg states of H_2 [76], while the other the same technique as the ensemble measurements of HD^+ in Paul traps which entails destructive state detection methods and co-trapping with Be^+ [37]. While measurements of the E2 transitions of the rovibrational transitions in H_2^+ are a great achievement, both approaches in their current state would not be feasible for an antimatter experiment using $\overline{H}_2^+$.

2.2.2 Hyperfine Structure

There have been two direct measurements of the HFS of H_2^+. Jefferts [77] measured 30 radio-frequency HFS transitions in rovibrational levels $v = 4 - 8$, $N = 1, 2$ with linewidths and uncertainties of 1.5 kHz. The results allow for the determination of HFS Hamiltonian coefficients, namely of the spin-spin scalar interaction coefficient b_F (see Eq. 2.3). For $N = 1$ the values agree with the theoretical prediction [63]. However, for all the v states measured, the experimental values are larger than the theoretical values by $5\text{-}10{\cdot}10^{-7}$ relatively. Menasian [78] measured three RF transitions in the HFS of H_2^+ down to a linewidth and precision of single Hz.

Besides direct measurements, rovibrational measurements relay information about the HFS as well. A rovibrational laser spectroscopic measurement on trapped ensembles of HD^+ ions allowed the determination of the spin-spin scalar interaction coefficients $E_4(0,0) = 906(17)$ MHz and $E_5(0,0) = 142.33(25)$ MHz (see Eq. 2.4) [79]. The more recent results of high-precision spectroscopy of HD^+, discussed above, do not allow the extraction of HFS Hamiltonian coefficients because the transitions depend on several such coefficients. Nevertheless, the combination of the available measurements allows to test HFS predictions down to 0.32 kHz [75]. However, a comparison of several measurements to HFS theory yields that while some measurements agree with HFS theory others deviate by up to 9 σ [5]. These large deviations pose a puzzle since HFS theory is used as an input parameter in the determination of fundamental mass ratios from these measurements. If attributed to E_5, the hypothetical error of the HFS theory would have to be at the level of $\sim$10 kHz [5], assuming correct treatment of the vibrational dependence of the E coefficients. In the measurements performed within this thesis, such a deviation would have been well resolved and the hypothesis can be rejected under the latter assumption.

Recently, nondestructive single-ion measurements of H_2^+ have been performed [41, 42]. The group demonstrated motional ground-state preparation and HFS measurement transitions with sub-100 Hz line widths and single-Hz statistical uncertainty (10^{-9} relative uncertainty). Here, in-trap production, buffer gas cooling, and co-trapping with a Be^+ ion were used and they achieved a trapping time of about 11 h. While these measurements are a great achievement the current techniques would not be feasible for an antimatter experiment using $\overline{H}_2^+$. However, the group is en-route to rovibrational spectroscopy with the aim of a high precision of up to 10^{-16}-10^{-17} [42]. These results will be exciting for the test of fundamental physics and/or the determination of fundamental constants.

All the measurements performed so far have tested HFS theory of MHI in the regime of low magnetic fields. In the work of this thesis, HFS theory was probed in strong magnetic fields.

2.2.3 Bound-Electron g Factor

In RF traps, the magnetic field applied for measurements is in the order of $1{\cdot}10^{-4}$ T [73]. The low absolute field strength coupled with the limited achievable precision in the calibration of the magnetic field compared to Penning traps, make high-precision measurements of magnetic field sensitive transitions and therefore molecular properties, such as the g_e factor, less feasible. For H_2^+, the theoretical prediction of the bound electron g factor has been confirmed in the past by a measurement at 0.9 ppm precision [80]. Here, the g factor of H_2^+ averaged over the vibrational states $v = 4 - 6$ was determined. An ensemble of ions were stored in a Penning trap, and the spin transitions were driven by RF fields, while the state detection was carried out destructively by spin-dependent charge-exchange collisions. Applying high-precision magnetic field determination techniques, developed in Penning traps for atomic ions, and demonstrating nondestructive internal quantum state detection has lead to orders of magnitude improvement for the determination of bound electron g factor of HD^+, in the work of this thesis.

2.2.4 Mass Measurements

Both H_2^+ and HD^+ have been used for high-precision mass measurements in dedicated Penning-trap setups, the Penning trap at Florida State University [81, 82] and LIONTRAP at the University of Mainz [83], respectively. For both setups, the MHI are produced in-situ by electron-impact ionization and demonstrate long confinement times on the order of months. Note, both setups do not allow for ion production or external ion loading of exotic species such as antimatter. The HD^+ mass was measured to be 3.021378241561(61) u [83] and was used in the evaluation of the measurement campaign determining the g_e factor and HFS coefficients in the work of this thesis.

H_2^+ was used along with D^+ for the determination of the deuteron-to-proton mass ratio [81, 82]. In these measurements, they could track the vibrational decay of single H_2^+ ions over months by resolving the mass difference of the ion related to a change of $\Delta v = -1$. Following $E = mc^2$ (energy equals mass times speed of light in vacuum squared), the relative mass increase per vibrational excitation quantum is at the level of about $1{\cdot}10^{-10}$. The energy per rotational quantum is about two orders of magnitude smaller. Therefore, different rotational quantum states could only be disentangled to a limited probability by post processing the data of a several-month-long measurement campaign, which nevertheless is an impressive achievement. Additionally, they showed that the vibrational decay rate can be increased by Stark quenching [84], achieved by placing the ion on a large cyclotron orbit in their magnetic field of $\sim$8.5 T.

3 Penning Traps

In the low energy, atomic-physics approach for tests of fundamental physics, confinement and low temperatures of the particles of interest has lead to high precision [85, 10, 86, 87]. Different types of trapping systems have been developed for charged particles, such as radio-frequency Paul traps [88] and Penning traps [89]. The latter were first described by Pierce in 1949 [90] and implemented by Hans Georg Dehmelt in the 1950s [89]. Since then, they have been used for various purposes, ranging from ion storage to high-precision measurements [85, 10, 24, 91].

Compared to other trapping techniques, Penning traps provide very stable, low-noise environments resulting from solely static trapping fields. At the same time the trap depth can be very deep compared to, for example, magnetic multipole traps for neutral particles [24], enabling the confinement of hot particles. It is well-established to have cryogenic Penning traps, allowing extremely good vacuum conditions and almost infinite storage times [91, 43]. Coupled with the non-destructive image-current read-out technique this allows for high-precision measurements of ions that are rare or hard to produce [91, 48]. However, compared to other atomic physics experiments, measurements in Penning traps are rather slow. Additionally, the strong magnetic field usually entails a superconducting NMR type magnet in which the trap electrodes are placed. Therefore, optical access to the trapping region is limited, often only with access along one axis. There are, of course, exceptions, such as the trap of the Bollinger group at NIST, with three dimensional optical access [92].

Here, I will give a brief overview of the principle of Penning traps, for details see Ref. [85]. For more details on the specifications of ALPHATRAP see Ref. [48]. At ALPHATRAP we trap and perform measurements on atomic and molecular ions. Although, in general Penning traps can be used to trap and perform measurements on other charged particles, such as electrons [85, 10] as well, I will from here onward, talk about ions as the trapped charged particles. Nevertheless, the basic principles introduced are at least qualitatively valid for other charged particles as well.

3.1 Basic Principles

Ideal Trap

In Penning traps three-dimensional confinement is achieved by superposition of a static homogeneous magnetic field: $\mathbf{B} = B_0 e_z$ and a static quadrupole electric field. A homogeneous magnetic field along the z axis generates a confining potential in the xy plane. Therefore, a charged particle in a static homogeneous magnetic field will follow a circular

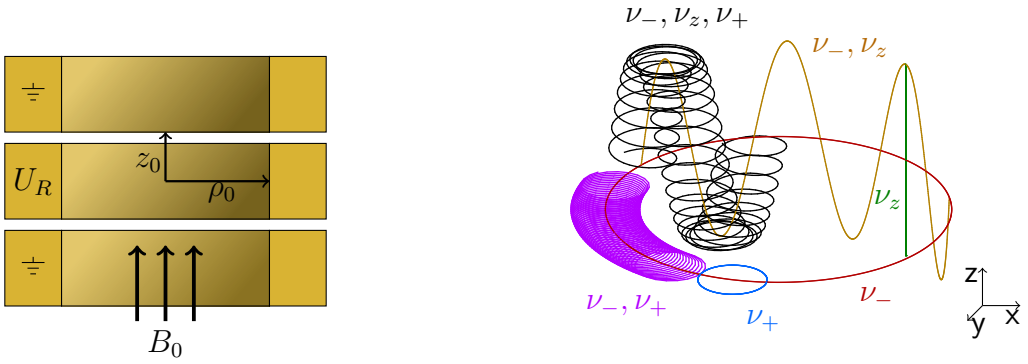

Figure 3.1: left: Schematic of a Penning trap. A vertical cut through three cylindrical electrodes: the ring electrode in the center at a voltage of U_R with a grounded endcap electrode above and below. Note, to generate a quadrupole electric field in a real trap either hyperbolically-shaped electrodes [85] or cylindrical correction electrodes inserted in between the ring and endcap electrodes [48] can be used. The magnetic field B_0 along the z axis is indicated by arrows at the bottom. The characteristic dimensions z_0 and ρ_0 are shown as arrows on the ring electrode. **right**: Motion of an ion in a Penning trap. The eigenmotions ν_-, ν_z, ν_+ are shown as a large red circle, green vertical line, and small blue circle, respectively. The superpositions ν_-, ν_z, ν_-, ν_+ and the full motion ν_-, ν_z, ν_+ are depicted as a yellow oscillation, magenta spiral and black trajectory. For better visibility, the frequencies and amplitudes are not to scale.

motion with the free-space cyclotron frequency ν_c

$$\nu_c = \frac{1}{2\pi}\frac{q}{m}B_0 \ , \tag{3.1}$$

where q is the charge of the particle and m its mass.

By applying voltages to a set of electrodes stacked along the z axis, a confining electric potential is generated along this dimension (z) and a deconfining one along the radial direction (x, y). The criterion for such a trap is that the confining force due to the magnetic field is stronger than the deconfining force due to the electric field in the xy plane. The static electric potential for a quadrupole electric field is given by [93]:

$$\Phi(z, \rho) = \frac{-U_R}{2}\frac{C_2}{d_{char}^2}(z^2 - \frac{\rho^2}{2}) \ . \tag{3.2}$$

Here, U_R is the voltage applied to the ring (center) electrode of the trap, $C_2 \sim 1$ is a dimensionless constant depending on the geometry of the trap, $d_{char} = \frac{1}{2}\sqrt{2z_0^2 + \rho_0^2}$ is the characteristic trap length, with z_0 and ρ_0 being the distance from the center of the trap to the endcap electrode (ground) and the radius of the ring electrode, respectively. $\rho = \sqrt{x^2 + y^2}$ is the radius in cylindrical coordinates. A schematic of a Penning trap is shown in Fig. 3.1.

When superimposing the electric and magnetic field, the motion becomes more complex than the free-space cyclotron motion. Generally, the equation of motion for a charged particle in an electromagnetic field is given by:

$$m\ddot{\boldsymbol{x}} = -q\boldsymbol{\nabla}\Phi + q\dot{\boldsymbol{x}} \times \boldsymbol{B} \ , \tag{3.3}$$

where $\boldsymbol{x} = \{x, y, z\}$ is the position vector, $\boldsymbol{\nabla}$ is the gradient operator, and $\times$ denotes the cross product. For the superposition of the homogeneous magnetic field with the static quadrupole electric field of the Penning trap, the z component can be written as [93]:

$$\ddot{z} + \frac{q(-U_R)C_2}{md_{char}^2} z = 0 \ , \tag{3.4}$$

resulting in the frequency of the eigenmotion in axial direction (ν_z):

$$\nu_z = \frac{1}{2\pi}\sqrt{\frac{q(-U_R)C_2}{md_{char}^2}} \ . \tag{3.5}$$

The equations of motion for the x and y direction are given as [93]:

$$\ddot{x} - 2\pi\nu_c\dot{y} - \frac{1}{2}(2\pi)^2\nu_z^2 x = 0 \ , \tag{3.6}$$

$$\ddot{y} + 2\pi\nu_c\dot{x} - \frac{1}{2}(2\pi)^2\nu_z^2 y = 0 \ . \tag{3.7}$$

$$\tag{3.8}$$

When solving these equations of motion, one arrives at the frequencies for the two radial eigenmotions of the particle, the modified cyclotron frequency ν_+ and the magnetron frequency ν_-:

$$\nu_+ = \frac{\nu_c}{2} + \frac{1}{2}\sqrt{\nu_c^2 - 2\nu_z^2} \ , \tag{3.9}$$

$$\nu_- = \frac{\nu_c}{2} - \frac{1}{2}\sqrt{\nu_c^2 - 2\nu_z^2} \ . \tag{3.10}$$

The motion of an ion within the Penning trap is depicted in Fig. 3.1. The squared sum of all three eigenfrequencies gives access to the free-space cyclotron frequency via the invariance theorem [85]:

$$\nu_c^2 = \nu_+^2 + \nu_z^2 + \nu_-^2 \ . \tag{3.11}$$

Using the invariance theorem for the determination of ν_c is advantageous as it is independent of some systematic shifts arising from imperfections of the setup. Such imperfections are impossible to avoid in a real-life setup due to finite precision in manufacturing of the electrodes and positioning of the trap in the magnet. Possible effects are a tilt of the magnetic and electrostatic fields with respect to each other due to finite precision in the positioning of the trap in the magnet and an elliptic deformation of the electrostatic potential due to finite precision in the manufacturing of ring-shaped electrodes that will differ from a perfectly circular shape.

The magnitude of frequencies of the ion are ordered as following: $\nu_c \gtrsim \nu_+ \gg \nu_z > \nu_-$. The total (potential and kinetic) energies of these modes (E_-, E_z, E_+) are given by [94]:

$$E_- = -h\nu_-(n_- + \frac{1}{2}) \approx -\frac{1}{4}m(2\pi)^2\nu_z^2 r_-^2 \Rightarrow -k_B T_- \tag{3.12}$$

$$E_z = h\nu_z(n_z + \frac{1}{2}) \quad = \frac{1}{2}m(2\pi)^2\nu_z^2 z^2 \quad \Rightarrow k_B T_z \tag{3.13}$$

$$E_+ = h\nu_+(n_+ + \frac{1}{2}) \quad \approx \frac{1}{2}m(2\pi)^2\nu_+^2 r_+^2 \quad \Rightarrow k_B T_+ \ , \tag{3.14}$$

Table 3.1: Approximate values for the frequencies, radii, and corresponding energies and temperatures of the eigenmotions of an HD^+ ion in the trap region for precision measurements in the ALPHATRAP setup.

	modified cyclotron	axial	magnetron
ν_i	20 MHz	650 kHz	10 kHz
T_i	277 K	9 K	0.14 K
$\hat{n}_i$	$288\,510$	$288\,510$	$288\,510$
$\hat{z}$, $\hat{r}_i$	10 μm	54 μm	10 μm

where h is the Planck constant, n_i is the quantum number of the respective motional mode, k_B is the Boltzmann constant, T_i the effective temperature of the respective motional mode, r_i the radius of the circular modes, and z the amplitude of the axial mode. Note the negative energy of the magnetron motion. In the case of the comparatively slow magnetron motion, the value of the negative potential energy is greater than the kinetic energy leading to a metastable eigenmode, contrary to the fast cyclotron motion where the kinetic energy is much larger.

In the absence of additional excitation fields, the three motional modes of the trapped ion are well decoupled. Adding radio frequency (RF) electric excitation fields the motional modes can be coupled to each other (described in Sec. 3.2.3), as is the case in the measurements performed in the work of this thesis (see Ch. 5). When coupled, the average quantum number $\hat{n}_i$ of the motional modes are equal. Thereby, the effective temperatures follow the relation: $T_i = T_j \frac{\nu_i}{\nu_j}$ which results in: $T_- < T_z < T_+$. When coupled, the average amplitudes of the eigenmotions relate as $\hat{r}_-^2 = \hat{r}_+^2 = \hat{z}^2 \frac{\nu_z}{\nu_+}$. Exemplary values for HD^+ in the ALPHATRAP setup are given in Tab. 3.1.

Imperfections

For a trap stack of cylindrical electrodes, which is the case at ALPHATRAP, the electrostatic potential deviates from the ideal case of Eq. 3.2. The electric potential can be expanded around the position $z = 0, \rho = 0$ by [93]:

$$\Phi(z,\rho) = \frac{U_R}{2} \sum_{n=0}^{\infty} \frac{C_n}{d_{char}^n} \sum_{k=0}^{floor(\frac{n}{2})} \frac{(-1)^k n!}{2^{2k}(n-2k)!(k!)^2} z^{n-2k} \rho^{2k} \ . \tag{3.15}$$

Additionally, the magnetic field in a real trap is not perfectly homogeneous. The magnetic field $\mathbf{B} = B_z e_z + B_\rho e_\rho$ can be expanded around $z = 0$, $\rho = 0$ [93]:

$$B_z(z,\rho) = \sum_{n=0}^{\infty} B_{z,n} \sum_{k=0}^{floor(\frac{n}{2})} \frac{(-1)^k n!}{2^{2k}(n-2k)!(k!)^2} z^{n-2k} \rho^{2k} \ , \tag{3.16}$$

$$B_\rho(z,\rho) = \sum_{n=0}^{\infty} B_{\rho,n} \sum_{k=1}^{floor(\frac{n+1}{2})} \frac{(-1)^k k n!}{2^{2k-1}(n-2k+1)!(k!)^2} z^{n-2k+1} \rho^{2k-1} \ . \tag{3.17}$$

Here, $floor()$, defining the upper bound of the sum, means to cut the decimal number of $\frac{n}{2}$ or $\frac{n+1}{2}$ to the next lower integer. (Therefore: $B_{\rho,n=0} = 0$, retaining $\boldsymbol{B}_0 = B_{z,0} e_z$,

without a radial component). Both the higher orders of the electric potential and the magnetic field shift the motional frequencies of the ion depending on the amplitude of each eigenmotion, due to the spacial dependence of the fields on z and ρ. The precision to which the motional radii are known determine how precisely the shifts of the motional frequencies can be corrected for. Therefore, the uncertainty in the radii leads to systematic uncertainties in measurements. Explicit equations for such frequency shifts are given in Ref. [93]. Systematic shifts to the measurements, carried out in the course of this thesis, are discussed in detail in Sec. 5.6.3. To minimize such effects, traps are designed and tuned to ideally have $C_n = 0$ for all $n > 2$ and $B_n = 0$ for all $n > 0$, approaching the ideal Penning trap. In a real setup, it is of course not possible to null all terms. Traps are designed and tuned to minimize the lower-order C_4, C_6 and sometimes C_8, C_{10}, while odd orders of the electric potential are mitigated to a large extent by the symmetry of the trapping field. For the electrostatic potential at ALPHATRAP, this is realized by adding correction electrodes between the ring and endcap electrodes, where the ring and correction electrodes have optimized lengths, and setting optimized voltages to them. B_1 and B_2 can be minimized as well, by fine-tuned positioning of ferromagnetic material in the trap chamber and by applying current to coils around the trap chamber. Terms of higher order scale with larger potentials of the spacial coordinates (z, ρ) and their effects are therefore strongly suppressed when the motional amplitudes of the ion ($\hat{z}^n$, $\hat{r}_i^n$) are small.

3.2 Image Current Detection

To detect an ion in a Penning trap, the image current induced in an electrode by the trapped oscillating ion can be measured. Here, I will outline the axial detector system since, at ALPHATRAP, it is used to cool the ion to the temperature of the cryostat as well as for frequency determination of not only the axial motion of the ion in the trap (ν_z) but also of both radial motional modes (ν_-, ν_+). The magnitude of the induced current in an electrode is given by

$$I_{ind} = q\frac{\dot{z}}{D_{eff}} \ , \tag{3.18}$$

where q is the charge of the ion, $\dot{z}$ the time derivative of the position, so the motion of the ion, and D_{eff} the effective electrode distance. These currents are typically at the fA scale and are therefore not straightforward to detect, requiring a resonant circuit introduced in the following.

3.2.1 Resonator Circuit

To measure such small, fA-scale image currents a cryogenic, high-impedance superconducting tank circuit (resonator) and a cryogenic amplifier are employed. The signal can be measured as a voltage drop across this system. A fast Fourier transformation (FFT) then relays the frequency information. The circuit is shown in Fig 3.2. It consists of an inductance L formed by a superconducting coil, a capacitance C which is a combination of parasitic capacitances e.g. of the trap electrode itself and added capacitance to tune the resonance frequency of the circuit, $\nu_{res} = \frac{1}{2\pi}\frac{1}{\sqrt{LC}}$, and a resistance R which is entirely

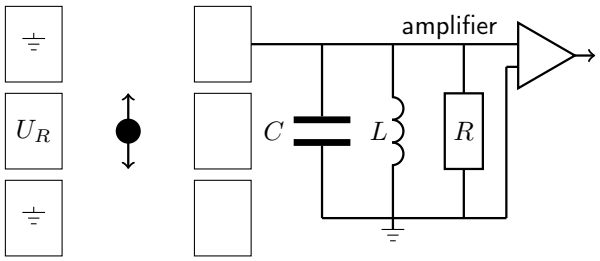

Figure 3.2: Circuit of the detection system. The ion is depicted as a black circle oscillating in a trap. The resonator circuit is connected to the upper endcap to pick up the image current. (In a real cylindrical trap it can instead be connected to a correction electrode.) The circuit consists of an inductance L, a capacitance C and a parasitic resistance R. The voltage drop across the resonator is amplified by a cryogenic amplifier. The signal then continues on to room temperature for further amplification and processing, indicated by the arrow.

parasitic. The total impedance Z_{res} of the circuit is given as:

$$Z_{res}(\nu) = \frac{1}{\frac{1}{i2\pi\nu L} + i2\pi\nu C + \frac{1}{R}} = \frac{R}{1 + iQ\left(\frac{\nu}{\nu_{res}} - \frac{\nu_{res}}{\nu}\right)} , \tag{3.19}$$

where Q is the quality factor, $Q = \nu_{res}/\Delta\nu_{res} = R\sqrt{\frac{C}{L}}$, with the full width at half maximum (FWHM) $\Delta\nu_{res}$.

The typical resonator line shape of the thermal noise detected with the cryogenic amplifier in a Fourier spectrum is shown in Fig 3.3. The basic line shape is given by the root-mean-square (rms) voltage U_{JN} of a bandwidth $\Delta\nu$, due to the thermal current noise (Johnson-Nyquist noise) of the circuit [95, 96]:

$$U_{JN} = \sqrt{4k_B T Re(Z_{res}(\nu))\Delta\nu} , \tag{3.20}$$

where, k_B is the Boltzmann constant, T the temperature, $Re(Z_{res}(\nu))$ is the real part of the impedance Z_{res} of the resonator circuit which is frequency (ν) dependent. Additionally, the cryogenic amplifier adds noise which can be approximated as white noise in a frequency range of a few kHz, U_{amp}. The transfer function of the system is slightly frequency dependent and can be approximated by a linear slope κ of the signal. The amplification of the signal is denoted as A. Therefore the final signal has the form [97]:

$$U_{res} = A(1 + \kappa 2\pi(\nu - \nu_{res}))\sqrt{U_{JN}^2 + U_{amp}^2} . \tag{3.21}$$

We analyze and fit the signals in dBV_{rms}, therefore the final FFT signal line shape of the resonator is given by $20\,log_{10}(U_{res})$.

3.2.2 Ion Signal and Thermalization

If the motional frequency on the trapped ion is in or close to resonance with the detection system, the signal of an ion hotter than the system appears as a peak in the Fourier

spectrum, visible in Fig 3.3, as well. The axial frequency of the ion can easily be tuned across a broad range due to its dependence on the applied ring voltage (see Eq. 3.5).

Additionally, the current induced in the electrode by the trapped ion is dissipated in the tank circuit, resulting in an effective cooling of the motion of the ion. In equilibrium, the cooling effect is canceled by the thermal Johnson-Nyquist noise of the tank circuit. Therefore, the eigenmotion that is coupled to the resonator is cooled to the temperature of the thermal Johnson-Nyquist noise. At ALPHATRAP the resonators and cryogenic amplifiers are thermally coupled to the 4 K of a liquid-helium cryostat. In equilibrium, the current induced by the ion in the resonator circuit then exactly cancels the Johnson-Nyquist noise so that the ion is visible as a dip in the frequency spectrum at ν_z [98], shown in Fig 3.3.

The cooling time constant τ for the motion of the ion is given as [48]:

$$\tau(\nu) = \frac{mD_{eff}^2}{q^2 Re(Z_{res}(\nu))} \ . \tag{3.22}$$

The dip line shape of the combined signal of an ion on the resonator can by derived by modeling the ion as a series LC circuit with $L_{ion} = \frac{mD_{eff}^2}{q^2}$ and $C_{ion} = \frac{q^2}{(2\pi)^2 \nu_z^2 m D_{eff}^2}$ as the inductance and capacitance, respectively [98, 48]. Consequently, the impedance of the ion is:

$$Z_{ion}(\nu) = i2\pi\nu L_{ion} + \frac{1}{i2\pi\nu C_{ion}} = i2\pi\nu \frac{mD_{eff}^2}{q^2}\left(1 - \frac{\nu_z^2}{\nu^2}\right) \ . \tag{3.23}$$

The voltage signal of the resonator and the ion is then given by plugging the combined impedance of both $Z_{tot}(\nu) = \left(\frac{1}{Z_{res}} + \frac{1}{Z_{ion}}\right)^{-1}$ into the rms voltage of the Johnson-Nyquist noise:

$$U_{res} = \sqrt{4k_B T Re(Z_{tot}(\nu))\Delta\nu} \ . \tag{3.24}$$

The spectral width of the dip signal of N identical ions (Γ) relates to the cooling time constant τ as follows [48]:

$$\Gamma = \frac{N}{2\pi\tau} \ . \tag{3.25}$$

This emphasizes that for a given resonator circuit and trap geometry the width of the dip signal of the ion as well as the cooling time strongly depend on its charge and mass. For more detail on the line shapes of the signals and their derivations and specifications of the ALPHATRAP detection system see Refs. [48, 97, 99].

3.2.3 Radial Modes

So far, I have explained how we cool and measure the axial frequency mode that is coupled and tuned to the detection system. Although modified cyclotron resonators are possible and implemented at ALPHATRAP by picking up the image current induced in radially split electrodes, they come with some challenges. First, the modified cyclotron frequency is essentially not tunable as it depends mostly on the magnetic field value (see Eq. 3.9) which is fixed for our setup. This would, therefore, require either building a frequency-matched resonator for each ion of interest or a resonator with a very broad tuning range. The latter is now implemented at ALPHATRAP, but had not been for the hyperfine structure measurements presented in this thesis. Second, the maximal impedance of the resonator

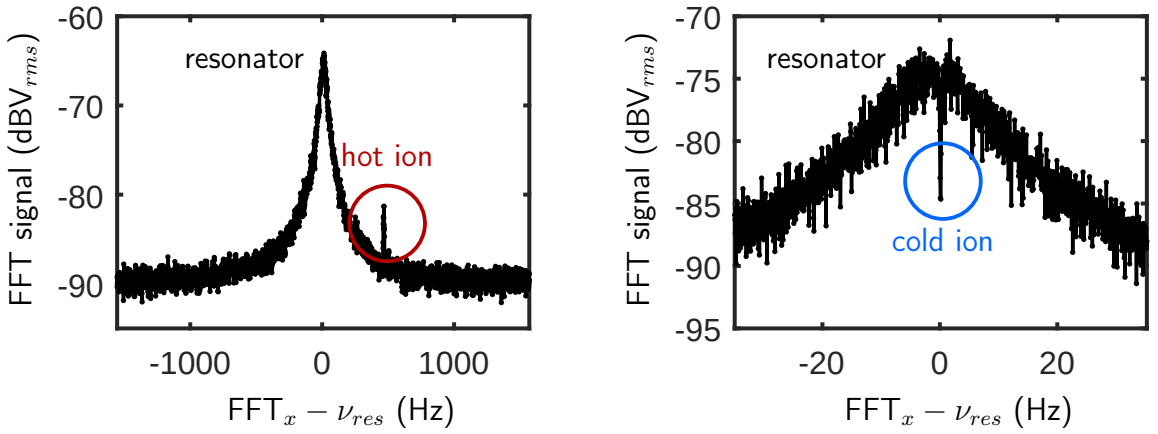

Figure 3.3: Typical resonator and ion signals. **left:** Spectral resonator signal with the peak signal of a hot ion detuned to higher frequencies. **right:** Resonator signal with the dip signal of a cold ion in resonance with the detection system. For both plots the x axis shows the frequency of the fast-Fourier transformation (FFT$_x$) centered at the resonator frequency (ν_{res}).

is given as $Z_{res}(\nu_{res}) = \frac{Q}{2\pi\nu_{res}C}$. The lower bound for C is fixed by the capacitance of the trap electrodes to the same order of magnitude as for the axial detection system. ν_{res} must match the modified cyclotron motion so at ALPHATRAP it is roughly a factor of 40 larger than for an axial detector and the Q value at these frequencies tend to be much lower than at axial frequencies (at ALPHATRAP about a factor of 20). Therefore, the cooling time constant/dip width of the ion are about 800 times larger/reduced (see Eq. 3.22). While peak detection is possible, this makes direct high-precision dip measurements unfeasible. Additionally, such a detection is not possible for the magnetron frequency. The negative energy of this mode results in radial loss of the ion if any energy is dissipated.

Alternatively, the radial modes can be coupled to the axial motion for thermalization and frequency determination by applying a RF red sideband drive at $\nu_{drive} = \nu_{\pm} \mp \nu_z$. The quadrupolar excitation for this coupling is realized by applying an electric RF signal on a radially split electrode axially off-center of the trap (not the ring electrode). The resulting electric field of the drive is proportional to $ze_x + xe_z$ [48]. (x is chosen arbitrarily without loss of generality.) Thereby, the strength of the drive depends on the position of the ion. Due to the coupling drive, energy is exchanged coherently between the two modes, whereby the amplitudes of both modes undergo Rabi oscillations and energy from both modes can be dissipated in the resonator circuit. When coupled, the average quantum numbers $\hat{n}_i$ of both modes are equal, resulting in the energy relations and exemplary values listed at the end of Sec. 3.1.

On the FFT spectrum of the axial resonator, the coupling of the axial to a radial mode results in two dip signals (sidebands), each one Rabi frequency higher or lower than the pure axial frequency dip, which is no longer visible, see Fig. 5.7. After measuring the axial frequency ν_z, switching on the coupling drive at ν_{drive} and measuring the two sideband dip positions left and right of the initial dip signal (ν_l ,ν_r), the radial frequency can be determined by:

$$\nu_{\pm} = \nu_{drive} \mp \nu_z \pm \nu_l \pm \nu_r \ . \tag{3.26}$$

This allows for a small detuning of ν_{drive}, which results in a slight asymmetric frequency difference of the sidebands with respect to the axial frequency.

Furthermore, by coupling the modes, amplitude and phase information is transferred as well which is important for phase-sensitive measurement techniques, such as *Pulse-and-Amplify* (PnA) [100], details given in Sec. 5.5.

4 ALPHATRAP

In this chapter, I will give an overview of the ALPHATRAP setup. For details see Ref. [48]. Here, I will introduce the cryogenic trap stack of electrodes and electronics at the heart of the setup, the cryostat and magnet in which it is placed, and the room-temperature beamline connecting to the ion sources, as well as the millimeter wave (MW) and laser setup. Furthermore, the new MHz excitation line for magnetic dipole (M1) transitions is described, that was simulated and implemented in this thesis work.

In this chapter, the current state of the setup is presented, along with a comparison of the status before and after the upgrade, which we performed in my time at ALPHATRAP. Note, that the hyperfine structure (HFS) measurements of HD^+ were carried out before the upgrade to the cryogenic setup. An overview of the beamline and trap setup is presented in Fig. 4.1.

4.1 Ion Sources and Beamline

Currently, there are three ion sources connected to the beamline at ALPHATRAP. There is a Heidelberg compact electron beam ion trap (HC-EBIT) [101], used for light-mass ions and medium-high charge states with single-keV ionization energies ranging from molecular hydrogen ions (MHI) to $^{40}Ar^{16+}$ and the Heidelberg EBIT, used for heavy highly charged ions with tens of keV ionization energies, such as $^{118}Sn^{49+}$ [102]. Both EBITs have a gas injection system. Furthermore, there is a laser ablation ion source (LIS) for singly charged ions ablated from a solid surface, such as $^{9}Be^{+}$ [103].

In the work of this thesis, the HC-EBIT was used to ionize HD gas for the production of HD^+ ion bunches that were guided to the trap along the beamline. Therefore, in the following, I will briefly describe the underlying principles of an EBIT. A schematic is shown in Fig. 4.2.

The ionization process in an EBIT is electron impact ionization. In the HC-EBIT, electrons are emitted from the cathode and accelerated by a voltage difference of single kV between the cathode ($\sim$-1.3 kV) and anode ($\sim$+1 kV), creating an electron beam. The electron beam is further accelerated by a single-kV voltage difference to the drift tube electrodes ($\sim$+2.3 kV), resulting in an electron beam energy of $\sim$3.6 keV. The collector behind the drift tubes is set to negative voltage to block and collect the electron beam. Ideally, the magnetic field is zero at the electron gun and the collector and maximal at the center of the trap, whereby the electron beam is compressed to form a dense beam for ionization and then diverges at the collector. The static magnetic field is generated by a stack of NdFeB permanent disk magnets in an iron yoke [101]. The gas of the species of interest is leaked into the EBIT via a fine-dosing valve. Axial confinement of the ions is

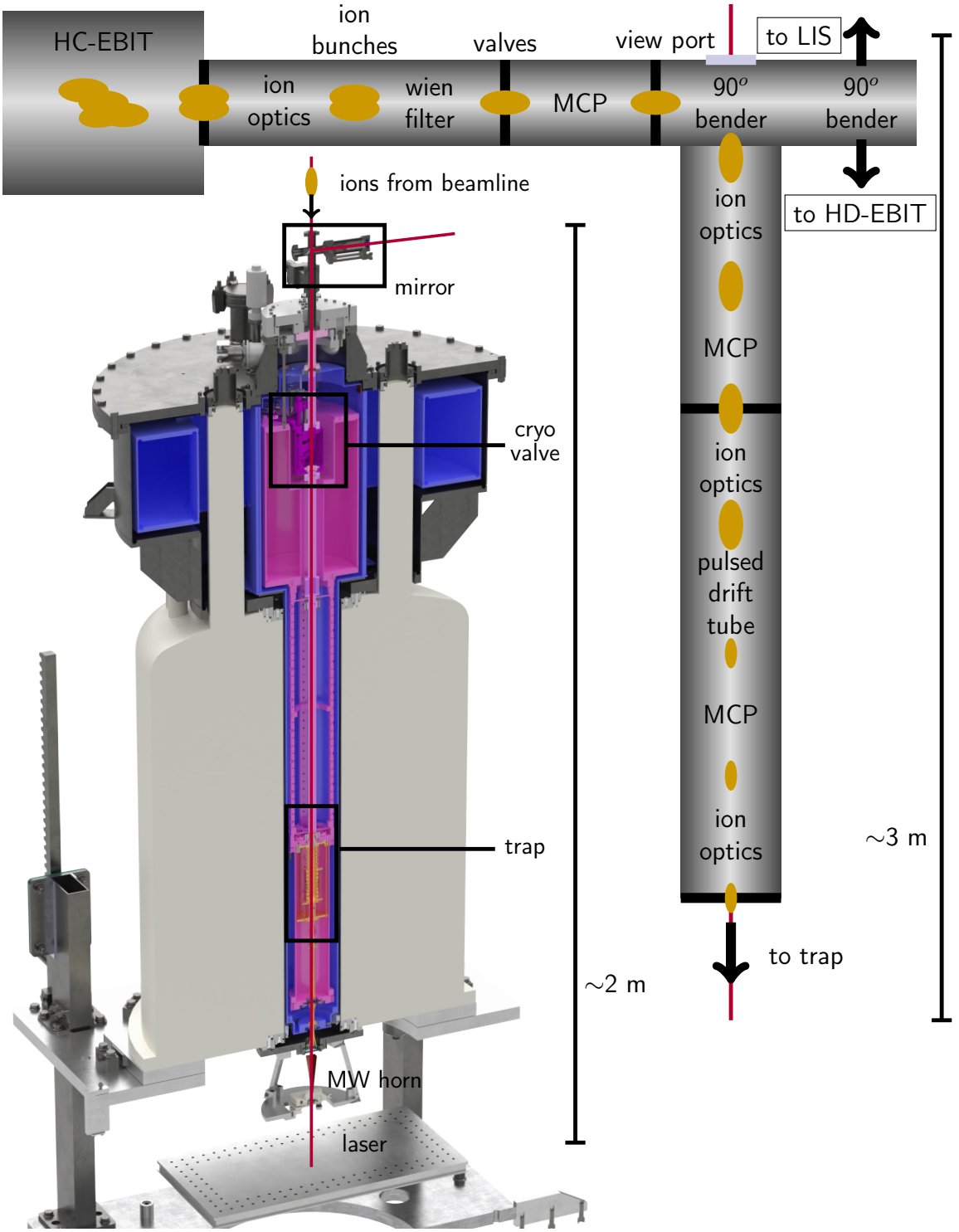

Figure 4.1: Overview of the beamline and trap setup. The HC-EBIT (top left) which is used for the measurements of this thesis and the horizontal and vertical parts of the beamline connecting from this source to the trap are shown schematically. The ion bunches schematically indicate the amount of ions. The beamline further connects to the laser ion source (LIS) and the Heidelberg (HD) EBIT, indicated by the arrows. The beamline is cut just above the trap setup which is displayed to the left. The magnet is cut open to show the cryostat and trap setup inside, the 77-K section is shown in blue and the 4-K in pink. The trap, the cryovalve and the mirror above the trap setup are marked by black boxes. The mirror can be removed from the ion or laser path, to allow ion loading into the trap or to align the laser beam to the top of the beamline. Below the magnet are a breadboard for optics and a holder for the MW horn.

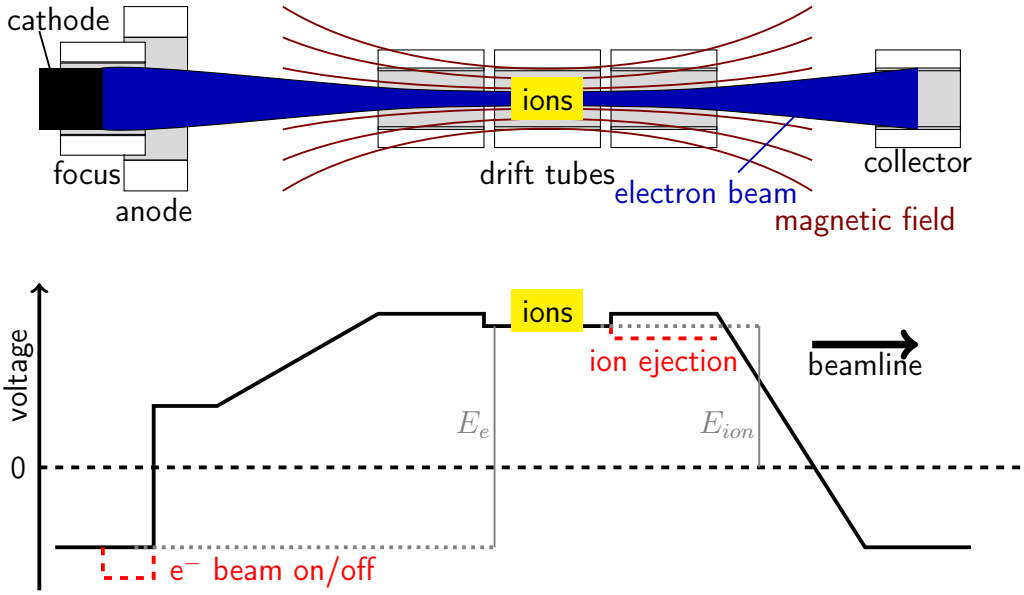

Figure 4.2: top: Working principle of an EBIT. Electrons are emitted from the cathode, focused and accelerated by the focus and anode electrode, respectively. The strong magnetic field gradient is indicated by the dark red lines, it focuses the electron beam to high density at the drift tubes. In the following low magnetic field region, the electron beam diverges and hits the collector. Ions are produced by electron impact ionization and trapped in the central drift tube. **bottom:** Voltages applied to the different sections. The red dashed lines indicate the voltages that are switched to either turn the electron beam off by switching the voltage of the focus electrode to more negative values than the cathode or to open the axial trapping potential to eject an ion bunch to the beamline. The kinetic energy of the electron beam (E_e) and the ion bunch (E_{ion}) are indicated by the thin gray lines.

achieved by applying voltages to the drift tube electrodes to generate a confining electrical potential. There are two contributions to radial confinement, one by the magnetic field and a second by the space charge of the electron beam acting on the positively charged ions. The axial trapping potential can be opened by switching the voltage of the downstream drift tube electrode, allowing to eject an ion bunch into the beamline towards the trap.

There are two main challenges when using an EBIT for the production of MHI. First, the energy of the electron beam should be low, so that the hydrogen gas is ionized but the molecules are not dissociated. Second, light, singly-charged MHI are more likely to escape the trapping region than heavier, multiply-charged residual gas ions after ion-ion collisions. Furthermore, if other ions with a similar charge to mass ratio ($\frac{q}{m}$) are produced, both species will be guided along the beamline to the Penning trap. In the case of HD^+, $\frac{q}{m} = \frac{1}{3}$, so it is beneficial to suppress the production of $^{12}C^{4+}$.

The first approach for the production of HD^+ was to lower the energy of the electron beam as much as possible. However, this led to sparks and unstable operation conditions with the concern of damaging the cathode by accidental back-reflection of the electron beam. Therefore, the EBIT was operated at an electron beam energy of ∼3.6 kV and an electron beam current of 3-5 mA. While this is not the optimal energy for ionization of HD,

the cross section for ionization is nevertheless larger than the cross section for dissociation.

To reduce repeated electron impact leading to dissociation of HD^+ and to production of heavier, multiply-charged ions from the background gas (mostly oxygen, nitrogen and carbon), it is advantageous to keep the charge breeding time low. This is defined as the time the ions are confined and interact with the electron beam. Simply reducing the total cycle time of the EBIT shortens the time between ion bunches in the beamline and the Penning trap which would require a high repetition rate of all the voltages that are switched in the beamline and the Penning trap for ion capture. To ensure short charge-breeding times, while keeping the ion bunch rate in a reasonable range for the beamline and Penning trap, the electron beam of the EBIT was pulsed. The voltage of the focus electrode was switched from $\sim$-1.3 kV to ~ -1.8 kV with the cathode at $\sim$-1.3 kV. If the voltage applied to the focus and cathode are about the same the electron beam emitted from the cathode is focused. When the focus voltage is more negative than the cathode voltage the electrons cannot leave the cathode and there is no electron beam. Before switching off the electron beam, the voltage on the drift tube towards the beamline is lowered and an ions bunch is ejected towards the Penning trap. When the electron beam is off, there is no space-charge potential for radial confinement. Thus, the accumulation of residual gas ions is suppressed and the EBIT is ready for the next HD^+ production cycle. Optimizing the production of HD^+ resulted in a charge-breeding time of 8 ms. This is enough time to ionize HD but not enough to dissociate the majority of the molecules or repeatedly ionize background gas, e.g. to produce $^{12}C^{4+}$. This cycle is carried out with a repetition rate of 10 Hz, which is slow enough for the beamline and capturing in the Penning trap.

After leaving the EBIT, the ion bunch goes through a Wien filter for $\frac{q}{m}$ separation. It is then guided downwards by a 90-degree electrostatic bender, after which a pulsed drift tube slows the ions down to $\sim$500 eV before they enter the Penning-trap region. About 100 ions per bunch are captured in the trap. Along the beamline, there are several electrostatic ion optics for beam manipulation and detection units on linear translation stages for optimization of the ion transport.

The high-vacuum conditions with pressures as low as a few 10^{-11} mbar is achieved by several turbo molecular pumps. We have a two-stage pre-vacuum system consisting of scroll pumps and a booster turbo pump. Additionally, the vertical section of the beamline that connects to the trap has a passive non-evaporative getter pump and a dual non-evaporative getter and active ion getter pump.[1] A schematic overview of the beamline, including the vacuum pumps is given in Fig. 4.3.

Mostly, this system runs smoothly. However we had two bursts of large CF160, 600 $\frac{L}{s}$ turbo molecular pumps during the course of my thesis, the first one during Dr. Tim Sailer's measurement campaign [104] affecting the lower pump of the vertical beamline. This violently loud experience seemed like a very unlikely event. Nevertheless, it repeated itself almost exactly one year later just after the beginning of the MHI measurement campaign, this time affecting the upper pump of the vertical beamline. Again, the pre-vacuum connection was torn off and the inrush of air left the vertical beamline covered in metal flakes and dust.[2] This time, the debris extended all the way down to the cryogenic valve in the 4-K section (cryovalve).

Figure 4.4 shows the state of the pump after the burst and an endoscope image of

[1] A CapaciTorr and a NEXTorr both from SAES Getters S.p.A.

[2] As a result, I spent some time vacuum cleaning our vacuum system.

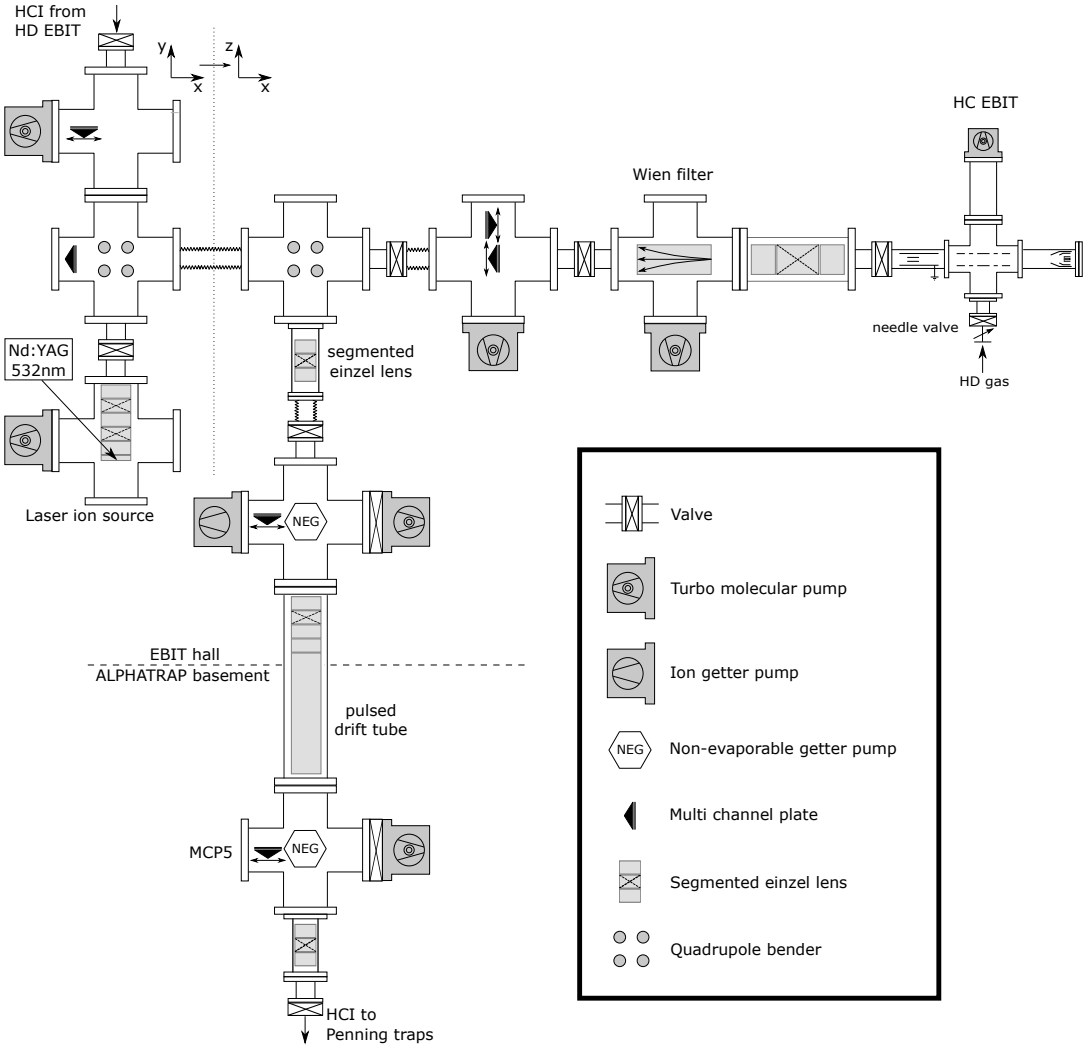

Figure 4.3: Schematic setup of the ALPHATRAP beamline. The HC EBIT and all components along the ion path from this source to just above the magnet are shown, including the diagnostic units and vacuum pumps. The prevacuum system including scroll pumps and the booster turbo molecular pump are not shown. This figure is adapted from Ref. [48].

the flakes on the cryovalve. The mechanical force of the abrupt halt of the pump bent the CF160 vacuum part and ruptured a weld seam on a part nearby. The interlock system closing the beamline valve was not fast enough to prevent an inrush of gas into the cryogenic vacuum of the Penning trap and consequently a contamination of the apparatus. Thus, a full thermal cycle of the trap was necessary.

During the warm up and the related thermal expansion, the 77-K MW guide pressed onto the room-temperature window of the bottom flange of the insulation vacuum of the cryostat below the magnet (see Fig 4.1), cracking the window. The 77-K MW guide was slightly shortened and the UV-grade fused silica window replaced by a CaF_2 window. All turbo molecular pumps at the beamline were exchanged afterwards. In a later thermal cycle, used to replace the window of the bottom flange of the cryostat that had cracked again but this time while the setup was cold and to tune the PT modified cyclotron resonator, we had electrical shorts between AT electrodes. This was most likely caused by the shifting of

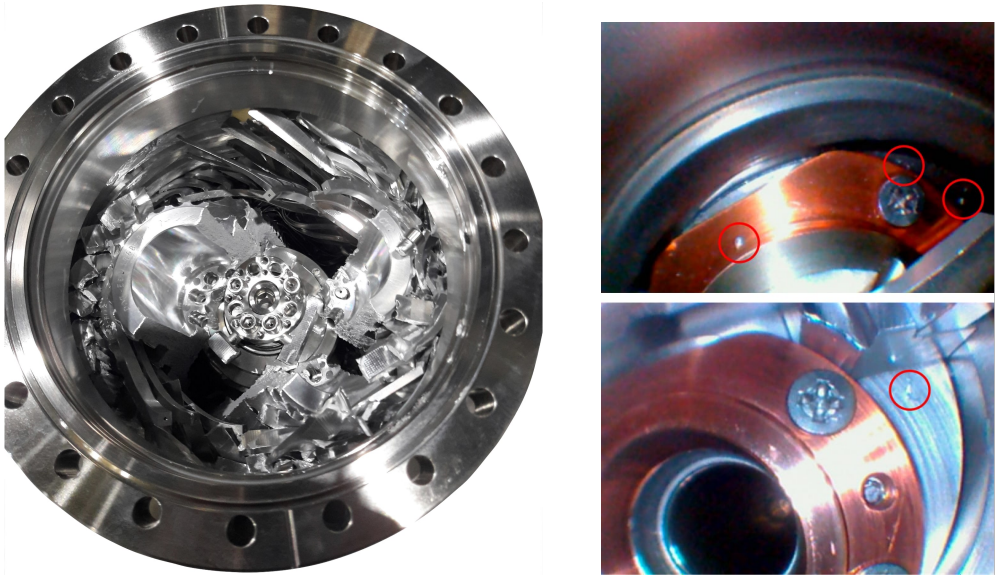

Figure 4.4: left: What was left of the Edwards STP-603 CF160 turbo molecular pump after the burst. **right:** Picture of metal flakes and dust on the cryovalve taken with an endoscope with the cryovalve closed (top) and open (bottom).

small remnant turbo pump fragments inside the trap stack and resulted in the repair and upgrade of the trap setup over the course of the following months.

4.2 Penning-Trap Setup

After passing through the beamline, the ions reach the Penning trap. The strong magnetic field is generated by a 4-T superconducting warm-bore magnet. The setup is inserted into the bore along with a dedicated cryostat for the experiment. In the following, I will first discuss the magnet and cryostat and then the trap itself.

4.2.1 Magnet and Cryostat

The left part of Fig. 4.1 shows cryostat and trap setup within the 4-T magnet, along with its connection to the beamline above and the windows for optical and MW access from below. The magnet has a liquid helium reservoir in which the superconducting coils are immersed. To keep helium consumption low, this is surrounded by a liquid nitrogen tank. Both are separated from each other and from room temperature by the insulation vacuum.

In the course of this thesis, the helium consumption of the magnet had increased drastically. According to the manual and previous experience, it can have a helium hold-up time of up to several months. The hold-up time had constantly decreased until the point where helium had to be refilled more than biweekly. Dropping below this filling cycle would heavily disrupt our measurement time, as the system needs time to settle and thermalize after filling, before a precise measurement is possible. At ALPHATRAP, the flow rate of helium evaporating from the magnet is continuously monitored and a corresponding increase in the evaporation rate by about a factor of 10 was observed. Since a degradation of the insulation vacuum can explain high helium consumption, we pumped the insulation

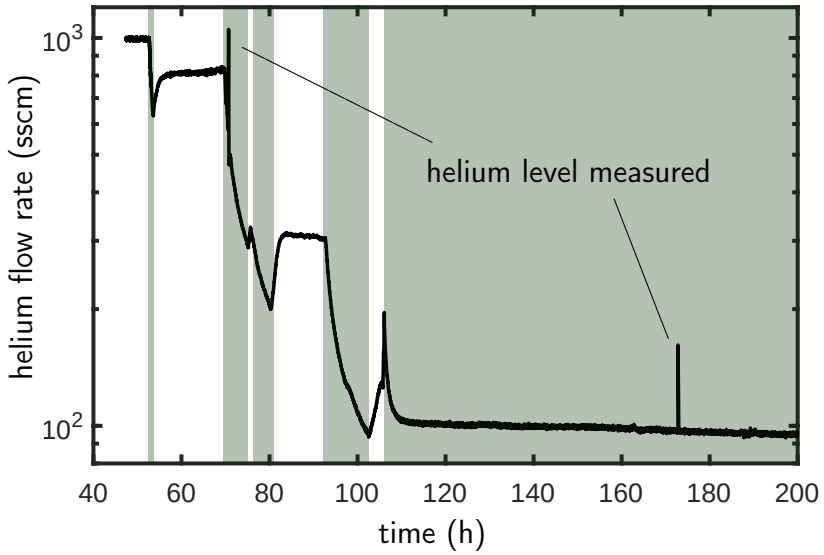

Figure 4.5: Helium consumption of the magnet shown by the helium flow rate evaporating from the helium reservoir of the magnet. The green areas show the hours the insulation vacuum was pumped by opening the valve of the insulation vacuum to a turbo molecular pump. The helium flow rate decreased with better insulation vacuum after pumping. Initially, the helium flow rate increased when the valve was closed again. Finally, the helium flow rate leveled off to about 100 sccm (standard cubic centimeters per minute) and later did not increase when closing the valve and removing the pump. Measuring the helium level in the reservoir leads to momentarily high helium consumption as can be seen by the two peaks (resistive measurement).

vacuum and saw an improvement of the helium flow evaporating from the magnet, shown in Fig. 4.5. When the valve closing off the insulation vacuum was initially opened towards the pump and a leak-tester measuring the helium pumping rate, the pressure readout at the pump decreased slightly while the helium pumping rate increased drastically. This indicates that the overall pressure of the insulation vacuum was in the expected range but the partial pressure of helium was elevated. Indeed, pumping until the helium leak rate from the insulation vacuum dropped by an order of magnitude and the helium evaporation rate settled at 100 sccm (standard cubic centimeters per minute) solved the issue for the time being. However, the helium hold-up time has continuously decreased again, but has been in a manageable range. The high partial pressure of helium leads to saturation of the surfaces in the insulation vacuum and subsequent release of helium after pumping, explaining a repeated degradation of the insulation vacuum and thus an increase in helium consumption for cooling. Furthermore, the partial pressure of helium in the room has been reduced by collecting all helium continuously evaporating from the magnet and experiment as well as during helium filling. If the elevated partial pressure of helium in the insulation vacuum was due to helium diffusion through aged rubber seals, the effect should now be reduced.

The magnet is a warm-bore magnet, so the central bore where experiments can be placed is at room temperature. In order to maintain ultra-high vacuum conditions and use superconducting, cryogenic resonant circuits for ion detection as well as to cool the ion motion, the Penning-trap setup is cooled to liquid helium temperatures as well. Therefore,

the trap setup has a dedicated liquid-bath cryostat with which it is placed inside the bore of the magnet. It uses the same two-level cooling technique as the magnet with a 77-K section surrounding the 4-K section which are separated both from each other and room temperature by insulation vacuum. The 77 K acts as a thermal radiation shield for the 4-K section. Without, the helium tank would be irradiated by room-temperature black body radiation, drastically increasing helium consumption. Before cooling the setup down, the trap vacuum is pumped via the beamline. After cooling down, the cryovalve, which is in the 4-K section, is closed to separate the room-temperature vacuum from the ultra-high vacuum of the cryogenic section, achieving a pressure below 10^{-16} mbar [48, 43]. Without the cryovalve there would be a constant influx of residual gas from the room-temperature vacuum. While most residual gas will freeze out and not spoil the vacuum, helium and hydrogen gas can only be adsorbed in single or few atomic layers and will therefore eventually saturate the surfaces and increase the pressure in the trap.

Upgrades

Before the upgrade, the cryovalve closed the trap section with a stainless steel lid. Therefore, it had to be opened not only for ion loading, but also for laser alignment through the trap. In Valentin Hahn's bachelor thesis work [105], the cryovalve was upgraded to include an optically transparent window (CaF_2), allowing laser alignment through the closed valve. Furthermore, the light of the laser used in measurements can exit the cryogenic section through the closed valve, allowing laser beam monitoring and most of the laser power can be dumped in the room-temperature and not in the 4-K section. Additionally, it reduces back reflection off the bottom of the closed valve in the trap.

Above the magnet in the room temperature section, a mirror on a linear translation stage was added for laser alignment through the trap, shown in Fig. 4.1. With this addition, the laser does not have to be aligned all the way to the top of the beamline ($\sim$5 m) but only through the magnet and Penning trap and can then be coupled out to the side. Thus, laser alignment through the trap is not impacted by the alignment of the Penning trap and magnet with respect to the beamline which are separated by a bellow. Furthermore, this allows monitoring the laser without keeping all valves of the vertical beamline open.

4.2.2 Trap Stack

Figure 4.6 shows a cut view of the full stack of trap electrodes in the 4-K trap vacuum chamber.

In the following, I will introduce the different trap sections, the capture trap (CT), the precision trap (PT), the analysis trap (AT) and the new spectroscopy trap (ST). All electrodes are ring shaped and, except for the AT ring electrode, are made from oxygen free high conductivity copper to mitigate paramagnetic effects of oxygen at cryogenic temperatures which would lead to magnetic field fluctuations. To avoid oxidization, all electrodes have a 10 μm gold coating with a 2 μm silver diffusion barrier below [48]. A selection of electrodes are split to half or quarter segments for excitations and coupling of the motion modes of the ion. Electronically all electrodes are well filtered to minimize voltage fluctuations due to both external and Johnson thermal noise. The MW guide just below the electrodes is connected to a charge amplifier and can be used to detect ion bunches passing through the trap in the ion loading process.

Upgrades

On the outside of the trap chamber we replaced the two self-shielding superconducting coils (NbTi) by a superconducting cylindrical NbTi shield, made from bulk material. Details on the improvement of the shielding are given in Dr. Jonathan Morgner's PhD thesis [102]. Furthermore, we added B_1 and B_2 shim coils. These superconducting NbTi coils can be charged as well as heated for quenching from the outside enabling to tune and minimize the unwanted magnetic field inhomogeneities in-situ, while measuring them out precisely with an ion. The holder with the coils is placed around the trap chamber, see Fig. 4.6. Alternatively, the magnetic field inhomogeneities could be tuned by in-bore room-temperature coils or by the existing in-magnet coils. However, in the the first case this would require a current source attached during high-precision measurements. Any fluctuations of this source would lead to fluctuations of the magnetic field inhomogeneities and could even lead to fluctuations of the magnetic field at the position of the ion. In the second case, the current applied to the coils can only by changed by inserting the charging rod into the magnet, risking a quench. Even if the magnetic field inhomogeneities are nulled, they might differ after removing the charging rod. Furthermore, in both cases the coils are further away from the trap and thus larger currents would be necessary to have the same effect at the position of the ion as with the implemented coils.

The simulation, winding, and offline testing of the coils was carried out in a student project by Anton Kabelac. A 0.1-mm NbTi wire in a copper matrix with formvar insulation was chosen. The B_1 coils is in antihelmholz configuration with 200 windings on either side, placed symmetrically around the PT center. The main part of the B_2 coil is positioned around the center of the PT center with 250 windings, with an additional Helmholtz geometry with 175 windings on either side to compensate the unwanted B_0, generated by the central part of the B_2 coil. The coils were designed and tested offline to compensate a B_1 of 3.7 mT/m and a B_2 of 120 mT/m^2 at 40 mA each. In practice, the B_2 coil could not hold this current in the 4-T field and only up to 50 mT/m^2 were achieved before quenching the coil. This is most likely due to issues with the superconducting joint of the coil.

MW and laser radiation enters the trap through two windows, one at the bottom flange of the insulation vacuum of the cryostat and the other at the bottom flange of the 4-K vacuum chamber of the trap (see Fig. 4.1). We exchanged both fused silica windows for CaF_2 windows. CaF_2 has a broader transmission spectrum in the mid-IR range, now allowing 5 μm light to pass into the trap [106], for potential single vibrational quantum excitation ($\Delta v = 1$) of MHI.

Capture Trap

The CT electrodes are labeled C1-C6 from top to bottom. In the capture process, the voltages applied to the capture electrodes C1 - C4 shape a flat potential at roughly the kinetic energy of the ions, thereby almost completely stopping the ions on their way down while the voltage applied to C5 and C6 blocks the ions. Once the ions are in the CT region, C1 and C2 are switched up to a confining potential before the ions have time to be repelled by the potential barrier of C5 and C6 and fly back up, out of the trap. The capture trap is used for storage of single ions and ion clouds during measurement campaigns. As a precaution in case of a power cut, the voltage of at least one electrode is backed up by a battery. The holes in the top three electrodes are for faster vacuum pumping of the region

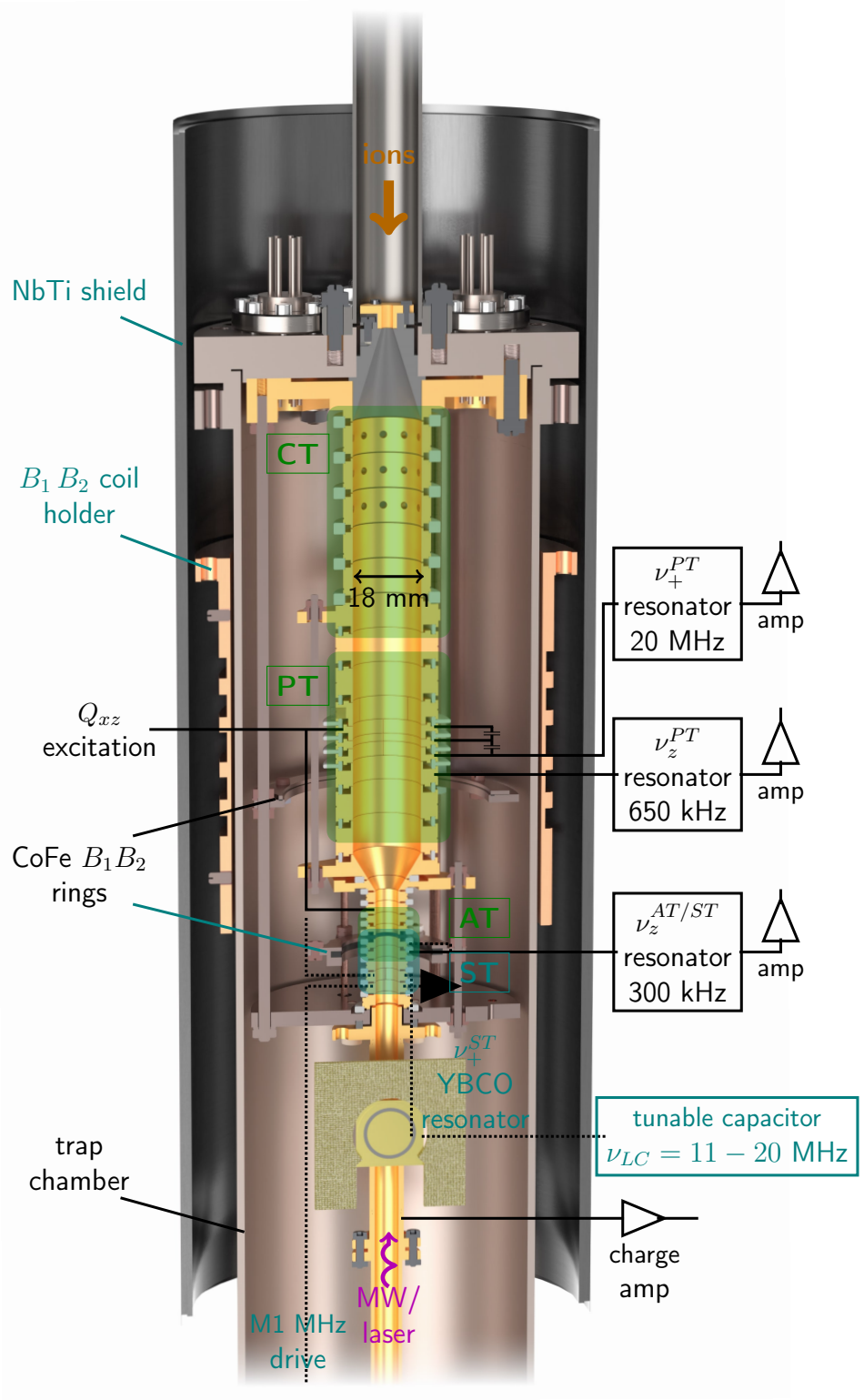

Figure 4.6: Full trap stack in the vacuum chamber after the upgrade, surrounded by the B_1 and B_2 coil holder and the superconducting NbTi shield. Only the connections to the resonators and the Q_{xz} excitation line are shown. Solid lines show connection not affected by the upgrade, dotted lines show newly added connections. The 3-mm-radius split electrode was moved from above the AT to below and is now in the ST. The CoFe rings around the lower PT and the ST compensate B_1 and B_2 introduced by the AT CoFe ring electrode in the respective trap centers. The latter was added in the upgrade. The planar cyclotron resonator below the trap was added in the upgrade as well. New components are labeled in cyan.

of the chamber around the trap electrodes before a cool down.

Precision Trap

As the name suggests, this is the trapping region used for high-precision measurements. The PT is designed to have an extremely homogeneous magnetic field as well as a close-to-perfect quadrupole electric field. The PT is a 9-mm-radius, 7-electrode trap which means it has two electric-field correction electrodes on either side of the central ring electrode. By optimizing the lengths of the ring and correction electrodes, as well as the voltages applied to the correction electrodes, it is possible to null the higher order terms C_4 and C_6 (see Eq. 3.15) and keep the next orders C_8 and C_{10} small [48]. The magnetic field is optimized by positioning a ferromagnetic CoFe ring (VACOFLUX50 [107]) around the PT, thereby compensating the residual B_1 and B_2 from the AT. The amount of material and position of the ring is optimized to minimize the higher order magnetic field components, B_1 and B_2 (see in Eqs. 3.16 and 3.17). This trap section was not changed in the upgrade, besides the amount of material and position of the CoFe compensation ring which had to be changed due to the addition of the CoFe ring of the ST.

The three central electrodes are half-split rings allowing radial excitations and coupling of the axial to radial modes (D_x,Q_{xz}). Additionally, the second upper correction electrode is quarter split to allow coupling of the two radial modes (Q_{xy}). In the measurements of this thesis only the Q_{xz} excitation line was used.

The axial resonator is connected to the second lower correction electrode. It can be switched from high-Q to low-Q mode. For the light, singly charged MHI only the high-Q mode was used. The detector frequency is $\sim$650 kHz. The cyclotron resonator is connected to all three half-split electrodes and can be tuned in-situ by a varactor by $\sim$170 kHz. In an intermediate upgrade, we tuned the frequency of the cyclotron resonator to $\sim$20 MHz to match the modified cyclotron frequency of HD^+.

Electronic feedback can be applied to the PT and AT resonators by capacitively feeding back the amplified and phase shifted Johnson noise of the resonator. The value of the phase shift defines the type of feedback, 0° results in positive and 180° in negative feedback [97]. This allows to reduce the effective temperature of the resonator-ion system and decreases the Q value, when applying negative feedback. The effective temperature initially reduces with increasing strength of the feedback signal. However, due to the finite electronic excess noise of the cryogenic amplifier this is limited to about a factor of three. Applying even stronger negative feedback signals then results in an increased effective temperature [108]. When applying positive feedback the effective temperature increases along with the effective Q value of the resonator and thus the signal strength/dip width of the ion increases as well. Both positive and negative feedback was used for the HD^+ HFS measurement campaign.

Analysis Trap

The AT is a 3-mm-radius, 5-electrode trap, so it has only one correction electrode on either side of the ring electrode. Nevertheless it is possible to null C_4 by an appropriate tuning voltage applied to the correction electrodes and to keep C_6 small, limited by the machining imperfection of the nominally compensated trap. As this trap is mainly for axial frequency detection for internal quantum state determination via the continuous Stern-Gerlach effect

(CSGE) [3] explained in the following, we rarely excite the ion to larger than thermal motion and do not require the electric field harmonicity of the PT.

The main characteristic of the AT is the ring electrode. In contrast to the other electrodes it is not made out of copper but out of ferromagnetic CoFe (VACOFLUX50 [107]). Therefore the AT has a large magnetic field inhomogeneity (magnetic bottle) of B_2∼42 kT/m^2. Following Eq. 3.16, the magnetic field in axial direction is then given by:

$$B_z = (B_0 + B_2(z^2 - \frac{\rho^2}{2}))e_z \ . \tag{4.1}$$

This adds an additional force to the electrostatic trapping field in axial direction, generating an axial frequency shift of: [48]

$$\Delta\nu_z = \frac{B_2}{(2\pi)^2 m\nu_z}\mu_z = \frac{B_2}{(2\pi)^2 m\nu_z}\left(\sum g_i m_i \mu_B + \frac{E_+}{B_0} - \frac{E_-}{B_0}\right) \ , \tag{4.2}$$

where μ_z is the total magnetic moment projection on the trap axis, m is the mass of the ion and $g_i m_i$ is the g factor times the quantum number of the spin projection of particles i. Therefore an electron spin flip in HD$^+$ leads to a jump of the axial frequency of the ion in the AT of about 12 Hz. The spin transitions between two Zeeman levels can be driven by resonant MW radiation thus determining the internal quantum state of the ion via the CSGE. Figure 4.7 shows an example of the axial frequency jump for a single HD$^+$ ion in the AT. Since the nuclear g factors are orders of magnitude smaller (see Ch. 2.1.2), the change of the axial frequency due to a nuclear spin transition is not detectable.

Equation 4.2 shows that the axial frequency is not only shifted by a change in spin projection but also by changes of the modified cyclotron and magnetron energy. This has two main implications. First, fluctuations of the energy of the radial modes lead to unwanted shifts of the axial frequency. In general, these fluctuations are small compared to the dip width of the ion signal (0.4 Hz) and especially so compared to the jump in axial frequency induced by an electron spin flip (12 Hz), when the ion is in the AT. After transporting the ion to the PT and back, the axial frequency can change by single Hz. Second, this effect can be used to measure the temperature of the ion, details on this are given in Sec. 5.1.4.

Upgrades

In the upgrade, we changed the connection of the axial detector in the AT to increase the signal strength by decreasing the effective electrode distance (D_{eff}). Before the upgrade, the image current signal was picked up from the lower endcap electrode, resulting in a dip width of a single HD$^+$ ion of only ∼0.4 Hz. This required long FFT acquisition times of 8 s with about 10 averages (80 s in total) for reliable detection of the ion dip signal. The time for the dip includes using positive feedback to increase the signal strength. Now, the axial detector is connected to both the lower endcap electrode as well as the lower correction electrode. The dip width of a single HD$^+$ ion is now ∼3 Hz and can be reliable detected at 5 averages with an FFT acquisition time of 2 s (10 s total without feedback), which significantly reduces the overall measurement time. Fig. 4.8 compares an axial frequency dip signal of a single HD$^+$ ion before and after the upgrade. Connecting the AT axial detector to two electrodes increases the overall capacitance of the detection system and thereby reduces the resonance frequency. However, it is nevertheless in a good range for measurements.

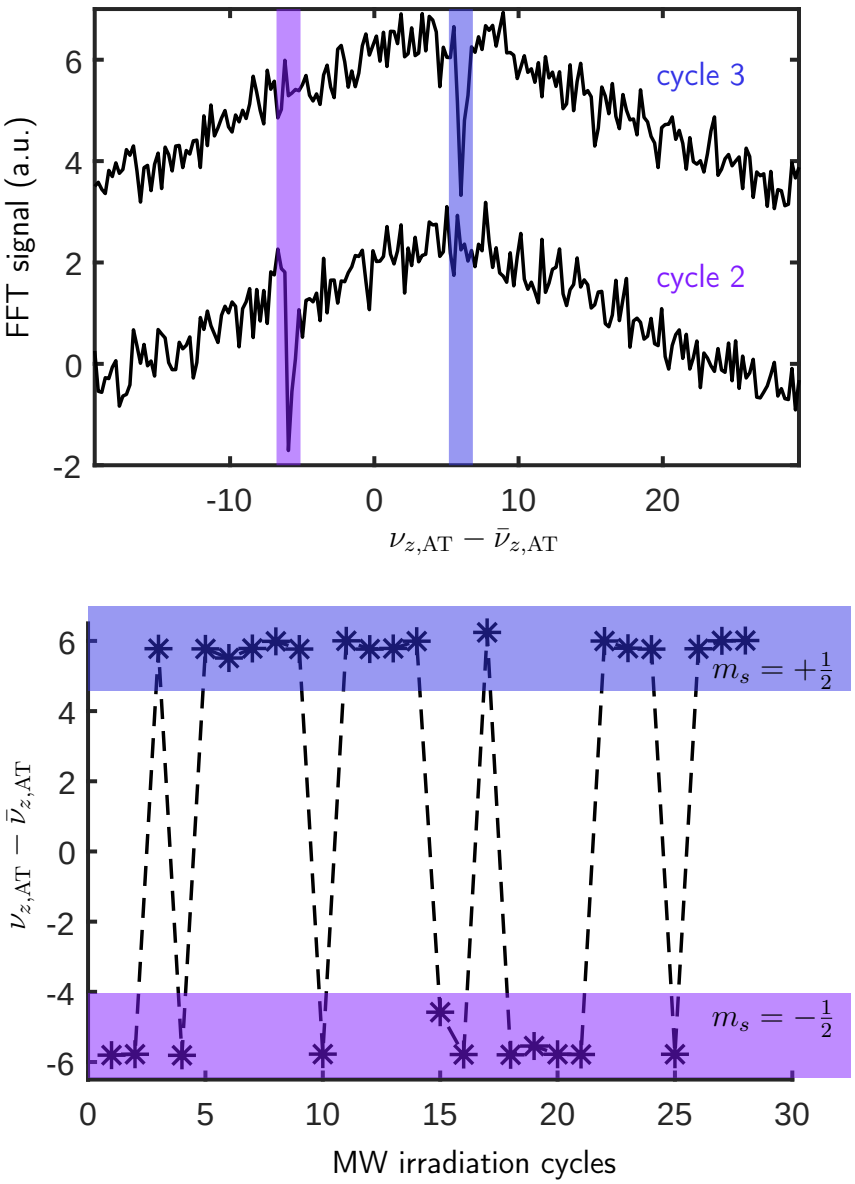

Figure 4.7: Axial frequency jump due to an electron spin flip of a single HD^+ ion in the AT before the upgrade. The data is from the measurement campaign of the HFS of HD^+. **top:** An example of the axial frequency dip signal in the FFT spectrum before (cycle 2) and after (cycle 3) resonant MW radiation. **bottom:** Each data point is an axial frequency measurement, alternating with resonant MW excitation. The ∼12 Hz jump of the axial frequency as well as the ∼50% spin-flip probability of the incoherent drive are visible.

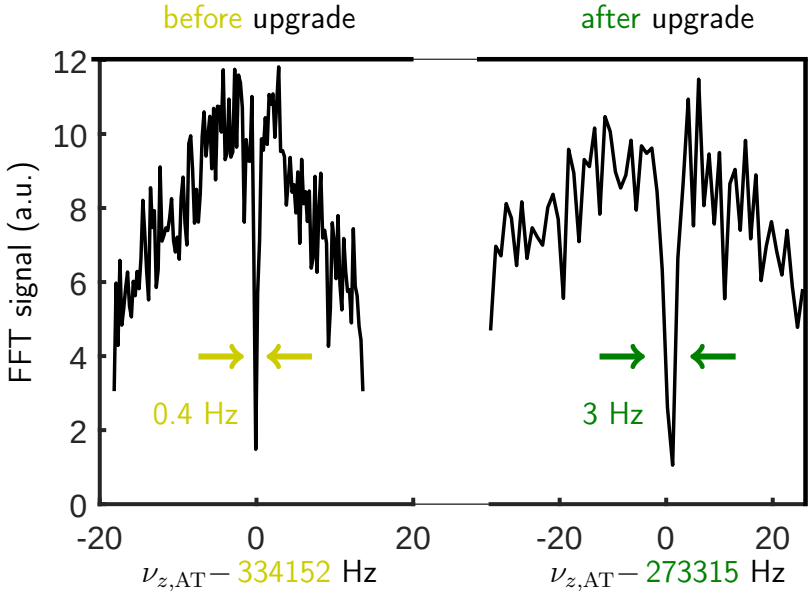

Figure 4.8: AT axial frequency dip signal comparison of a single HD^+ ion before and after the upgrade. Before, the resonator was connected to the lower endcap electrode while now it is connected to both the lower correction and lower endcap electrode (see Fig. 4.6). Picking up the signal closer to the center of the trap increases D_{eff} and therefore results in a broader dip signal. This leads to faster detection and the possibility to see an ion signal even if it is off resonance to the detector. Note, that for the spectrum before the upgrade positive feedback is applied which increases the effective Q value. Even with positive feedback, a longer FFT acquisition time, hence smaller frequency steps in the FFT spectrum, was necessary to resolve the dip before the upgrade. The arrows indicate the dip width of the ion signal.

Upgrades: Spectroscopy Trap

In the HD^+ HFS measurements before the upgrade, the electrodes below the AT were used as a ion storage region only. Due to the large radius of the PT electrodes the D_{eff} of the electrode to which the axial detection system is connected is limited. To reliable detect the ion dip signal of a single MHI long FFT acquisition times and many averages are needed, similar to the AT before the upgrade.

In the upgrade the aim was, therefore, to create a dedicated trapping region for IR spectroscopy of MHI with the 3-mm-radius electrodes. Since the rovibrational transitions are much less sensitive to the magnetic field compared to transitions between hyperfine and Zeeman states, systematic effects of ν_c, for instance due to electric field anharmonicities and magnetic field inhomogeneities, have an equivalently reduced effect on the achievable precision of the spectroscopy. For example, for the $(0,0) \rightarrow (5,1)$ transition, this is reduced by more than eight orders of magnitude.

The electrode three below the AT ring was defined as the ring electrode for the ST. Since no new electrodes were available at the time, the length of the electrodes of this trap are not optimized and thus the electrodes do not form a compensated trap, where $C_4 = C_6 = 0$, simultaneously. To make the trap as symmetric as possible, the ring

Table 4.1: Compensation of magnetic field inhomogeneities arising from the ferromagnetic AT ring (CoFe) at the positions of the PT and ST. The tables gives the simulated B_1 and B_2 values for all three traps without and with the optimized compensation rings.

	AT	ST	PT
$B_1^{\text{no comp}}$ (T/m)	-1.5647	4.216	-0.0100
B_1^{comp} (T/m)	1.08949	0.002759	-0.0011
$B_2^{\text{no comp}}$ (T/m^2)	44826.23	136.769	0.379
B_2^{comp} (T/m^2)	46427.49	0.03858	0.00874

Table 4.2: Height, inner and outer radius, and position with respect to the AT center are given for both compensation rings.

	inner radius (mm)	outer radius (mm)	height (mm)	position (mm from AT)
ST	12.158	14.820	1.70	-1.7
PT	28.000	29.625	0.35	36.6

electrode was chosen so that the two next-neighbor electrodes on either side are equally long. Axially asymmetric correction electrodes result in non-zero odd-order field coefficients $C_{n,odd} \neq 0$. Nevertheless, the relevant lowest-order coefficients can be nulled $C_4 = C_3 = 0$ by appropriate tuning of the voltages of the three electrodes.

Compared to the PT the ST is located in very close proximity to the CoFe ring of the AT, resulting in large residual B_1 and B_2 if not compensated. To lower the magnetic field inhomogeneities and make a precision measurement possible, we added an additional CoFe ring of the same material around the ST. The amount of material and its position are optimized using COMSOL Multiphysics [109]. Due to the additional ferromagnetic material of the ST compensation ring, the PT compensation ring had to be adjusted. The calculated magnetic field along the trap axis is shown in Fig. 4.9 and the values for B_1 and B_2 without and with optimized compensation rings for the three trap sections are given in Tab. 4.1. The resulting sizes and positions for the two compensation rings are listed in Tab. 4.2. Note that machining and positioning imperfections of the compensation rings as well as fluctuations in the magnetic properties of the material can lead to final values of B_1 and B_2 that deviate from the simulated ones.

To allow fast reliable axial frequency dip detection the shared AT axial resonator is connected to an electrode adjacent to the ring of the ST, which is the lower endcap of the AT. The 3-mm split electrode was repositioned adjacent to the ST ring on the opposite side to allow for axial-to-radial mode coupling by Q_{xz} excitation. Additionally, the split electrode allows for resonator coupling of the modified cyclotron motion. When coupling the modified cyclotron motion mode directly to a resonator, lower temperatures can be reached compared to coupling the axial motion to a resonator and cooling the radial modes via the double-dip type RF method, see Secs. 3.1 and 6.4.2. We placed a planar YBCO resonator into the trap chamber and connected it to the other side of the split electrode. The planar YBCO resonator was developed in Fabian Raab's bachelor thesis [110]. The resonator is connected to an in-situ mechanically tunable capacitor in the electronics section, allowing a tuning range of > 10 MHz for the resonance frequency of the cyclotron resonator [102]. There is no amplifier connected to this resonator, so while it can be used for thermalization of the modified cyclotron motion, it cannot be used for signal readout.

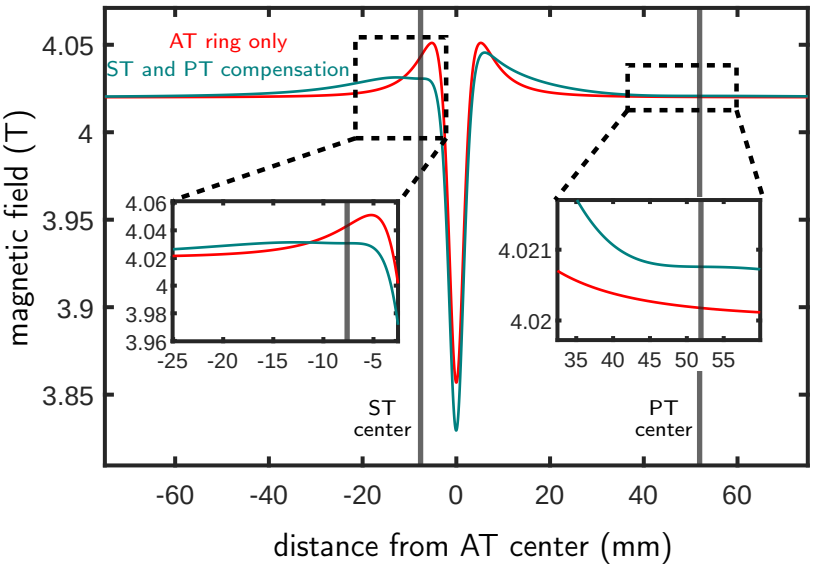

Figure 4.9: Magnetic field along the trap axis, with and without the PT and ST CoFe compensation rings. The two inserts show zoom-ins at the ST and PT centers. Here, the magnetic field with both compensation rings shows less inhomogeneity than without, visible as little to no slope (B_1 suppressed) or curvature (B_2 suppressed). The values for B_1 and B_2 are given in Tab. 4.1.

Furthermore, the new M1 MHz excitation line, developed in the work of this thesis, is connected to the next-lower electrode. Details are described in Sec. 4.4. This allows to directly address nuclear spin and rotational projection transitions for state preparation and may enable precision measurements of both. If measured to the same relative precision as the electron spin flip transitions of this work, the latter would give access to the bound-nuclear and rotational g factors of MHI and allow to determine the $E_4(0,0)$ and $E_5(0,0)$ coefficients to orders of magnitude improved values. Furthermore, these transitions would be more sensitive to extensions to the HFS Hamiltonian of HD^+, Eq. 2.4, than electron spin flip transitions, see Sec. 2.1.2.

4.3 Millimeter Wave and Optical Setup

The MW are generated with an Anritsu MG3694C synthesizer with a frequency range of 0-40 GHz. The signal is frequency tripled to ∼112 GHz and amplified to 25 dBm and passes through a programmable attenuator, after which a 1:9 power splitter allows to monitor the MW power while most of the power passes on towards the trap. The MW are guided to the experimental setup using WR10 hollow metal waveguides. We use horn-to-horn free-space transitions through the windows into the vacuum. The overall transmission efficiency is frequency-dependent [111].

The MW generator, as well as all function generators and the FFT analyzer, are locked to an external 10 MHz reference. In previous measurements at ALPHATRAP, the bound-electron g factors of atomic ions with zero nuclear spin have been measured [48]. Therefore, there is no HFS and the Zeeman levels (electron spin up and down) are a two-level system.

In these cases, the magnetic field exactly cancels in the ratio of the transition frequency (Larmor frequency) and the free-space cyclotron frequency of the ion in the trap, $\Gamma = \frac{\nu_L}{\nu_c}$. Due to this cancellation, any offset of the reference signal to 10 MHz cancels out as well. For HD^+ this is not the case. Both nuclei have a spin, leading to the HFS introduced in Sec. 2.1.2. At the 4-T magnetic field of the trap, the HFS and Zeeman splitting is in the Paschen–Back regime and the contribution of the HFS to the electron-spin-flip transitions (at ∼112 GHz) is in the hundreds of MHz range. This contribution does not depend on the magnetic field and therefore offsets of the reference signal to 10 MHz cancel out only partially. Albeit reduced by more than two orders of magnitude, this measurement depends on the accuracy of the 10 MHz reference signal. Therefore, the 10 MHz reference signal is supplied by a GNSS[3]-monitored hydrogen maser with a 5 MHz output that is frequency doubled. The GNSS-monitoring gives a maser frequency offset of $+2.4 \cdot 10^{-11}$ fractionally, with a frequency drift (change) that occurred from beginning until the end of the measurement campaign of approximately $0.05 \cdot 10^{-11}$. This setup was used for the hyperfine structure measurements of HD^+.

When moving towards rovibrational laser spectroscopy, the MW guides were replaced by larger WR28 components which allow a 2 mm hole in the waveguide for the laser to pass into the trap and did not reduce the transmitted MW power by more than 5 dBm. Since alignment of the laser and the MW horn proved to be delicate, we changed the waveguides back to WR10, using an open end of the waveguide instead of a horn. In this configuration the MW setup is smaller and the laser can be aligned next to the MW guide.

The laser setup has been built up, during the course of this thesis work, in collaboration with Prof. Stephan Schiller's group from the Heinrich-Heine University Düsseldorf. Ivan Kortunov and Victor Vogt (both PhD students) brought the hardware and know-how to our group. Note, so far the system has not been used for spectroscopy measurements at ALPHATRAP. The spectroscopy laser is a 1.15 μm Toptica diode laser (DLC TA PRO HP) in a dedicated laser lab. The light from the spectroscopy laser travels along a 50-m fiber with active fiber-noise cancellation to the breadboard below the magnet and is then aligned through the Penning trap to exit at the top of the beamline (∼5 m, see Fig. 4.1).

In the initial attempts, the laser setup was rudimentary and was refined throughout the following months. At first, the spectroscopy laser was locked to a wavemeter that we previously calibrated with light from a frequency comb from Apl. Prof. Dr. José R. Crespo López-Urrutia's group. In the full laser setup, the spectroscopy laser is locked to a Menlo frequency comb [112] which is locked to a 1.5 μm laser locked in turn to a ultra-stable cavity. The optical setup is referenced to the same GNSS-monitored hydrogen maser as the rest of the experiment. This setup can achieve a single-Hz linewidth and has a stable lock for more than 20 h. For details see the upcoming theses of Ivan Kortunov and Victor Vogt. A schematic of the full MW and laser setup is depicted in Fig. 4.10.

4.4 Upgrades: M1 MHz Excitation

Since the magnetic moments of the proton and deuteron are orders of magnitude smaller than that of the electron, the frequencies for proton and deuteron spin transitions are in a completely different frequency range. As spin transitions between Zeeman levels are M1

[3] global navigation satellite system

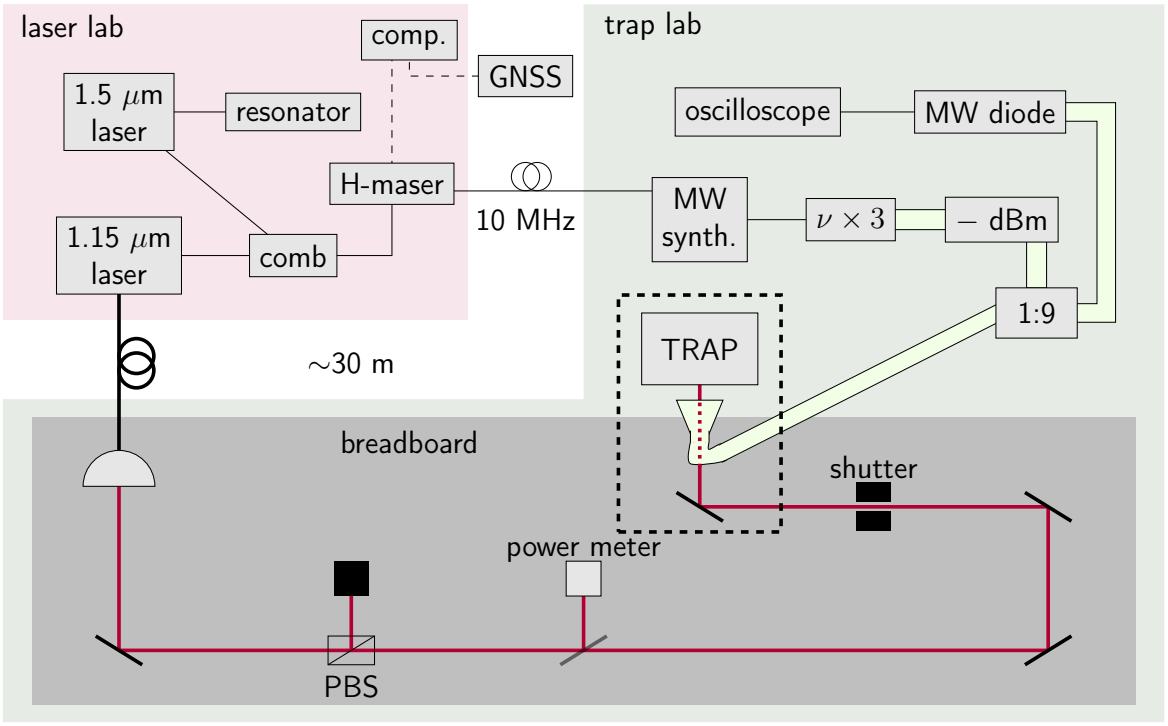

Figure 4.10: Schematic of the MW and optical setup. The laser lab is displayed in the top-left (red background). All thin solid black lines depict frequency locks while the dashed black lines are for comparison only. The thin black line connecting the laser lab to the trap lab (green background) represents a cable transmitting the 10 MHz signal to which the MW synthesizer is locked. The thick black line connecting the 1.15 μm laser to the breadboard in the trap lab represents the fiber transmitting the laser light. The labs are about 30 m apart. The top right shows a schematic of the MW generation, details are given in the text. Here, black lines represent cables and the thick light green connections represent waveguides. On the breadboard, the semicircle represents the collimator where the light exits the fiber, thick black lines are mirrors, the thick gray line is a beam splitter followed by a power meter (light gray square), PBS is a polarizing beam splitter followed by a beam dump (black square). The red lines represents the laser light. Note that the last mirror reflects the light upwards into the trap. The parts in the dashed frame are aligned vertically above the horizontal breadboard.

transitions, they require an oscillating magnetic field. For HD^+, at 4 T, electron spin transitions occur at ∼112 GHz. At ALPHATRAP, they are addressed by the transversal-oscillating magnetic field of the irradiated MW. Proton spin transitions occur only at hundreds of MHz and deuteron spin transitions at tens of MHz (see Fig. 2.2). Transitions between rotational quantum orientations (m_N) in rovibrational excited states are M1 transitions as well and lie in the tens of MHz range for both HD^+ and H_2^+. These frequencies cannot be irradiated the same way as the MW, as their wavelengths are much larger than the trap diameter. Therefore, near-field excitation is required to address these transitions directly. At ALPHATRAP this had not yet been implemented.

When considering the possibilities for excitation in this frequency range, we decided against the spin-flip coils used in other setups [91, 45]. Such coils are on the outside of the nearly closed cylinder of trap electrodes. Thus, the currents necessary to obtain an oscillating magnetic field of sufficient strength raised concerns about heating effects. Therefore, we pursued the alternative idea of passing electric current in two half circles through an electrode [113]. Figure 4.11 shows a schematic of the general idea.

The required amplitude of the magnetic field of the drive (B_d) can be estimated by considering the transition probability of Rabi oscillations:

$$P(eSF) = \frac{\Omega_R^2}{\Omega_R^2 + \Delta_R^2} \sin\left(\frac{1}{2}\sqrt{\Omega_R^2 + \Delta_R^2}t\right)^2 , \tag{4.3}$$

where Ω_R is the Rabi rate and Δ_R the detuning of the drive frequency from the transition frequency $\omega = 2\mu B_0/\hbar$ for which μ, B_0, and $\hbar$ are magnetic dipole moment of the transition, the magnetic field at the position of the ion, and the reduced Planck constant. To prevent the maximal amplitude from dropping below 50%, $\Omega_R > \Delta_R$. The detuning can be approximately given by the magnetic field fluctuations during the drive (ΔB) as $\Delta_R \approx \frac{\Delta B}{B_0}\omega$ and the Rabi rate is given by $\Omega_R = \mu B_d/\hbar$. Therefore, $\frac{B_d}{2B_0} > \frac{\Delta B}{B_0} \approx 10^{-9}$, which results in $B_d > 8$ nT.

4.4.1 Simulation

Initially, the drive was designed for the PT, but was later implemented for the smaller trap electrodes of the ST. Using Comsol Multiphysics, the magnetic field of the drive for different input electrodes, namely the correction electrodes and the first endcap of the PT and ST was simulated. Figure 4.11 shows the simulated magnetic field of the drive. The simulation indicated drive strengths of 100 nT at input currents of 30 mA which are realistic values for implementation.

4.4.2 Test Setup

A stack of spare PT and CT electrodes was used to test the drive offline. The inner wire of a coax cable was connected to one side of an electrode and the outer conductor to the other side, as shown in Fig. 4.11. The signal was generated by a vector network analyzer and applied through an operational amplifier. The resulting magnetic field component of the drive was measured at the expected position of the ion. Table 4.3 shows values measured for different drive frequencies. To get the maximum current through the electrode the length of the signal carrying cable is varied to match the wavelength of the drive.

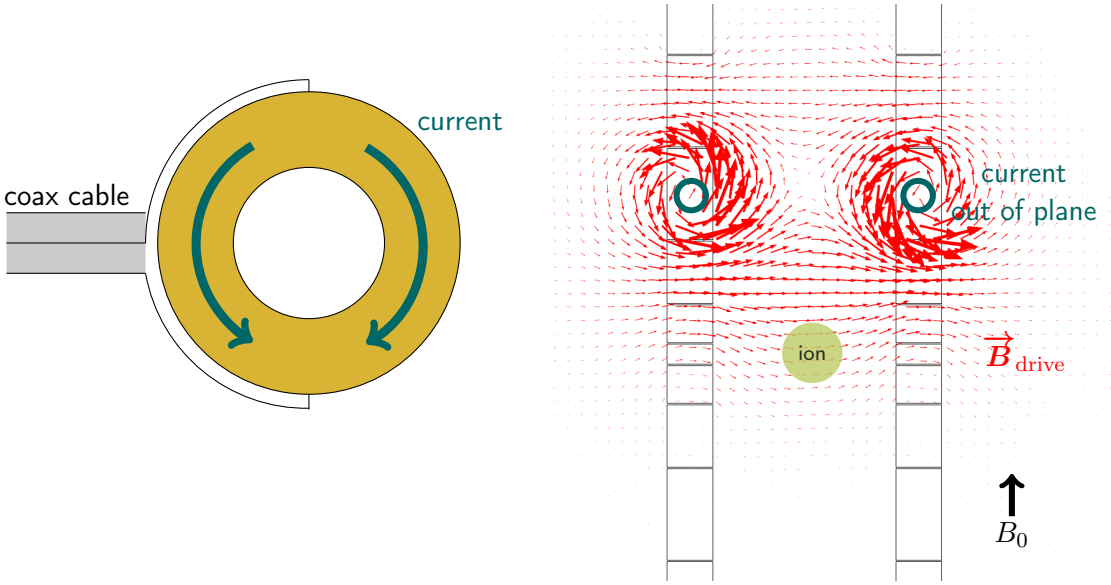

Figure 4.11: left: Top view of a ring electrode with the M1 MHz signal applied via a coax cable. The resulting current in the electrode is shown by the cyan arrows. **right**: Front view of a vertical cut through the stack of trap electrodes. The simulation results of the M1 MHz excitation for an ion in the PT with the excitation current applied to the upper endcap electrode of the PT is displayed. The resulting magnetic field of the drive is shown as red arrows. At the position of the ion, the magnetic field of the drive is perpendicular to the external magnetic field of the trap (B_0), as required for nuclear spin transitions.

Table 4.3: Offline MHz excitation test using spare PT and CT electrodes. For all frequencies except for 75 MHz the length of the cable was optimized to the wavelength of the excitation in the cable. For 75 MHz the length was purposely chosen to be off resonant for comparison.

frequency [MHz]	B at ring [nT]	voltage drop [mV]	current [mA]
59.8	24.3	34.2	10.3
75 (off resonant)	5.9	15.0	5.3
119	16.0	36.1	8.2
179.5	15	28.4	7.6
399.5	2.2	18.1	5.7

4.4.3 Implementation

The details of the implementation in the Penning-trap setup were constrained by the little available space and by the acceptable heat load of the signal cable and the drive. For space constraints, the SMA feedthrough was placed in the bottom flange of the trap chamber, not the top where all other connections are. The window in the bottom flange of the trap chamber had to be reduced in size from 1.5 inch to 1 inch. Additionally, this placement should help to limit noise coupling from this unfiltered line to the trap electrodes and detection systems.

For the cable, a balance of good transmission for the signal and low heat conductivity

between the room temperature and cryogenic section was chosen. Therefore, low-loss, low-thermal-conductivity stainless steel coax cables were used to bring the signal from room temperature to the 77-K section and from there to the bottom flange of the trap chamber at 4 K. Since both the bottom flange of the trap chamber as well as the trap electrodes are at 4 K, it was possible to use a copper coax cable here. At 77 K, the line is thermally anchored by an SMA i-piece fixed to the holder for the 77-K MW horn. At the electrode the cable connects to a small PCB board with two 3 nF capacitors, for the inner and outer conductor of the cable, to DC-decouple the excitation line and the electrode.

This M1 MHz excitation was implemented in the most recent upgrade. So far, it has not been tested for the drive of nuclear spin flip transitions. We have seen increased noise level in the trap that is, however, most likely not attributed to the new drive. We have also measured a slight ($\sim$10%) increase in liquid helium consumption which may be due to the placement of the components of the drive in the 77-K section.

5 Measurements of the Hyperfine Structure of HD^+

In this chapter, I will describe the main measurement campaign of this work. The measurement of all six electron-spin-flip (eSF) transitions in the rovibrational ground state of HD^+ allowed the extraction of the spin-spin interaction coefficients $E_4(0,0)$ and $E_5(0,0)$ of the HFS and the bound electron g factor $g_e(0,0)$. The precision of the results surpasses the previous experimental precision as well as the precision of the theoretical prediction.

This chapter begins with a description of ion preparation and characterization measurements of the trap. Afterward, the initial search for the eSF transitions, the observed spontaneous changes of the nuclear spin orientation, and the MW-induced electron and nuclear spin-flip transitions are described. The following sections report on the measurement cycle for the high-precision eSF measurements and the analysis of the data.

5.1 Characterization Measurements

This section describes the preparation of a single ion and measurements for the tuning and characterization of the trap as well as for evaluation of systematic effects of the measurement results.

5.1.1 Singe Ion Preparation

After capturing an ion cloud ($\sim$100 ions), the cloud is split asymmetrically in the CT section. The ion cloud is confined at -50 V on a single electrode. The neighboring electrode above is set to -30 V and the one below to a lower absolute voltage between -20 and -30 V depending on the size and temperature of the ion cloud. The -50-V-potential is then ramped to 0 V and the ion cloud is asymmetrically split to the neighboring electrodes above and below. The ion cloud from the lower electrode is then transported to the PT. This scheme routinely worked to separate 1-5 ions from a larger cloud.

In the PT, the remaining small cloud of single ions is cleaned until a single cold HD^+ ion remains. This is done by broad-band heating, covering the range of magnetron frequency of possible ion species in the trap. Simultaneously, cooling of the magnetron mode is applied only at the motional frequency of HD^+. This magnetron heating alternates with excitations of the axial mode at all but the motional frequency of HD^+. After thus increasing the motional amplitudes of all but the HD^+ ions, the PT voltage is dipped from -74 V to ~ -1.6 V. Thus, hot ions at large motional amplitudes are lost from the trap. If more than one HD^+ ion remained, the PT electric potential was detuned by changing the voltages of

the correction electrodes, thus adding anharmonic contributions (see Eq. 3.15). The axial frequency then depends on the motional amplitude of the ions. The remaining ion cloud is excited in the axial mode, after which the ions appear as peaks in the FFT spectrum. Depending on the initial phase of the motion of each ion, it is excited to a different amplitude and thus each ion in the detuned trap has a unique axial frequency. The axial frequency of the ion with the smallest amplitude remains closest to the resonator and thus cools back to 4 K fastest. In the meantime, the ions at larger amplitude can be further excited, shifting their axial frequencies away from the resonator. The trap potential is then dipped to ~ -1.6 V again after which only the cold ion remains trapped. This scheme routinely worked to isolate a single ion, sometimes requiring some iterations. In general, the time from splitting the ion cloud to a single HD^+ ion varied from 20 minutes to two hours.

Since the dip width of the signal in the FFT spectrum depends on the number of ions of the same type (Eq. 3.22), it relays the number of ions of the same species in the trap. Stable trap operation, no appreciable heating by PT-AT-PT transports and stable PnA phases, indicate very low chances of contaminant ions of other species. Furthermore, contaminant ions should from magnetron coupled systems. Therefore, in a detuned trap (in the presence of an electric field anharmonicity C_4), the axial frequency of the ion would undergo seemingly random frequency shifts after repeated cooling of the magnetron motion, as this would change the separation of the ions. See, Ref. [104] for magnetron coupling of two ions at ALPHATRAP.

The correct identification of an HD^+ is guaranteed by measuring its motion frequencies. For example, ions with similar charge-to-mass ratios (q/m) that are possible in the trap are $^{12}C^{4+}$ from the ion source and H_3^+ from molecular reaction in the trap. Their q/m ratios differ by only 0.7% [114] and 0.2% [115], respectively. However, this leads to axial and modified cyclotron frequency differences of hunderes of Hz and tens of kHz between HD^+ and the closer-lying H_3^+. These differences are easily distinguishable.

5.1.2 Tuning Ratio

In a 5-electrode trap the tuning ratio is defined by the ratio of the voltages applied to the ring and correction electrodes. An optimization of this ratio leads to a suppression of anharmonicities of the electric trapping field and therefore to smaller shifts of the axial frequency as a function of the motional amplitudes and radii. In the AT the optimization was carried out by exciting the ion axially and observing the drift of the axial frequency while cooling to the resonator temperature. After this rough adjustment, the tuning ratio was scanned while sampling an axial dip at each step and optimized by the quality of the dip. While not applicable for all cases, here, the narrow dip of HD^+ of 0.4 Hz in the AT smears out and becomes less visible if the tuning ratio is not optimal. As no high-precision measurement is performed in this trap section, this leads to a sufficiently good electric trapping field.

In a 7-electrode trap there are two sets of correction electrodes. In previous work by Dr. Tim Sailer [104], the ion in the PT was shifted along the trap axis and the position of minimal B_2 was determined. This resulted in a slightly shifted trap configuration, the asymmetric PT. This asymmetric PT has been used since then for high-precision measurements. The asymmetry of the trap can introduce odd-order electric field anharmonicities, C_3 and higher. The effect of these terms ($C_3 \cdot C_3$, $C_3 \cdot C_4$,..) and possible cross terms with B_1, have

been evaluated in previous work [104] and are well below the measurement precision of the measurements of this thesis.

Since the asymmetric PT was already optimized in previous measurements [104, 102], it was sufficient to fine-tune the combined tuning ratio of both pairs of correction electrodes. For this optimization, the shift of the axial frequency due to excited magnetron radii was measured. Neglecting the odd-order terms, the first-order anharmonicity C_4 results in a quadratic dependence of the axial frequency on the magnetron radius, while the next order C_6 adds an z^4 dependence (see Eq. 3.15 and Ref. [93]). Repetition of this measurement for several tuning ratios yields the optimal one. The same measurement was repeated with modified cyclotron excitations instead of magnetron excitations. Now the axial frequency shift depends not only on electric field anharmonicities C_4,.., but also on magnetic field inhomogeneities, B_2 and on frequency shifts due to special relativity effects (see Sec. 5.6.3).

Figure 5.1 shows data for both magnetron and cyclotron excitations in the asymmetric PT taken throughout this measurement campaign. The initial tuning ratio scan was performed before the start of the HFS measurements of HD^+. It was repeated at intermediate times as a cross-check. Using the values of the PT $C_2 = 0.590325$ and $d_{char} = 9.156$ mm [48], an upper limit for the absolute values of $C_4 < 2{\cdot}10^{-5}$, $C_6 < 6.3{\cdot}10^{-4}$, and $B_2 < 10$ mT/m^2 were determined. In previous work, B_1 in the PT has been determined as 2.638(24) mT/m [48].

5.1.3 Calibration of the PnA Radius

The frequencies of the radial motional modes can be measured by RF coupling to the axial mode and fitting the resulting double-dip feature in the FFT spectrum, as described in Sec. 3.2.3. As the largest frequency of the motional modes, the uncertainty of the modified cyclotron frequency ν_+ dominates the uncertainty of ν_c. For uncorrelated uncertainties

$$\delta\nu_c = \sqrt{\sum_i \left(\frac{\nu_i}{\nu_c}\right)^2 \delta\nu_i^2}\ , \tag{5.1}$$

follows from the invariance theorem (Eq. 3.11). To reach higher precision, i.a. by being independent of the dip lineshape model in the determination of ν_+, phase-sensitive measurement techniques can be applied. For the measurement of the HFS transitions of HD^+ *Pulse-n-Amplify* (PnA) [48] was used.

Here, the motional phase of the modified cyclotron motion is measured as a function of time. For this, a motional phase ϕ_{init} is imprinted on this mode by an electric dipole excitation pulse resonant to the modified cyclotron motion. This excites the ion to a larger than thermal radius r_+^{PnA}.

Motional-amplitude-dependent systematic effects scale with r_+^{PnA}, therefore, it must be calibrated. For all dipole excitation pulses, the voltage amplitude was kept constant at 0.2 V and the excitation time was varied. This requires that the modified cyclotron frequency is know to better than $\pm\frac{1}{2}t_{exc}^{-1}$ for the longest excitation time (t_{exc}) used, so to $\sim \pm 1$ Hz. After each pulse, the resulting modified cyclotron radius r_+ was measured by changing the voltages of the correction electrodes to introduce a small anharmonicity C_4 of the electric potential. This shifts the axial frequency depending on the motional amplitudes, therefore r_+ can be measured by the shift of the axial frequency, compared to r_+ at thermal

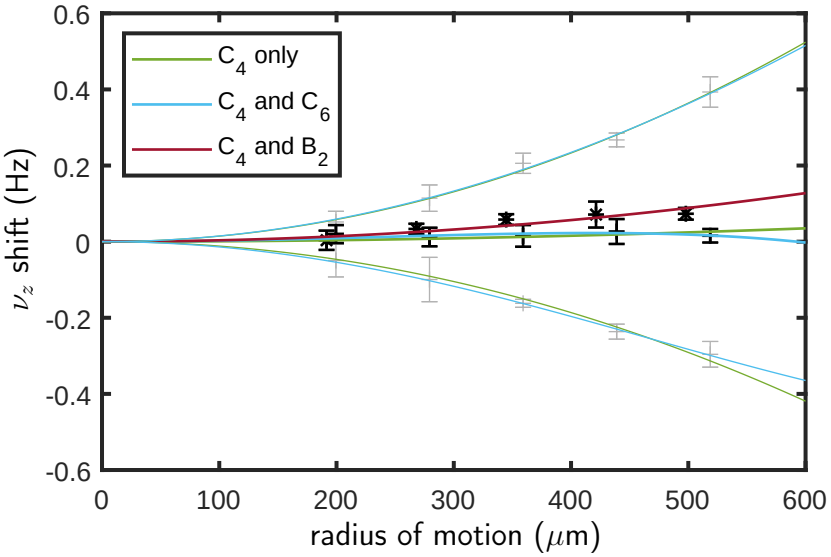

Figure 5.1: Tuning-ratio measurement in the asymmetric PT. If the tuning ratio is not optimized the axial frequency of the particle scales as a function of the radius of motion, shown for a change in tuning ratio of ± 0.001 (gray data). After optimization (tuning ratio: $\mathrm{TR}_{\mathrm{comb}} = 1.003430$), this scaling is suppressed for magnetron (+) and modified cyclotron (*) excitations. In the latter case, the axial frequency can still scale as a function of the modified cyclotron radius due to magnetic field inhomogeneities and special relativity effects. Each point shown is an average value of several scans and the errorbars give the uncertainty of the average. The electric field anharmonicities C_4, C_6 and magnetic field inhomogeneity B_2 are extracted by polynomial fits, $a \cdot x^2$ or $a \cdot x^2 + b \cdot x^4$. Terms $C_3 C_4 x^3$ and $C_3 C_6 x^5$ are not included in the fit, however they approach zero along with $C_4 x^2$ and $C_6 x^4$ in the optimization.

equilibrium (see Eq. 3.15). This is repeated for several excitation times. The data and fit are shown in Fig. 5.2

5.1.4 Ion Temperature

As in previous measurement campaigns at ALPHATRAP, the ion temperature was determined by measuring the distribution of the axial frequency of the ion in the AT, after repeated coupling of the modified cyclotron mode to the axial mode on resonance to the resonator circuit in the PT. Following Eq. 4.2, the axial frequency in the AT depends on the energy of the radial modes. Since the frequency of the modified cyclotron motion is much larger than the frequency of the magnetron motion, the effect on the axial frequency in the AT is much larger for the first.

When coupling the modified cyclotron mode to the axial mode on resonance to the resonator circuit, the modified cyclotron mode thermalizes to the effective temperature of this system. After the coupling is turned off, the energy and thus the radius of the modified cyclotron mode is fixed.

By repeatedly coupling the modes in the PT, decoupling, transporting the ion to the

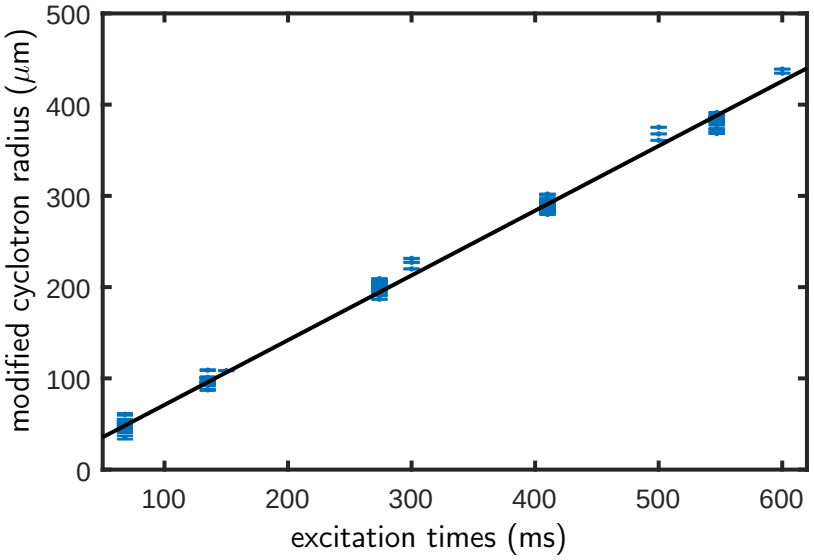

Figure 5.2: Data and fit for the PnA radius calibration. The length of the excitation pulse of the modified cyclotron motion was varied at a constant excitation voltage of 0.2 V. After each pulse, the resulting radius was measured and then the modified cyclotron motion was cooled back to thermal equilibrium. The fit is a linear function with zero offset: $r_+ = a \cdot t$, resulting in a=0.7095. To account for possible fluctuations, for example slight variation in the calibration due to hardware changes by recabling over the course of several months, an uncertainty of 10% is assigned for the calibration.

AT, detecting the axial frequency there, and transporting back to the PT, the Boltzmann distribution of the thermal bath of the resonator system can be sampled. The probability density ($\rho(E_+, T_+)$) for a certain axial frequency offset ($\Delta\nu_z^{\mathrm{AT}}$), arising from a nonzero modified cyclotron energy (E_+), as a function of temperature is given by the exponential one-dimensional Boltzmann distribution [48]:

$$\rho(E_+, T_+) = \frac{1}{T_+ k_B} e^{-\frac{E_+}{T_+ k_B}} \ , \tag{5.2}$$

$$E_+ = (2\pi)^2 \, m_{\mathrm{ion}} \, \nu_z^{\mathrm{AT}} \, \frac{B_0^{\mathrm{AT}}}{B_2^{\mathrm{AT}}} \, \Delta\nu_z^{\mathrm{AT}} \ , \tag{5.3}$$

where T_+ is the average temperature of the Boltzmann distribution of the modified cyclotron motion, k_B is the Boltzmann constant, E_+ is the energy of the modified cyclotron mode in each cycle. It is determined by the shift of the axial frequency in the AT from a '0-K' cold particle $\Delta\nu_z^{\mathrm{AT}}$, the mass of the ion m_{ion}, the axial frequency in the AT ν_z^{AT}, and the ratio between the magnetic field in the AT B_0^{AT} and the strength of the magnetic bottle B_2^{AT}. The axial temperature in the PT is related to T_+^{AT} by:

$$T_z^{\mathrm{PT}} = T_+^{\mathrm{AT}} \, \frac{\nu_z^{\mathrm{PT}}}{\nu_+^{\mathrm{AT}}} \, \frac{B_0^{\mathrm{AT}}}{B_0^{\mathrm{PT}}} \ . \tag{5.4}$$

For example, for an HD^+ ion at ALPHATRAP, the mean cyclotron radius corresponding to 9-K axial temperature gives an axial frequency shift in the AT of about 300 Hz compared to 0 K.

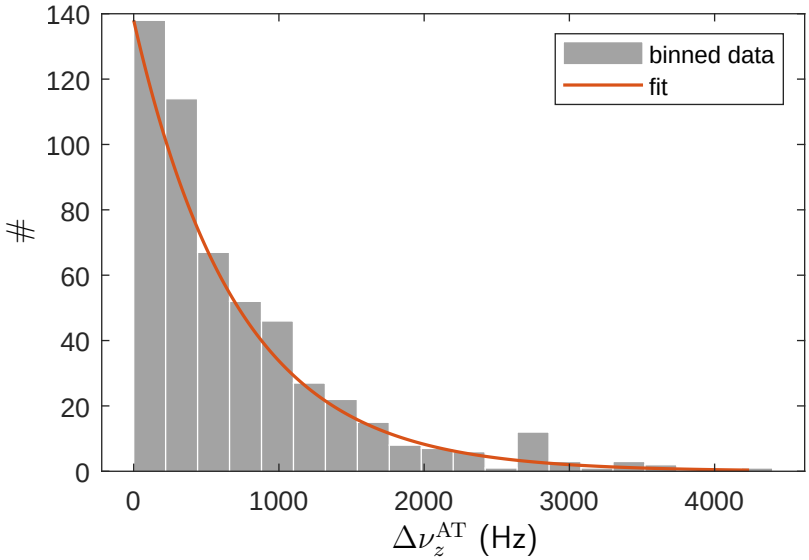

Figure 5.3: AT temperature measurement, showing a histogram for the shift of the axial frequency of the ion compared to the coldest particle measured for 525 measurement cycles. The temperature of the ion is derived by a maximum likelihood fit of the unbinned data with the one-dimensional Boltzmann distribution (Eq. 5.2) shown by the orange line.

In contrast to previous measurement campaigns, the AT temperature determination was carried out in a dedicated measurement, instead of data collection throughout the main measurement cycles. Since the signal strength of HD^+ in the AT was small, it was not efficient to search the full AT frequency range possible with dip sampling in each cycle throughout the HFS measurement campaign. Instead in the dedicated temperature measurement, the HD^+ ion was excited to a fixed axial amplitude after ν_+-ν_z coupling in the PT and then transported to the AT. With this axial excitation, the ion could be detected as a peak off-resonant to the detection system, and waiting for a reliable dip signal was not necessary.

Repeating 525 cycles, each resampling from the thermal Boltzmann distribution, resulted in a spread of the axial frequency in the AT, shown in Fig. 5.3. With a maximum likelihood fit of the exponential one-dimensional Boltzmann distribution, the axial temperature was determined to be 9.6(4) K.

Measuring with negative feedback at about a factor of 3 signal-to-noise ratio (SNR) suppression of the resonator in the FFT spectrum results in a temperature of 2.3(2) K. The negative feedback was only added during the coupling of ν_+ and ν_z.

Since the measured temperature was higher than expected, the temperature was additionally measured by analyzing the jitter of the axial frequency in a detuned PT configuration after repeated cyclotron (and magnetron) excitation. The procedure was followed as for the measurement explained in Ref. [97]. The temperature resulting from cyclotron excitation agrees with the AT measurement, while the magnetron measurement resulted in about 20 K. The higher value for the magnetron measurement is most likely due to heating of the ion by the RF coupling of the motional modes which in this case is only 10 kHz off the resonator frequency. Additionally, the phase jitter in the PnA measurement agrees with a $\sim$10 K temperature as well.

In this measurement campaign, several measurement techniques were applied to measure the effective ion temperature. All methods include coupling of the axial motion to the radial motions. Therefore, it is not possible to disentangle whether the axial temperature of the ion is hotter than in previous campaigns measuring $T_z \approx 5$ K [102, 104] or whether the coupling drive heats the ion. To get an idea of whether the measured temperature is due to heating from the coupling drive, temperature measurements could be carried out with several different coupling drive strengths. This was not done here, as the uncertainty resulting from the slightly increased temperature does not limit the precision of the HFS measurement campaign.

5.1.5 PT Voltage Drift (ν_z Drift)

At ALPHATRAP, it has been observed that the axial frequency drifts after ion transports [104, 116]. At the time, the drift was attributed to thermal effects in the ultra-stable voltage supply StaReP [117]. In the HD^+ campaign, this was re-investigated. First, the available voltage sources were compared using a high-precision multimeter. The output voltages were switched in 10 V steps. Drifts of several 10 μV for 10-20 s were measured between the voltage sources, which, however, cannot explain the $\sim$200 s time-scale of the drifts of the axial frequency observed in the trap.

Next, a switch box was implemented, which allows to keep the voltage output of the StaReP constant at the trapping voltages and switches to another power supply for ion transports. The voltages for the five central electrodes of the PT are supplied by StaReP, while the voltages for the endcap electrodes are supplied by LoCepps, an in-house-built stable power supply [118]. The initial test compared a standard ion transport ramping the StaReP voltages with an ion transport for which the switch box is used with an independent power supply and additionally applying the function of the Locepps to switch the endcaps to ground after transport. Both methods resulted in approximately the same drift of the axial frequency of $>$100 mHz for $\sim$250 s, see Fig. 5.4.

Several tests were carried out, changing the voltage of only single electrodes. All tests resulted in a drift of the axial frequency. The sign and strength of the drift depended on the change in voltage and the impact the electrode has on the PT trapping potential. An example is shown in Fig. 5.4. While the results do not rule out thermal effects in the power supplies, they surely relate that there is at least another effect causing the voltages at the electrodes to drift after voltage changes.

Currently, we assume that this drift is related to the soakage effect in the capacitors used in the room-temperature, 77-K, and 4-K RC filters between the voltage supplies and the electrodes [102]. The soakage properties of different capacitors were investigated by another PhD student (Athulya Kulangara Thottungal George). The tests have shown that this should be taken into account when choosing capacitors, especially for cryogenic RC filters. In the upgrade, we replaced a majority of the NP0 capacitors with polypropylene ones based on the test results. Unfortunately, so far no improvement of the axial frequency drift has been observed. The effect on the measurements can be mitigated by waiting for the drift to stabilize after transports, however, this increases the cycle time of measurements.

Furthermore, the axial drift makes high-precision measurements of magnetic field sensitive transitions based on ion swapping almost impossible. Here, the magnetic field would be determined by a highly charged ion (HCI) for good SNR and low thermal modified cyclotron

radius, and then the ion of interest, e.g. a MHI would be transported into the same position for probing the transition of interest. This only works if the time between ion swapping is small compared to the temporal stability of the magnetic field. Such a measurement would be beneficial, since the modified cyclotron motion of the ion of interest would not have to be coupled to the axial frequency and thus the resonator. Therefore, r_+ and thus ν_z^{AT} would remain constant, which would significantly shorten the measurement time in the AT (no need to search for the ion in the AT and not necessarily needed to drive a spin flip in the AT). Measurements following this procedure have been carried out at BASE [91] with ion swapping times of ∼10 s [21]. Furthermore, using a HCI would reduce the measurement time in the PT as well and could lead to a more precise determination of the magnetic field [102].

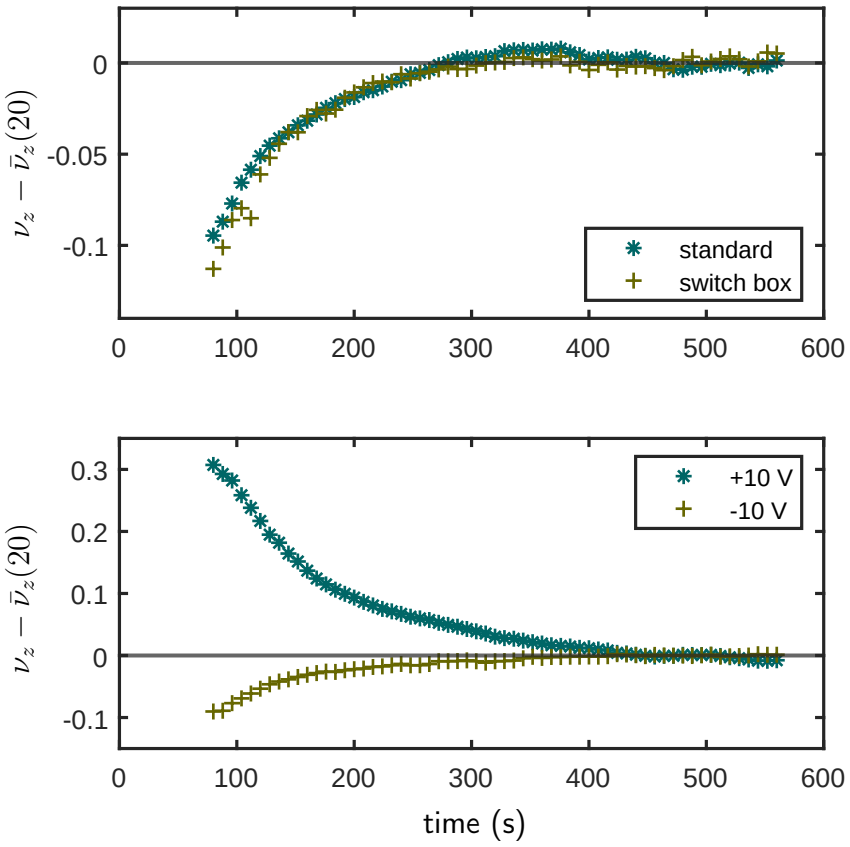

Figure 5.4: Axial frequency drift after ion transport and after varying the voltages of PT electrodes. **top:** Measured axial frequency after ion transport without (standard) and with the switch box. **bottom:** Measured axial frequency after setting the two lower endcap electrodes of the PT to either +10 V or - 10 V and then back to 0 V. For all measurements FFT spectra are saved after the PT voltages are set back to their nominal values. Each FFT spectrum has an acquisition time of 8 s. For reliable dip fitting a running average of 20 spectra is used for dip fitting to determine the axial frequency. The axial frequency value of each fit result is plotted at the center of the 20 spectra. Therefore, the first data point is 80 s after setting the voltages back to nominal PT settings, as it is derived from the first 20 spectra each acquired for 8 s. The mean of the last 20 values ($\bar{\nu}_z(20)$) is subtracted from each data point. Each displayed point is the average over 30 runs.

5.2 Initial Search of HFS Transitions

5.2.1 First eSF of HD^+ in the AT

We observed the first MW-induced HFS transition in the AT. The theoretical prediction of the eSF transition frequencies was 0.1 ppm, limited by the uncertainty of the theoretical g_e-factor prediction [4]. Due to the ion motion in the strong magnetic bottle of the AT, the magnetic field at the position of the ion varies by about 40 ppm relatively, assuming a 3-K temperature due to negative feedback. Therefore, the magnetic field sensitive eSF transitions are broadened to about 40 ppm, well beyond the precision of the prediction, however not as much as to overlap the different eSF transitions. The transitions differ by more than 100 MHz, 0.1% relatively, from each other. First, a dip spectrum is sampled to obtain the axial frequency of the ion ($\sim$ 2 min), then MW pulses of single seconds alternate with dip spectra to see whether the MW pulse successfully drove an eSF transition. A change in electron-spin orientation causes the axial frequency to jump by 12 Hz (see Sec. 4.2.2). This is repeated by successively probing the six possible eSF frequencies until a transition is observed via a jump in the axial frequency of the ion. Due to the 50 % spin flip probability of the incoherent drive, this takes 12 attempts on average, resulting in an average total time of 24 minutes. This is depicted in Fig. 5.5.

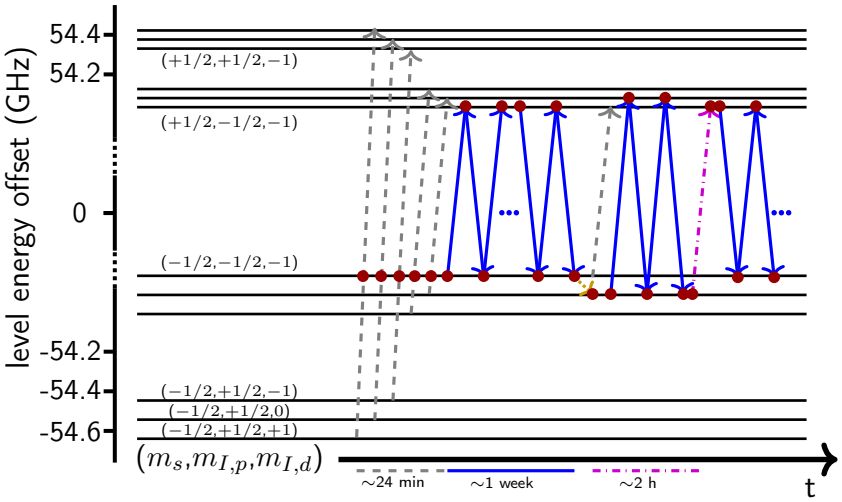

Figure 5.5: The 12 levels of the HFS of the (0,0) state of HD^+ are shown in the AT at $B_0 = 3.8700$ T, for details on the level structure see Fig. 2.2. For initial state detection in the AT, the six possible frequencies for an electron spin flip are irradiated successively until a transition is observed (first blue arrow) which takes about 24 minutes. This frequency can then be irradiated repeatedly driving eSF transitions. On average, after about a week, a non-driven change in nuclear spin orientation occurred. For both the proton and deuteron spin this happened from either level of the previous eSF transition. After such an event, no eSF is observed at the previous MW frequency. The other possible MW frequencies are successively irradiated again until a MW-induced eSF in observed, thus determining the new HFS state. The ion can be brought back to the previous eSF transition states by a MW-induced combined electron and nuclear spin-flip transition (dash-dotted pink arrow). This figure is adapted from Ref. [119].

5.2.2 Finding eSF transitions of HD^+ in the PT

In absence of the magnetic bottle, there is no broadening of the line in the PT. Here, the linewidth of an eSF transition mainly depends on the magnetic-field jitter during the probe time. This also determines the precision with which the magnetic field can be measured.

Using a 5-s phase evolution time in a PnA cycle, we measured a phase jitter of below 20 degrees, which relates to a relative uncertainty of the magnetic field determination of 0.55 ppb. Therefore, the full width at half maximum (FWHM) was expected to be on the order of single ppb. Using our maximum available MW power of ∼25 dBm at the output of the multiplier, the transitions can be broadened to about 50 ppb.

For the initial search, we used the fact that r_- and r_+ remain almost constant as long as the radial motions are not coupled to the axial motion or to each other. Adiabatically transporting the ion from AT to PT and back resulted in a jitter of the axial frequency in the AT of only single Hz, which is smaller than the axial frequency jump of 12 Hz due to an electron spin flip. Therefore, the spin state of the electron had to be determined only once in the AT. For the following measurement cycles, the state could be inferred directly from the dip position without requiring MW-induced electron spin flips in the AT. More importantly, this allows to not re-cool the modified cyclotron mode in between measurement cycles, which would necessitate searching for the ion in the AT (see Sec. 5.1.4).

This enables fast measurement cycles of ∼5 minutes of the following type: Initially, the magnetic field is measured in the PT after which the ion is transported to the AT, found, and centered on the resonator. Then, the hyperfine state and electron spin orientation is determined. The expected MW frequency for an eSF transition in the PT is calculated based on these results. The first cycle then starts by transport to the PT, where several MW pulses are irradiated, stepping through the uncertainty of the prediction. For irradiation times above single ms, the drive looses coherence due to magnetic field fluctuations, resulting in a maximum spin flip probability of 50%. Therefore, the step sweeps were repeated several times.

Once a sweep range with an electron spin flip was found, the range was narrowed down until the transition was known to less than the power broadened line width. From here on the power was reduced in steps while probing an increasingly smaller frequency range. Note, the magnetic field jitter from cycle to cycle is ∼2.5 ppb or lower which means that only from this linewidth on it becomes necessary to measure the magnetic field in the PT in each cycle.

5.3 Non-Driven Nuclear Spin Transitions

In the absence of any interaction, HD^+ should remain in the $(0, 0)$ state in the cryogenic environment of the trap and the hyperfine states of HD^+ should have basically infinite lifetimes. Thus, in the HFS campaign the orientation of the nuclear spins should remain constant with respect to the external trapping field, since the frequencies of the irradiated MW address only the orientation of the electron spin. For the possibility of combined electron and nuclear spin transitions at similar MW frequencies see Sec. 5.4. However, throughout the campaign, we observed several non-driven changes of the hyperfine state by a change of the approximate quantum numbers of the nuclear magnetic moments $m_{I,p}$, $m_{I,d}$. An overview of the detected eSF transitions is given in Fig. 5.6. On average once

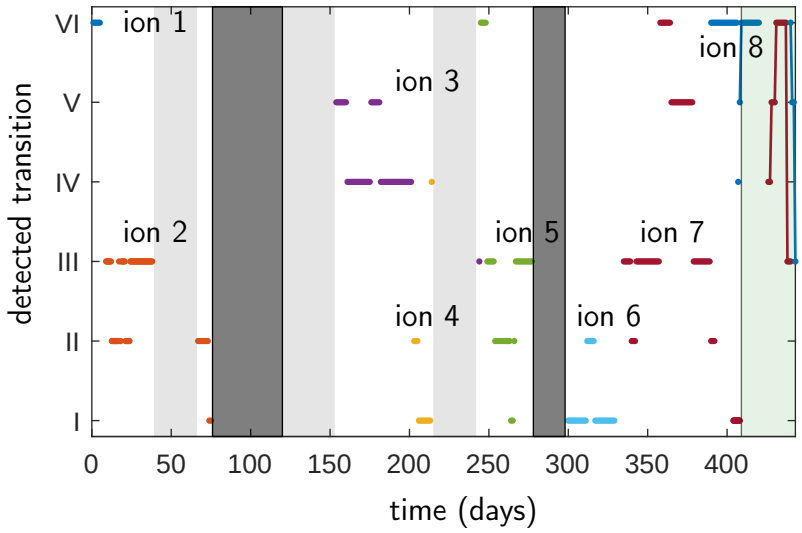

Figure 5.6: Detected eSF transitions throughout the measurement campaign. Day 0 corresponds to the start of the measurement campaign (August 25^{th}, 2021). The transitions are numbered according to the level diagram in Fig. 2.2. The dark gray bands are measurement breaks with subsequent ion reloading, while the light gray bands depict measurement time for systematic studies that did not involve electron spin flips. Ion 5, ion 7, and ion 8 were loaded into the trap along with ion 3 and ion 6, respectively and were thus trapped for more than 100 days. Note that ion 6, ion 7, and initially ion 3 were not lost but stored and reused later or purposely ejected, mainly to choose an ion in a different hyperfine state. Throughout more than a year of measurements only a single ion loss, ion 3 at day 244, is unexplained and could be due to collisions with residual gas. All other ion losses can be explained by human or technical errors, such as power cuts and vacuum pump failures. All changes of the detected transitions, except for the light green band at the end, are due to non-driven changes of one of the nuclear spin orientations. At the end of the campaign (light green band), simultaneous electron and nuclear spin transitions were driven for ions 7 and 8 to prepare the hyperfine state.

a week, the hyperfine state of the ion jumped by either $\Delta m_{I,p} = \pm 1$ or $\Delta m_{I,d} = \pm 1$. A direct accidental drive of nuclear spin flips can be excluded, as no frequency was introduced that would drive either nuclear spin flip or coupled electron and nuclear spin flips.

Possible explanations are collisions with residual gas or black-body radiation (BBR) driving rovibrational excitations with subsequent decays back to the ground state for which nuclear spin flips can occur to fractional probability in the excitation or decay. We attempted to increase the BBR by placing a 10 W light bulb in front of the view port below the magnet. We did not see an effect after several hours, the nuclear spin state of the ion remained constant. At the time of the measurement, neither explanation could be confirmed or excluded. This will be revisited in Sec. 6.2.

5.4 Weak MW Transitions

The radii of the AT and the MW guides below are 3 mm. The nuclear-spin-flip transitions lie in the range between 44-635 MHz (see Fig. 2.2), corresponding to wavelengths of 0.5-7 m. The required near-field drive for this frequency range was implemented after the measurement campaign, see Sec. 4.4.

In the HFS campaign, the most feasible option to address the nuclear spin orientations was through coupled electron and nuclear spin-flip transitions, changing $\Delta m_s = \pm 1$ and $\Delta m_{I,p} = \pm 1$ or $\Delta m_{I,d} = \pm 1$ at the same time. The frequencies of these transitions lie in the 100 GHz regime of the electron-spin-transition and can be irradiated into the trap. They are, however, suppressed by more than two orders of magnitude compared to the transitions changing only the electron spin [120].

Contrary to the eSF transitions, which require a perpendicular oscillating B-field component of the drive with respect to the external magnetic trapping field, these transitions require a parallel one. At ALPHATRAP, the MW are irradiated from below in axial direction, so in parallel to the magnetic trapping field. Hence, there is mainly a perpendicular oscillating B-field component of the drive on the center trap axis. However, the PT acts as an over-moded waveguide (trap diameter $\gg 1.84/\pi$ wavelength), resulting in parallel components of the oscillating B-field of the drive off-center to the trap axis. Preparing the ion on a 1-mm magnetron and a 0.5 mm modified cyclotron radius the ion moves over a larger area in the radial plane and thus probes the parallel components of the MW field. Stepping the frequency of the MW drive through a $2{\cdot}10^{-8}$ range in $1{\cdot}10^{-9}$ steps for each attempt at maximum available MW power resulted in the drive of the electron and nuclear spin-flip transitions with $\sim$20% probability. The first successfully driven transitions are marked in the light green shaded area in Fig. 5.6.

5.5 Measurement Principle and Cycle

Initially, the measurement begins with the hyperfine state detection in the AT. Here, the MW frequencies for the six possible eSF transitions are probed successively, alternating with FFT dip signal sampling, until a spin flip is observed. Thus, knowing the nuclear spin orientation, the measurement transition is set, see Fig 5.5. For all AT cycles positive feedback on the resonator is used to increase the effective dip width and thus reduce the acquisition time of the FFT spectrum for a faster cycle time (see Sec. 4.2.2). For MW irradiation, the phase of the feedback is switched by 180 degrees for negative feedback. Thus, the effective axial temperature of the ion is reduced, and the motional amplitude in the magnetic bottle is damped. This was done as a precaution, in case the broadening would cause an overlap of the eSF transitions in the AT.

Each subsequent measurement cycle begins in the AT with an electron spin flip indicating whether the spin points up or down ($m_s = +\frac{1}{2}$ or $m_s = -\frac{1}{2}$). The ion is then transported to the PT for the precision measurement. An overview of the measurement cycle is given in Fig 5.7.

The PT measurement begins with a 120 s waiting time for the voltages to settle, thus avoiding large systematic effects due to the axial frequency drifts after ion transports (Sec. 5.1.5). Then, the modified cyclotron frequency is measured by the double-dip tech-

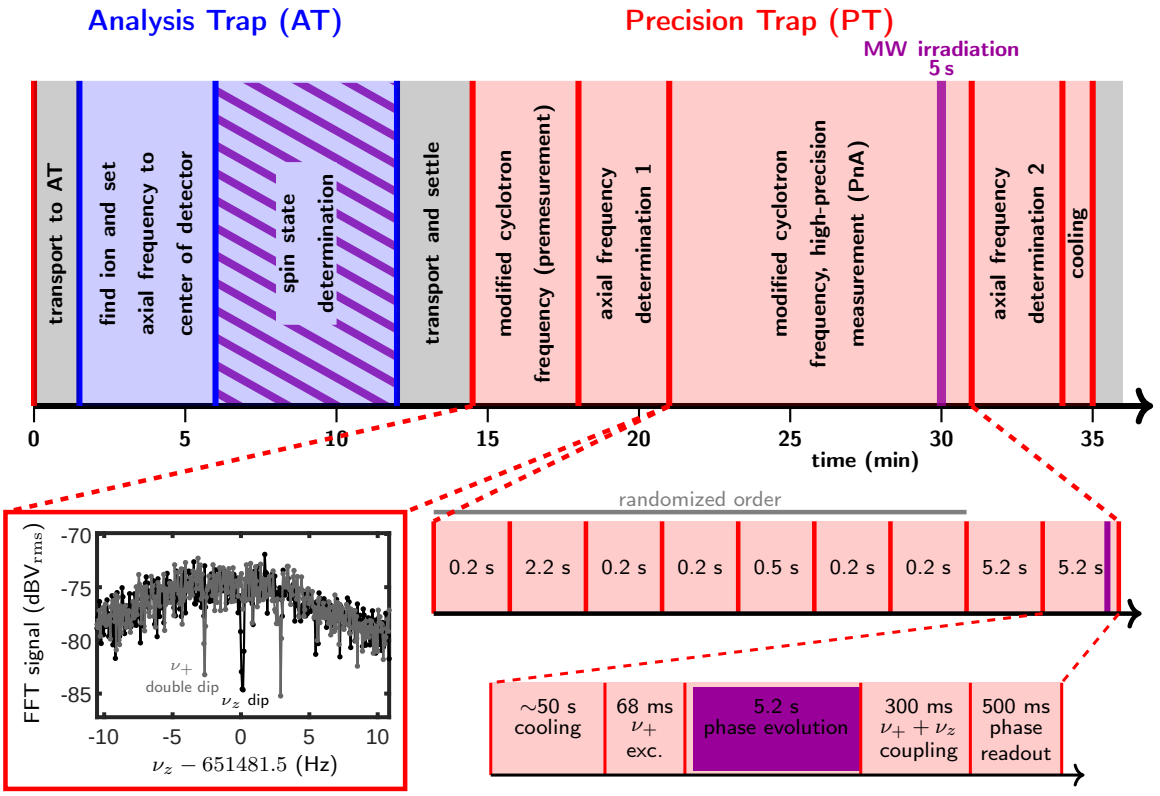

Figure 5.7: Schematic of a typical measurement cycle of the HFS campaign. The blue sections represent the state determination in the AT and the red the precision measurement in the PT. MW irradiation is shown in purple and is not to scale for better visibility. In the AT, MW irradiation and dip sampling alternates until an electron spin flip is observed. Due to the $\sim 50\%$ spin-flip probability this takes a varying amount of attempts. The variable number of MW irradiation is depicted by the slanted purple lines.

nique, coupling this mode to the axial one by an RF drive at $\nu_{\mathrm{RF}} = \nu_+ - \nu_z$. This serves as a premeasurement of ν_+ and is used as an input value for the more precise subsequent PnA measurement. The double dip is sampled with positive feedback on the resonator to shorten the measurement time. After the ν_+ premeasurement, the axial frequency dip is sampled. Here, no feedback is used to avoid systematic effects, as ν_z from the dip measurement is used for the magnetic field determination.

Following the axial dip, the PnA measurement begins. In a single PnA cycle, an excitation at ν_+ of the modified cyclotron mode imprints a phase on this motion ϕ_{init} and prepares the ion on the measurement radius r_+^{PnA}. It evolves at this radius unperturbed for a given free evolution time $t_{\mathrm{evol}}^{\mathrm{PnA}}$, after which the phase of the motion ϕ_{PnA} is transferred to the axial motion, via a quadrupole coupling pulse at $\nu_{\mathrm{RF}} = \nu_+ + \nu_z$. Additionally, this pulse amplifies both motional amplitudes for axial peak detection. The phase of the axial motion of the ion is encoded in the resulting peak signal of the ion in the FFT spectrum. To avoid a shift of the axial frequency after RF pulses seen in the past [104], the cryogenic switches remain in the closed setting (strong suppression) through out the PnA measurement and a pulse shaping routine was used [102]. For details on this shift and the implementation of

pulse shaping, see Refs. [104, 102]. ϕ_{PnA} relates to the modified cyclotron frequency via:

$$\phi_{\mathrm{PnA}} = 2\pi\nu_+ \, t_{\mathrm{evol}}^{\mathrm{PnA}} + \phi_{\mathrm{init}} \ . \tag{5.5}$$

This is followed by thermalization of the axial mode with the resonator and re-cooling of the modified cyclotron mode by RF coupling of the modes ($\nu_+ - \nu_z$). This PnA cycle is repeated nine times, five times with $t_{\mathrm{evol}}^{\mathrm{PnA}} = 0.2$ s, for the reference phase, once at each $t_{\mathrm{evol}}^{\mathrm{PnA}} = 0.5$ s and $t_{\mathrm{evol}}^{\mathrm{PnA}} = 2.2$ s for intermediate phase unwrapping steps, and twice at $t_{\mathrm{evol}}^{\mathrm{PnA}} = 5.2$ s. The order of the five reference phase and two unwrapping step cycles is randomized, followed by the two long evolution times. The five determined reference phases are averaged and compared with the phases determined with longer $t_{\mathrm{evol}}^{\mathrm{PnA}}$. The intermediate unwrapping steps are necessary to ensure that the number of full cycles in the longest free evolution time are counted correctly and are used to check for systematic effects.

The ν_+ value determined from the first $t_{\mathrm{evol}}^{\mathrm{PnA}} = 5.2$ s cycle, along with ν_z from the dip measurement and a previously measured ν_- value, are used to determine ν_c via the invariance theorem Eq. 3.11. This ν_c value is used to update the magnetic field value in the trap and to thus predict the transition frequency for the eSF transition. Finally, the ninth PnA cycle is carried out at $t_{\mathrm{evol}}^{\mathrm{PnA}} = 5.2$ s with simultaneous 5 s MW irradiation at either the newly calculated frequency or at an offset for scanning the resonance. ν_+ of this PnA cycle is used for the final magnetic field determination, carried out simultaneously to the MW irradiation probing the transition. For transition II a larger $t_{\mathrm{evol}}^{\mathrm{PnA}}$ was used. Here, a single cycle with $t_{\mathrm{evol}}^{\mathrm{PnA}} = 5.2$ s was used as a third unwrapping step and two cycles with $t_{\mathrm{evol}}^{\mathrm{PnA}} = 10.2$ s were carried out as the last two PnA cycles. Longer PnA evolution times can lead to higher precision in the determined motional frequency if the phase stability is not reduced. However, in the measurements of transition II this was not the case.

PnA is followed by another axial dip measurement. As this is closer in time to the last PnA cycle and thus the MW irradiation, this ν_z value is used for the final magnetic field determination. Approximately once a day, ν_- is measured via the double-dip technique. As it is by far the smallest frequency, its uncertainty does not limit the magnetic field determination and does not have to be measured more often.

Both radial modes are cooled via RF-coupling to the axial mode before transport to the AT. For the modified cyclotron mode, negative feedback is used while cooling to lower the effective temperature of this mode (see Sec. 4.2.2). This reduces the spread of likely axial frequencies in the AT (see Sec. 5.1.4) and therefore reduces the time needed to find the ion in the AT. As a result of the cyclotron re-cooling, the ion has a random cyclotron energy sampled from the Boltzmann distribution, when entering the AT. Consequently, its exact axial frequency in the magnetic bottle has to be determined. In this campaign, a 200 Hz range was checked for the ion signal, if it is not in this range the ion is transported back to the PT for re-cooling, hence resampling of r_+ from the thermal Boltzmann distribution. On average, one re-cooling step was necessary per measurement cycle. Once the ion is found in the AT, the voltages are adjusted to center the ion on the resonator. Then the orientation of the electron spin is measured by inducing a spin flip. The adiabatic nature of the ion transports between the trap sections prevents changes to the energy and HFS state of the ion. This has been verified in the past [48] and can been seen from the single-Hz jitter of the axial frequency in the AT after repeated ion transports in the initial search of the transition in the PT, Sec. 5.2.2.

The electron spin orientation before and after the PT cycle is compared, relaying the

information whether the attempt to drive the transition in the PT was successful or not. On average, such a fully automated measurement cycle took ∼35 minutes. The time can vary from cycle to cycle, since the re-cooling process of the modified cyclotron mode is a statistical process and the number of attempts until an eSF is driven in the AT varies. Since overall the MW transmission efficiency is frequency dependent (see Sec. 4.3 and Ref. [111]), the MW power had to be adjusted for each transition, to not saturate and thus broaden the resonance. This results in eSF rates below 50%, that may vary from one transition to the next.

As a result of a spontaneous change of a nuclear spin orientation, no electron spin flips are observed at the measurement transition anymore. After 20 unsuccessful AT attempts, the measurement starts over at the initial step, where all six possible MW frequencies are probed successively, until the new state is determined. After observing an electron spin flip, the measurement begins at the new transition.

One of the main challenges of this campaign compared to measurements of heavier, more-highly charged ions are the very narrow dips of ∼0.4 Hz in the AT and ∼0.3 Hz in the PT. Therefore, longer acquisition times of the FFT and an increased number of averages are necessary for reliable fits and result in long sampling times for each dip or double dip of three and six minutes, respectively. The ion signal is not always well distinguishable from noise leading to some data cuts in the AT and in the PT. Furthermore, the light mass leads to larger thermal amplitudes, which has two important consequences. First, it increases the shift of ν_z^{AT}, see Eq. 4.2. While this is beneficial for the large ν_z jump due to an electron spin flip, it also increases the range of likely ν_z^{AT} values after sampling r_+ from the thermal Boltzmann distribution. Second, the larger thermal r_+, required a larger PnA measurement radius of at least 48 μm for reliable phase imprint and thus low phase jitter. Larger measurement radii lead to larger systematic effects. This radius is used for transitions I-V, while transition VI was measured at 96 μm.

By reducing the effective temperature and thus the initial thermal radius of the modified cyclotron motion, the use of negative feedback in the PnA cycle can allow smaller measurement radii at equal phase stability. Besides lowering the effective temperature, negative feedback reduces the Q value of the resonator and thus increases the cooling time constant of the ion. The cooling time constant for the modified cyclotron motion with RF coupling to the axial motion when applying negative feedback is on the order of several seconds. To ensure thermalization and thus a decreased thermal radius, multiple cooling time constants should be waited while coupling. Therefore, applying negative feedback would increase the time for each PnA cycle and thus the time for each full measurement cycle. The increased measurement time and the chance of adding systematic effects due to feedback, compared to the rather low relative systematic uncertainty of ν_c due to the PnA radius without feedback of up to 1.8 ppb, led to the decision to carry out the measurements without negative feedback in the PnA cycle. Negative feedback was only used for cooling the modified cyclotron mode before transport to the AT and during MW irradiation in the AT.

5.6 Analysis

The analysis of the FFT spectra for the determination of the motional frequencies of the ion via dip fitting and PnA phase unwrapping was carried out following the usual procedure

at ALPHATRAP.

5.6.1 Single Resonances

During spectroscopy, the collected data point for each measurement cycle k of the transition consists of the current magnetic field value $B(k)$ obtained by the determination of $\nu_c(k)$ by the measurement of the motional frequencies of the ion. It further consists of the value of the MW frequency $\nu_{\mathrm{MW}}(k)$ probing the transition during the last PnA free evolution time of the ν_+ measurement and the binary information $D(k) = 0, 1$ whether the transition was successfully driven or not. Diagonalizing the Hamiltonian H, Eq. 2.7, with $B(k)$ and the theoretical values $g_{\mathrm{e}}(0,0)_{th}$, $E_4(0,0)_{th}$, $E_5(0,0)_{th}$ the predicted transition frequency $\nu_{\mathrm{theo}}(k)$ can be calculated. This is the predicted transition frequency at the magnetic field $B(k)$ at the time of the MW irradiation. Since the magnetic field fluctuates in time, $B(k)$ and thus $\nu_{\mathrm{theo}}(k)$ are different for each measurement cycle. Instead of using $g_{\mathrm{e}}(0,0)_{th}$, $E_4(0,0)_{th}$, $E_5(0,0)_{th}$, a set of values $g_{\mathrm{e}}(0,0)^0$, $E_4(0,0)^0$, $E_5(0,0)^0$ can be used. These values can be shifted arbitrarily as long as the they are constant for all data points of the resonance, resulting in $\nu'_{\mathrm{theo}}(k)$. For example, the reference values were adjusted after measuring a transition for a better prediction of the following ones. Using $\nu'_{\mathrm{theo}}(k)$, each data point is assigned a detuning, defined by the difference between the predicted transition frequency at $B(k)$ and irradiation MW frequency:

$$\Delta\nu_{\mathrm{HFS}}(k) = \nu_{\mathrm{MW}}(k) - \nu'_{\mathrm{theo}}(k) \ . \tag{5.6}$$

After completion of the measurements, the resonance line data $\{\Delta\nu_{\mathrm{HFS}}(k), D(k)\}_k$ are fitted by a maximum-likelihood distribution with a Gaussian line shape, using the following function:

$$P(\Delta\nu_{\mathrm{HFS}}) = A\, e^{-\frac{(\Delta\nu_{\mathrm{HFS}} - \Delta\nu_{\mathrm{center}})^2}{2\sigma^2}} \ , \tag{5.7}$$

where A is the amplitude, $\Delta\nu_{\mathrm{center}}$ is the center of the resonance, and σ is the standard deviation of the normally distributed data.

The data and the Gaussian maximum likelihood fits of each resonance using the final $g_{\mathrm{e}}(0,0)_{exp}$, $E_4(0,0)_{exp}$, $E_5(0,0)_{exp}$ values are displayed in Fig. 5.8 and the fit results along with measurement parameters are given in Tab. 5.1. The uncertainties are derived from a change of the probability of the maximum likelihood fit by 0.5 due to a change of each parameter, followed by a refitting of the remaining two. The result of variation of one parameter and refitting the remaining two is displayed in Fig. 5.9 and demonstrates the low correlation of the center position with the amplitude and width of the curve. Width and amplitude in turn show a slight correlation to each other.

The fit results show full width at half maximum (FWHM) of the lines of 280-600 Hz (2.5-5.4 ppb). The dominant contributions arise from the phase-imprint jitter due to the thermal motional amplitude of the ion coupled with special relativity effects, temporal magnetic field fluctuations during the magnetic field determination, and a SNR dependent readout jitter of the PnA phase. The center of the lines are determined with a statistical uncertainty approximately equal to $10\,\%$ of the FWHM. As can be seen in Fig. 5.8 and Tab. 5.1, transition V is broader and has larger uncertainties compared to the other transitions. Both for transition V and transition II there are less data points contributing

Table 5.1: Results of the Gaussian maximum likelihood fits for each of the six electron spin flip resonances along with the number of successful PT spin flips (SF) and the total amount of data points (attempts), the radius of the modified cyclotron radius during PnA, and the free evolution time during MW irradiation.

	center [Hz]	width [Hz]	amplitude [%]	SF/attempts	r_+^{PnA} (μm)	t_{evol}^{PnA} (s)
I	-21(22)	118(20)	37(5)	56/352	48(5)	5.2
II	-22(47)	155(42)	31(9)	16/197	48(5)	10.2
III	37(24)	104(22)	18(5)	25/399	48(5)	5.2
IV	21(20)	127(21)	26(4)	59/494	48(5)	5.2
V	26(89)	255(76)	31(13)	14/99	48(5)	5.2
VI	-34(24)	127(20)	33(5)	45/365	96(10)	5.2

to the data set for the transition, mostly due to random HFS state changes of the ion. Furthermore, for transition V there is a single eSF at a larger value of $\Delta\nu_{\mathrm{HFS}}$ compared to the other transitions. The measurement data was cross checked and there is no indication that this data point is incorrect[1]. Combined with the low statistics, this resulted in the broader line and increased uncertainties.

5.6.2 Determination of $g_e(0,0)$, $E_4(0,0)$, and $E_5(0,0)$

All data points $\{B(k), \nu_{\mathrm{MW}}(k), D(k)\}_k$ of the six measured transitions were used for the extraction of $g_e(0,0)$, $E_4(0,0)$, and $E_5(0,0)$. Again, diagonalization of the Hamiltonian H, Eq. 2.7, with $B(k)$ and initial reference values $g_{\mathrm{e}}(0,0)^0$, $E_4(0,0)^0$, $E_5(0,0)^0$, result in the initial predicted transition frequency $\nu'_{\mathrm{theo}}(k)$ and thus detuning $\Delta\nu_{\mathrm{HFS}}(k)$ (Eq. 5.6) for each data point of each transition. The final values of $g_{\mathrm{e}}(0,0)$, $E_4(0,0)$, $E_5(0,0)$ are derived from a combined Gaussian maximum likelihood fit of the full data set of all six transitions $(\{\Delta\nu_{\mathrm{HFS}}(k), D(k)\}_k)_i$, using:

$$P_i(\Delta\nu_{\mathrm{HFS}}) = A_i\, e^{-\frac{(\Delta\nu_{\mathrm{HFS}})^2}{2\sigma_i^2}} \quad , \tag{5.8}$$

where A_i and σ_i are the amplitude and standard deviation of the normally distributed data for each transition, respectively. For every variation of $g_{\mathrm{e}}(0,0)$, $E_4(0,0)$, $E_5(0,0)$ in the fitting process, the reevaluation of $\nu'_{\mathrm{theo}}(k)$ and therefore, $\Delta\nu_{\mathrm{HFS}}(k)$ for each data point of every transition is required. The six value each for A_i and σ_i are fitted along with $g_{\mathrm{e}}(0,0)$, $E_4(0,0)$, $E_5(0,0)$. The result of the combined fit on the six resonances is reported in Figure 5.10.

The systematic uncertainty of the six resonances is not equal due to the larger ν_+^{PnA} radius for transition VI. Therefore, a jitter was added to the data with the systematic uncertainty of ν_c. The same analysis procedure as for the center, width, and amplitude of the individual transitions, described in Sec. 5.6.1, was used to extract the statistical uncertainty of $g_e(0,0)$, $E_4(0,0)$, and $E_5(0,0)$. The surface plots in Fig. 5.11 show the

[1] There was no excess noise in the FFT spectra of this measurement cycle and the ion dip and double dip signals were fitted reliably. The PnA phase data showed no exceptional behavior and the environmental data in the lab showed no disruption of the pressure stabilization systems of the cryogenic liquids or increased helium consumption.

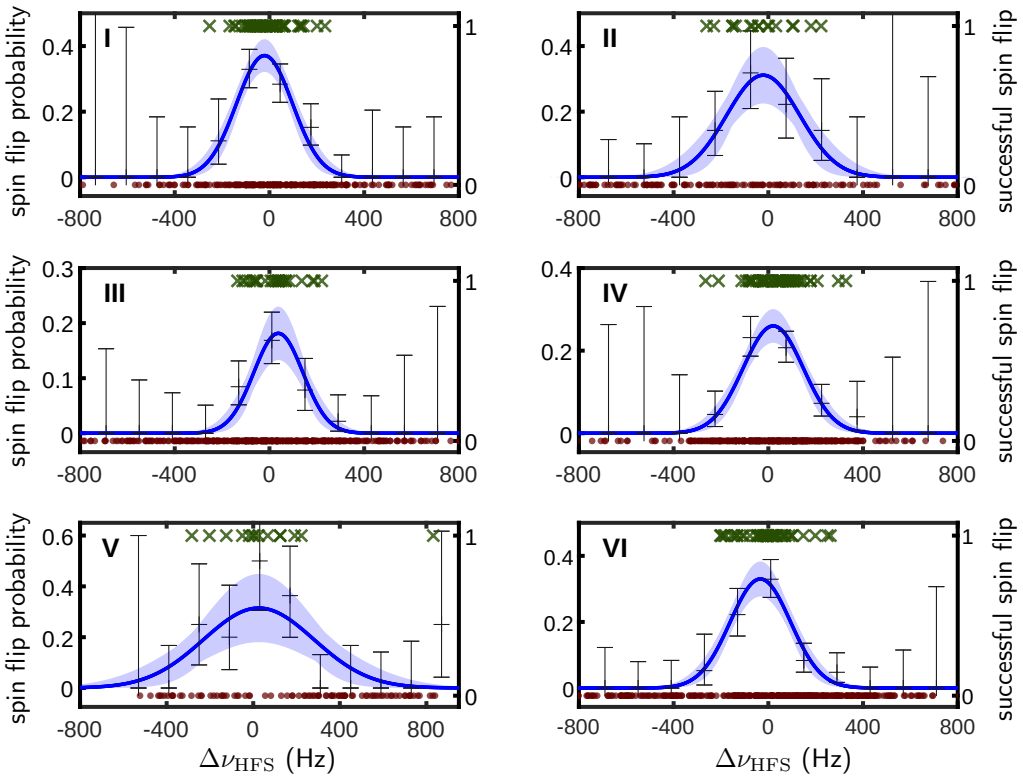

Figure 5.8: Results of all six individual HFS resonances. The electron-spin-flip probability is shown as a function of the offset of the irradiated MW frequency from the theoretically predicted transition frequency at the determined B field for each data point ($\Delta\nu_{\mathrm{HFS}}$). The data points are displayed as dark green X at the top of the plot for successful spin flips and dark red • at the bottom for unsuccessful spin flip attempts (right axis). The blue curves are Gaussian maximum-likelihood fits to the data, the shaded areas are the confidence band of the fits. The black data points are binned sets of data with binomial uncertainties to guide the eye and are not used for fitting or extraction of values.

change in likelihood of the fit due to variation and refitting of the parameters. The closed elliptical surface shapes demonstrate the low correlation between the three parameters $g_e(0,0)$, $E_4(0,0)$, and $E_5(0,0)$ in the fit. The systematic uncertainty of $g_e(0,0)$, $E_4(0,0)$, and $E_5(0,0)$ is extracted by 'bootstrapping'. The input data is varied by the systematic uncertainty and the spread of the final values of $g_e(0,0)$, $E_4(0,0)$, and $E_5(0,0)$ gives the final systematic uncertainty.

The final results and their uncertainties were compared to a linearization approach. The variation of the center fit position of the individual transitions ($\nu_{\mathrm{fit}}^{i,(0)}$) is linearized with respect to small variations of the reference parameters $g_{\mathrm{e}}(0,0)^0$, $E_4(0,0)^0$, $E_5(0,0)^0$. This is characterized by coefficients $c_g^i = (\partial\nu_{\mathrm{fit}}^{i,(0)}/\partial g_e)$, etc. The total squared deviation

$$\sum_i (\Delta\nu_{\mathrm{fit}}^{i,(0)} + c_g^i\,\Delta g_e + c_4^i\,\Delta E_4 + c_5^i\,\Delta E_5)^2/u(\Delta\nu_{\mathrm{fit}}^{i,(0)})^2 \tag{5.9}$$

is minimized by varying Δg_{e}, ΔE_4, ΔE_5, which are defined as $g_{\mathrm{e}}^{(0)} - g'_{\mathrm{e}}$, $E_4^{(0)} - E'_4$, $E_5^{(0)} - E'_5$,

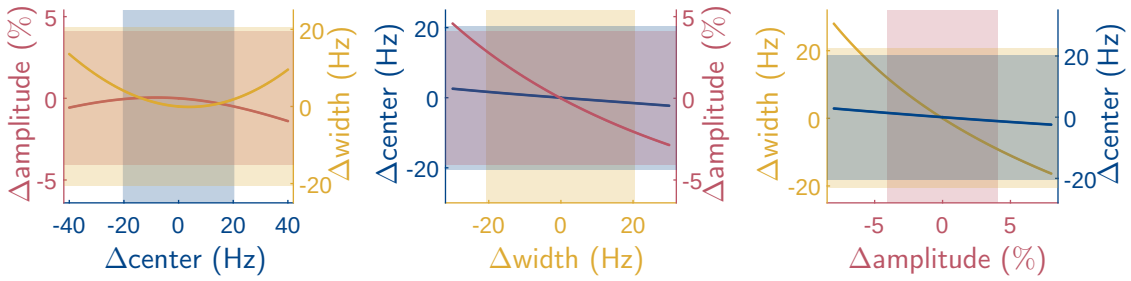

Figure 5.9: Determination of the uncertainties of the fit parameters of the Gaussian maximum likelihood fit of a single resonance, shown for transition IV. Alternately, one parameter is shifted from its final value and the other two are redetermined by the fit. The variation of the remaining two parameters is shown as a function of the offset of the first parameter to its final value. The shaded areas show the uncertainty band of each parameter. The center of the line is shown in blue, the width of the line in yellow, and the amplitude in red, for each plot. The figure demonstrates very small correlation of the center to the other two parameters, while amplitude and width correlate slightly. This is evident in the middle and right figure as the red (amplitude) and yellow (width) lines have a significant slope compared to their uncertainty band when varying the other while the center value does not.

respectively. After minimization, g_e', E_4', E_5' represent the final results. The reference parameters $g_e(0,0)^0$, $E_4(0,0)^0$, $E_5(0,0)^0$ were chosen close enough to the experimentally determined ones, to allow linearization. For the linearization approach the systematics are added as additional uncertainties of the center position, by a squared sum of statistical and systematical uncertainties.

The $E_4(0,0)$ and $E_5(0,0)$ values from both approaches agree well within their uncertainties and $g_e(0,0)$ within 2 σ of the combined uncertainties. The larger of the statistical uncertainties from the different approaches was assigned as the final statistical uncertainties of the experimental values. The values of the experimentally determined $g_e(0,0)$, $E_4(0,0)$, and $E_5(0,0)$ are listed in Tab. 5.2

Table 5.2: Results of the combined fit of all six HFS transitions, allowing the determination of $g_e(0,0)$, $E_4(0,0)$, and $E_5(0,0)$. The first row 't. w.' lists the results of the fit to the experimental data obtained in this work. The second and third row list the theoretical prediction and its deviation Δ to the experimental value normalized to the combined uncertainties σ, respectively. Note, recent theoretical work has improved the theoretical value of $g_e(0,0)$ to a relative uncertainty below 0.1 ppb and agrees with the experimental value within the experimental uncertainty. The publication is in preparation [72, 67].

	$g_e(0,0)$	$E_4(0,0)$ [kHz]	$E_5(0,0)$ kHz
t. w.	$-2.002\,278\,540\,82(18)_{\mathrm{st}}(35)_{\mathrm{sys}}$	$925\,395.757(39)_{\mathrm{st}}(11)_{\mathrm{sys}}$	$142\,287.821(20)_{\mathrm{st}}(8)_{\mathrm{sys}}$
theory	$-2.002\,278\,46(20)$ [4]	$925\,394.16(86)$ [70, 63]	$142\,287.556(84)$ [70, 63]
Δ/σ	-0.4	1.9	3.1

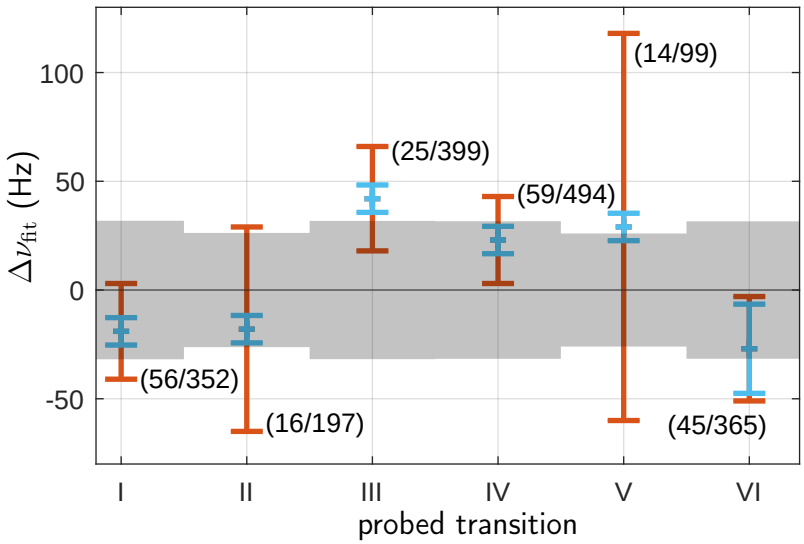

Figure 5.10: Result of the combined Gaussian maximum likelihood fit of the six transitions resulting in the determination of $g_e(0,0)$, $E_4(0,0)$, and $E_5(0,0)$. The plot shows the resulting line centers of the transitions ($\Delta\nu_{\mathrm{fit}}$) as orange data points with the statistical uncertainties. Additionally, the systematic uncertainties are shown as light blue error bars. The gray bands are the uncertainties of the predicted line centers, using the values and uncertainties of $g_e(0,0)$, $E_4(0,0)$, and $E_5(0,0)$ determined in this work. The number pairs next to the points are the number of successful PT spin flips (SF) and the total number of data points for each transition (cycles): (SF/cycles).

5.6.3 Systematic Effects

In this section, I will list and briefly explain the systematic effects considered in the HD+ HFS measurement campaign.

Shifts and uncertainties of ν_c

In the following the systematic effects of the free-space cyclotron frequency are discussed. All values are summarized in Tab 5.3.

Special Relativity:

For the phase sensitive measurement of ν_+ the ion has to be initialized to a radial orbit larger than the thermal motion ($\hat{\rho}_+^{\mathrm{thermal}} \sim 10\ \mu$m). For transitions I-V the excitation pulse was set to 68 ms, corresponding to a radius (ρ_+) of $48(5)\,\mu$m and for transition VI to 135 ms, corresponding to $\rho_+ = 96(10)\,\mu$m. The resulting frequency shift for the free cyclotron frequency is given as [121]:

$$\frac{\Delta\nu_c}{\nu_c} \approx -\frac{(2\pi\nu_+\rho_+)^2}{2c^2}\,, \tag{5.10}$$

leading to 0.25 and 0.9 ppb shifts, respectively. The uncertainty of this shift is given by the uncertainty of the PnA radius calibration ($\sim 10\,\%$) resulting in a 20 % shift uncertainty.

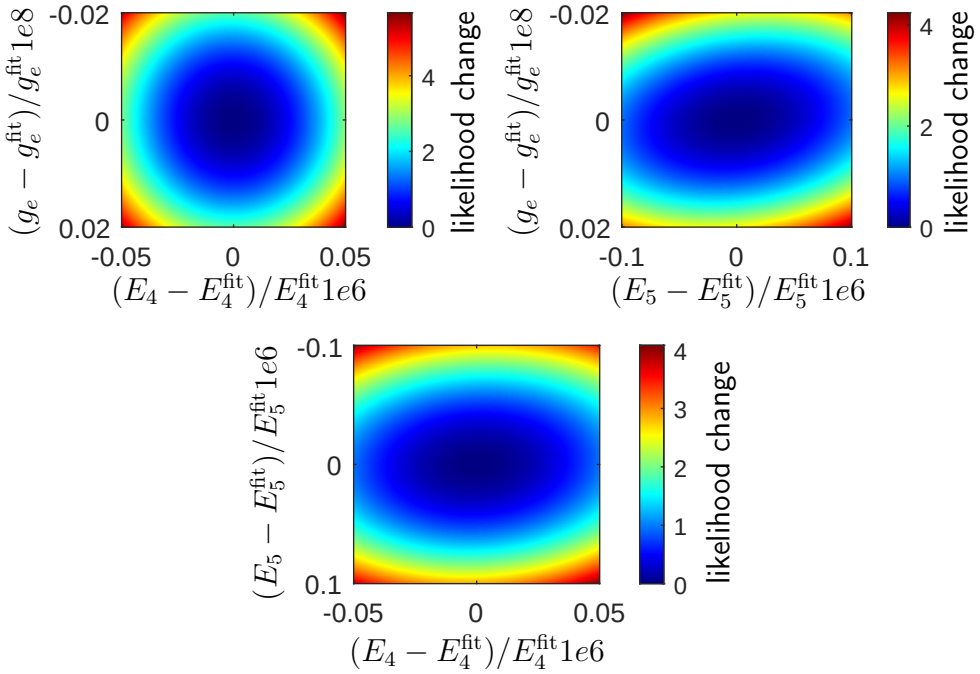

Figure 5.11: Two-dimensional correlation plots of the fit parameters $g_e(0,0)$, $E_4(0,0)$, and $E_5(0,0)$. For each plot two parameters are varied while the third is fitted using the same Gaussian maximum-likelihood fit as for the overall fit of the data. The color map shows the difference of the fit likelihood after varying the parameters compared to the optimized case. All three variations result in closed elliptical shapes demonstrating very low correlation between the parameters.

Table 5.3: Systematic effects for the determination of the magnetic field by the measurement of ν_c. The two values in the first row are for the two different modified cyclotron radii of the ion during PnA.

shift	$\Delta\nu_c/\nu_c \times 10^{-10}$
special relativity [121]	$-2.5(5)$; $-9.0(18)$
polarization [83, 122]	$-0.210(1)$
image charge shift [123]	$-0.038(2)$
C_4 shift	$0.00(2)$
$C_{n>4}$ shift	$0.0000(3)$
B_2 shift	$0.00(2)$
line shape ν_z	$0.00(1)$
ν_-	$0.00(15)$
ion mass [83]	$0.00(20)$

Polarizability:

The polarizability of the rovibrational ground state of HD^+ arises from the mixing of this state (0,0) with with the closest-lying rovibrational excited state (0,1,$\pm$1). For HD^+ in the rovibrational ground state the polarizability is given as $\alpha_{\mathrm{pol}} = 395.31$ a.u. [122]. The modified cyclotron motion of the ion induces a motional electric field which, in turn, induces an electric dipole pointing toward the center of the trap. The shift to the free-space cyclotron frequency is given by: [97, 124]

$$\frac{\Delta\nu_c}{\nu_c} = -\alpha_{\mathrm{pol}}\frac{B^2}{m_{\mathrm{ion}}} \tag{5.11}$$

which, for the polarizability in atomic units (a.u.) can be written as [97]:

$$\frac{\Delta\nu_c}{\nu_c} = -9.929\cdot 10^{-15}\alpha_{\mathrm{pol}}/[a.u.]\frac{(B/[T])^2}{m_{\mathrm{ion}}/[u]}\ . \tag{5.12}$$

For HD^+ in the rovibrational ground state in the PT this results in a relative shift of the free-space cyclotron frequency of -2.10(1)$\cdot 10^{-11}$.

In the $(0,1)$ state which is populated in our trap by BBR, the polarizability is a tensor of rank two, due to the rotation of the molecule, with a static term $\alpha_s = 3.99$ a.u. and a tensor term $\alpha_t = 175.48$ a.u. [122]. For $N > 0$ states, the contributions from $N \pm 1$ states partially cancel in the polarizability. While the α_t values arise mainly from the other rovibrational states, the α_s term are dominated by contributions from excited electronic states [122].

Image Charge:

The image charges induced by the ion in the trap electrodes, on the one hand allow nondestructive dection of the ion. On the other hand, they act back on the ion shifting the motional frequencies. The shift of the free-space cyclotron frequency is given by: [123]

$$\frac{\Delta\nu_c}{\nu_c} \approx \frac{m_{\mathrm{ion}}}{4\pi\epsilon_0 B^2\rho_0^3} = 3.8\cdot 10^{-12} \tag{5.13}$$

where m_{ion} is the mass of the ion, ϵ_0 is the vacuum permittivity, B is the strength of the magnetic field, and $\rho_0 = 9$ mm is the radius of the trap electrodes. The uncertainty of the shift is 0.2$\cdot 10^{-12}$.

Inhomogeneities and Anharmonicities

The magnetic field inhomogeneities and electric field anharmonicities cause systematic shifts to the frequencies of the motional modes of the ion in the Penning trap and thus to the free-space cyclotron frequency used for the determination of the magnetic field. The tuning ratio scan of the PT, see Sec. 5.1.2 allows the determination of upper limits for C_4, C_6, and B_2. Taking into account these values and the largest radial amplitude during PnA ($\rho_+ = 96$ μm) a 2 ppt systematic uncertainty due to C_4 and B_2 is determined. The effect of higher order terms is well below this value, for the relatively small measurement radii.

Ion Mass

Penning-trap mass spectrometry has determined the mass of HD^+ as 3.021378241561(61) u [83]. It is, therefore, known to 2.0 $\cdot 10^{-11}$ and does thus not limit the results here.

ν_z Line Shape:

The determination of this uncertainties follows the procedures of Refs. [104, 97, 125]. The main effect is the image-current shift due to an interaction of the resonator and the ion. If the axial frequency of the ion and the resonator frequency do not match exactly, the axial frequency is shifted closer to the latter. The lineshape model of the fit corrects for this effect, but uncertainties or shifts of the resonator frequency and Q value in the fit can nevertheless result in a remaining uncertainty or shift of the axial frequency.

Previous work [104, 97] has shown that the magnitude of this effect can be estimated by first varying the fit range of the resonator, and then using the variation in the fitted resonator parameters as input in the dip fit. Here, the fit range for the resonator was varied from the full range of 780 Hz to 15 Hz. This resulted in a variation of ν_{res} of $\sim$1 Hz. Subsequently, the dip signal of the ion is fitted with fixed resonator parameters, repeated for the different values derived from the variable fit range. This resulted in an uncertainty of ν_z of less than 1 mHz. This then leads to an upper limit of the systematic uncertainty of ν_c of 1 ppt. As expected by the narrow dip signal of HD^+ (< 0.3 Hz), this uncertainty is small compared to the overall uncertainty of the measurement.

ν_- Coupling Strength:

In this measurement campaign, ν_- was always measured with the same strength of the RF signal, coupling this mode to the axial one. From experience the determined value of ν_- varies in our setup depending on the RF coupling strength. Based on previous results with heavier ions [102], this effect is estimated to add a $1.5{\cdot}10^{-11}$ relative uncertainty for ν_c for HD^+.

Sidebands

As transition IV was the first transition measured to high precision, the magnetron and axial sidebands were probed to make sure we had found the transition, i.e. the carrier frequency, and were not measuring a motional sideband. The assumed sidebands were probed with the low MW power of the high-precision measurement and with MW power increased by 20 dBm. Overall, no spin flips were observed for the sidebands. For the high MW power, a spin-flip probability of 32(20;46)% (6 spin-flips/19 attempts) was measured for the assumed carrier, 0(0;14)% (0 spin-flips/12 attempts) for the magnetron sidebands, and 0(0;23)% (0 spin-flips/7 attempts) for both axial sidebands. The numbers in brackets indicate the upper and lower limit of the binomial 68% uncertainty. This confirms that we correctly identified the transition and did not measure a sideband.

Resonance Line Shape

The Gaussian maximum likelihood fit is well suited for this case, because the line shape is dominated by magnetic field jitter. Uncertainties due to the model and asymmetries have been estimated to be at the $1{\cdot}10^{-13}$ level [126]. If the MW power saturates the line, the transition is power broadened and the line shape is mostly given by a Lorentzian distribution. As a cross check the transitions were all fitted with a Lorentzian distribution. This results in center of line values which are all in agreement with the Gaussian fit results. For comparison, Fig. 5.12 shows transition IV with a Gaussian and a Lorentzian fit. The position of the ion in the PT is optimized to reduce B_2 to less than 10 mT/m^2. Therefore, asymmetric

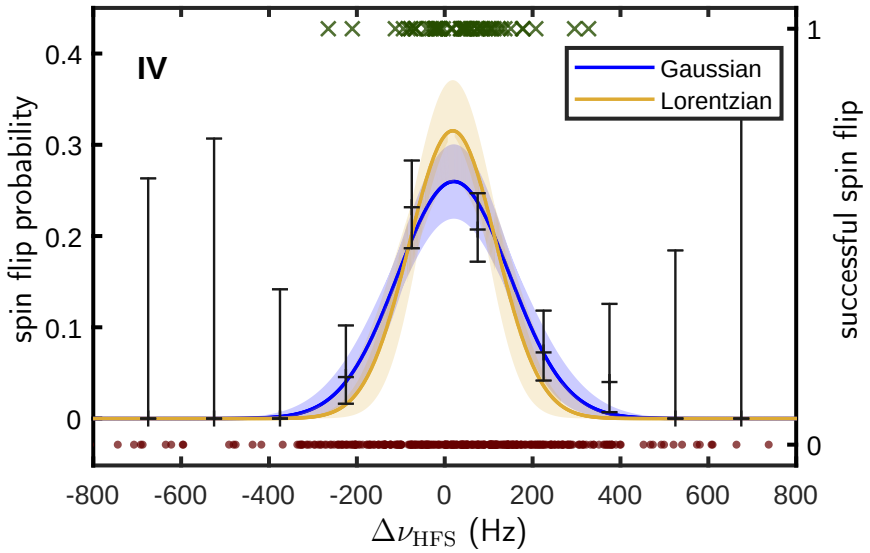

Figure 5.12: Lorentzian versus Gaussian maximum likelihood fit for transition IV. The measurement data, binned data, and Gaussian fit are the same as in Fig. 5.8 and are compared to a Lorentzian fit, shown with its uncertainty bands (shaded yellow area). Although, the resulting width and amplitude are slightly different, the center positions of both fits differ only by a fraction of the uncertainty of the fit, 10%-60% depending on the transition.

contributions to the resonance line shape due to even-order magnetic field inhomogeneities (B_2) are not significant. This effect has been analyzed in detail in Refs [104, 126, 127, 128]

ν_{MW} Relativity Effect

Relativistic shifts arise due to the fast motion of the modified cyclotron mode. The magnetic field in the rest frame of the ion B' is shifted compared to magnetic field in the lab frame B by: [126, 129]

$$B' = \gamma B \ , \tag{5.14}$$

neglecting small terms due to electric fields and velocity components parallel to the magnetic field. γ is the Lorentz factor defined as:

$$\gamma = \sqrt{1 - \frac{v^2}{c^2}}^{-1} \approx \sqrt{1 - \frac{\omega_+^2 r_+^2}{c^2}}^{-1} \ , \tag{5.15}$$

where v is the velocity of the ion, c is the speed of light in vacuum, ω_+ is the modified cyclotron frequency in rad/s and r_+ is the radius of the modified cyclotron motion. For the larger PnA radius in this measurement campaign $\gamma - 1 \approx 8{\cdot}10^{-10}$.

The boost back to the lab frame adds a $1/\gamma$ shift to the full transition frequency, including the HFS terms that are not affected by the γB shift of the magnetic field in the rest frame of the ion. So the transition frequency in the lab frame ν compared to the transition frequency in the rest frame of the ion ν', is given by:

$$\nu = \nu' \frac{1}{\gamma} \ . \tag{5.16}$$

In an order of magnitude approximation, this will result in a relative shift of the HFS terms by γ. Even at the largest PnA radius measured, $\gamma - 1$ is more than an order of magnitude smaller than the relative measurement precision of $E_4(0,0)$ and $E_5(0,0)$. The shift was determined to be negligible.

In absence of HFS, the boost of the spin dynamics back to the lab frame ('Thomas Precession'), adds a shift given by: [126]

$$\frac{\delta\nu_L}{\nu_L} = \frac{\delta\nu_c}{\nu_c}\frac{\nu_c}{\nu_L} \ , \tag{5.17}$$

where ν_c is the free-space cyclotron motion, $\frac{\delta\nu_c}{\nu_c} = \gamma - 1$, and ν_L is the Larmor precession frequency of the electron spin. This can serve as an order of magnitude estimate for the final effect on the $g_e(0,0)$ factor and is therefore negligible, since it is below $2 \cdot 10^{-13}$ relatively.

Time Reference

As described in Sec. 4.3 the setup is referenced to a GNSS-monitored hydrogen maser. The HFS measurements have a reduced sensitivity to the absolute frequency uncertainty, as this effects both the magnetic field determination via ν_c and the irradiated MW frequency. The sensitivity to the absolute frequency uncertainty depends of the contribution of the HFS to the electron-spin-flip transitions, which is at hundreds of MHz out of ∼112 GHz, so less than 1%. Therefore, the offset ($+2.4 \cdot 10^{-11}$) as well as the frequency drift ($\sim 0.05 \cdot 10^{-11}$ from beginning to end of the measurement campaign) of the maser are insignificant compared to our measurement uncertainty.

Stark shifts

To estimate Stark shifts the possible electric fields the ion can interact with and the Stark shift coefficients of the hyperfine states involved have to be examined. The d.c. electric field of the trap as well as the electric fields arising from the motion of the ion in the magnetic field and from the MW are small. The scalar Stark shift coefficients for the upper and lower states of an electron-spin-flip transition are nearly equal, so that the differential Stark shift is suppressed [130]. The Stark shift coefficients with consideration of HFS have been computed for zero magnetic field [122].

These state-dependencies have been estimated by Stephan Schiller and Dimitar Bakalov to amount to sub-Hertz corrections and their impact on the electron-spin-flip transition frequencies is further reduced [130, 67]. Furthermore, vector and tensor Stark shifts are zero because the studied level has zero rotational angular momentum.

Corrections to the HFS Hamiltonian

As mentioned in Sec. 2.1.2 terms extending the zero-field HFS Hamiltonian (Eq. 2.4) have been evaluated, such as ($\propto I_p \cdot I_d$) [64]. This term adds shifts proportional to quantum numbers $m_{I,p}$ and $m_{I,d}$. Since they remain constant for the eSF transitions of this measurement campaign, the effects are below the measurement precision.

Possible higher order magnetic field effects on the eSF transition frequencies were evaluated by Dimitar Bakalov, see Sec. 2.1.2. The hyperfine-assisted Zeeman shift, adding a term linear in B and m_s to the Hamiltonian, the dipole diamagnetic shift of g_e, E_4, and E_5

describing the B^2 dependence of these quantities, and the quadrupole diamagnetic shift due to the electric quadrupole moment of the nuclei, all contribute well below the uncertainty of the measurement [130, 67].

6 Towards High-Precision Rovibrational Spectroscopy of MHI in Penning Traps

In this chapter, I will describe the efforts we have made towards rovibrational spectroscopy of HD^+ at ALPHATRAP, intermediate results, and an outlook for possible improvements and considerations for future measurements on H_2^+ and its antimatter counterpart.

6.1 Towards (0,0)→(5,1) Rovibrational Spectroscopy of HD^+

Figure 6.1 shows a selection of rovibrational levels and the transitions that have been measured to high precision in RF Paul traps.

There are several criteria to consider when choosing the first transition to attempt in a Penning trap. We decided on the $(0,0) \rightarrow (5,1)$ transition for multiple reasons. First, HD^+ decays to the rovibrational ground state in the cryogenic environment of our trap and initially we assumed it would remain in this state indefinitely. Therefore, the measurement transition should include the $(0,0)$ state. Furthermore, the spin-averaged frequency of this transition is theoretically predicted and experimentally confirmed to the 10-ppt level by a previous measurement carried out by our collaboration partner [35]. Moreover, at the wavelength of ∼1.15 μm it is convenient to work with optical fibers and lasers at high powers of hundreds of mW are readily available, compared to the wavelengths of the lower-lying transitions.

6.1.1 Possible Measurement Schemes for (0,0)→(5,1) Spectroscopy

In the measurement, we plan to utilize the unambiguously state-dependent eSF frequencies to identify the current rovibrational level. Figure 6.2 shows the rovibrational levels involved after driving the $(0,0) \rightarrow (5,1)$ transition. The $(5,1)$ state will predominantly decay via $\Delta v = -1$ E1 transitions ($\Delta N = \pm 1$) to either the $(4,0)$ or $(4,2)$ state. These states then predominantly follow the same decay scheme until the ion reaches the $(0,0)$ state again. Other decay paths are possible, involving $\Delta v = 0$ or $\Delta v < -1$ transitions, but these are less likely to occur. For dipole transitions in HD^+, the transition rate per unit of time (W)

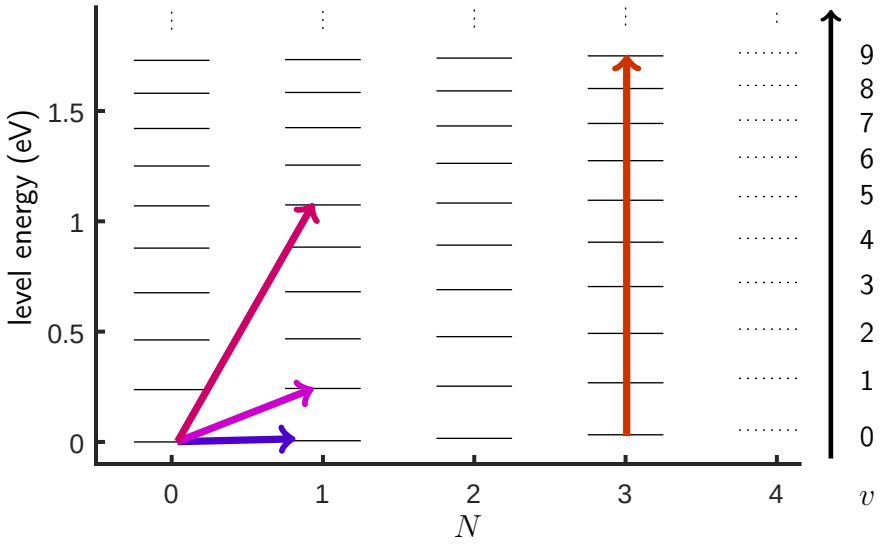

Figure 6.1: A selection of lower rovibrational levels of HD^+. Each level is labeled according to the vibrational v and rotational N quantum number indicated by the numbers on the right and bottom, respectively. The y axis on the left denotes the energy of each level with respect to the $(v = 0, N = 0)$ state. The energies of the rovibrational states are taken from Ref. [55]. The arrows indicate transitions that have been measured to high precision in RF Paul traps: $(0,0) \rightarrow (0,1)$ [73], $(0,0) \rightarrow (1,1)$ [75], $(0,0) \rightarrow (5,1)$ [35], and $(0,3) \rightarrow (9,3)$ [74].

is given as: [56]

$$W = 2\alpha^3 \Delta E^2 f(\Delta E) \ , \tag{6.1}$$

where α is the fine structure constant, ΔE is the energy difference between the two rovibrational levels, and $f(\Delta E)$ is the the dimensionless dipole oscillator strength for the transition which scales linearly with ΔE as well. Therefore, for no change in v, the decay rate depends on N and is at least an order of magnitude lower than for the $\Delta v = -1$ decay due to the smaller energy difference, despite the larger dipole moment of the transitions. For each additional step in v the decay rate decreases by about an order of magnitude as well due to the reduced dipole moments of such transitions [56, 131].

The eSF drive for state detection has to be timed no later than the full decay time of the $(5,1)$ state back to the $(0,0)$ state after the laser excitation. All $(v > 0, N)$ states have lifetimes at or below ∼50 ms and thus decay rather quickly compared to the measurement times in the trap. However, the $(0, N)$ states exhibit longer lifetimes in the seconds range, with the longest lifetime in the $(0,1)$ state even above 100 s. Most decay paths from the $(5,1)$ state pass this long-lived level. Therefore, the full decay time of the $(5,1)$ state back to the $(0,0)$ state is dominated by this long lifetime, giving ample time for nondestructive state detection.

There are two possibilities for the state detection via eSF, either the eSF is probed at the $(0,0)$ frequency or the eSF is probed at the frequency of an excited rovibrational state, which could, for example, be the $(5,1)$ state itself or the long-lived $(0,1)$ state reached in the decay. In the first case, a reduction of the eSF probability and in the latter cases the

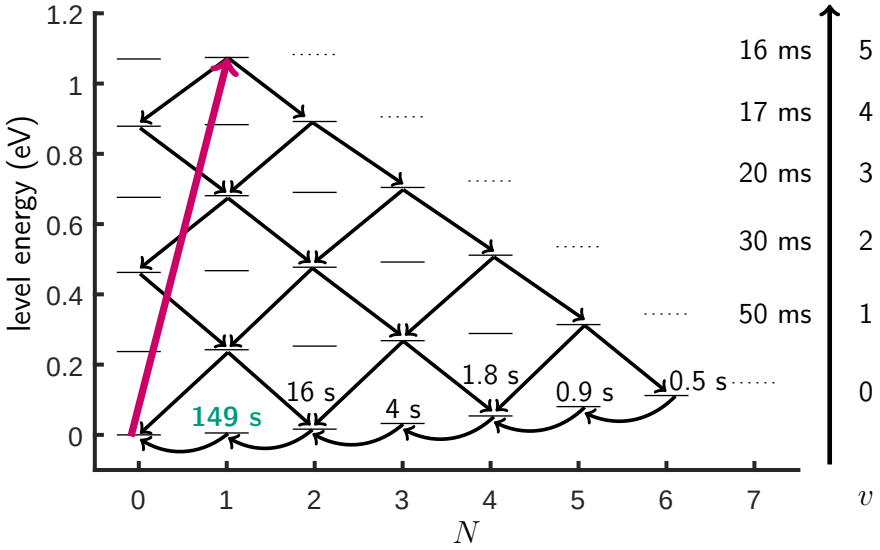

Figure 6.2: Level scheme showing the levels involved for a laser excitation of the $(0,0) \rightarrow (5,1)$ transition and the subsequent decay back to the $(0,0)$ state. The laser excitation is depicted as the red arrow and the strongest possible decay paths as the smaller black arrows. The decay rates for $\Delta v < -1$ and $\Delta v = 0$ are at least an order of magnitude smaller than the $\Delta v = -1$ decay paths shown here [56]. The approximate lifetimes of the levels are given on the right for $v > 0$, as the lifetimes of the states does not vary greatly for the N values shown. For $v = 0$ the approximate lifetimes of the states are given for each N individually. The lifetime of the $(0,1)$ state is highlighted as it is the longest lifetime and most decay paths pass this state. The values for the lifetimes are taken from Ref. [56]. Note, each (v, N) state has a subsplitting of hyperfine and Zeeman levels.

success of an eSF would herald the success of the laser transition.

Distinguishing between the eSF frequencies of these levels is possible, since each (v, N) state has a unique underlying structure of $12 \times (2\,N + 1)$ HFS and Zeeman states. For all HFS states (nuclear spin orientations $m_{I,p}$, $m_{I,d}$ and m_N), the $(0,1)$ and $(5,1)$ eSF frequencies differ by at least 100 ppm with respect to the eSF frequency of the respective HFS state of the $(0,0)$ level at 4 T. For comparison, Tab. 6.1 lists eSF frequencies of the $(0,0)$, the $(0,1)$, and the $(5,1)$ state for the nuclear spin orientation of transition VI of the HFS measurement as an example, see Ch. 5 and Fig 2.2.

If the eSF should be detected in the (5,1) state it has to be done quickly with the MW irradiation either well-timed after the laser excitation within the 16-ms lifetime of this state or simultaneously to the laser irradiation. In principle, it is possible to achieve an eSF transition via coherent π pulses within less than 1 ms or to perform adiabatic rapid passage (ARP) within the lifetime of the excited state. The former has been demonstrated for eSF transitions at ALPHATRAP for Ne^{9+} [104] and is demonstrated for HD^+ below. However, this requires a good calibration of the power and pulse duration at the respective frequency. Alternatively, driving the eSF in the (0,1) or (0,0) state is less time-critical.

The rovibrational spectroscopy could be performed either with the double-trap technique used in the HFS campaign or in the AT alone. For the double-trap technique, each cycle

Table 6.1: eSF frequencies for the $(0,0)$, $(0,1)$, and $(5,1)$ states for the nuclear spin orientation corresponding to transition VI of the $(0,0)$ state, see HFS measurements Ch. 5 and Fig. 2.2. All frequencies in this table are given at $B = 4.02$ T and are calculated with published theoretical values for g factors [4, 59, 66] and E coefficients [70, 5, 63, 62] or if not available for the $(5,1)$ state were extrapolated with a 2nd degree polynomial from the published values. The uncertainty of the calculated frequencies are given by the uncertainty of the g_e factors at 0.1 ppm [4]. For the excited states the eSF frequencies of the three possible m_N states are given and the anisotropy of g_e [71] is taken into account. All values are given in GHz.

[GHz]	$m_N = -1$	$m_N = 0$	$m_N = +1$
$(0,0)$	/	112.055 01	/
$(0,1)$	112.034 81	112.032 48	112.098 22
$(5,1)$	112.100 37	112.098 92	112.148 18

must include state detection in the AT and a transport to the PT where the rovibrational transition is probed, followed by a transport back to the AT for subsequent state detection. Spectroscopy in the AT alone does not require ion transports and can thus be much faster. With the stronger ion signal in the AT after the upgrade, cycle times down to ∼10 s plus laser irradiation time are possible, which is short compared to a typical ion transport that takes at least 60 s. The disadvantage of a measurement in the AT alone is that the strong magnetic bottle leads to shifts and broadening of transitions.

However, since rovibrational transitions are less sensitive to the magnetic field than the eSF transitions (Ch. 5), these transitions are less affected by relative broadening or shift in the AT due to the strong magnetic bottle. For the $(0,0) \rightarrow (5,1)$ transitions this amounts to ∼1 kHz broadening or shift, depending on whether the energy of the axial motion is resampled from the thermal bath of the resonator during the laser excitation. Whether this resampling occurs or not can be tuned by the offset of the axial frequency of the ion with respect to the resonator. Far detuned, the ion does not interact with the resonator and the energy of the axial mode and thus the motional amplitude in the strong magnetic bottle is fixed. Thus, the average magnetic field experienced by the ion is shifted compared to zero motional amplitude and the transition frequency is also shifted accordingly. If ion and resonator are in resonance, they interact and the energy of the axial mode and thus the amplitude of the motion is resampled from the thermal bath of the resonator. If this happens on time scales faster than the excitation time of the transition, this will broaden the transition. A measurement in the AT would therefore be limited in precision compared to a measurement in the PT, but it could be used to find the transition and narrow the search range for a later high-precision measurement in the PT.

Figure 6.3, shows a simplified level diagram with only the mainly involved rovibrational states and a possible measurement scheme in the AT and a scheme for a double-trap measurement with AT and PT. A possible measurement scheme in the AT would first determine the hyperfine state of the ion via an eSF driven in the $(0,0)$ state, followed by a laser pulse or scan after which the same $(0,0)$ eSF frequency is probed until an eSF is observed again. Comparing the number of attempts until an eSF is driven after repeated measurement cycles with the laser on and off resonance, should show an increased number of attempts needed to drive the eSF at the $(0,0)$ frequency when the laser is on resonance

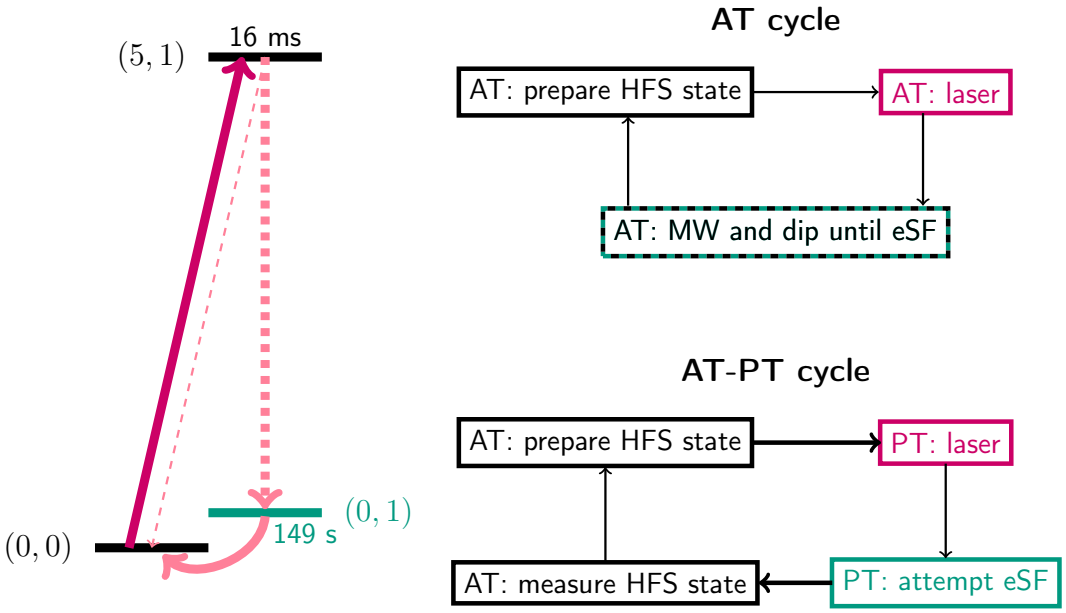

Figure 6.3: left: Simplified level scheme for the $(0,0) \rightarrow (5,1)$ transition, showing only the three levels involved. These are the $(0,0)$ and $(5,1)$ states, connected by the red arrow symbolizing the laser excitation, and the long-lived $(0,1)$ state, marked in green. The decay paths from the $(5,1)$ state are simplified by the dashed light-red arrows and only the decay from $(0,1)$ to $(0,0)$ is shown as a full arrow since no intermediate levels are omitted here. **right:** Measurement cycles for an AT and double-trap (AT-PT) campaign. The thick arrows in the lower cycle depict ion transports from one trapping region to the other. The colors correspond to the rovibrational level the ion is in at this measurement step, assuming a successful laser transition: red for $(5,1)$ state, green for the $(0,1)$ state, and black for the $(0,0)$ state. In the dashed step of the AT cycle, the ion starts in the $(0,1)$ state and decays to the $(0,0)$ state, assuming a successful laser transition.

and the rovibrational transition is driven. The increased number of attempts is given by the time it takes the ion to decay back to the $(0,0)$ state after successful laser excitation during which no eSF can be driven at the $(0,0)$ eSF frequency.

In principal, the same scheme could be carried out driving the eSF at a $(0,1)$ frequency, comparing the time until no eSF is observed anymore. Note, here there are three possible eSF frequencies, one for each of the HFS states with the different $m_N = 0, \pm 1$ projections. However, in this case observing no eSFs at all would not necessarily mean that the laser frequency is off-resonant. For example, a nondriven change in nuclear spin orientation would have the same effect and therefore go undetected. In the former case, this would be easily noticeable, since after the change in nuclear spin orientation no eSF would be driven at this $(0,0)$ MW frequency anymore and the new HFS state could be determined.

A future double-trap measurement would have to involve an eSF attempt in the PT subsequent or simultaneously to the laser probe, since the time for the ion transport to the AT would give the ion ample time to decay back to the ground state. A possible measurement scheme is to measure the orientation of the electron spin in the AT, transport the ion to the PT, followed by a laser pulse or scan with an eSF attempt in the PT. If subsequent the eSF attempt could, in principle, be carried out at either the $(0,0)$ or $(0,1)$

frequency. If the eSF attempt and the laser irradiation are carried out simultaneously the eSF could be carried out in the $(5,1)$ state. Afterwards, the ion is transported back to the AT, where the orientation of the electron spin is measured again and compared to the orientation before the PT cycle, similarly to the HFS measurement campaign.

If the eSF attempt in the PT is carried out noncoherently, in the same way as in the HFS measurement, the maximum achievable spin-flip probability is 50%. Thus, even if the laser would drive the rovibrational transition each cycle, the 50% eSF probability would limit the detection efficiency. This can be improved by using coherent π pulses or ARP. eSF transition probabilities of up to 100% are feasible in both methods. Both have been demonstrated for atomic ions at ALPHATRAP [104, 116] and were revisited for HD^+.

Furthermore, once reliable laser excitation is achieved, it can be used to measure eSF transitions of the excited rovibrational states and thus gain insight in the HFS and g factors of these states. For the $(5,1)$ state the short lifetime would limit the achievable measurement precision, but the long lifetime of the $(0,1)$ state has the potential for a high-precision measurement of eSF transitions. This would allow to cross check the scaling of $g_e(v,N)$, $E_4(v,N)$, and $E_5(v,N)$ with increasing rotational quantum number and would give access to experimental values for the anisotropic shift of the g_e factor of HD^+ and the next larger HFS coefficient $E_1(0,1)$.

Coherent eSF drive

One option to achieve up to 100% eSF probability is to perform coherent π pulses. π times of below 1 ms have been demonstrated at ALPHATRAP for Ne^{9+} [104] and was tested here for HD^+. In this measurement, the orientation of the electron spin $m_s = +1/2$ or $m_s = -1/2$ is determined in the AT, then the ion is transported to the PT where a ν_c measurement, via axial dip and modified cyclotron double dip, determines the magnetic field and a subsequent short resonant MW pulse is used to attempt an eSF, after which the ion is transported back to the AT to determine m_s again. Note, the ν_c measurement was only carried out every third to fifth cycle to reduce the measurement time, since we assume the magnetic field to be stable enough. The MW pulse time is varied in the expected range for the coherent Rabi oscillations between 100 μs and 1 ms. Each pulse time is repeated to accumulate statistics for the eSF probability at several pulse durations. The binned data is fitted to determine the Rabi frequency and thus the time for the π pulse by:

$$P_{\mathsf{eSF}}(t_{\mathrm{MW}}) = \frac{\Omega_R^2}{\Omega_R^2 + \Delta_R^2} \sin\left(\frac{1}{2}\sqrt{\Omega_R^2 + \Delta_R^2}\, t_{\mathrm{MW}}\right)^2 , \tag{6.2}$$

where Ω_R is the Rabi rate, Δ_R is the detuning, and t_{MW} is the length of the MW pulse. Since the ion is excited by black body radiation (BBR) to the $(0,1)$ state, $P_{\mathsf{eSF}}(t_{\mathrm{MW}})$ cannot reach 100% even at $\Delta_R = 0$ with respect to the $(0,0)$ eSF frequency, as there are measurement cycles in which the ion is rotationally excited and no eSF can be driven. However, since these measurements were performed before the upgrade, when the BBR in the trap was lower, this is not taken into account for the fit.

The data and fit for transition III and VI are shown in Fig. 6.4 and result in a π time of 250 μs and of 1090 μs, respectively. Both measurements were carried out with the same MW power entering the setup. The difference in Rabi rates is probably due to the frequency-dependent transmission of the MW to the ion which has been shown in simulations [111].

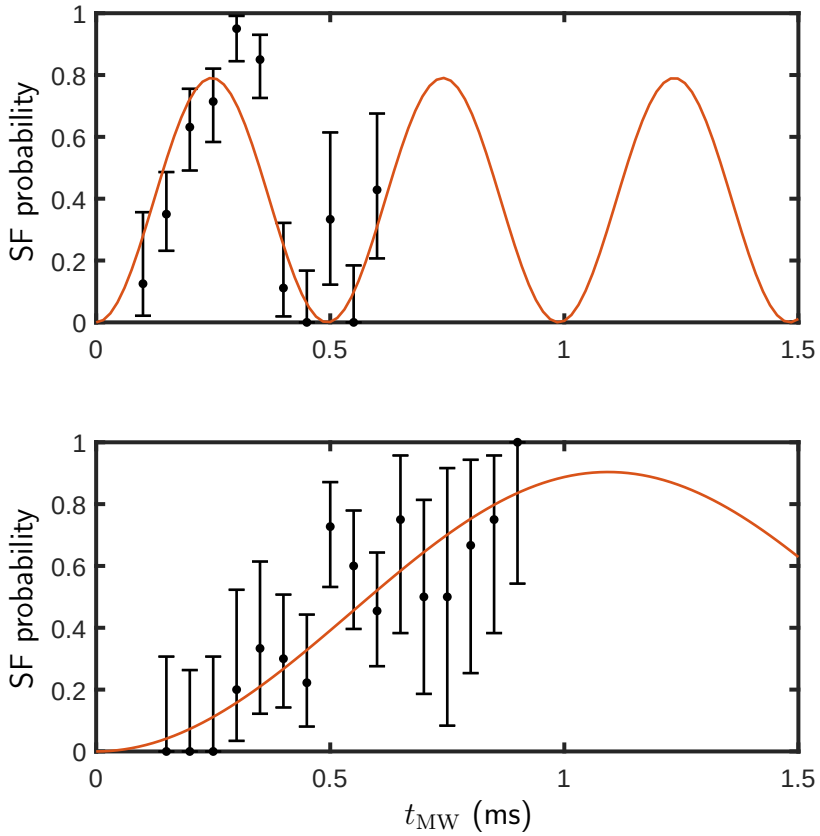

Figure 6.4: Coherent drive of eSF transitions of HD^+. These measurements were carried out for transitions III and VI to calibrate the π time for enhanced eSF probability compared to the incoherent drive.

The measurements were carried out with the overmoded WR28 MW guides with a hole in the 90 degree bend, in preparation for a laser measurement.

Adiabatic Rapid Passage

ARP has been demonstrated at ALPHATRAP using $^{40}Ar^{13+}$ [116] by placing Helmholtz coils around the magnet and thus sweeping the eSF transition by ramping the magnetic field from the outside keeping the irradiated MW frequency constant. To allow for a more controlled ARP, our MW generator has been upgraded for coherent frequency sweeps and two other options of implementing ARP have been tested as well. The first one sweeps the output frequency of the MW generator by sweeping the 10 MHz reference frequency to which it is locked. The second one keeps the irradiation MW frequency constant and uses the small magnetic field inhomogeneity of the PT to sweep the transition frequency by moving the ion in the trap and thus changing the magnetic field experienced by the ion.

The first two methods, using the built-in sweep of the MW generator and sweeping the 10 MHz reference, were tested but their implementation was not straightforward. After the successful ARP using the last method, the other two were not pursued further. The

last method was implemented using $^{12}C^{5+}$. To move the ion, the voltage of the first upper correction electrode, adjacent to the ring electrode, was ramped by $\Delta V = -10$ V to $\Delta V = +10$ V from its nominal setting in 20 steps. This voltage change shifts the position of the ion by ± 0.6 mm in either direction. Due to the linear magnetic field inhomogeneity $B_1 \approx 1.5$ mT/m this results in a total relative change of the magnetic field by 0.45 ppm and thus of the eSF transition frequency by about 0.45 ppm as well. Using these parameters with both the WR10 MW setup and the WR28 MW setup, including a hole in the MW guide for the laser to pass into the setup, resulted in close to 100% eSF rate (84/90 and 178/189 successful attempts, respectively).

Implementation of this ARP technique for HD^+ is in progress. Currently, it is unclear why an eSF rate of close to 100% has not been reached[1]. Possibly, the choice of the split first upper correction electrode was not ideal and causes effects that have not been accounted for which are enhanced for the lighter HD^+ compared to $^{12}C^{5+}$.

6.1.2 MW Setups

In the HFS measurement campaign, WR10 hollow metal MW guides were used to bring the MW to the trap along a 90 degree bend after which the waveguide widened to a horn for the transition through the first vacuum window to the MW horn at 77 K, see Fig. 4.1. In this setup there is no hole in the waveguide for the laser to pass to the trap and the horn is too large to allow the laser to pass alongside the horn while both laser and MW are aligned.

We tested two options to allow both MW and laser alignment[2]. First, we added waveguide adapters changing from the small WR10 to larger WR28 waveguides which allow for a larger, 2 mm, hole in the 90 degree bend. In this solution, the laser can pass through the larger hole without extra focusing and can enter the trap, see Fig. 4.10. Second, we used the WR10 waveguide and 90 degree bend but removed the horn entirely. Thus, the MW transition into the vacuum is not by horn-to-horn but by open waveguide-to-horn to the 77-K section of the apparatus. In this solution, the waveguide is small enough to allow the laser to pass alongside the MW setup.

For the first case, we compared the AT eSF rate at several MW powers with the WR10 setup from the HFS campaign and the overmoded WR28 setup with the large hole. Here we observed only about 5 dBm less MW power at the position of the ion using the overmoded setup. Furthermore, the 250 μs π time of the coherent eSF for transition III was measured with this horn setup, see Fig. 6.4. This π time is comparable to the π times measured for Ne^{9+} [104] and recently for $^{12}C^{5+}$ ($\sim$300 μs) with the WR10 MW setup. In the second case, 8/12 eSF attempts were successful at MW pulse times of 350 μs for HD^+. This was measured after the upgrade when the probability for HD^+ to be in the ground state was

[1] The ion populates to $(0,0)$ state only $\sim$50% of the time, due to the rotational excitation by BBR. Therefore a successful ARP at $(0,0)$ eSF frequency would result in 50% eSF probability. However, subsequent ARPs every cycle at the $(0,0)$ and the three possible $(0,1)$ eSF frequencies should result in close to 100% eSF probability

[2] To combine MW at this frequency range and laser light a coupler had been developed [111]. Since the wavelength of the MW is below 3 mm and the size of the waveguide is therefore below 2 mm, the hole in the MW guide for the laser to pass through to the trap is only 1.3 mm in diameter. To use this setup, the laser would have had to be focused or a part of the beam would have been clipped. Neither option seemed beneficial at the time.

only about 50%. Therefore, this shows that the π time is of the same order of magnitude as with the WR10 MW setup including a horn and the WR28 MW setup. In conclusion, comparable MW power reaches the ion with either MW setup.

6.1.3 Prediction of the Transition Frequency

The spin-averaged transition frequency at zero magnetic field is known to 2.3 ppt (600 Hz) by spectroscopy performed in a RF Paul trap at 260 THz [35]. For spectroscopy in the Penning trap several effects shifting the frequency have to be considered.

Hyperfine and Zeeman shift

Depending on the hyperfine state of the ion, the actual rovibrational transition frequency is shifted by the hyperfine and Zeeman shift of this state, with respect to the spin-averaged frequency.

This shift can be calculated by diagonalizing the HFS Hamiltonian including the magnetic field terms for the $(0,0)$ and the $(5,1)$ state. Subtracting the energy of the HFS state of the $(0,0)$ level from the $(5,1)$ level then gives the shift to the spin-averaged transition frequency. In the process of calculating this shift, it became evident that the published explicit HFS matrix for $N=1$ states [58] is not traceless, so the sum of all eigenvalues does not equal zero. However, tracelessness is a requirement for the HFS Hamiltonian. After probing the effect, two sign changes were found that restore tracelessness to the matrix and allow to correctly predict the hyperfine shift of the rovibrational transition frequency [72]. These sign changes are in two of the diagonal terms of the zero-field HFS Hamiltonian, which should be given as:

$$h_{s22}(1) = \sqrt{3}(2\mathcal{E}_{1+2} + .. \tag{6.3}$$

$$h_{s1010}(1) = -\sqrt{3}(2\mathcal{E}_{1+2} + .. , \tag{6.4}$$

where $\mathcal{E}_{1+2} = \mathcal{E}_1 + \mathcal{E}_2$, so the two terms $\mathcal{E}_1$ and $\mathcal{E}_2$ are added and not subtracted. Here, $\mathcal{E}_i = hE_i$ and h is the Planck constant.

For the excited rovibrational states, the anisotropy of the g_e factor has to be included in the prediction, which takes into account that the interaction of the molecule and the magnetic field can differ depending on the orientation of the molecular axis with respect to the external magnetic field. This effect arises because spherical symmetry in a molecule is not given, which results in the treatment of g_e as a g tensor [71, 4]. This results in the scalar value of the g_e factor depending on the magnetic quantum number of the rotational state m_N and is given with respect to the perpendicular and parallel g_e components as: [71]

$$g_e(v,N,m_N) = \frac{2}{3}g_\perp(v,N) + \frac{1}{3}g_\parallel(v,N) + \frac{2}{3}\frac{3m_N^2 - N(N+1)}{(2N-1)(2N+3)}(g_\perp(v,N) - g_\parallel(v,N)) , \tag{6.5}$$

where $g_\perp$ and $g_\parallel$ are the tensor components introduced in Sec. 2.1.2.

Overall, the shifts of the spin-averaged rovibrational transition frequency due to the HFS and Zeeman effect amount to single to several ten MHz and the anisotropy of g_e contributes at the kHz level, both depending on the exact HFS states involved. This results

in a relative magnetic field sensitivity of the rovibrational transition of 40 ppb for all HFS levels, so a relative variation of the magnetic field by 0.1 ppm results in single-Hz frequency changes of the rovibrational transition.

The uncertainty of the HFS and Zeeman shift depends on the uncertainties of all input parameters, the g factors (g_e, g_p, g_d, g_N) and the E_i coefficients (i=1-9) for both rovibrational states. For the $(0,0) \rightarrow (5,1)$ transition, this amounts to about 1 kHz uncertainty in total, dominated by $\frac{\Delta g_N}{g_N} \approx 50$ ppm when using the improved values for $g_e(v,N)$[3].

Systematic Effects/ Higher Order Effects

There are several more shifts to the rovibrational transition frequency to consider, besides the HFS, with no external magnetic field dependence, and the Zeeman shift, with a linear magnetic field dependence. For example, at 4 T, the diamagnetic shift with a quadratic magnetic field dependence becomes sizable compared to the other uncertainties of the prediction and the scan range of our system. This effect is estimated to be in the 100 kHz range. The prediction of the numerical value is ongoing theory work and is estimated to reach a precision of single Hz [130]. Once the prediction is finalized, this effect will not limit the extraction of mass ratios at the ppt level from rovibrational spectroscopy. Furthermore, if H_2^+ and $\overline{H}_2^-$ are measured in the same setup, it should not affect a CPT test beyond current limits. All other effects and uncertainties considered so far are expected to be at or below the single kHz level and should allow finding the transition in our setup.

6.1.4 Expected Rabi Rates and Sidebands

The Rabi rate Ω_R of an electric dipole transition in HD^+ is given by:

$$\hbar\Omega_R = fEd\,, \tag{6.6}$$

where $\hbar$ is the reduced Planck constant, $f = 0.4$ is a reduction factor [120], E is the amplitude of the electric field of the laser, and $d = 0.00027$ Debye $\approx 9{\cdot}10^{-34}$ Cm is the dipole moment of the transition of interest [131]. E relates to the intensity I of the laser light via:

$$I = \frac{cn\epsilon_0}{2}|E|^2\,, \tag{6.7}$$

where c is the speed of light in vacuum, n is the refractive index of the medium, and ϵ_0 is the vacuum permittivity. The intensity of the light for the transition depends on the available laser power P, the radius of the beam waist of the laser at the position of the ion r_w and whether the linewidth of the laser is broader than the natural linewidth Γ of the transition of interest. For the $(0,0)$ to $(5,1)$ transition the natural linewidth is given by the lifetime $\tau \approx 16$ ms of the excited state as ~10 Hz. The laser system allows similar linewidths of the laser at powers of $P \approx 100$ mW.

For the initial attempts, we decided on a beam waist of the laser of $r_w = 2$ mm to ensure that the laser hits the ion. Focusing the laser to a smaller waist raised concerns of misalignment which would be difficult to diagnose. In total, this then results in an expected Rabi rate of approximately $10\,000$ rad/s for a hypothetical ion at 0 K motional temperature.

[3] publication in progress [72]

At the moment, the only laser access at ALPHATRAP is along the trap axis. Therefore, the amplitude of the axial motion must be considered to determine the amount of motional sidebands for this transition. Using negative feedback the effective axial temperature is $T_z \approx 3$ K, resulting in an average motion amplitude $\hat{z} \approx 32$ μm in the PT and $\hat{z} \approx 70$ μm in the AT due to the smaller motional frequency. Thus, the amplitude of motion is significantly larger than the wavelength of the laser, ~ 1.15 μm, resulting in a multitude of sidebands. Averaging over the amplitudes of the Bessel functions, which give the strength of each sideband, for the thermal distribution of $\hat{z}$, results in a factor of 20 reduction of the Rabi rate of the carrier in the PT and a reduction factor of 30 in the AT, see Fig. 6.5.

The laser is aligned to the physical trap axis. In a perfect trap where there is zero angle between the trap axis and the magnetic field, perfect laser alignment would result in exactly 90 degrees between the direction of the radial motion in the trap and the propagation of the laser.

Conservatively assuming an upper limit of one degree for the misalignment, the effective amplitude of the radial motion in direction of the laser propagation is small compared to the wavelength of the laser. Therefore, if occurring at all, the first motional sideband of either radial motion is suppressed compared to the carrier and the carrier transition strength is not significantly reduced by the radial motion.

Taking the reduction of the Rabi rate due to the ion temperature into account, we expect a transition rate of ~ 80 Hz in the PT and ~ 50 Hz in the AT at 100 mW laser power.

This sets limits for frequency scans in the measurement. Possible measurement parameters are each frequency step lasting 75 ms for an efficient excitation probability and frequency steps no larger than ~ 20 Hz to not step over the transition. To keep the probability that the ion has decayed back to the $(0, 0)$ state after laser excitation low, the state detection (eSF) should be carried about 10 s after the rovibrational excitation, limiting the scan time. This results in about 100 frequency steps of 20 Hz per measurement cycle.

To achieve enough statistics to distinguish a successful laser transition in the presence of the current BBR level in the trap (see Sec. 6.2) such a cycle has to be repeated several times. For the AT cycle proposed above (Sec. 6.1.1), it would require on the order of 1000 measurement cycles, allowing to scan ~ 2 kHz in 24 h.

6.1.5 First Attempts and Laser Alignment

The first tests combining the spectroscopy laser and the trap were carried out with the spectroscopy laser locked only to a wavemeter, resulting in ~ 1 MHz linewidths which reduces the Rabi rate. In this setting, the laser light was aligned from the breadboard all the way through the trap and out of the top of the beamline, ~ 5 m above, for the first time.

While performing test measurements, the laser was aligned into the trap at 100 mW for approximately 4 hours. This was before the upgrades and thus the cryovalve did not have a transparent window, so the full laser power was dissipated on the stainless steel closed cryovalve heating the 4-K surface. The heating resulted in a noticeable increase in helium consumption and in the release of residual gas from the cryogenic surfaces. This became apparent as all HD^+ ions in the trap had reacted upon collision with H_2 to H_3^+ or H_2D^+.

The measurements were interrupted after the room-temperature window to the insula-

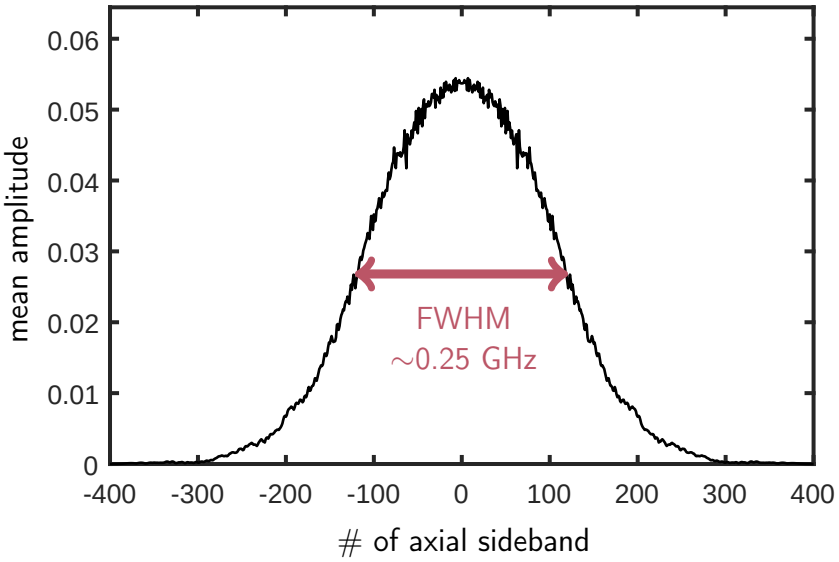

Figure 6.5: Reduced carrier strength of the $(0,0) \rightarrow (5,1)$ transition due to the large amplitude of motion compared to the wavelength of the laser. The figure shows the mean value of the Bessel functions averaged over the thermal distribution of axial amplitudes. The sidebands are spaced 650 kHz apart (ν_z^{PT}) and can be easily resolved with the 10 Hz laser line width.

tion vacuum below the magnet cracked, triggering a thermal cycle of the setup for repairs. In this thermal cycle, we lifted the setup out of the magnet to tune the modified cyclotron resonator of the PT to match the motion frequency of HD^+. If the modified cyclotron frequency of HD^+ and a 4-K resonator are in resonance, this motional mode can be cooled below what is achievable with RF coupling to the axial mode. Therefore, the spread of possible axial frequencies in the AT would be reduced, shortening the overall time of measurement cycles.

After reloading HD^+ we realized that there were now two electrical shorts in the AT, namely the ring electrode and the lower correction electrode were shorted and the upper correction electrode and the neighboring endcap electrode. Some attempts were made to find a solution to work around the shorts[4] however, it was not possible to find a viable solution. The trap setup had to be warmed up again for more extensive repairs.

The following months were therefore spent repairing and upgrading the trap setup. At the same time, the metrology lab with the frequency comb and stable reference laser were setup, by Ivan Kortunov and Victor Vogt. Details on the upgrades and a description of the optical setup are given in Ch. 4.

6.2 Black Body Radiation

After the reassembly of the trap setup, HD^+ was loaded again. At first, the overmoded WR28 MW setup was used to allow MW and laser access to the trap. It quickly became

[4] dubbed the crApTrap (AT)

apparent that the eSF rate in the AT was significantly lower than the usual 50%. The initial assumption was that not enough MW power reached the ion. Therefore, each component of the MW setup was tested, the alignment of the MW horn was optimized and then finally the MW setup was switched to the well-tested WR10 setup of the HFS campaign. Despite these steps, no improvement of the eSF rate could be achieved.

The cross check the system, $^{12}C^{5+}$ was loaded. The larger mass and higher charge state result in a larger signal strength for faster measurements and in smaller motional amplitudes, for less sensitivity to magnetic field inhomogeneities and electric field anharmonicities. Furthermore, as an atomic ion without nuclear spin, the Zeeman splitting of the electron spin is a 2-level system, which is less prone to unexpected effects than the molecular system. For $^{12}C^{5+}$ a 50% eSF rate was measured in both the AT and the PT.

After loading HD^+ again, it was observed that not only was the eSF rate lowered, but also the rate of changes of the nuclear spin orientation, so of the HFS state, had increased to about once per day in the upgraded setup. Previously, these state changes occurred only about once a week, see Fig. 5.6. Initially, it was considered whether the change in nuclear spin orientation could be driven by noise, as the noise level in the setup after the upgrade was higher over a large range of frequencies. For example, the new planar resonator or the newly implemented nuclear spin flip drive were considered as possible sources. However, this would not explain the lower eSF rate.

In the upgrade we changed the electrode connection of the AT axial resonator, see Sec. 4.2.2. This now enabled fast FFT sampling of the dip and thus measurement of the axial frequency of the ion of ∼10 s, compared to the ∼80 s that were needed previously. Thus, the measurement time for an attempt to drive an eSF in the AT - axial dip, MW irradiation of typically 1-5 s, axial dip - was much faster. While carrying out repeated eSF cycles in the AT, we observed times of ∼50% eSF rate ('bright') alternating with 'dark times' with 0% eSF rate, see Fig 6.6. To test the hypothesis that the ion is excited to the $(0, 1)$ state, the same measurement was repeated, now irradiating the MW frequency for eSF in the $(0, 1)$ state for the different m_N values ($\nu_{\mathrm{MW}}(0, 0, m_N)$). Again, we made the same observation of alternating bright and dark periods, see Fig 6.6. Averaging over times significantly longer than the lifetime of the $(0, 1)$ state, the eSF rate at $\nu_{\mathrm{MW}}(0, 0)$ was about 25% and for each of the three possible $\nu_{\mathrm{MW}}(0, 0, m_N)$ about 8%. Thereby, the hypothesis was confirmed that in our trap HD^+ populates not only the ground state but also at least the first rotationally excited state. From the eSF of the different states and the amount of dark times when irradiating $\nu_{\mathrm{MW}}(0, 0)$, we conclude that for about 50% of the time HD^+ is in the ground state and excitations occur every few minutes.

Before the upgrade, the observation of the 'dark times' for the eSF which occur when the ion is in the excited state would not have been possible, as the duration of a single eSF attempt was at the same order of magnitude as the lifetime of the $(0, 1)$ state. However, to estimate whether such excitations occurred before the upgrade, the distribution of the number of attempts needed to drive an eSF in the AT can be compared. Figure 6.7 compares the number of attempts before and after the upgrade with a simulation assuming the ion is always in the $(0, 0)$ state and a simulation including rotational excitations. For the first simulation, the histograms of the distribution of the number of attempts for an eSF, especially for the one after the upgrade, clearly show a longer tail in the data than in the simulation. In the second simulation, the histograms overlap including the longer tail not covered by the first simulation. We therefore reached the conclusion that before the

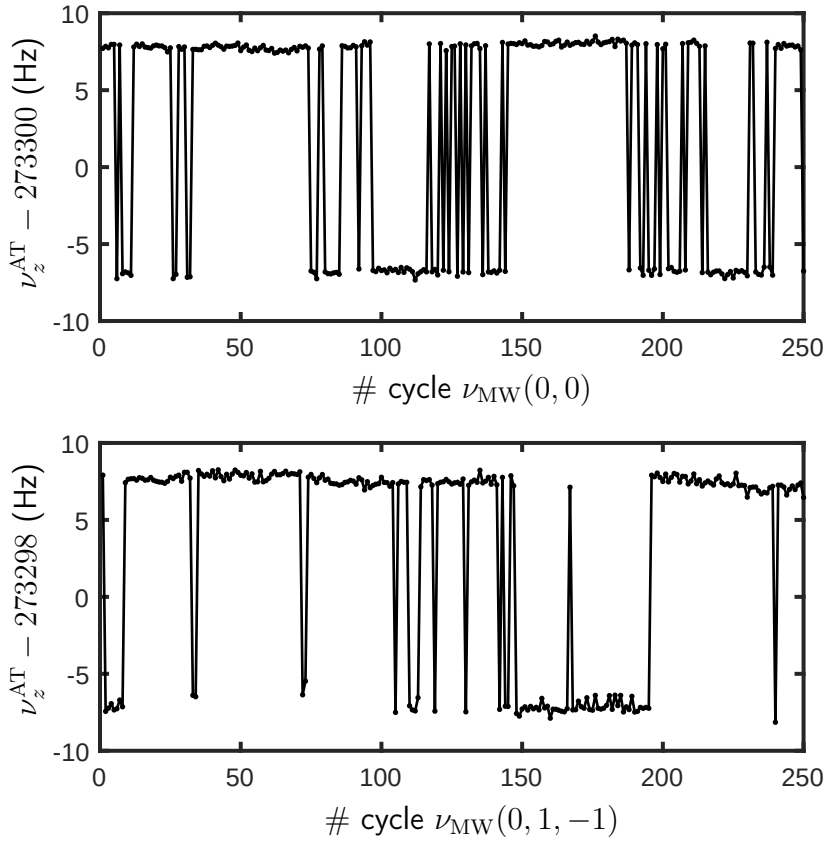

Figure 6.6: eSF in the AT at $(0,0)$ and $(0,1)$ MW frequencies. **top:** AT measurement cycles alternating ν_z dip measurements and MW irradiation at the eSF frequency of the rovibrational ground state $\nu_{\mathrm{MW}}(0,0)$. The data shows sections of high ($\sim$50%) eSF probability and sections of 'dark times' with no eSF. **bottom:** The same measurement was repeated but now at the MW frequency of eSF of the first rotational state, choosing the $m_N = -1$ state $\nu_{\mathrm{MW}}(0,1,-1)$. The data clearly shows eSF driven at this MW frequency.

upgrade rotational excitations took place as well, however at a smaller rate than now. Which corresponds to the increase of changes in nuclear spin orientations after the upgrade.

Comparing the transition dipole moment of the rotational transition for which the HFS state (the orientation of the particle spins) remains constant, to the dipole moment of a rotational transition changing a nuclear spin orientation, leads to a ratio of approximately 1/500 to 1/1000 [120]. This means that in most cases, when the ion is excited rotationally $\Delta N = 1$, it decays back to the ground state without a change in HFS state, however in approximately 1/500-1/1000 cases it decays with a change of a nuclear spin orientation. This is in the same order of magnitude as the ratio of the observed rotational excitations and the observed changes of a nuclear spin orientation (one per single minutes versus one per day). As of now, we have not observed a nondriven change in electron spin orientation. This aligns with the about four orders of magnitude smaller transition dipole moment for the rotational decay coupled with such an HFS state change.

Hypothetically, the excitations of HD^+ could be caused by collisions with residual gas.

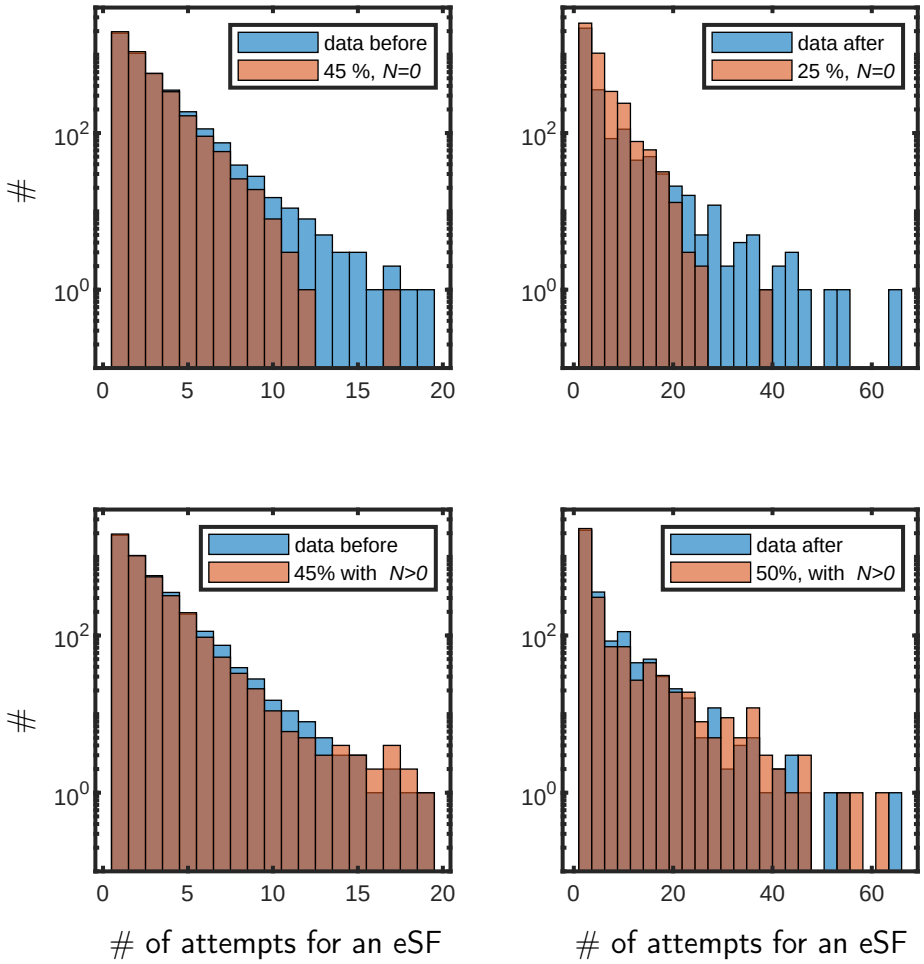

Figure 6.7: Histograms of the number of attempts needed to successfully drive an eSF in the AT. **left:** AT data of the HFS measurements campaign (before the upgrades) and **right:** data taken after the upgrades. **top:** Simulation assuming the measured average eSF probability and that the ion is only in the ground state. **bottom:** Simulation including rotational excitations. For all figures the measurement data is shown in blue and the simulation is shown in orange (the orange histograms are slightly opaque so that the blue histogram behind remains visible). The data and the prediction simply assuming a lowered eSF rate do not agree. In both the HFS campaign and in measurements after the upgrade there is a tail of high number of attempts for driving an eSF not covered by the prediction. This behavior can be explained by the simulation including rotational excitations.

Calculation for rotationally inelastic collisions of H_2^+ and He can be found [132], investigations for neutral H_2 have recently been published [133] and it has been suggested that the rate of change of the hyperfine state for H_2^+ in a Paul trap depends on the helium background pressure [42].

At ALPHATRAP, the direct 'line of sight' from the room-temperature vacuum to the cryogenic 4-K trap vacuum is closed off by the cryovalve. This prevents warm residual gas from entering the trap and interacting with the ion. Therefore, on its way to the trap vacuum any residual gas particle would undergo several collisions with the 4-K surfaces of the cryovalve and surroundings. Consequently, only He or H_2 residual gas particles are possible inside the trap since all other elements and molecules freeze out.

When H_2 and HD^+ collide, the probability of inducing a molecular reaction is high, as was observed after the first tests with the laser in the trap before the upgrade, see Sec. 6.1.5. Since we have not observed such events after the upgrade, these collisions seem unlikely.

If collisions of HD^+ with He were the cause of the observed rotational excitations, there would have to be a significant energy and momentum transfer in such a collision. Considering the low average kinetic energy of a He atom at 4 K, this would most likely imply that collisions occur regularly and only the fraction that transfer enough energy for the rotational excitation are detected. Considering the average kinetic energy at 4 K, collision with He are unlikely to excite HD^+ rotationally. Furthermore, several collisions of the trapped ion with He atoms are unlikely for two reasons. First, we did not observe charge exchange reactions of the trapped $^{12}C^{5+}$, leading to $^{12}C^{4+}$ or lower charge states. This would be the case if a He background were prevalent. Second, the axial frequency of the HD^+ ion remained stable below a Hz in the AT if no ion transport or voltage changes were carried out. As the axial frequency in the AT strongly depends on the radial amplitudes of motion, this sets stringent limits especially on amplitude changes of the modified cyclotron motion. Furthermore, we opened the cryovalve for about 1 h, exposing the ion to a direct line of sight to the room temperature vacuum, but saw no effect on the rate of excitations to the $(0, 1)$ state. Overall, this make collisions as the cause of the rotational excitations very unlikely.

At room temperature, rotational excitation can be driven by BBR, however at 4 K, the BBR radiation is negligible. At ALPHATRAP, the ion has a direct line of sight to 77 K and even room temperature through the windows at the bottom of the trap chamber and below the magnet. In the upgrade, a window was added to the cryovalve as well. The purpose is for the laser light to pass through and not deposit the full laser power in the 4 K section, as this had caused surface heating before the upgrade. On the other hand, this window adds another line of sight from the ion to room temperature above the trap, however the solid angle is negligible compared to the windows below the trap.

In the upgrade the UV grade fused silica 4-K window was replaced by a CaF_2 window. At room temperature, CaF_2 has a broad transmission range from the UV to the mid IR up to about 10 μm, a negligible transmission in the range from 10-200 μm and a rather good transmission at longer wavelengths in the MW regime [106]. Based on these characteristics, it transmits all irradiated wavelengths but blocks the intermediate THz regime of BBR. However, due to the observed rotational excitations of HD^+, we conclude that the spectral transmission properties of CaF_2 shift at cryogenic temperatures, allowing THz-range BBR to enter the trap. Figure 6.8 compares the spectral radiance ($R(\nu, T)$) as a function of the photon frequency ν of the BBR spectra for temperatures T of 4 K, 77 k, and 300 K (room

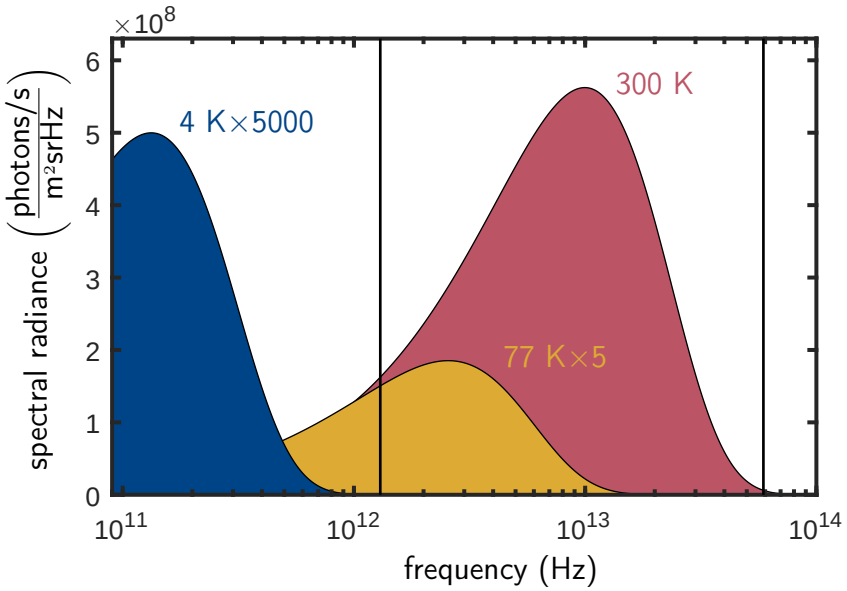

Figure 6.8: BBR spectral radiance at 4 K, 77 K, and 300 K. The 77 K and 4 K spectra are multiplied by 5 and 5000 for better visibility, respectively. For reference, without this amplification the 4-K BBR spectrum is about two orders of magnitude smaller than the 300-K BBR spectrum at 10^{11} Hz and more than six order of magnitude smaller at 1.3 THz. The $\Delta N = 1$ rotational transition at 1.3 THz and the $\Delta v = 1, \Delta N = 1$ lowest rovibrational transition at 59 THz are marked by the black lines.

temperature) in units of photon count per area, solid angle, and Hz $\left(\frac{\text{photons/s}}{\text{m}^2\text{srHz}}\right)$ calculated by:

$$R(\nu, T) = \frac{2\nu^2}{c^2} \frac{1}{e^{h\nu/k_B T} - 1}, \tag{6.8}$$

where c is the speed of light in vacuum, h is the Planck constant, and k_B is the Boltzmann constant. The spectra show that the $\Delta N = 1$ fundamental rotational transition from the ground state at 1.3 THz can be easily driven by 300 K and reduced in photon count by a factor of 5 also by 77 K BBR. For the 4 K BBR spectrum the photon count at 1.3 THz is reduced by a factor of $2{\cdot}10^7$ compared to room temperature, leading to a basically zero possible excitation rate. The photon count for the first rovibrational transition ($\Delta v = 1, \Delta N = 1$) at 59 THz is only practically non-zero in the 300 K spectrum which is lower than for 1.3 THz by about a factor of 25. Combined with the about ten times smaller transition dipole moment of the rovibrational transition [131], therefore these excitations by BBR are possible but far more reduced compared to purely rotational excitations. It is possible, that HD^+ is further excited from the $(0, 1)$ state to the $(0, 2)$ state by BBR. However, combined eSF probability of the $(0, 0)$ and $(0, 1)$ state agrees with 50% within the uncertainty of single %. Thus, if a second excitation step occurs, the occupation time of the $(0, 2)$ state is expected to be small at only single %.

Possible improvements to the setup to reduce the rotational excitations would be to go back to a UV fused silica window for the 4 K trap chamber. However, this would not transmit mid-IR for $\Delta v = 1$ transitions in MHI. Alternatively, the 77-K and/or 4-K sections between the windows and the trap could be altered to reduce THz transmission, for example

by black coating of the inner surfaces of the MW guides. It would have to be ensured that it does not reduce electrical conductivity of the parts or lower the MW transmission.[5]

6.3 Measurement of (0,1) eSF Transitions

During the ongoing work of predicting the $(0,0) \rightarrow (5,1)$ transition frequency for our trap conditions, developing a promising measurement scheme, and work on the laser setup, we started taking data on eSF transitions of the $(0,1)$ state that is populated by BBR. We followed the same steps for finding the transitions as in the HFS measurements of the $(0,0)$ state, so first driving eSF in the AT and then initially without a magnetic field measurement at each eSF attempt in the PT.

The two main differences to the campaign on the eSF transitions in the $(0,0)$ state are, firstly, the very low spin flip rate of $\sim 8\%$ since the ion is in the $(0,1)$ state only $\sim 50\%$ of the time and thus only a third of this time in each m_N HFS state. Therefore, the data is taken at high MW power saturating the line to ensure the highest possible eSF rate which however also broadens the line. Since the line is broadened, the modified cyclotron frequency is not determined with the more precise PnA technique but via a double-dip fit. So far, data on the $(0,1)$ eSF transitions has been taken in the symmetric PT with $B_2 \sim 100$ mT/m^2. Therefore, the asymmetry of the line due to the magnetic field inhomogeneity including the saturation must be taken into account in a future detailed evaluation [129, 128].

Secondly, while the increased BBR make this measurement possible by populating the $(0,1)$ state, it also causes changes in the nuclear spin orientation about once a day, compared to the $\sim$7 days of the previous campaign. Therefore, it is not possible to measure a single eSF transition, collecting data for several days. Figure 6.9 shows the combined data of the eSF transitions of different HFS states collected so far. All HFS states probed are states with $m_N = -1$.

While a qualitative statement on the line center or the parameters (g factors, E coefficients) contributing to the transition frequencies cannot be made yet, quantitatively the eSF transitions follow the theoretical prediction at the kHz level, see the x-axis in Fig. 6.9. The theoretical prediction is made using the corrected Hamiltonian matrix including the anisotropic g_e factor, see Sec. 6.1.3. As input parameters the E coefficients from Ref. [70], $g_e(0,1)$ from Ref. [4], and $g_N(0,1)$ from Ref. [66] were used, along with the free-particle nuclear g factors [59]. g_e, E_4, and E_5 were shifted by the same relative value by which the ground state measurement results differ from their respective theoretical prediction, see Tab. 5.2.

6.4 Outlook: Towards the Lamb Dicke Regime

In the current setup, the amplitude of motion in the PT in direction of the laser propagation is about a factor of 30 larger than the wavelength of the transition of interest, therefore this is far outside the Lamb Dicke regime and thus in the regime with a multitude of motional sidebands, see Fig. 6.5. Furthermore, this reduces the Rabi rate for the transition

[5] Here, I would like to especially thank Holger Kreckel for the very insightful discussion about molecular collision reactions and BBR in cryogenic systems.

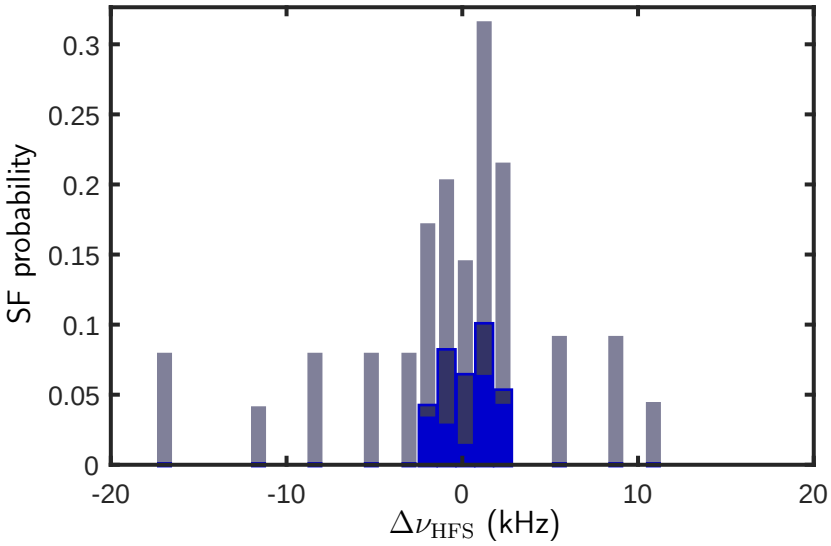

Figure 6.9: First data on MW driven eSF transitions in the first rotationally excited state of HD^+. Here, the eSF transitions of several HFS states with $m_N = -1$ but with different nuclear spin orientation were probed, due to the BBR induced HFS state changes once a day. The binned data, shows the eSF probability as a function of the offset of the irradiated MW frequency from the theoretically predicted transition frequency, $\Delta\nu_{\mathrm{HFS}}$. The gray bars are the binomial error for each bin.

as discussed above. Therefore, we aim to move towards a system in which the motional amplitude is small compared to the wavelength of the transition, to ideally enter a regime without sidebands and reduction of the Rabi rate, the Lamb Dicke regime.

6.4.1 THz Spectroscopy

Since the figure of merit is the ratio between the wavelength of the transition and the motional amplitude, one option is to increase the wavelength. Of course, this is only possible if the system features transitions at larger wavelengths. In MHI, this is the case. Instead of driving rovibrational transitions in the IR range, single-THz purely rotational transitions are possible as well. For HD^+, the $(0,0) \rightarrow (0,1)$ transition frequency is at 1.3 THz. This is equivalent to a wavelength of 230 μm which is larger than the average axial amplitude of motion ($\hat{z}^{\mathrm{PT}}$ ≈30 μm). This would lead to a reduction of only 1.2 of the Rabi rate of the carrier for a measurement in the PT and 2.2 for a measurement in the AT, assuming a 2-K axial temperature.

Several such transitions for different HFS states have been measured to 50 ppt relative precision in an RF Paul trap [73], allowing a precise prediction of the transition. Therefore this would be a good candidate for spectroscopy in a Penning trap. Furthermore, the transition dipole moment for this transition is about a factor of 3000 larger than for the $(0,0) \rightarrow (5,1)$ transition [131].

However, the lower transition frequency, compared to rovibrational transitions, and the second-order Doppler shift, if the ion motion is not cooled further, can ultimately limit the achievable relative precision of the spectroscopy. If the axial and the modified cyclotron

motion are cooled to a 2-K axial resonator and the radius of the modified cyclotron motion during irradiation is known by measuring the shift of the axial frequency in the AT, the uncertainty of the second-order Doppler shift can be reduced to below the ppt level. In the following, options to reach or get closer to the Lamb Dicke regime by reducing the motional amplitude of the ion for laser spectroscopy in Penning traps are considered.

6.4.2 Selection of Small Modified Cyclotron Radii

The idea of the selection of small modified cyclotron radii, is to repeatedly cool the modified cyclotron mode of the ion, thereby resampling from the thermal Boltzmann distribution, until a small radial amplitude is reached by chance. The amplitude of the modified cyclotron motion can be measured in the AT as the shift of the axial frequency compared to a '0-K' particle, see Sec 5.1.4.

After transporting the particle to the PT, the energy of the axial and modified cyclotron modes can be swapped by an RF π pulse at $\nu_{\mathrm{RF}} = \nu_+ - \nu_z$, leading to a correspondingly reduced axial amplitude. This must be off resonant to the axial detection system to avoid thermalization of the axial mode with the resonator.

Assuming for now a perfect RF π pulse and the goal of an axial amplitude of 1.15 μm or smaller, sampling from a 2-K thermal distribution of the axial resonator via double-dip type RF cooling would statistically only lead to a small enough modified cyclotron radius in 2/1000 cooling cycles. Such a cooling cycle would involve transporting the ion from the AT to the PT for the double-dip type RF cooling and back to the AT to measure the new r_+ via $\Delta\nu_z^{\mathrm{AT}}$. Such a cooling cycle takes about three minutes, thus on average it would take more than a day to find a cold ion. This is therefore not a feasible option.

To achieve more efficient cooling of the modified cyclotron motion, the planar resonator was added to the ST in the upgrade. The goal was to achieve a lower T_+, thereby sampling r_+ from a colder Boltzmann distribution and require less cooling cycles to statistically reach a low r_+. A similar approach, using a modified cyclotron resonator to achieve a colder Boltzmann distribution of r_+ for low radii selection, has been demonstrated at BASE for antiprotons [134]. If this resonator has an effective temperature of $\sim$5 K which can be suppressed to $\sim$2 K by applying negative feedback, r_+ would be sampled from a much colder thermal Boltzman distribution. Note, the temperature of the modified cyclotron mode after double-dip type RF cooling is given by: $T_+ = T_z \frac{\nu_+}{\nu_z}$, see Sec. 3.1. With such a cold modified cyclotron resonator, a small enough r_+ could be sampled in 5% of the cooling cycles. Due to the rather long cooling time of the ion and this resonator, several minutes are needed for each cooling cycle here as well, leading to a small enough r_+ after about 1-2 h.

Unfortunately, the modified cyclotron resonator did not have an effective temperature of single K. When tuning the resonator to the ν_+ frequency of HD^+ a larger spread of r_+ was measured than by double-dip type RF cooling in the PT. In conclusion, the effective temperature of the resonator is above 100 K. Since the YBCO resonator however reaches its superconducting state, it is impossible that this corresponds to the physical temperature of the resonator. The high effective temperature could, for example, be due to excess noise in the system.

Even if the ion has a small enough r_+, this radius would have to stay constant throughout the AT to PT transport. We have observed a jitter of a few Hz of ν_z^{AT} after AT-PT-AT

transports due to a jitter in r_+. Mapped on to the axial amplitude, this translates to a several μm jitter due to ion transports, which is larger than the wavelength of the transition.

6.4.3 Radial Irradiation

Another option to gain a more favorable ratio of the motional amplitude of the ion in direction of irradiation and the wavelength of the transition is to irradiate the laser in the radial plane instead of in axial direction. Using double-dip type cooling for the radial modes with an axial resonator with negative feedback at 2-K effective temperature results in average radii of both the modified cyclotron and the magnetron mode of about 4 μm. This would result in a reduction factor for the Rabi rate of the carrier of about seven for each radial motion.

However, the modified cyclotron mode could be cooled to lower temperatures and thus lower motional amplitudes by coupling directly to a resonator. Assuming this resonator would also reach effective temperatures of 2 K with negative feedback and the magnetron motion is coupled to this motion via an RF signal, the average radial amplitudes would be lowered to about 0.75 μm, resulting in a reduction factor of only $\sim$3 per radial motion.

Implementation of radial laser access in the Penning-trap setup at ALPHATRAP was discussed along with a trap design based on selective laser-induced etching technology. The trap design was carried out in the thesis work of Dr. Jonathan Morgner [102]. In principle, radial irradiation could be implemented with a standard trap design using copper electrodes as well.

6.4.4 Sympathetic Laser Cooling

Laser cooling of atoms and ions is a well-established technique and allows to reach sub-mK temperatures [135] and therefore motional amplitudes well below the wavelength of the transitions of interest. However, the absence of bound excited electronic states and the long lifetimes of the rovibrational states make direct laser cooling of MHI impossible. To nevertheless reach cold temperatures, generally ions can be cooled sympathetically by interacting with a laser-cooled species.

Sympathetic laser cooling has been established in Paul trap by co-trapping laser-coolable ions and the ions of interest, as for example done for rovibrational spectroscopy of HD^+ [73, 74, 75, 35]. In Penning traps, co-trapping ions in the same trap section alters the harmonic electric trapping field at the position of the ion of interest by the Coulomb interaction with the cooling ion. This modifies the ion motion which interferes with the precise determination of the motional frequencies. A sympathetic cooling scheme coupling ions via Coulomb interaction, is currently being developed in Penning traps, using a microfabricated coupling trap to bring the ions close together. This scheme requires separation and fast transport of the ions without significant heating [136, 137]. Sympathetic cooling of negatively charged ions, such as $\overline{H}_2^-$ adds the additional complexity of opposite charges of the ion of interest and the positively charged laser coolable ions.

Another option for sympathetic cooling is for the ions to interact via the induced image currents in the trap electrodes. The ions can be confined in separate trap sections thus not disturbing the harmonicity of the electric trapping field. The ions then interact either solely through the induced currents in a common endcap electrode or by a resonant tank circuit

coupled to both trapping regions. This had been investigated at ALPHATRAP [138] and the proton g-factor experiment in Mainz within the BASE collaboration [139]. In the latter case with a common tank circuit, a balance has to be found between the ions heating to the temperature of the resonator and a strong coupling for the ions to interact, which can limit the achievable temperature [138, 139]. So far temperatures of 170 mK for a sympathetically cooled proton have been reached [140].

Without a common resonator, so solely by coupling via the image currents in a common endcap, the Rabi rate Ω_R for the energy exchange between two ions, without damping via laser cooling or heating via Johnson noise of a resonator and with both ions in resonance to each other at an axial frequency ω_z, is given by: [138]

$$\Omega_R = \frac{q_1 q_2}{\omega_z D_1 D_2 C_T} \sqrt{\frac{N_1 N_2}{m_1 m_2}} \,, \tag{6.9}$$

where q_i are the charge states, m_i the masses, and N_i the amount of cooling ions and ions of interest, respectively. D_i are the respective effective electrode distances to the common endcap for both ion species and C_T is the equivalent parallel capacitance of the common endcap. In Ref. [138] $\Omega_R/(2\pi)$ was estimated to be $\sim$9 mHz for H_2^+ and 100 Be^+ ions, using $C_T = 10$ pF, $D_1 = D_2 = 4.6$ mm, and $\omega_z/2\pi = 500$ kHz. This requires a similar good matching of the axial frequencies and therefore stability of the axial frequency to single mHz and a similar damping rate for laser cooling of the Be^+ ions, which are both experimentally challenging.

In principle, any of the quantities can be tuned for a more efficient interaction strength to improve the Rabi rate of energy exchange. Changing the properties of the common endcap itself, scales linearly with the Rabi rate, thus it is beneficial to lower C_T and D_i. C_T is mainly given by the surface area of the electrode and its distance to the surfaces of other electrodes and the electrical ground potential. Therefore, it can, in principal, be lowered by reducing the total size of the electrode and increasing the gap to neighboring electrodes. Figure 6.10 shows a possible design of a coupling trap with a common endcap with a reduced C_T. The three smaller central electrodes are AC shorted to act as one common endcap, but allow different DC voltages for ion transports and possibly for trap tuning. This design results in a C_T of about 0.5-1 pF and D_i in the order of 4 mm, depending on the exact sizes of the electrodes and the positions of the ions. Assuming all other parameters to be the same as in Ref. [138], the reduction in C_T would increase $\Omega_R/2\pi$ by a factor of 20 to $\sim$180 mHz. This would loosen the requirements for axial frequency matching and stability and for the laser cooling rate of Be^+.

However, manufacturing a stack of electrodes with a length of 1 mm and radius of 1.5 mm (or smaller) to high precision is challenging using standard copper electrodes. Therefore, a 1 mm thick Al_2O_3 circuit board with a silver coated 3 mm via was designed and ordered from CERcuits [141] to be used as the central electrode of the common endcap, see Fig 6.10. There are several open questions remaining for the design of such a trap, such as the exact dimension of the electrodes for optimal tuning of the electric trapping field and whether it is feasible to use such a circuit board as a trap electrode. There are several questions to address, such as the surface roughness in the via and the purity of the board material as well as of the conductive silver coating. Alternatively, a coupling trap with small electrode sizes and thus low C_T of a common endcap could possibly be fabricated using selective laser-induced etching technology.

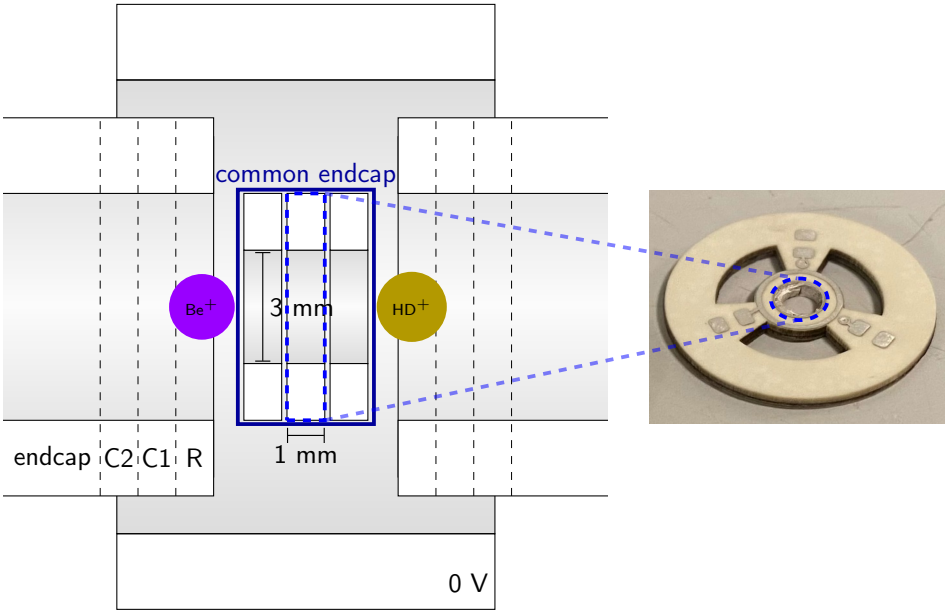

Figure 6.10: left: A cut through a side view of a potential coupling trap design for sympathetic laser cooling in a Penning trap. The common endcap is reduced in radius compared to the other trap electrodes (ring R, correction 1 C1, correction 2 C2, endcap) to reduce its capacitance C_T. It is split into three AC-shorted electrodes to allow different DC voltages on each electrode for ion transports. The R, C1, C2, and endcap electrodes are separated by dashed lines indicating the variable size of each electrode for optimizing the effective electrode distances of the ions to the common endcap D_i and for tuning the electric trapping field. **right:** A top view of a possible implementation of the small electrodes. The central common endcap electrode is fabricated as a 1 mm Al_2O_3 circuit board with a silver coated 3 mm via on which a voltage can be applied.

The Doppler limit for Be^+, the lower limit for the temperature achievable with Doppler laser cooling, is $T_D \approx 0.5$ mK [138]. Assuming the same axial temperature was reached for HD^+ this would lead to an average axial amplitude of motion of $\sim$0.36 μm and a reduction of the carrier of less than a factor of 2.

6.5 Outlook: Ion Production and Nondestructive State Detection for $H_2^+/\overline{H}_2^-$

In this section, I will first consider possibilities and challenges for ionizing standard-matter molecular hydrogen and for the potential production of an antimatter molecular ion ($\overline{H}_2^-$) for future rovibrational spectroscopy comparing matter and antimatter. Then, I will briefly discuss the prediction uncertainty of eSF transition frequencies of H_2^+ in relation to the variation of these frequencies in different rovibrational levels.

6.5.1 Ionization of Molecular Hydrogen

The complete setup of ALPHATRAP is described in detail in Chapter 4. As shown there, the trap is connected to a beamline with ion sources based on electron-impact ionization. When ionizing molecular hydrogen via electron-impact ionization, the resulting MHIs populate a range of rovibrational states. The vibrational state population is given by the Frank-Condon factors which result in a distribution of vibrational levels, where $v = 0 - 10$ states have a population probability $> 1\%$ [142, 143]. The rotational state population, on the other hand, is related to the distribution of rotational states of the hydrogen gas which is given by a thermal distribution [142, 144]. A black-body-radiation-induced room-temperature distribution of the rotational states of HD^+ can be found in [145].

As explained in Sec. 2.1, for HD^+ the excited rovibrational state lifetimes are short compared to our measurement time and therefore, in the cryogenic environment of the trap (see Chapter 4) assuming no incoming BBR, they decay to and remain in the rovibrational ground state for the measurement. So the population of multiple excited rovibrational levels in electron-impact ionization is of no concern for initial state preparation for the measurement. For H_2^+, on the other hand, this is not the case, as due to the symmetry of the molecule the rovibrational state lifetimes are much longer (see Sec. 2.1).

As an option to enhance the population in the lower rotational states, we investigated supersonic expansion in Alexander Wallach's bachelor thesis work [146]. H_2^+ in vibrational excited states is of less concern than rotational excitation for initial state determination and possibly state preparation for several reasons. First, since the energy spacing between vibrational states is larger than between rotational ones, they are distinguishable by the mass increase due to a vibrational excitation [81, 82], at a precision of $1{\cdot}10^{-10}$. This is more realistically achievable in a setup not dedicated to high-precision mass measurements than distinguishing rotational states which would require about two order of magnitude more precision. Secondly, MHI in excited vibrational states can be dissociated by 313 nm light, while the MHI in the ground vibrational state would remain trapped [147]. Furthermore, the vibrational excited states exhibit shorter lifetimes than the pure rotational excited states (see Sec. 2.1) and given a large enough magnetic field the rovibrational decay rate can be reduced by Stark quenching, allowing to reach the vibrational ground state in a reasonable time compared to trapping times in cryogenic Penning traps [84]. Lastly, when preparing a rovibrational state of interest by actively driving rovibrational transitions, there are less constraints on the change of the vibrational quantum state than on the rotational one (see Sec 2.1). A single transition in H_2^+ must follow $\Delta N = 0, \pm 2$ (without loss of multiple orders of magnitude of transition strength), while Δv follows no strict selection rule.

Since the ionization of MHI worked straightforwardly in our existing ion source and schemes for future antimatter $\overline{H}_2^-$ production result in excited rovibrational states as well (see Sec 6.5.2), we decided not to pursue alternative ionization methods that offer state selectivity such as multi-photon ionization [148].

6.5.2 Possible Production Techniques for $\overline{H}_2^-$

First, I would like to state that up until now, there is no evidence that $\overline{H}_2^-$ has been produced in laboratories. Here I will name possible production schemes, the challenges and their influence on the internal state of the antimatter ion. In literature, two proposed

production pathways have been analyzed:

$$\overline{\mathrm{H}}^{+} + \overline{\mathrm{p}} \rightarrow \overline{\mathrm{H}}_2^{-}(v, N) + e^{+} \ , \tag{6.10}$$

$$\overline{\mathrm{H}}(2s) + \overline{\mathrm{H}}(2s) \rightarrow \overline{\mathrm{H}}_2^{-}(v, N) + e^{+} \ . \tag{6.11}$$

An estimation for the first pathway was carried out in Ref. [2]. It depends on a reliable production of single cold $\overline{\mathrm{H}}^{+}$ ($\overline{\mathrm{p}}e^{+}e^{+}$) which has not been demonstrated but is actively pursued by the GBAR experiment [149]. Using the design goal for $\overline{\mathrm{H}}^{+}$ production and considering competing reaction channels, the production rate of $\overline{\mathrm{H}}_2^{+}$ was estimated to $5{\cdot}10^{-5}\,\mathrm{s}^{-1}$ [2]. Since this reaction is exothermic $\overline{\mathrm{H}}_2^{+}$ will be produced in excited rovibrational states with $8 \leq v \leq 27$, explicit numbers on the rotational quantum number were not given [2].

Laser excitation of the antihydrogen atom ($\overline{\mathrm{H}}$) from the 1S ground state to 2S has been accomplished at the ALPHA experiment [150]. In Ref. [49], the production cross section for the second pathway was estimated to $10^{-2}\,\mathrm{s}^{-1}$ using predicted future experimental conditions and low-energy extrapolations of thermal rates. However, recently Ref. [50] suggested that a competing reaction rate is larger than assumed which would lead to more losses and a lower production rate of $\overline{\mathrm{H}}_2^{-}$. Since this process is exothermic as well, it will also lead to $\overline{\mathrm{H}}_2^{-}$ in excited rovibrational states, explicit values are not given.

6.5.3 State Identification

In this section, I would like to demonstrate the importance of the improved g_e values of this work and the ongoing theory work for nondestructive state detection of H_2^{+} and its antimatter counterpart by eSF transitions.

Looking at the HFS Hamiltonian, Eq. 2.3, the eSF frequencies for the excited rovibrational states with $N > 0$ depend not only on the $g_e(v, N)$ factor but also on HFS coefficients b_F, c_e, c_I, d_1, and d_2. Therefore, the eSF frequencies of states with $N > 0$ and $m_N \neq 0$ differ significantly from the ground state eSF frequency and differ by more than the 0.1 ppm uncertainty of the g_e factor from one rovibrational state to the next. Thus, besides accidental coincidences, these states should be distinguishable by their respective eSF frequency.

However, the eSF transition frequencies of all states with $N = 0$ do not depend on the HFS coefficients, and states with $N > 0$ but a rotational projection $m_N = 0$ do so only very weakly. Values of eSF transition frequencies for a selection of such states are given in Tab. 6.2. The values reveal that if the rotational or vibrational quantum number is known, the eSF transition frequency should deterministically lead to the respective other quantum number even at its current uncertainty. However, if both v and N are unknown, there are rovibrational states for which the eSF transition frequencies are the same within the 0.1 ppm uncertainty of the g_e factors.

Therefore, it is favorable for the prediction of eSF transition frequencies, and thus the g_e factor, to be more precise than the magnitude of the deviations of the eSF frequencies between rovibrational states, thus enabling to distinguish these states[6]. The experimental

[6] If the internal state of the ions is unclear by the eSF frequency, rovibrational state detection can be carried out in a two-step process by addressing not only eSF transitions but also transitions changing m_N or m_I if $I = 1$ [2]. These transition would have to be coupled with an eSF transition before and after to see the HFS state change by a change in eSF frequency. However, this would add complexity to the setup and the detection scheme.

Table 6.2: H_2^+ eSF transition frequencies between states with quantum numbers: $(v, N, m_N = 0, m_s = \pm 1/2)$, $v = 0 - 4$, $N = 0, 2, 4$ at $B = 4.02\,\mathrm{T}$. The frequencies are determined by subtracting the respective eigenvalues of the HFS Hamiltonian. For the explicit matrix forms, see the Appendix for states with $N = 0$ and $N = 2$ and Ref. [58] for $N = 4$. $g_e(v, N)$ values are taken from [71] including the anisotropy of the g_e factor, $g_N(v, N)$ from [65], and $c_e(v, N)$ from [61]. The uncertainty of the calculated frequencies is given by the uncertainty of the g_e factors at 0.1 ppm [71]. All values are given in MHz.

v/N [MHz]	0	2	4
0	112 658.01	112 658.09	112 658.21
1	112 658.07	112 658.14	112 658.25
2	112 658.13	112 658.19	112 658.28
3	112 658.18	112 658.24	112 658.32
4	112 658.22	112 658.28	112 658.35

$g_e(0,0)$ result of the HFS campaign can be used to enhance the prediction of g_e-factor values in other rovibrational states as well as for other MHI isotopologues, such as H_2^+. The higher-order QED terms of $g_e(0,0)$ of HD^+ can be extracted as the difference between the experimental and theory result, excluding these terms but including leading-order relativistic corrections which have been carried out for H_2^+ [71]:

$$\delta g_e(0,0)^{\mathrm{QED}}_{\mathrm{HD}^+} = g_e(0,0)^{\mathrm{exp}}_{\mathrm{HD}^+} - g_e(0,0)^{\mathrm{th}}_{\mathrm{HD}^+} \ . \tag{6.12}$$

Since the higher-order QED terms depend only weakly on v and N, $g_e(v,N)_{\mathrm{HD}^+}$ can be predicted by:

$$g_e(v,N)_{\mathrm{HD}^+} \simeq g_e(v,N)^{\mathrm{th}}_{\mathrm{HD}^+} + \delta g_e(0,0)^{\mathrm{QED}}_{\mathrm{HD}^+} \ , \tag{6.13}$$

adding a fraction of $\delta g_e(0,0)^{\mathrm{QED}}_{\mathrm{HD}^+}$ to the uncertainty for each increase in v [72]. The higher-order QED term is not expected to vary much from one MHI isotopologues to the next. Therefore, $g_e(v,N)_{\mathrm{H}_2^+}$ can be obtained as well, by:

$$g_e(v,N)_{\mathrm{H}_2^+} \simeq g_e(v,N)^{\mathrm{th}}_{\mathrm{H}_2^+} + \delta g_e(0,0)^{\mathrm{QED}}_{\mathrm{HD}^+} \ . \tag{6.14}$$

7 Conclusion

In the work of this thesis, it has been demonstrated that the Penning-trap experiment ALPHATRAP can be used for high-precision measurements of the properties of MHI. Specifically, the possibility to load MHI from an external ion source and to confine the ions for several months was demonstrated. The internal quantum state of the MHI was determined via MW-induced resonant eSFs coupled with the CSGE in the strong magnetic bottle of the AT [3]. For HD^+, this allowed verification of the rovibrational ground state along with which of the 12 hyperfine and Zeeman sublevels was populated. After an unforeseen increase in BBR, this method allowed to verify the population of the first rotationally excited state, along with which of the 36 hyperfine and Zeeman sublevels was populated, by eSFs driven at the frequencies of these states.

This non-destructive state determination allowed to track changes of the hyperfine, Zeeman and rotational level of a single HD^+ ion for several months. State changes were either due to intentional Zeeman transitions (electron spin flips) induced by resonant MW radiation or due to random rotational excitations driven by BBR which occasionally resulted in a change of a nuclear spin orientation in the subsequent decay to the rovibrational ground state. A measurement scheme was implemented to address the nuclear spin orientation, by resonant MW-induced HFS transitions changing the electron and nuclear spin orientation.

In the HFS measurement campaign, the non-destructive state detection was used for a high-precision measurement of all six eSF transitions in the rovibrational ground state of HD^+. This resulted in the experimental determination of the bound-electron g factor and the hyperfine coefficients characterizing the strength of the electron-and-proton and electron-and-deuteron spin-spin interactions: $g_e(0,0)$, $E_4(0,0)$, and $E_5(0,0)$, respectively. The experimental values of this thesis work along with the currently published respective theoretical predictions are listed in Tab. 5.2. For data evaluation, I set up the explicit matrix form of the effective Hamiltonian describing the HFS and Zeeman splitting of HD^+ for the rotational quantum number $N = 0$ (Eq. 2.7) in the high field basis, see Appendix A.1.

The $g_e(0,0)$ factor was determined to 0.20 ppb relative precision and agrees with the theoretical prediction within the 0.1 ppm uncertainty of the latter. This is the first experimental determination of a g_e factor of HD^+ and the most precise experimental determination of a molecular g_e factor so far. For comparison, g_e of H_2^+ has been experimentally determined to 0.09 ppm precision for a selection of vibrational states [80]. The precision of the experimental value $g_e(0,0)$ of this work surpasses the precision of the state-of-the-art theoretical values at the time of the measurements by almost three orders of magnitude [4]. This measurement demonstrates a method for high-precision g factor determination of molecular systems for tests of QED calculations in the molecular regime.

The experimental $g_e(0,0)$ results can be used to enhance the prediction of g_e-factor values in other rovibrational states as well as for other MHI isotopologues, such as H_2^+,

by extracting uncalculated higher-order QED terms of $g_e(0,0)$ of HD^+ as the difference between the experimental and theoretical result. These higher-order terms are expected to vary only weakly from one rovibrational level to the next as well as from one isotopologue to the next. On the theoretical side, there is ongoing work to improve the precision of the theoretical prediction of the g_e factor of HD^+ and H_2^+ by about three orders of magnitude by calculation of higher-order QED terms. The publication of the calculations along with high-precision g_e theory values is in preparation and a preliminary comparison has revealed agreement between the experimental results of this work and the new theoretical work, within the then dominating experimental uncertainty [72]. This will enable a more stringent test of g_e-factor calculations by orders of magnitude, and thus orders of QED, than previously possible in molecular systems. The good agreement of the g_e factor with theory, affirms the reliability of the experimental results and the theoretical calculations. The improvement of the prediction of g_e in MHI and its experimental verification is important for unambiguous nondestructive state detection by eSFs in $H_2^+/\overline{H_2^+}$, see Sec. 6.5.3.

The spin-spin coupling coefficients of the HFS of HD^+ in the rovibrational ground state, $E_4(0,0)$ and $E_5(0,0)$, were determined to 41 Hz and 22 Hz uncertainty, corresponding to 44 ppb and 151 ppb, respectively, and show a slight 2 and 3 σ tension to the theoretical prediction. The precision surpasses previous experimental determination by approximately 5 and 4 orders of magnitude, respectively [79], see Sec. 2.2 and the state-of-the-art theoretical values by factors of 20 and 4, respectively [63], see Tab. 5.2. Interestingly, for both $E_4(0,0)$ and $E_5(0,0)$, our measured values are 1.7 ppm larger than the theoretical values.

The uncertainties of the results of this work are more than an order of magnitude smaller than for measurements of spin-spin interaction HFS coefficients of H_2^+ [77], see Sec. 2.2. Also here, the experimental values are larger than the theoretical values, by 0.5-1 ppm. Recent rovibrational spectroscopy of HD^+ [73, 74, 75, 35] has also tested HFS calculations [63], without the explicit determination of HFS coefficients, down to the 0.32-kHz level [75]. However, while some show agreement with theory within their experimental uncertainties, others deviate by up to $9\,\sigma$ [5].

With the near-agreement between the measurement results of this work and their theoretical predictions, we can confirm that HFS-theory predictions for E coefficients hold in the rovibrational ground state. Assuming correct treatment of the vibrational dependence of the E coefficients, the slight tension between the E coefficients determined in this work and their theoretical prediction is an order of magnitude too small, to explain the deviation seen between HFS theory and one of the rovibrational measurements [5]. Following this assumption, the $E_4(0,0)$ and $E_5(0,0)$ values of this work can be combined with *ab initio* theory [63] to reduce the uncertainty of these coefficients for other rovibrational states of HD^+, an important benefit for future rovibrational studies. For example, a reduced uncertainty in the HFS prediction may allow to reduce the number of hyperfine components that are necessary to be measured in rovibrational spectroscopy for the determination of the spin-averaged transition frequencies [120].

Furthermore, the experimental uncertainties of this work are small enough to be sensitive to the higher-order non-recoil QED contribution to E_4, a vibrational contribution, for the first time [63]. Once a more stringent agreement between the experimental and theoretical values is reached, this contribution could be resolved and potentially experimentally verified. Moreover, the close proximity of the nuclei in the molecule enables sensitivity to potential beyond SM spin-dependent forces between nuclei. Once a more precise HFS theory becomes

available, the experimental results of the HFS of this work can be used to set upper bounds on their existence [120].

In the upgrade of the setup, the implemented features not only aim to reduce systematic effects and the time per measurement cycle in general, by increasing the signal strength in the AT, increasing the temporal magnetic field stability, allowing in-situ tuning of the magnetic field inhomogeneity, and potentially reducing the drift of the axial frequency after changing trap voltages. They additionally aim to improve the feasibility of future laser spectroscopy of rovibrational states in MHI, by defining a dedicated trapping region with an excitation line addressing the nuclear spin orientation and a resonator to couple directly to the modified cyclotron mode and by adding a window to the cryovalve and changing the bottom windows of the trap to CaF_2 for broader spectral transmission in the IR range.

The work towards rovibrational spectroscopy of HD^+, included the addition of a laser system for Hz-level line widths at 1.15 μm wavelengths by the collaboration with Prof. Stephan Schiller's group from the Heinrich-Heine University Düsseldorf and subsequent alignment through the trap. Furthermore, there are ongoing efforts towards the prediction of the rovibrational transitions frequencies in the 4-T magnetic field of our trap and towards increasing the achievable Rabi rates for spectroscopy in the trap environment. Currently, first data has been collected on eSF transitions in the first rotationally excited state of HD^+ in the AT and the PT. The AT data demonstrates the nondestructive state detection outside of the rovibrational ground state. The PT data demonstrates the possibility for high-precision spectroscopy of eSF transitions in excited rovibrational states. This can lead to experimental values for the scaling of g_e, E_4, E_5 with N (and possibly v) and for the anisotropic shift of the g_e factor in excited rovibrational states as well as for E_1 and other smaller HFS coefficients.

Outlook

As an outlook, let's consider the feasibility of $\overline{H}_2^-$ measurements in Penning traps. The first step towards a possible measurement of $\overline{H}_2^-$ after its production is trapping the externally-produced MHI in the Penning trap, as antiprotons require high-energy accelerators for production and are thus currently only obtainable from the antiproton decelerator at CERN. Therefore, a Penning-trap setup would either have to be placed there or receive ions from a transportable trap which are currently in development [151, 152]. Due to the estimated low production rates, see Sec. 6.5.2 there will not be many $\overline{H}_2^-$ ions available for measurements. Thus, extremely good vacuum conditions, ensuring the ion would not annihilate due to collisions with residual gas, for long confinement times and nondestructive state detection coupled with the possibility of high-precision spectroscopy are essential. In the work of this thesis, these steps have been demonstrated for MW spectroscopy of a MHI (HD^+) and efforts are being made towards laser spectroscopy.

To switch from H_2^+ to its antimatter counterpart in a future Penning-trap measurement, no changes are required to either the apparatus or the spectroscopy sources, except for the change of the polarity of the voltages applied to the trap electrodes. In particular, compared to possible nondestructive quantum logic spectroscopy of a single MHI in an RF Paul trap [41, 42], this technique would not depend on a co-trapped auxiliary 'logic' ion, which would cause distinct difficulties when working with the negatively charged $\overline{H}_2^-$.

Summary

In summary, in the work of this thesis nondestructive internal quantum state detection of a single MHI was demonstrated along with external production and month-long confinement in a Penning trap. These techniques can be applied to other molecular ions with non-zero electron spin. This contributes to the field of research based on quantum state control and precision measurements of molecular ions which is actively pursued by novel experiments [153, 154, 155].

The demonstrated techniques were applied for the high-precision determination of $g_e(0,0)$, $E_4(0,0)$, and $E_5(0,0)$ of HD^+ by MW spectroscopy. Furthermore, the work of this thesis focused on developments towards single-ion, high-precision rovibrational spectroscopy in Penning traps. Such measurements can not only be used for QED tests, the determination of fundamental constants, or for probing physics beyond the SM [35, 70, 33], but additionally for, in my opinion a very noteworthy physics case and one for which Penning traps promise to be highly advantageous systems, the high-precision comparison of the rovibrational energies of H_2^+ and its antimatter counterpart $\overline{H}_2^-$ for tests of CPT symmetry violation [1, 2].

List of Publications

Tank-Circuit Assisted Coupling Method for Sympathetic Laser Cooling, B. Tu, F. Hahne, I. Arapoglou, A. Egl, F. Heiße, M. Höcker, C. König, J. Morgner, T. Sailer, A. Weigel, R. Wolf, and S. Sturm, Adv. Quantum Technol., **4**: 2100029, 2021. [138]

Measurement of the bound-electron g-factor difference in coupled ions, T. Sailer, V. Debierre, Z. Harman, F. Heiße, C. König, J. Morgner, B. Tu, A. V. Volotka, C. H. Keitel, K. Blaum, and S. Sturm, Nature **606**, 479-483 (2022). [156]

Stringent test of QED with hydrogen-like tin, J. Morgner, B. Tu, C. M. König., T. Sailer, F. Heiße, H. Bekker, B. Sikora, C. Lyu, V. A. Yerokhin, Z. Harman, J. R. Crespo López-Urrutia, C. H. Keitel, S. Sturm, and K. Blaum, Nature **622**, 53-57 (2023). [43]
The research briefing: **Testing the limits of the standard model of particle physics with a heavy, highly charged ion**, Charlotte M. König and Fabian Heiße, https://www.nature.com/articles/d41586-023-02620-7 (2023)

High-Precision Determination of g Factors and Masses of $^{20}Ne^{9+}$ and $^{22}Ne^{9+}$, F. Heiße, M. Door, T. Sailer, P. Filianin, J. Herkenhoff, C. M. König., K. Kromer, D. Lange, J. Morgner, A. Rischka, C.. Schweiger, B. Tu, Y.N. Novikov, S. Eliseev, S. Sturm, and K. Blaum, Phys. Rev. Lett. **131**, 253002 (2023). [157]

Listening to electrons talk: g-factor measurement of lithium-like tin, J. Morgner, V. A. Yerokhin, C. M. König, F. Heiße, B. Tu, T. Sailer, B. Sikora, Z. Harman, J. Crespo López-Urrutia, C. H. Keitel, S. Sturm, K. Blaum, *submitted*

g Factor of Boron-like Sn, J. Morgner, B. Tu, C. M. König, F. Heiße, T. Sailer, M. Moretti, B. Sikora, N. S. Oreshkina, V. A. Yerokhin, Z. Harman, C. H. Keitel, S. Sturm, and K. Blaum, *accepted, Phys. Rev. Lett.*

Nondestructive Control of the Rovibrational Ground State of a Single Molecular Hydrogen Ion in a Penning Trap, C. M. König, F. Heiße, J. Morgner, T. Sailer, B. Tu, D. Bakalov, K. Blaum, S. Schiller and S. Sturm, *submitted*

Hyperfine Spectroscopy of a Single HD^+ Molecular Ion in a Penning Trap, C. M. König, F. Heiße, J. Morgner, H. D. Nogueira, T. Sailer, B. Tu, D. Bakalov, K. Blaum, J.-P. Karr, O. Kullie, S. Schiller and S. Sturm, *in preparation*

A Appendix

A.1 Explicit Matrices for HFS Hamiltonians of MHI

The procedure for setting up the explicit matrix form of the HFS Hamiltonians (Sec. 2.1.2) follows the steps laid out in the Feynman lectures on Physics, volume III, chapter 12: 'The Hyperfine Splitting in Hydrogen' [158]. In the following all matrices and vectors are given in bold font. Vectors are additionally marked with an arrow and · indicates the scalar product of two vectors.

A.1.1 Hyperfine Structure and Zeeman Effect in HD^+ in the Rotational Ground State

In this section I will explain how I set up the matrix from of $\boldsymbol{H}^{\mathrm{HD}^+}_{total}(v,0)$, Eq. 2.7, given again below:

$$\begin{aligned}\boldsymbol{H}^{\mathrm{HD}^+}_{total}(v,0) =& hE_4(v,0)(\vec{\boldsymbol{I}}_{\boldsymbol{p}} \cdot \vec{\boldsymbol{s}}_{\boldsymbol{e}}) + hE_5(v,0)(\vec{\boldsymbol{I}}_{\boldsymbol{d}} \cdot \vec{\boldsymbol{s}}_{\boldsymbol{e}}) - \mu_B g_e(v,0)(\vec{\boldsymbol{B}} \cdot \vec{\boldsymbol{s}}_{\boldsymbol{e}}) \\ & - \mu_B g_p(v,0)(\vec{\boldsymbol{B}} \cdot \vec{\boldsymbol{I}}_{\boldsymbol{p}}) - \mu_B g_d(v,0)(\vec{\boldsymbol{B}} \cdot \vec{\boldsymbol{I}}_{\boldsymbol{d}}) \ .\end{aligned} \tag{A.1}$$

As the structure of the Hamiltonian remains the same for all $(v, N = 0)$ states, the matrix form is valid for any of these states as well. From here on, the dependence of the Hamiltonian, the E coefficients, and g factors will not be given explicitly anymore.

Basis

The explicit matrix form in the weak-field basis has been published [58][1]. Since the measurements were carried out at 4 T, thus far in the Paschen-Back regime, the matrix form was set up in the in the high-field basis as well. The bases are introduced in Sec 2.1.2. For the high-field basis the 12 levels are ordered by their energies at large magnetic fields. Thus, the lowest lying state with approximate quantum numbers $m_s = -\frac{1}{2}, m_{I,p} = +\frac{1}{2}, m_{I,d} = +1$, is defined as basis state $|1\rangle$:

$$|1\rangle = |-,+,+\rangle = \left\{ \begin{pmatrix} 0 \\ 1 \end{pmatrix}_e, \begin{pmatrix} 1 \\ 0 \end{pmatrix}_p, \begin{pmatrix} 1 \\ 0 \\ 0 \end{pmatrix}_d \right\} \ . \tag{A.2}$$

[1] While the matrix form was available in the collaboration before its publication (2023), this was not yet the case at the start of the measurement campaign mid-2021.

HD^+ $(v,0)$		H_2^+ $(v,2)$	
$\|1\rangle$	$\|-,+,+\rangle$	$\|1\rangle$	$\|-,++\rangle$
$\|2\rangle$	$\|-,+,0\rangle$	$\|2\rangle$	$\|-,+\rangle$
$\|3\rangle$	$\|-,+,-\rangle$	$\|3\rangle$	$\|-,0\rangle$
$\|4\rangle$	$\|-,-,+\rangle$	$\|4\rangle$	$\|-,-\rangle$
$\|5\rangle$	$\|-,-,0\rangle$	$\|5\rangle$	$\|-,--\rangle$
$\|6\rangle$	$\|-,-,-\rangle$	$\|6\rangle$	$\|+,--\rangle$
$\|7\rangle$	$\|+,-,-\rangle$	$\|7\rangle$	$\|+,-\rangle$
$\|8\rangle$	$\|+,-,0\rangle$	$\|8\rangle$	$\|+,0\rangle$
$\|9\rangle$	$\|+,-,+\rangle$	$\|9\rangle$	$\|+,+\rangle$
$\|10\rangle$	$\|+,+,-\rangle$	$\|10\rangle$	$\|+,++\rangle$
$\|11\rangle$	$\|+,+,0\rangle$		
$\|12\rangle$	$\|+,+,+\rangle$		

Table A.1: HFS basis states of the high-field basis for HD^+ in $(v,0)$ states and H_2^+ in $(v,2)$ states. Each state is defined by the projections of the approximate magnetic quantum numbers of the HFs state with respect to the external magnetic field m_s, $m_{I,p}$, $m_{I,d}$ and m_s, m_N, respectively.

The basis states are defined by the projections of the approximate quantum numbers of the states with respect to the external magnetic field, see Fig 2.2. Table A.1 lists the 12 basis states.

Matrix and Eigenvalues

Following Eq. A.1, the Hamiltonian for the hyperfine structure for $N = 0$ states in the absence of a magnetic field is given as:

$$\boldsymbol{H}_{\mathrm{HFS}} = hE_4 \vec{\boldsymbol{s}}_{\boldsymbol{e}} \cdot \vec{\boldsymbol{I}}_{\boldsymbol{p}} + hE_5 \vec{\boldsymbol{s}}_{\boldsymbol{e}} \cdot \vec{\boldsymbol{I}}_{\boldsymbol{d}} \ . \tag{A.3}$$

Writing out the scalar products of the spin operators gives:

$$\boldsymbol{H}_{\mathrm{HFS}} = hE_4 \sum_{i=x,y,z} (\boldsymbol{s_{e,i} I_{p,i}}) + hE_5 \sum_{i=x,y,z} (\boldsymbol{s_{e,i} I_{d,i}}) \tag{A.4}$$

Adding the magnetic field as $\vec{B} = B_z e_z$ gives:

$$\boldsymbol{H}_{\mathrm{total}} = \boldsymbol{H}_{HFS} + \boldsymbol{H}_{Zeeman} \ , \tag{A.5}$$

with

$$\boldsymbol{H}_{\mathrm{Zeeman}} = -\mu_B B_z (g_e \boldsymbol{s_{e,z}} + g_p \boldsymbol{I_{p,z}} + g_d \boldsymbol{I_{d,z}}) \ . \tag{A.6}$$

The spin operator matrices for spin $\frac{1}{2}$ (electron, proton) and spin 1 (deuteron) are [159]:

$$\boldsymbol{s}_{e,x} = \boldsymbol{I}_{p,x} = \frac{1}{2}\begin{pmatrix} 0 & 1 \\ 1 & 0 \end{pmatrix}, \boldsymbol{s}_{e,y} = \boldsymbol{I}_{p,y} = \frac{1}{2}\begin{pmatrix} 0 & -i \\ i & 0 \end{pmatrix}, \boldsymbol{s}_{e,z} = \boldsymbol{I}_{p,z} = \frac{1}{2}\begin{pmatrix} 1 & 0 \\ 0 & -1 \end{pmatrix} \tag{A.7}$$

$$\boldsymbol{I}_{d,x} = \frac{1}{\sqrt{2}} \begin{pmatrix} 0 & 1 & 0 \\ 1 & 0 & 1 \\ 0 & 1 & 0 \end{pmatrix}, \boldsymbol{I}_{d,y} = \frac{1}{\sqrt{2}} \begin{pmatrix} 0 & -i & 0 \\ i & 0 & -i \\ 0 & i & 0 \end{pmatrix}, \boldsymbol{I}_{d,z} = \begin{pmatrix} 1 & 0 & 0 \\ 0 & 0 & 0 \\ 0 & 0 & -1 \end{pmatrix} \quad \text{(A.8)}$$

Computing all 144 matrix elements $\langle i|H_{total}|j\rangle$ gives the total Hamiltonian in matrix form, luckily most terms are zero:

.

$$\boldsymbol{H}_{total} = \frac{h}{2} \begin{pmatrix} H_{11} & 0 & 0 & 0 & 0 & 0 & 0 & 0 & 0 & 0 & 0 & 0 & 0 & 0 & 0 & 0 \\ 0 & H_{22} & 0 & 0 & 0 & 0 & 0 & 0 & 0 & 0 & 0 & 0 & 0 & 0 & 0 & 0 \\ 0 & 0 & H_{33} & 0 & 0 & 0 & 0 & 0 & 0 & 0 & 0 & 0 & 0 & 0 & 0 & 0 \\ 0 & 0 & 0 & H_{44} & 0 & 0 & 0 & 0 & 0 & 0 & 0 & 0 & 0 & 0 & 0 & 0 \\ 0 & 0 & 0 & 0 & H_{55} & 0 & 0 & 0 & 0 & 0 & 0 & 0 & 0 & 0 & 0 & 0 \\ 0 & 0 & 0 & 0 & 0 & H_{66} & 0 & 0 & 0 & 0 & 0 & 0 & 0 & 0 & 0 & 0 \\ 0 & 0 & 0 & 0 & 0 & 0 & H_{77} & 0 & 0 & 0 & 0 & 0 & 0 & 0 & 0 & 0 \\ 0 & 0 & 0 & 0 & 0 & 0 & 0 & H_{88} & 0 & 0 & 0 & 0 & 0 & 0 & 0 & 0 \\ E_4 & 0 & 0 & 0 & 0 & 0 & 0 & 0 & H_{99} & 0 & 0 & 0 & 0 & 0 & 0 & 0 \\ 0 & E_4 & 0 & 0 & 0 & 0 & 0 & 0 & 0 & H_{1010} & 0 & 0 & 0 & 0 & 0 & 0 \\ 0 & 0 & E_4 & 0 & 0 & 0 & 0 & 0 & 0 & 0 & H_{1111} & 0 & 0 & 0 & 0 & 0 \\ 0 & \sqrt{2}E_5 & 0 & 0 & 0 & 0 & 0 & 0 & 0 & 0 & 0 & H_{1212} & 0 & 0 & 0 & 0 \\ \sqrt{2}E_5 & 0 & 0 & 0 & 0 & 0 & 0 & 0 & 0 & 0 & 0 & 0 & H_{1313} & 0 & 0 & 0 \\ 0 & \sqrt{2}E_5 & 0 & 0 & 0 & 0 & 0 & 0 & 0 & 0 & 0 & 0 & 0 & H_{1414} & 0 & 0 \\ 0 & 0 & \sqrt{2}E_5 & 0 & 0 & 0 & 0 & 0 & 0 & 0 & 0 & 0 & 0 & 0 & H_{1515} & 0 \\ 0 & 0 & 0 & \sqrt{2}E_5 & 0 & 0 & 0 & 0 & 0 & 0 & 0 & 0 & 0 & 0 & 0 & H_{1616} \end{pmatrix} \quad \text{(A.9)}$$

The diagonal entries are given by:

$$H_{11} = -\frac{hE_4}{2} - hE_5 - \mu_B B(-g_{e,HD} + g_{p,HD} + 2g_{d,HD}) \tag{A.10}$$

$$H_{22} = -\frac{hE_4}{2} - \mu_B B(-g_{e,HD} + g_{p,HD}) \tag{A.11}$$

$$H_{33} = -\frac{hE_4}{2} + hE_5 - \mu_B B(-g_{e,HD} + g_{p,HD} - 2g_{d,HD}) \tag{A.12}$$

$$H_{44} = \frac{hE_4}{2} - hE_5 - \mu_B B(-g_{e,HD} - g_{p,HD} + 2g_{d,HD}) \tag{A.13}$$

$$H_{55} = \frac{hE_4}{2} - \mu_B B(-g_{e,HD} - g_{p,HD}) \tag{A.14}$$

$$H_{66} = \frac{hE_4}{2} + hE_5 - \mu_B B(-g_{e,HD} - g_{p,HD} - 2g_{d,HD}) \tag{A.15}$$

$$H_{77} = -\frac{hE_4}{2} - hE_5 - \mu_B B(g_{e,HD} - g_{p,HD} - 2g_{d,HD}) \tag{A.16}$$

$$H_{88} = -\frac{hE_4}{2} - \mu_B B(g_{e,HD} - g_{p,HD}) \tag{A.17}$$

$$H_{99} = -\frac{hE_4}{2} + hE_5 - \mu_B B(g_{e,HD} - g_{p,HD} + 2g_{d,HD}) \tag{A.18}$$

$$H_{1010} = \frac{hE_4}{2} - hE_5 - \mu_B B(g_{e,HD} + g_{p,HD} - 2g_{d,HD}) \tag{A.19}$$

$$H_{1111} = \frac{hE_4}{2} - \mu_B B(g_{e,HD} + g_{p,HD}) \tag{A.20}$$

$$H_{1212} = \frac{hE_4}{2} + hE_5 - \mu_B B(g_{e,HD} + g_{p,HD} + 2g_{d,HD}) \tag{A.21}$$

The traceless of the matrix can be confirmed by the sum of all 12 eigenvalues equaling zero.

Since the matrix has many zero entries and thus not all rows are correlated, it is possible to write it in separate smaller matrices. Rows 6 and 12 contain only the diagonal term and therefore directly give the two eigenvalues of the stretched states by '1x1' matrices $\boldsymbol{H}(6)$ and $\boldsymbol{H}(12)$. Rows 1,9,11 and rows 3,5,7 form a 3x3 matrix each ($\boldsymbol{H}(1,9,11)$ and

matrix	m_F
$\boldsymbol{H}(6)$	-2
$\boldsymbol{H}(12)$	+2
$\boldsymbol{H}(1,9,11)$	+1
$\boldsymbol{H}(3,5,7)$	-1
$\boldsymbol{H}(2,4,8,10)$	0

Table A.2: Separation of the HFS Hamiltonian matrices for HD^+ for the possible values of the total angular moment projection with respect to the external magnetic field.

$\boldsymbol{H}(3,5,7)$) and rows 2,4,8,10 a 4x4 matrix ($\boldsymbol{H}(2,4,8,10)$):

$$\boldsymbol{H}(6) = \frac{1}{2} H_{66} \tag{A.22}$$

$$\boldsymbol{H}(12) = \frac{1}{2} H_{1212} \tag{A.23}$$

$$\boldsymbol{H}(1,9,11) = \frac{1}{2} \begin{pmatrix} H_{11} & E_4 & \sqrt{2}E_5 \\ E_4 & H_{99} & 0 \\ \sqrt{2}E_5 & 0 & H_{1111} \end{pmatrix} \tag{A.24}$$

$$\boldsymbol{H}(3,5,7) = \frac{1}{2} \begin{pmatrix} H_{33} & 0 & E_4 \\ 0 & H_{55} & \sqrt{2}E_5 \\ E_4 & \sqrt{2}E_5 & H_{77} \end{pmatrix} \tag{A.25}$$

$$\boldsymbol{H}(2,4,8,10) = \frac{1}{2} \begin{pmatrix} H_{22} & 0 & E_4 & \sqrt{2}E_5 \\ 0 & H_{44} & \sqrt{2}E_5 & 0 \\ E_4 & \sqrt{2}E_5 & H_{88} & 0 \\ \sqrt{2}E_5 & 0 & 0 & H_{1010} \end{pmatrix} \tag{A.26}$$

The level energies can be obtained by numerically solving for the eigenvalues of the matrices and the transition energies by subtracting the level energies accordingly. Solving for the eigenvalues of both the high-field and the low-field matrices leads to the same result and therefore confirms that the matrices are the same only written in different bases.

Note, these matrices separate the eigenstates into $m_F = \sum_i m_i$ values, where m_F is the total angular moment projection with respect to the external field, see Tab. A.2.

A.1.2 HFS and Zeeman Splitting in H_2^+

The same procedure described above for HD^+ was applied for the HFS of $(v, N = 0)$ and $(v, N = 2)$ in H_2^+. The even values of N require nuclear spin $I = 0$. Following Eqs. 2.3 and 2.5, the $N = 0$ case is trivial as all terms in $\boldsymbol{H}^{H_2^+}_{HFS}(v,0)$ are zero and therefore:

$$\boldsymbol{H}^{H_2^+}_{total}(v,0) = \boldsymbol{H}^{H_2^+}_{Zeeman}(v,0) = -\mu_B g_e(v,0)(\vec{\boldsymbol{B}} \cdot \vec{\boldsymbol{s}}_{\boldsymbol{e}}) \ . \tag{A.27}$$

The $(v,0)$ states of H_2^+ have no HFS and in $\vec{\boldsymbol{B}} = B_z e_z$ are split in two Zeeman states $m_s = \pm\frac{1}{2}$ with energies give by:

$$Eig(1,2) = \pm\frac{1}{2} g_e(v,0)\mu_B B_z \ . \tag{A.28}$$

For $N = 2$ states, the HFS and Zeeman Hamiltonian is given by:

$$\boldsymbol{H}^{\mathsf{H}_2^+}_{total}(v,2) = hc_e(v,2)(\vec{\boldsymbol{N}} \cdot \vec{\boldsymbol{s}}_{\boldsymbol{e}}) - \mu_B g_e(v,2)(\vec{\boldsymbol{B}} \cdot \vec{\boldsymbol{s}}_{\boldsymbol{e}}) - \mu_B g_N(v,2)(\vec{\boldsymbol{B}} \cdot \vec{\boldsymbol{N}}) \ . \quad \text{(A.29)}$$

The spin operator matrices for spin $\frac{1}{2}$ (electron) is given above (Eq. A.7) and for spin 2 (rotation) are given by: [159]

$$\boldsymbol{N}_x = \frac{1}{2}\begin{pmatrix} 0 & 2 & 0 & 0 & 0 \\ 2 & 0 & \sqrt{6} & 0 & 0 \\ 0 & \sqrt{6} & 0 & \sqrt{6} & 0 \\ 0 & 0 & \sqrt{6} & 0 & 2 \\ 0 & 0 & 0 & 2 & 0 \end{pmatrix}, \quad \text{(A.30)}$$

$$\boldsymbol{N}_y = \frac{1}{2i}\begin{pmatrix} 0 & 2 & 0 & 0 & 0 \\ -2 & 0 & \sqrt{6} & 0 & 0 \\ 0 & -\sqrt{6} & 0 & \sqrt{6} & 0 \\ 0 & 0 & -\sqrt{6} & 0 & 2 \\ 0 & 0 & 0 & -2 & 0 \end{pmatrix}, \quad \text{(A.31)}$$

$$\boldsymbol{N}_z = \begin{pmatrix} 2 & 0 & 0 & 0 & 0 \\ 0 & 1 & 0 & 0 & 0 \\ 0 & 0 & 0 & 0 & 0 \\ 0 & 0 & 0 & -1 & 0 \\ 0 & 0 & 0 & 0 & -2 \end{pmatrix} \ . \quad \text{(A.32)}$$

Again using the basis depending on the projection of the orientation of the angular momentum with respect to the external magnetic field ($\vec{B} = B_z e_z$) and ordering the basis states by their energies at 4 T, the lowest lying state $m_s = -\frac{1}{2}$, $m_N = +2$ can be written as:

$$|1\rangle = |-,++\rangle = \left\{ \begin{pmatrix} 0 \\ 1 \end{pmatrix}_e, \begin{pmatrix} 1 \\ 0 \\ 0 \\ 0 \end{pmatrix}_d \right\} \ . \quad \text{(A.33)}$$

A full list of the basis states is given in Tab A.1.

Following the same procedure as for HD^+ leads to two 1x1 and four 2x2 matrices for the ten eigenstates, again this separates the eigenstates into $m_F = \sum_i m_i$ values, where m_F is the total angular moment projection with respect to the external field. The dependence

of the coefficients on the rovibrational state is not explicitly written:

$$\boldsymbol{H}(5) = hc_e + \left(\frac{1}{2}g_e + 2g_N\right)\mu_B B \tag{A.34}$$

$$\boldsymbol{H}(10) = hc_e - \left(\frac{1}{2}g_e + 2g_N\right)\mu_B B \tag{A.35}$$

$$\boldsymbol{H}(4,6) = \begin{pmatrix} \frac{1}{2}hc_e + \left(\frac{1}{2}g_e + g_N\right)\mu_B B & hc_e \\ hc_e & -hc_e - \left(\frac{1}{2}g_e - 2g_N\right)\mu_B B \end{pmatrix} \tag{A.36}$$

$$\boldsymbol{H}(3,7) = \begin{pmatrix} \frac{1}{2}g_e\mu_B B & \frac{\sqrt{6}}{2}hc_e \\ \frac{\sqrt{6}}{2}hc_e & -\frac{1}{2}hc_e - \left(\frac{1}{2}g_e - g_N\right)\mu_B B \end{pmatrix} \tag{A.37}$$

$$\boldsymbol{H}(2,8) = \begin{pmatrix} -\frac{1}{2}hc_e + \left(\frac{1}{2}g_e - g_N\right)\mu_B B & \frac{\sqrt{6}}{2}hc_e \\ \frac{\sqrt{6}}{2}hc_e & -\frac{1}{2}g_e\mu_B B \end{pmatrix} \tag{A.38}$$

$$\boldsymbol{H}(1,9) = \begin{pmatrix} -hc_e + \left(\frac{1}{2}g_e - 2g_N\right)\mu_B B & hc_e \\ hc_e & \frac{1}{2}hc_e - \left(\frac{1}{2}g_e + g_N\right)\mu_B B \end{pmatrix} . \tag{A.39}$$

Since the matrices here are at most of dimension 2x2, they can be solved analytically. For example, the eigenvalues of $\boldsymbol{H}(3,7)$ are:

$$Eig(3,7) = -\frac{1}{4}hc_e + \frac{1}{2}\mu_B B g_N \mp \sqrt{\left(\frac{5}{4}hc_e + \frac{1}{2}\mu_B B(g_e - g_N)\right)^2 - hc_e\mu_B B(g_e - g_N)} . \tag{A.40}$$

A.2 Confirming the $^{40}Ar^{13+}$ g Factor

In the previous measurement of the bound-electron g factor of $^{40}Ar^{13+}$, the theoretical prediction ($g_{e,th} = 0.66364812(58)$) had an uncertainty of 0.87 ppm [160]. At the ∼37 GHz eSF frequency, this uncertainty covers the eSF transition as well as possible sidebands of the magnetron motion (∼10 kHz). Previously, this had not been considered. To cross check that the carrier was indeed measured and not a motional sideband, $^{40}Ar^{13+}$ was reloaded and the assumed carrier and magnetron sidebands were probed. Note, that this required a different MW setup than for HD^+ (Fig. 4.10), since the frequency is in a different range. In this campaign, we used the same MW generator both directly and with a frequency doubler and amplifier. For the measurement, the same procedure was used as in Ioanna Arapoglou's work [116].

If the previous measurement had studied a sideband at $\nu_{\mathrm{eSF,old}}$, a higher spin-flip probability would be expected at the carrier $\nu_{\mathrm{eSF,old}} \pm \nu_-$ compared to the second sideband $\nu_{\mathrm{eSF,old}} \mp \nu_-$.

210 data points were taken at the assumed carrier and 82 and 88 at either magnetron motional sideband at varying MW power. Overall, for the assumed carrier a 22(3)% spin-flip probability was measured, while only 1 and 2 (2(3)%, 1(3)%) spin flips were observed at the sideband frequencies. This verifies the correctness of the previous measurement and shows that there are no strong magnetron sidebands for this measurement.

A.3 Values and Constants

For completeness and reproducibility, all values and constants used in the evaluation of measurement data are listed.

constant	value
m_{HD^+}	3.021378241561 u [83]
u (unit mass)	$1.66053906660 \cdot 10^{-27}$ kg[59]
e	$1.602176634 \cdot 10^{-19}$ C[59]
μ_B/h	$1.39962449171 \cdot 10^{10}$ Hz/T[59]
μ_n/h	$7.6225932188 \cdot 10^{6}$ Hz/T[59]
c	299792458 m/s [59]
k_B	$1.380649 \cdot 10^{-23}$ J/K [59]
h	$6.62607015 \cdot 10^{-34}$ J/Hz [59]
ϵ_0	$8.8541878188 \cdot 10^{-12}$ F/m [59]
g_e (free electron)	-2.00231930436092[59]
g_p (free electron)	$3.04206440050 \cdot 10^{-3}$[59]
g_d (free deuteron)	$4.669754562 \cdot 10^{-4}$[59]

Table A.3: Constants and values used in the evaluation of measurement data.

Bibliography

[1] H. Dehmelt, Economic synthesis and precision spectroscopy of anti-molecular hydrogen ions in Paul trap, Physica Scripta 1995 (T59) (1995) 423. doi:10.1088/0031-8949/1995/T59/060. p. V, 3, 7, 106

[2] E. G. Myers, CPT tests with the antihydrogen molecular ion, Phys. Rev. A 98 (2018) 010101. doi:10.1103/PhysRevA.98.010101. p. V, 3, 7, 9, 15, 101, 106

[3] H. Dehmelt, Continuous Stern-Gerlach effect: Principle and idealized apparatus, Proc. Natl. Acad. Sci. USA 83 (1986) 2291–2294. doi:10.1073/pnas.83.8.2291. p. V, 40, 103

[4] R. A. Hegstrom, g factors and related magnetic properties of molecules. Formulation of theory and calculations for H_2^+, HD^+, and D_2^+, Phys. Rev. A 19 (1979) 17–30. doi:10.1103/PhysRevA.19.17. p. V, 14, 15, 59, 69, 80, 85, 94, 103

[5] M. Haidar, V. I. Korobov, L. Hilico, J.-P. Karr, Higher-order corrections to the spin-orbit and spin-spin tensor interactions in HD^+, Phys. Rev. A 106 (2022) 042815. doi:10.1103/PhysRevA.106.042815. p. V, 4, 11, 16, 80, 104

[6] M. Tanabashi, K. Hagiwara, K. Hikasa, K. Nakamura, Y. Sumino, F. Takahashi, J. Tanaka, K. Agashe, G. Aielli, C. Amsler, M. Antonelli, D. M. Asner, H. Baer, S. Banerjee, R. M. Barnett, T. Basaglia, C. W. Bauer, J. J. Beatty, V. I. Belousov, J. Beringer, S. Bethke, A. Bettini, H. Bichsel, O. Biebel, K. M. Black, E. Blucher, O. Buchmuller, V. Burkert, M. A. Bychkov, R. N. Cahn, M. Carena, A. Ceccucci, A. Cerri, D. Chakraborty, M.-C. Chen, R. S. Chivukula, G. Cowan, O. Dahl, G. D'Ambrosio, T. Damour, D. de Florian, A. de Gouvêa, T. DeGrand, P. de Jong, G. Dissertori, B. A. Dobrescu, M. D'Onofrio, M. Doser, M. Drees, H. K. Dreiner, D. A. Dwyer, P. Eerola, S. Eidelman, J. Ellis, J. Erler, V. V. Ezhela, W. Fetscher, B. D. Fields, R. Firestone, B. Foster, A. Freitas, H. Gallagher, L. Garren, H.-J. Gerber, G. Gerbier, T. Gershon, Y. Gershtein, T. Gherghetta, A. A. Godizov, M. Goodman, C. Grab, A. V. Gritsan, C. Grojean, D. E. Groom, M. Grünewald, A. Gurtu, T. Gutsche, H. E. Haber, C. Hanhart, S. Hashimoto, Y. Hayato, K. G. Hayes, A. Hebecker, S. Heinemeyer, B. Heltsley, J. J. Hernández-Rey, J. Hisano, A. Höcker, J. Holder, A. Holtkamp, T. Hyodo, K. D. Irwin, K. F. Johnson, M. Kado, M. Karliner, U. F. Katz, S. R. Klein, E. Klempt, R. V. Kowalewski, F. Krauss, M. Kreps, B. Krusche, Y. V. Kuyanov, Y. Kwon, O. Lahav, J. Laiho, J. Lesgourgues, A. Liddle, Z. Ligeti, C.-J. Lin, C. Lippmann, T. M. Liss, L. Littenberg, K. S. Lugovsky, S. B. Lugovsky, A. Lusiani, Y. Makida, F. Maltoni, T. Mannel, A. V. Manohar,

W. J. Marciano, A. D. Martin, A. Masoni, J. Matthews, U.-G. Meißner, D. Milstead, R. E. Mitchell, K. Mönig, P. Molaro, F. Moortgat, M. Moskovic, H. Murayama, M. Narain, P. Nason, S. Navas, M. Neubert, P. Nevski, Y. Nir, K. A. Olive, S. Pagan Griso, J. Parsons, C. Patrignani, J. A. Peacock, M. Pennington, S. T. Petcov, V. A. Petrov, E. Pianori, A. Piepke, A. Pomarol, A. Quadt, J. Rademacker, G. Raffelt, B. N. Ratcliff, P. Richardson, A. Ringwald, S. Roesler, S. Rolli, A. Romaniouk, L. J. Rosenberg, J. L. Rosner, G. Rybka, R. A. Ryutin, C. T. Sachrajda, Y. Sakai, G. P. Salam, S. Sarkar, F. Sauli, O. Schneider, K. Scholberg, A. J. Schwartz, D. Scott, V. Sharma, S. R. Sharpe, T. Shutt, M. Silari, T. Sjöstrand, P. Skands, T. Skwarnicki, J. G. Smith, G. F. Smoot, S. Spanier, H. Spieler, C. Spiering, A. Stahl, S. L. Stone, T. Sumiyoshi, M. J. Syphers, K. Terashi, J. Terning, U. Thoma, R. S. Thorne, L. Tiator, M. Titov, N. P. Tkachenko, N. A. Törnqvist, D. R. Tovey, G. Valencia, R. Van de Water, N. Varelas, G. Venanzoni, L. Verde, M. G. Vincter, P. Vogel, A. Vogt, S. P. Wakely, W. Walkowiak, C. W. Walter, D. Wands, D. R. Ward, M. O. Wascko, G. Weiglein, D. H. Weinberg, E. J. Weinberg, M. White, L. R. Wiencke, S. Willocq, C. G. Wohl, J. Womersley, C. L. Woody, R. L. Workman, W.-M. Yao, G. P. Zeller, O. V. Zenin, R.-Y. Zhu, S.-L. Zhu, F. Zimmermann, P. A. Zyla, J. Anderson, L. Fuller, V. S. Lugovsky, P. Schaffner, Review of particle physics, Phys. Rev. D 98 (2018) 030001. doi:10.1103/PhysRevD.98.030001. p. 1, 2

[7] M. Dine, A. Kusenko, Origin of the matter-antimatter asymmetry, Rev. Mod. Phys. 76 (2003) 1–30. doi:10.1103/RevModPhys.76.1. p. 1, 2

[8] P. J. E. Peebles, B. Ratra, The cosmological constant and dark energy, Rev. Mod. Phys. 75 (2003) 559–606. doi:10.1103/RevModPhys.75.559. p. 1

[9] W. E. Lamb, R. C. Retherford, Fine structure of the hydrogen atom by a microwave method, Phys. Rev. 72 (1947) 241–243. doi:10.1103/PhysRev.72.241. p. 2

[10] X. Fan, T. G. Myers, B. A. D. Sukra, G. Gabrielse, Measurement of the electron magnetic moment, Phys. Rev. Lett. 130 (2023) 071801. doi:10.1103/PhysRevLett.130.071801. p. 2, 4, 19

[11] D. P. Aguillard, T. Albahri, D. Allspach, A. Anisenkov, K. Badgley, S. Baeßler, I. Bailey, L. Bailey, V. A. Baranov, E. Barlas-Yucel, T. Barrett, E. Barzi, F. Bedeschi, M. Berz, M. Bhattacharya, H. P. Binney, P. Bloom, J. Bono, E. Bottalico, T. Bowcock, S. Braun, M. Bressler, G. Cantatore, R. M. Carey, B. C. K. Casey, D. Cauz, R. Chakraborty, A. Chapelain, S. Chappa, S. Charity, C. Chen, M. Cheng, R. Chislett, Z. Chu, T. E. Chupp, C. Claessens, M. E. Convery, S. Corrodi, L. Cotrozzi, J. D. Crnkovic, S. Dabagov, P. T. Debevec, S. Di Falco, G. Di Sciascio, B. Drendel, A. Driutti, V. N. Duginov, M. Eads, A. Edmonds, J. Esquivel, M. Farooq, R. Fatemi, C. Ferrari, M. Fertl, A. T. Fienberg, A. Fioretti, D. Flay, S. B. Foster, H. Friedsam, N. S. Froemming, C. Gabbanini, I. Gaines, M. D. Galati, S. Ganguly, A. Garcia, J. George, L. K. Gibbons, A. Gioiosa, K. L. Giovanetti, P. Girotti, W. Gohn, L. Goodenough, T. Gorringe, J. Grange, S. Grant, F. Gray, S. Haciomeroglu, T. Halewood-Leagas, D. Hampai, F. Han, J. Hempstead, D. W. Hertzog, G. Hesketh, E. Hess, A. Hibbert, Z. Hodge, K. W. Hong, R. Hong, T. Hu, Y. Hu, M. Iacovacci, M. Incagli,

P. Kammel, M. Kargiantoulakis, M. Karuza, J. Kaspar, D. Kawall, L. Kelton, A. Keshavarzi, D. S. Kessler, K. S. Khaw, Z. Khechadoorian, N. V. Khomutov, B. Kiburg, M. Kiburg, O. Kim, N. Kinnaird, E. Kraegeloh, V. A. Krylov, N. A. Kuchinskiy, K. R. Labe, J. LaBounty, M. Lancaster, S. Lee, B. Li, D. Li, L. Li, I. Logashenko, A. Lorente Campos, Z. Lu, A. Lucà, G. Lukicov, A. Lusiani, A. L. Lyon, B. MacCoy, R. Madrak, K. Makino, S. Mastroianni, J. P. Miller, S. Miozzi, B. Mitra, J. P. Morgan, W. M. Morse, J. Mott, A. Nath, J. K. Ng, H. Nguyen, Y. Oksuzian, Z. Omarov, R. Osofsky, S. Park, G. Pauletta, G. M. Piacentino, R. N. Pilato, K. T. Pitts, B. Plaster, D. Počanić, N. Pohlman, C. C. Polly, J. Price, B. Quinn, M. U. H. Qureshi, S. Ramachandran, E. Ramberg, R. Reimann, B. L. Roberts, D. L. Rubin, L. Santi, C. Schlesier, A. Schreckenberger, Y. K. Semertzidis, D. Shemyakin, M. Sorbara, D. Stöckinger, J. Stapleton, D. Still, C. Stoughton, D. Stratakis, H. E. Swanson, G. Sweetmore, D. A. Sweigart, M. J. Syphers, D. A. Tarazona, T. Teubner, A. E. Tewsley-Booth, V. Tishchenko, N. H. Tran, W. Turner, E. Valetov, D. Vasilkova, G. Venanzoni, V. P. Volnykh, T. Walton, A. Weisskopf, L. Welty-Rieger, P. Winter, Y. Wu, B. Yu, M. Yucel, Y. Zeng, C. Zhang, Measurement of the Positive Muon Anomalous Magnetic Moment to 0.20 ppm, Phys. Rev. Lett. 131 (2023) 161802. doi:10.1103/PhysRevLett.131.161802. p. 2

[12] D. P. Aguillard, T. Albahri, D. Allspach, A. Anisenkov, K. Badgley, S. Baeßler, I. Bailey, L. Bailey, V. A. Baranov, E. Barlas-Yucel, T. Barrett, E. Barzi, F. Bedeschi, M. Berz, M. Bhattacharya, H. P. Binney, P. Bloom, J. Bono, E. Bottalico, T. Bowcock, S. Braun, M. Bressler, G. Cantatore, R. M. Carey, B. C. K. Casey, D. Cauz, R. Chakraborty, A. Chapelain, S. Chappa, S. Charity, C. Chen, M. Cheng, R. Chislett, Z. Chu, T. E. Chupp, C. Claessens, M. E. Convery, S. Corrodi, L. Cotrozzi, J. D. Crnkovic, S. Dabagov, P. T. Debevec, S. Di Falco, G. Di Sciascio, S. Donati, B. Drendel, A. Driutti, V. N. Duginov, M. Eads, A. Edmonds, J. Esquivel, M. Farooq, R. Fatemi, C. Ferrari, M. Fertl, A. T. Fienberg, A. Fioretti, D. Flay, S. B. Foster, H. Friedsam, N. S. Froemming, C. Gabbanini, I. Gaines, M. D. Galati, S. Ganguly, A. Garcia, J. George, L. K. Gibbons, A. Gioiosa, K. L. Giovanetti, P. Girotti, W. Gohn, L. Goodenough, T. Gorringe, J. Grange, S. Grant, F. Gray, S. Haciomeroglu, T. Halewood-Leagas, D. Hampai, F. Han, J. Hempstead, D. W. Hertzog, G. Hesketh, E. Hess, A. Hibbert, Z. Hodge, K. W. Hong, R. Hong, T. Hu, Y. Hu, M. Iacovacci, M. Incagli, P. Kammel, M. Kargiantoulakis, M. Karuza, J. Kaspar, D. Kawall, L. Kelton, A. Keshavarzi, D. S. Kessler, K. S. Khaw, Z. Khechadoorian, N. V. Khomutov, B. Kiburg, M. Kiburg, O. Kim, N. Kinnaird, E. Kraegeloh, V. A. Krylov, N. A. Kuchinskiy, K. R. Labe, J. LaBounty, M. Lancaster, S. Lee, B. Li, D. Li, L. Li, I. Logashenko, A. Lorente Campos, Z. Lu, A. Lucà, G. Lukicov, A. Lusiani, A. L. Lyon, B. MacCoy, R. Madrak, K. Makino, S. Mastroianni, J. P. Miller, S. Miozzi, B. Mitra, J. P. Morgan, W. M. Morse, J. Mott, A. Nath, J. K. Ng, H. Nguyen, Y. Oksuzian, Z. Omarov, R. Osofsky, S. Park, G. Pauletta, G. M. Piacentino, R. N. Pilato, K. T. Pitts, B. Plaster, D. Počanić, N. Pohlman, C. C. Polly, J. Price, B. Quinn, M. U. H. Qureshi, S. Ramachandran, E. Ramberg, R. Reimann, B. L. Roberts, D. L. Rubin, M. Sakurai, L. Santi, C. Schlesier, A. Schreckenberger, Y. K. Semertzidis, D. Shemyakin, M. Sorbara, J. Stapleton, D. Still, D. Stöckinger, C. Stoughton, D. Stratakis, H. E. Swanson, G. Sweetmore, D. A. Sweigart, M. J. Syphers, D. A. Tarazona, T. Teubner, A. E. Tewsley-Booth, V. Tishchenko, N. H. Tran, W. Turner,

E. Valetov, D. Vasilkova, G. Venanzoni, V. P. Volnykh, T. Walton, A. Weisskopf, L. Welty-Rieger, P. Winter, Y. Wu, B. Yu, M. Yucel, Y. Zeng, C. Zhang, Detailed report on the measurement of the positive muon anomalous magnetic moment to 0.20 ppm, Phys. Rev. D 110 (2024) 032009. doi:10.1103/PhysRevD.110.032009. p. 2

[13] A. Boccaletti, S. Borsanyi, M. Davier, Z. Fodor, F. Frech, A. Gerardin, D. Giusti, A. Y. Kotov, L. Lellouch, T. Lippert, A. Lupo, B. Malaescu, S. Mutzel, A. Portelli, A. Risch, M. Sjo, F. Stokes, K. K. Szabo, B. C. Toth, G. Wang, Z. Zhang, High precision calculation of the hadronic vacuum polarisation contribution to the muon anomaly (2024). arXiv:2407.10913, doi:10.48550/arXiv.2407.10913. p. 2

[14] A. D. Sakharov, Violation of CP in variance, asymmetry, and baryon asymmetry of the universe, JETP Lett. 5 (1967) 24–27.
URL http://jetpletters.ru/ps/1643/article_25089.pdf p. 2

[15] V. Andreev, D. G. Ang, D. DeMille, J. M. Doyle, G. Gabrielse, J. Haefner, N. R. Hutzler, Z. Lasner, C. Meisenhelder, B. R. O'Leary, C. D. Panda, A. D. West, E. P. West, X. Wu, ACME Collaboration, Improved limit on the electric dipole moment of the electron, Nature 562 (2018) 355–360. doi:10.1038/s41586-018-0599-8. p. 2

[16] P. Aggarwal, H. L. Bethlem, A. Borschevsky, M. Denis, K. Esajas, P. A. B. Haase, Y. Hao, S. Hoekstra, K. Jungmann, T. B. Meijknecht, M. C. Mooij, R. G. E. Timmermans, W. Ubachs, L. Willmann, A. Zapara, The NL-eEDM collaboration, Measuring the electric dipole moment of the electron in BaF, The European Physical Journal D 72 (2018) 197. doi:10.1140/epjd/e2018-90192-9. p. 2

[17] N. J. Fitch, J. Lim, E. A. Hinds, B. E. Sauer, M. R. Tarbutt, Methods for measuring the electron's electric dipole moment using ultracold YbF molecules, Quantum Science and Technology 6 (2020) 014006. doi:10.1088/2058-9565/abc931. p. 2

[18] T. S. Roussy, L. Caldwell, T. Wright, W. B. Cairncross, Y. Shagam, K. B. Ng, N. Schlossberger, S. Y. Park, A. Wang, J. Ye, E. A. Cornell, An improved bound on the electron's electric dipole moment, Science 381 (6653) (2023) 46–50. doi:10.1126/science.adg4084. p. 2

[19] E. Widmann, C. Amsler, S. Arguedas Cuendis, H. Breuker, M. Diermaier, P. Dupré, C. Evans, M. Fleck, A. Gligorova, H. Higaki, Y. Kanai, B. Kolbinger, N. Kuroda, M. Leali, A. M. M. Leite, V. Mäckel, C. Malbrunot, V. Mascagna, O. Massiczek, Y. Matsuda, D. J. Murtagh, Y. Nagata, A. Nanda, D. Phan, C. Sauerzopf, M. C. Simon, M. Tajima, H. Spitzer, M. Strube, S. Ulmer, L. Venturelli, M. Wiesinger, Y. Yamazaki, J. Zmeskal, Hyperfine spectroscopy of hydrogen and antihydrogen in ASACUSA, Hyperfine Interactions 240 (1) (2018) 5. doi:10.48550/arXiv.1809.00875. p. 2

[20] C. Smorra, S. Sellner, M. J. Borchert, J. A. Harrington, T. Higuchi, H. Nagahama, T. Tanaka, A. Mooser, G. Schneider, M. Bohman, K. Blaum, Y. Matsuda,

C. Ospelkaus, W. Quint, J. Walz, Y. Yamazaki, S. Ulmer, A parts-per-billion measurement of the antiproton magnetic moment, Nature 550 (7676) (2017) 371–374. doi:10.1038/nature24048. p. 2

[21] M. J. Borchert, J. A. Devlin, S. R. Erlewein, M. Fleck, J. A. Harrington, T. Higuchi, B. M. Latacz, F. Voelksen, E. J. Wursten, F. Abbass, M. A. Bohman, A. H. Mooser, D. Popper, M. Wiesinger, C. Will, K. Blaum, Y. Matsuda, C. Ospelkaus, W. Quint, J. Walz, Y. Yamazaki, C. Smorra, S. Ulmer, A 16-parts-per-trillion measurement of the antiproton-to-proton charge-mass ratio, Nature 601 (7891) (2022) 53–57. doi:10.1038/s41586-021-04203-w. p. 2, 9, 58

[22] M. Hori, H. Aghai-Khozani, A. Sótér, D. Barna, A. Dax, R. Hayano, T. Kobayashi, Y. Murakami, K. Todoroki, H. Yamada, D. Horváth, L. Venturelli, Buffer-gas cooling of antiprotonic helium to 1.5 to 1.7 k, and antiproton-to–electron mass ratio, Science 354 (6312) (2016) 610–614. doi:10.1126/science.aaf6702. p. 2, 9

[23] P. Moskal, A. Gajos, M. Mohammed, J. Chhokar, N. Chug, C. Curceanu, E. Czerwiński, M. Dadgar, K. Dulski, M. Gorgol, J. Goworek, B. C. Hiesmayr, B. Jasińska, K. Kacprzak, Ł. Kapłon, H. Karimi, D. Kisielewska, K. Klimaszewski, G. Korcyl, P. Kowalski, N. Krawczyk, W. Krzemień, T. Kozik, E. Kubicz, S. Niedźwiecki, S. Parzych, M. Pawlik-Niedźwiecka, L. Raczyński, J. Raj, S. Sharma, S. Choudhary, R. Y. Shopa, A. Sienkiewicz, M. Silarski, M. Skurzok, E. Ł. Stępień, F. Tayefi, W. Wiślicki, Testing CPT symmetry in ortho-positronium decays with positronium annihilation tomography, Nature Communications 12 (1) (2021) 5658. doi:10.1038/s41467-021-25905-9. p. 2

[24] C. Amole, G. Andresen, M. Ashkezari, M. Baquero-Ruiz, W. Bertsche, P. Bowe, E. Butler, A. Capra, P. Carpenter, C. Cesar, S. Chapman, M. Charlton, A. Deller, S. Eriksson, J. Escallier, J. Fajans, T. Friesen, M. Fujiwara, D. Gill, A. Gutierrez, J. Hangst, W. Hardy, R. Hayano, M. Hayden, A. Humphries, J. Hurt, R. Hydomako, C. Isaac, M. Jenkins, S. Jonsell, L. Jørgensen, S. Kerrigan, L. Kurchaninov, N. Madsen, A. Marone, J. McKenna, S. Menary, P. Nolan, K. Olchanski, A. Olin, B. Parker, A. Povilus, P. Pusa, F. Robicheaux, E. Sarid, D. Seddon, S. Seif El Nasr, D. Silveira, C. So, J. Storey, R. Thompson, J. Thornhill, D. Wells, D. van der Werf, J. Wurtele, Y. Yamazaki, The ALPHA antihydrogen trapping apparatus, NIM-A 735 (2014) 319–340. doi:10.1016/j.nima.2013.09.043. p. 2, 19

[25] M. Ahmadi, B. X. R. Alves, C. J. Baker, W. Bertsche, E. Butler, A. Capra, C. Carruth, C. L. Cesar, M. Charlton, S. Cohen, R. Collister, S. Eriksson, A. Evans, N. Evetts, J. Fajans, T. Friesen, M. C. Fujiwara, D. R. Gill, A. Gutierrez, J. S. Hangst, W. N. Hardy, M. E. Hayden, C. A. Isaac, A. Ishida, M. A. Johnson, S. A. Jones, S. Jonsell, L. Kurchaninov, N. Madsen, M. Mathers, D. Maxwell, J. T. K. McKenna, S. Menary, J. M. Michan, T. Momose, J. J. Munich, P. Nolan, K. Olchanski, A. Olin, P. Pusa, C. Ø. Rasmussen, F. Robicheaux, R. L. Sacramento, M. Sameed, E. Sarid, D. M. Silveira, S. Stracka, G. Stutter, C. So, T. D. Tharp, J. E. Thompson, R. I. Thompson, D. P. van der Werf, J. S. Wurtele, Observation of the hyperfine spectrum of antihydrogen, Nature 548 (7665) (2017) 66–69. doi:10.1038/nature23446. p. 2

[26] M. Ahmadi, B. X. R. Alves, C. J. Baker, W. Bertsche, A. Capra, C. Carruth, C. L. Cesar, M. Charlton, S. Cohen, R. Collister, S. Eriksson, A. Evans, N. Evetts, J. Fajans, T. Friesen, M. C. Fujiwara, D. R. Gill, J. S. Hangst, W. N. Hardy, M. E. Hayden, C. A. Isaac, M. A. Johnson, J. M. Jones, S. A. Jones, S. Jonsell, A. Khramov, P. Knapp, L. Kurchaninov, N. Madsen, D. Maxwell, J. T. K. McKenna, S. Menary, T. Momose, J. J. Munich, K. Olchanski, A. Olin, P. Pusa, C. Ø. Rasmussen, F. Robicheaux, R. L. Sacramento, M. Sameed, E. Sarid, D. M. Silveira, G. Stutter, C. So, T. D. Tharp, R. I. Thompson, D. P. van der Werf, J. S. Wurtele, Characterization of the 1S-2S transition in antihydrogen, Nature 557 (7703) (2018) 71–75. doi:10.1038/s41586-018-0017-2. p. 2, 9

[27] M. Ahmadi, B. X. R. Alves, C. J. Baker, W. Bertsche, A. Capra, C. Carruth, C. L. Cesar, M. Charlton, S. Cohen, R. Collister, S. Eriksson, A. Evans, N. Evetts, J. Fajans, T. Friesen, M. C. Fujiwara, D. R. Gill, P. Granum, J. S. Hangst, W. N. Hardy, M. E. Hayden, E. D. Hunter, C. A. Isaac, M. A. Johnson, J. M. Jones, S. A. Jones, S. Jonsell, A. Khramov, P. Knapp, L. Kurchaninov, N. Madsen, D. Maxwell, J. T. K. McKenna, S. Menary, J. M. Michan, T. Momose, J. J. Munich, K. Olchanski, A. Olin, P. Pusa, C. Ø. Rasmussen, F. Robicheaux, R. L. Sacramento, M. Sameed, E. Sarid, D. M. Silveira, C. So, D. M. Starko, G. Stutter, T. D. Tharp, R. I. Thompson, D. P. van der Werf, J. S. Wurtele, The ALPHA Collaboration, Investigation of the fine structure of antihydrogen, Nature 578 (7795) (2020) 375–380. p. 2

[28] M. Arzano, J. Kowalski-Glikman, W. Wiślicki, A bound on planck-scale deformations of cpt from muon lifetime, Physics Letters B 794 (2019) 41–44. doi:10.1016/j.physletb.2019.05.025. p. 2

[29] R. Bluhm, V. A. Kostelecký, C. D. Lane, CPT and lorentz tests with muons, Phys. Rev. Lett. 84 (2000) 1098–1101. doi:10.1103/PhysRevLett.84.1098. p. 3

[30] B. Quinn, Cpt- and lorentz-violation tests with muon g-2 (2019). arXiv:1907.00162. p. 3

[31] S. Acharya, D. Adamová, A. Adler, J. Adolfsson, G. Aglieri Rinella, M. Agnello, N. Agrawal, Z. Ahammed, S. Ahmad, S. U. Ahn, I. Ahuja, Z. Akbar, A. Akindinov, M. Al-Turany, S. N. Alam, D. Aleksandrov, B. Alessandro, H. M. Alfanda, R. Alfaro Molina, B. Ali, Y. Ali, A. Alici, N. Alizadehvandchali, A. Alkin, J. Alme, G. Alocco, T. Alt, I. Altsybeev, M. N. Anaam, C. Andrei, D. Andreou, A. Andronic, V. Anguelov, F. Antinori, P. Antonioli, C. Anuj, N. Apadula, L. Aphecetche, H. Appelshäuser, S. Arcelli, R. Arnaldi, I. C. Arsene, M. Arslandok, A. Augustinus, R. Averbeck, S. Aziz, M. D. Azmi, A. Badalá, Y. W. Baek, X. Bai, R. Bailhache, Y. Bailung, R. Bala, A. Balbino, A. Baldisseri, B. Balis, D. Banerjee, Z. Banoo, R. Barbera, L. Barioglio, M. Barlou, G. G. Barnaföldi, L. S. Barnby, V. Barret, C. Bartels, K. Barth, E. Bartsch, F. Baruffaldi, N. Bastid, S. Basu, G. Batigne, D. Battistini, B. Batyunya, D. Bauri, J. L. Bazo Alba, I. G. Bearden, C. Beattie, P. Becht, I. Belikov, A. D. C. Bell Hechavarria, F. Bellini, R. Bellwied, S. Belokurova, V. Belyaev, G. Bencedi, S. Beole, A. Bercuci, Y. Berdnikov, A. Berdnikova, L. Bergmann, M. G. Besoiu, L. Betev, P. P. Bhaduri, A. Bhasin, I. R. Bhat, M. A. Bhat, B. Bhattacharjee,

P. Bhattacharya, L. Bianchi, N. Bianchi, J. Bielčik, J. Bielčikova, J. Biernat, A. Bilandzic, G. Biro, S. Biswas, J. T. Blair, D. Blau, M. B. Blidaru, C. Blume, G. Boca, F. Bock, A. Bogdanov, S. Boi, J. Bok, L. Boldizsár, A. Bolozdynya, M. Bombara, P. M. Bond, G. Bonomi, H. Borel, A. Borissov, H. Bossi, E. Botta, L. Bratrud, P. Braun-Munzinger, M. Bregant, M. Broz, G. E. Bruno, M. D. Buckland, D. Budnikov, H. Buesching, S. Bufalino, O. Bugnon, P. Buhler, Z. Buthelezi, J. B. Butt, A. Bylinkin, S. A. Bysiak, M. Cai, H. Caines, A. Caliva, E. Calvo Villar, J. M. M. Camacho, R. S. Camacho, P. Camerini, F. D. M. Canedo, M. Carabas, F. Carnesecchi, R. Caron, J. Castillo Castellanos, E. A. R. Casula, F. Catalano, C. Ceballos Sanchez, I. Chakaberia, P. Chakraborty, S. Chandra, S. Chapeland, M. Chartier, S. Chattopadhyay, S. Chattopadhyay, T. G. Chavez, T. Cheng, C. Cheshkov, B. Cheynis, V. Chibante Barroso, D. D. Chinellato, S. Cho, P. Chochula, P. Christakoglou, C. H. Christensen, P. Christiansen, T. Chujo, C. Cicalo, L. Cifarelli, F. Cindolo, M. R. Ciupek, G. Clai, J. Cleymans, F. Colamaria, J. S. Colburn, D. Colella, A. Collu, M. Colocci, M. Concas, G. Conesa Balbastre, Z. Conesa del Valle, G. Contin, J. G. Contreras, M. L. Coquet, T. M. Cormier, P. Cortese, M. R. Cosentino, F. Costa, S. Costanza, P. Crochet, R. Cruz-Torres, E. Cuautle, P. Cui, L. Cunqueiro, A. Dainese, M. C. Danisch, A. Danu, P. Das, P. Das, S. Das, S. Dash, A. De Caro, G. de Cataldo, L. De Cilladi, J. de Cuveland, A. De Falco, D. De Gruttola, N. De Marco, C. De Martín, S. De Pasquale, S. Deb, H. F. Degenhardt, K. R. Deja, R. Del Grande, L. Dello Stritto, W. Deng, P. Dhankher, D. Di Bari, A. Di Mauro, R. A. Diaz, T. Dietel, Y. Ding, R. Diviá, D. U. Dixit, Ø. Djuvsland, U. Dmitrieva, J. Do, A. Dobrin, B. Dönigus, A. K. Dubey, A. Dubla, S. Dudi, P. Dupieux, M. Durkac, N. Dzalaiova, T. M. Eder, R. J. Ehlers, V. N. Eikeland, F. Eisenhut, D. Elia, B. Erazmus, F. Ercolessi, F. Erhardt, A. Erokhin, M. R. Ersdal, B. Espagnon, G. Eulisse, D. Evans, S. Evdokimov, L. Fabbietti, M. Faggin, J. Faivre, F. Fan, W. Fan, A. Fantoni, M. Fasel, P. Fecchio, A. Feliciello, G. Feofilov, A. Fernández Téllez, A. Ferrero, A. Ferretti, V. J. G. Feuillard, J. Figiel, V. Filova, D. Finogeev, F. M. Fionda, G. Fiorenza, F. Flor, A. N. Flores, S. Foertsch, S. Fokin, E. Fragiacomo, E. Frajna, A. Francisco, U. Fuchs, N. Funicello, C. Furget, A. Furs, J. J. Gaardhøje, M. Gagliardi, A. M. Gago, A. Gal, C. D. Galvan, P. Ganoti, C. Garabatos, J. R. A. Garcia, E. Garcia-Solis, K. Garg, C. Gargiulo, A. Garibli, K. Garner, P. Gasik, The ALICE Collaboration, Measurement of anti-3He nuclei absorption in matter and impact on their propagation in the Galaxy, Nature Physics 19 (1) (2023) 61–71. doi:10.1038/s41567-022-01804-8. p. 3

[32] R. N. Hill, Proof that the H^- Ion Has Only One Bound State, Phys. Rev. Lett. 38 (1977) 643–646. doi:10.1103/PhysRevLett.38.643. p. 3

[33] S. Schiller, J.-P. Karr, Prospects for the determination of fundamental constants with beyond-state-of-the-art uncertainty using molecular hydrogen ion spectroscopy, Phys. Rev. A 109 (2024) 042825. doi:10.1103/PhysRevA.109.042825. p. 3, 7, 106

[34] V. I. Korobov, J.-P. Karr, Rovibrational spin-averaged transitions in the hydrogen molecular ions, Phys. Rev. A 104 (2021) 032806. doi:10.1103/PhysRevA.104.032806. p. 3, 7, 9

[35] S. Alighanbari, I. V. Kortunov, G. S. Giri, S. Schiller, Test of charged baryon interaction with high-resolution vibrational spectroscopy of molecular hydrogen ions, Nat. Phys. 19 (2023) 1263–1269. doi:10.1038/s41567-023-02088-2. p. 3, 7, 9, 15, 77, 78, 85, 97, 104, 106

[36] M. Germann, S. Patra, J.-P. Karr, L. Hilico, V. I. Korobov, E. J. Salumbides, K. S. E. Eikema, W. Ubachs, J. C. J. Koelemeij, Three-body QED test and fifth-force constraint from vibrations and rotations of HD^+, Phys. Rev. Research 3 (2021) L022028. doi:10.1103/physrevresearch.3.l022028. p. 3, 7, 9, 15

[37] M. R. Schenkel, S. Alighanbari, S. Schiller, Laser spectroscopy of a rovibrational transition in the molecular hydrogen ion H_2^+, Nat. Phys. 20 (2024) 383–388. doi:10.1038/s41567-023-02320-z. p. 3, 9, 16

[38] J.-P. Karr, H_2^+ and HD^+: Candidates for a molecular clock, J. Mol. Spectrosc 300 (2014) 37–43. doi:10.1016/j.jms.2014.03.016. p. 3, 7, 9

[39] S. Schiller, D. Bakalov, V. I. Korobov, Simplest Molecules as Candidates for Precise Optical Clocks, Phys. Rev. Lett. 113 (2014) 023004. doi:10.1103/PhysRevLett.113.023004. p. 3, 7, 9

[40] C. Wellers, M. R. Schenkel, G. S. Giri, K. R. Brown, S. Schiller, Controlled preparation and vibrational excitation of single ultracold molecular hydrogen ions, Molecular Physics 120 (19-20) (2022) e2001599. doi:10.1080/00268976.2021.2001599. p. 3, 16

[41] N. Schwegler, D. Holzapfel, M. Stadler, A. Mitjans, I. Sergachev, J. P. Home, D. Kienzler, Trapping and Ground-State Cooling of a Single H_2^+, Phys. Rev. Lett. 131 (2023) 133003. doi:10.1103/PhysRevLett.131.133003. p. 3, 16, 105

[42] D. Holzapfel, F. Schmid, N. Schwegler, O. Stadler, M. Stadler, A. Ferk, J. P. Home, D. Kienzler, Quantum control of a single H_2^+ molecular ion (2024). arXiv:2409.06495. p. 3, 16, 92, 105

[43] J. Morgner, B. Tu, C. M. König, T. Sailer, F. Heiße, H. Bekker, B. Sikora, C. Lyu, V. A. Yerokhin, Z. Harman, J. R. Crespo López-Urrutia, C. H. Keitel, S. Sturm, K. Blaum, Stringent test of QED with hydrogen-like tin, Nature 622 (2023) 53–57. doi:10.1038/s41586-023-06453-2. p. 4, 19, 36, 107

[44] S. G. Karshenboim, Precision physics of simple atoms: QED tests, nuclear structure and fundamental constants, Physics Reports 422 (1) (2005) 1–63. doi:10.1016/j.physrep.2005.08.008. p. 4

[45] A. Schneider, B. Sikora, S. Dickopf, M. Müller, N. S. Oreshkina, A. Rischka, I. A. Valuev, S. Ulmer, J. Walz, Z. Harman, C. H. Keitel, A. Mooser, K. Blaum, Direct measurement of the $^3He^+$ magnetic moments, Nature 606 (7916) (2022) 878–883. doi:10.1038/s41586-022-04761-7. p. 4, 47

[46] S. Dickopf, B. Sikora, A. Kaiser, M. Müller, S. Ulmer, V. A. Yerokhin, Z. Harman, C. H. Keitel, A. Mooser, K. Blaum, Precision spectroscopy on 9Be overcomes limitations from nuclear structure, Nature 632 (8026) (2024) 757–761. doi:10.1038/s41586-024-07795-1. p. 4

[47] BIMP, CIPM, CCU, The International System of Units (SI) (2019). URL https://www.bipm.org/documents/20126/41483022/SI-Brochure-9-EN.pdf p. 4

[48] S. Sturm, I. Arapoglou, A. Egl, M. Höcker, S. Kraemer, T. Sailer, B. Tu, A. Weigel, R. Wolf, J. Crespo López-Urrutia, K. Blaum, The ALPHATRAP experiment, Eur. Phys. J. Special Topics 227 (2019) 1425–1491. doi:10.1140/epjst/e2018-800225-2. p. 5, 19, 20, 25, 26, 29, 33, 36, 39, 40, 44, 53, 55, 64

[49] M. C. Zammit, M. Charlton, S. Jonsell, J. Colgan, J. S. Savage, D. V. Fursa, A. S. Kadyrov, I. Bray, R. C. Forrey, C. J. Fontes, J. A. Leiding, D. P. Kilcrease, P. Hakel, E. Timmermans, Laser-driven production of the antihydrogen molecular ion, Phys. Rev. A 100 (2019) 042709. doi:10.1103/PhysRevA.100.042709. p. 7, 101

[50] J. Taylor, B. Vargo, D. Hoffman, T. J. Price, R. C. Forrey, Formation of antihydrogen molecular ions by associative ionization, Phys. Rev. A 109 (2024) 052816. doi:10.1103/PhysRevA.109.052816. p. 7, 101

[51] A. Carrington, I. R. McNab, C. A. Montgomerie, R. A. Kennedy, Electronic spectrum ($2p\sigma_u$ -$1s\sigma_g$) of the D_2^+ ion, Molecular Physics 67 (4) (1989) 711–738. doi:10.1080/00268978900101401. p. 7

[52] G. Hunter, A. W. Yau, H. O. Pritchard, Rotation-vibration level energies of the hydrogen and deuterium molecule-ions, Atomic Data and Nuclear Data Tables 14 (1) (1974) 11–20. doi:10.1016/S0092-640X(74)80027-6. p. 7, 8, 10

[53] D. R. Bates, K. Ledsham, A. L. Stewart, Wave functions of the hydrogen molecular ion, Philosophical Transactions of the Royal Society of London. Series A, Mathematical and Physical Sciences 246 (1953) 215–240. doi:10.1098/rsta.1953.0014. p. 8

[54] S. Alighanbari, private communication. p. 8

[55] R. Moss, Calculations for vibration-rotation levels of HD^+, in particular for high n, Molecular Physics 78 (2) (1993) 371–405. doi:10.1080/00268979300100291. p. 8, 78

[56] H. Olivares Pilón, D. Baye, Dipole transitions in the bound rotational-vibrational spectrum of the heteronuclear molecular ion HD^+, Phys. Rev. A 88 (2013) 032502. doi:10.1103/PhysRevA.88.032502. p. 8, 9, 10, 78, 79

[57] H. O. Pilón, D. Baye, Quadrupole transitions in the bound rotational–vibrational spectrum of the hydrogen molecular ion, J. Phys. B: At. Mol. Opt. Phys. 45 (2012) 065101. doi:10.1088/0953-4075/45/6/065101. p. 8, 9, 10

[58] S. Schiller, Precision spectroscopy of molecular hydrogen ions: an introduction, Contemporary Physics 63 (2023) 247–279. doi:10.1080/00107514.2023.2180180. p. 9, 10, 12, 14, 85, 102, 109

[59] CODATA 2022 (2024).
URL https://pml.nist.gov/cuu/Constants/ p. 9, 12, 14, 15, 80, 94, 116

[60] I. R. M. A. D. J. Critchley, A. N. Hughes, R. E. Moss, Energy shifts and forbidden transitions in H_2^+ due to electronic g/u symmetry breaking, Molecular Physics 101 (4-5) (2003) 651–661. doi:10.1080/0026897021000021886. p. 10

[61] V. I. Korobov, L. Hilico, J.-P. Karr, Hyperfine structure in the hydrogen molecular ion, Phys. Rev. A 74 (2006) 040502. doi:10.1103/PhysRevA.74.040502. p. 11, 102

[62] D. Bakalov, V. I. Korobov, S. Schiller, High-Precision Calculation of the Hyperfine Structure of the HD^+ Ion, Phys. Rev. Lett. 97 (2006) 243001. doi:10.1103/PhysRevLett.97.243001. p. 11, 14, 80

[63] J.-P. Karr, M. Haidar, L. Hilico, Z.-X. Zhong, V. I. Korobov, Higher-order corrections to spin-spin scalar interactions in HD^+ and H_2^+, Phys. Rev. A 102 (2020) 052827. doi:10.1103/PhysRevA.102.052827. p. 11, 14, 16, 69, 80, 104

[64] V. I. Korobov, Precision Spectroscopy of the Hydrogen Molecular Ions: Present Status of Theory and Experiment, Physics of Particles and Nuclei 53 (2022) 787–789. doi:10.1134/S1063779622040086. p. 11, 75

[65] J.-P. Karr, V. I. Korobov, L. Hilico, Vibrational spectroscopy of $H_2{}^+$: Precise evaluation of the zeeman effect, Phys. Rev. A 77 (2008) 062507. doi:10.1103/PhysRevA.77.062507. p. 12, 102

[66] D. Bakalov, V. Korobov, S. Schiller, Magnetic field effects in the transitions of the HD^+ molecular ion and precision spectroscopy, J. Phys. B: At. Mol. Opt. Phys. 44 (2011) 025003. doi:10.1088/0953-4075/44/2/025003. p. 12, 14, 80, 94

[67] C. M. König, F. Heiße, J. Morgner, H. D. Nogueira, T. Sailer, B. Tu, D. Bakalov, K. Blaum, J.-P. Karr, O. Kullie, S. Schiller, S. Sturm, Hyperfine Spectroscopy of a Single HD^+ Molecular Ion in a Penning Trap, *in preparation*. p. 12, 69, 75, 76

[68] G. D. Fletcher, S. J. Lipson, D. J. Larson, Observation of a magnetic-field–dependent g-factor ratio, Phys. Rev. Lett. 58 (1987) 2535–2538. doi:10.1103/PhysRevLett.58.2535. p. 14

[69] N. Fortson, New term in atomic Zeeman energy, Phys. Rev. Lett. 59 (1987) 988–990. doi:10.1103/PhysRevLett.59.988. p. 14

[70] J.-P. Karr, J. C. J. Koelemeij, Extraction of spin-averaged rovibrational transition frequencies in HD^+ for the determination of fundamental constants, Molecular Physics 121 (17-18) (2023) e2216081. doi:10.1080/00268976.2023.2216081. p. 14, 15, 69, 80, 94, 106

[71] J.-P. Karr, Leading-order relativistic corrections to the g factor of H_2^+, Phys. Rev. A 104 (2021) 032822. doi:10.1103/PhysRevA.104.032822. p. 15, 80, 85, 102

[72] J. P. Karr, private communication. p. 15, 69, 85, 86, 102, 104

[73] S. Alighanbari, G. S. Giri, F. L. Constantin, V. I. Korobov, S. Schiller, Precise test of quantum electrodynamics and determination of fundamental constants with HD^+ ions, Nature 581 (2020) 152 – 158. doi:10.1038/s41586-020-2261-5. p. 15, 17, 78, 95, 97, 104

[74] S. Patra, M. Germann, J.-P. Karr, M. Haidar, L. Hilico, V. I. Korobov, F. M. J. Cozijn, K. S. E. Eikema, W. Ubachs, J. C. J. Koelemeij, Proton-electron mass ratio from laser spectroscopy of HD^+ at the part-per-trillion level, Science 369 (2020) 1238–1241. doi:10.1126/science.aba0453. p. 15, 78, 97, 104

[75] I. V. Kortunov, S. Alighanbari, M. G. Hansen, G. S. Giri, V. I. Korobov, S. Schiller, Proton-electron mass ratio by high-resolution optical spectroscopy of ion ensembles in the resolved-carrier regime, Nat. Phys. 17 (2021) 569–573. doi:10.1038/s41567-020-01150-7. p. 15, 16, 78, 97, 104

[76] I. Doran, N. Hölsch, M. Beyer, F. Merkt, Zero-Quantum-Defect Method and the Fundamental Vibrational Interval of H_2^+, Phys. Rev. Lett. 132 (2024) 073001. doi:10.1103/PhysRevLett.132.073001. p. 16

[77] K. B. Jefferts, Hyperfine Structure in the Molecular Ion H_2^+, Phys. Rev. Lett. 23 (1969) 1476–1478. doi:10.1103/PhysRevLett.23.1476. p. 16, 104

[78] S. C. Menasian, High resolution study of the $(F\ F_2) = (3/2\ 1/2) \rightarrow (1/2\ 1/2)$ HFS transitions in stored H_2^+ molecular ions, Ph.D. thesis, University of Washington (1973). p. 16

[79] U. Bressel, A. Borodin, J. Shen, M. Hansen, I. Ernsting, S. Schiller, Manipulation of Individual Hyperfine States in Cold Trapped Molecular Ions and Application to HD^+ Frequency Metrology, Phys. Rev. Lett. 108 (2012) 183003. doi:10.1103/PhysRevLett.108.183003. p. 16, 104

[80] R. Loch, R. Stengler, G. Werth, Measurement of the electronic g factor of H_2^+, Phys. Rev. A 38 (1988) 5484–5488. doi:10.1103/PhysRevA.38.5484. p. 17, 103

[81] D. J. Fink, E. G. Myers, Deuteron-to-Proton Mass Ratio from the Cyclotron Frequency Ratio of H_2^+ to D^+ with H_2^+ in a Resolved Vibrational State, Phys. Rev. Lett. 124 (2020) 013001. doi:10.1103/PhysRevLett.124.013001. p. 17, 100

[82] D. J. Fink, E. G. Myers, Deuteron-to-proton mass ratio from simultaneous measurement of the cyclotron frequencies of h_2^+ and d^+, Phys. Rev. Lett. 127 (2021) 243001. doi:10.1103/PhysRevLett.127.243001. p. 17, 100

[83] S. Rau, F. Heiße, F. Köhler-Langes, S. Sasidharan, R. Haas, D. Renisch, C. E. Düllmann, W. Quint, S. Sturm, K. Blaum, Penning trap mass measurements of the deuteron and the HD^+ molecular ion, Nature 585 (2020) 43–47. doi:10.1038/s41586-020-2628-7. p. 17, 71, 72, 116

[84] J.-P. Karr, Stark quenching of rovibrational states of h_2^+ due to motion in a magnetic field, Phys. Rev. A 98 (2018) 062501. doi:10.1103/PhysRevA.98.062501. p. 17, 100

[85] L. S. Brown, G. Gabrielse, Geonium theory: Physics of a single electron or ion in a Penning trap, Rev. Mod. Phys. 58 (1986) 233–311. doi:10.1103/RevModPhys.58.233. p. 19, 20, 21

[86] A. Aeppli, K. Kim, W. Warfield, M. S. Safronova, J. Ye, Clock with 8×10^{-19} systematic uncertainty, Phys. Rev. Lett. 133 (2024) 023401. doi:10.1103/PhysRevLett.133.023401. p. 19

[87] H. N. Hausser, et al., An ^{115}In$^+$-^{172}Yb$^+$ Coulomb crystal clock with 2.5×10^{-18} systematic uncertainty (2 2024). arXiv:2402.16807. p. 19

[88] W. Paul, Electromagnetic traps for charged and neutral particles, Rev. Mod. Phys. 62 (1990) 531–540. doi:10.1103/RevModPhys.62.531. p. 19

[89] H. Dehmelt, Experiments with an isolated subatomic particle at rest, Rev. Mod. Phys. 62 (1990) 525–530. doi:10.1103/RevModPhys.62.525. p. 19

[90] J. R. Pierce, Theory and Design of Electron Beams, D. van Nostrand Co., New York, 1949. p. 19

[91] Smorra, C., Blaum, K., Bojtar, L., Borchert, M., Franke, K.A., Higuchi, T., Leefer, N., Nagahama, H., Matsuda, Y., Mooser, A., Niemann, M., Ospelkaus, C., Quint, W., Schneider, G., Sellner, S., Tanaka, T., Van Gorp, S., Walz, J., Yamazaki, Y., Ulmer, S., BASE – The Baryon Antibaryon Symmetry Experiment, Eur. Phys. J. Special Topics 224 (16) (2015) 3055–3108. doi:10.1140/epjst/e2015-02607-4. p. 19, 47, 58

[92] T. B. Mitchell, J. J. Bollinger, D. H. E. Dubin, X.-P. Huang, W. M. Itano, R. H. Baughman, Direct observations of structural phase transitions in planar crystallized ion plasmas, Science 282 (5392) (1998) 1290–1293. doi:10.1126/science.282.5392.1290. p. 19

[93] J. Ketter, Theoretical treatment of miscellaneous frequency-shifts in Penning traps with classical perturbation theory, Ph.D. thesis, Ruperto-Carola-University of Heidelberg, Germany (2015). doi:https://hdl.handle.net/11858/00-001M-0000-0026-BF31-9. p. 20, 21, 22, 23, 53

[94] J. L. Verdú Galiana, Ultrapräzise Messung des elektronischen g-Faktors in wasserstoffähnlichem Sauerstoff, Ph.D. thesis, Johannes Gutenberg-Universität Mainz, Germany (2003). p. 21

[95] J. B. Johnson, Thermal Agitation of Electricity in Conductors, Phys. Rev. 32 (1928) 97–109. doi:10.1103/PhysRev.32.97. p. 24

[96] H. Nyquist, Thermal Agitation of Electric Charge in Conductors, Phys. Rev. 32 (1928) 110–113. doi:10.1103/PhysRev.32.110. p. 24

[97] S. Rau, High-precision measurement of the deuteron's atomic mass, Ph.D. thesis, Ruperto-Carola-University of Heidelberg, Germany (2020). doi:10.11588/heidok.00029010. p. 24, 25, 39, 56, 72, 73

[98] X. Feng, M. Charlton, M. Holzscheiter, R. A. Lewis, Y. Yamazaki, Tank circuit model applied to particles in a Penning trap, Journal of Applied Physics 79 (1) (1996) 8–13. doi:10.1063/1.360947. p. 25

[99] A. Weigel, Detection Electronics Design and First Observation of Bound-Electron Spin Transitions at the ALPHATRAP g-Factor Experiment, Ph.D. thesis, Ruperto-Carola-University of Heidelberg, Germany (2019). doi:10.11588/heidok.00025998. p. 25

[100] S. Sturm, A. Wagner, B. Schabinger, K. Blaum, Phase-sensitive cyclotron frequency measurements at ultralow energies, Phys. Rev. Lett. 107 (2011) 143003. doi:10.1103/PhysRevLett.107.143003. p. 27

[101] P. Micke, S. Kühn, L. Buchauer, J. R. Harries, T. M. Bücking, K. Blaum, A. Cieluch, A. Egl, D. Hollain, S. Kraemer, T. Pfeifer, P. O. Schmidt, R. X. Schüssler, C. Schweiger, T. Stöhlker, S. Sturm, R. N. Wolf, S. Bernitt, J. R. Crespo López-Urrutia, The Heidelberg compact electron beam ion traps, Review of Scientific Instruments 89 (2018) 063109. doi:10.1063/1.5026961. p. 29

[102] J. Morgner, Stringent Test of Bound-State Quantum Electrodynamics with Highly Charged Tin, Ph.D. thesis, Ruperto-Carola-University of Heidelberg, Germany (2024). p. 29, 37, 43, 53, 57, 58, 63, 64, 73, 97

[103] A. Egl, High-Precision Laser Spectroscopy of the Fine Structure in $^{40}Ar^{13+}$ at ALPHATRAP, Ph.D. thesis, Ruperto-Carola-University of Heidelberg, Germany (2020). doi:10.11588/heidok.00028293. p. 29

[104] T. Sailer, Direct Bound-Electron g-Factor Difference Measurement of Coupled Ions at ALPHATRAP, Ph.D. thesis, Ruperto-Carola-University of Heidelberg, Germany (2022). doi:10.11588/heidok.00031317. p. 32, 52, 53, 57, 63, 64, 73, 74, 79, 82, 84

[105] V. Hahn, Design and Commissioning of an Optically Transparent Cryogenic Valve for the ALPHATRAP Experiment (2023). p. 36

[106] I. A. Kaplunov, G. I. Kropotov, V. E. Rogalin, A. A. Shakhmin, Optical properties of some crystalline fluorides in the terahertz region of the spectrum, Optical Materials 115 (2021) 111019. doi:10.1016/j.optmat.2021.111019. p. 37, 92

[107] VACUUMSCHMELZE, VACOFLUX50, VACUUMSCHMELZE GmbH, Grüner Weg 37, D-63450 Hanau, Germany. p. 39, 40

[108] S. Sturm, The g-factor of the electron bound in $^{28}Si^{13+}$: The most stringent test of bound-state quantum electrodynamics, Ph.D. thesis, Johannes Gutenberg-Universität in Mainz, Germany (2011).
URL https://pure.mpg.de/rest/items/item_1566155_3/component/file_1566154/content p. 39

[109] Comsol Multiphysics ®v. 6.0. www.comsol.com. COMSOL AB, Stockholm, Sweden. p. 43

[110] F. Raab, Designing and Characterization of a Novel Cryogenic Cyclotron Resonator (2022). p. 43

[111] T. Steinsberger, Microwave injection for the ALPHATRAP experiment and developments of the multi-reflection time-of-flight technique of the ISOLTRAP experiment (2018).
URL https://hdl.handle.net/21.11116/0000-0001-AA22-9 p. 44, 65, 82, 84

[112] MenloSystems, Fiber Comb type FC1500. p. 45

[113] J. DiSciacca, M. Marshall, K. Marable, G. Gabrielse, Resolving an Individual One-Proton Spin Flip to Determine a Proton Spin State, Phys. Rev. Lett. 110 (2013) 140406. doi:10.1103/PhysRevLett.110.140406. p. 47

[114] M. Wang, W. Huang, F. Kondev, G. Audi, S. Naimi, The ame 2020 atomic mass evaluation (ii). tables, graphs and references, Chinese Physics C 45 (3) (2021) 030003. doi:10.1088/1674-1137/abddaf. p. 52

[115] S. Hamzeloui, J. A. Smith, D. J. Fink, E. G. Myers, Precision mass ratio of $^3\mathrm{He}^+$ to HD^+, Phys. Rev. A 96 (2017) 060501. doi:10.1103/PhysRevA.96.060501. p. 52

[116] I. Arapoglou, First measurement of the ground-state g-factor of boronlike argon $^{40}\mathrm{Ar}^{13+}$ in ALPHATRAP, Ph.D. thesis, Ruperto-Carola-University of Heidelberg, Germany (2019). doi:10.11588/heidok.00026909. p. 57, 82, 83, 115

[117] C. Böhm, S. Sturm, A. Rischka, A. Dörr, S. Eliseev, M. Goncharov, M. Höcker, J. Ketter, F. Köhler, D. Marschall, J. Martin, D. Obieglo, J. Repp, C. Roux, R. Schüssler, M. Steigleder, S. Streubel, T. Wagner, J. Westermann, V. Wieder, R. Zirpel, J. Melcher, K. Blaum, An ultra-stable voltage source for precision penning-trap experiments, Nuclear Instruments and Methods in Physics Research Section A: Accelerators, Spectrometers, Detectors and Associated Equipment 828 (2016) 125–131. doi:10.1016/j.nima.2016.05.044. p. 57

[118] T. Sailer, Aufbau Einer Präzisionsspannungsquelle Für Das ALPHATRAP-Experiment (2015). p. 57

[119] C. M. König, F. Heiße, J. Morgner, T. Sailer, B. Tu, D. Bakalov, K. Blaum, S. Schiller, S. Sturm, Nondestructive Quantum State Detection and Control of a Single Molecular Hydrogen Ion in a Penning Trap, *submitted*. p. 59

[120] S. Schiller, private communication. p. 62, 86, 90, 104, 105

[121] J. Ketter, T. Eronen, M. Höcker, M. Schuh, S. Streubel, K. Blaum, Classical calculation of relativistic frequency-shifts in an ideal Penning trap, International Journal of Mass Spectrometry 361 (2014) 34–40. doi:10.1016/j.ijms.2014.01.028. p. 70, 71

[122] S. Schiller, D. Bakalov, A. K. Bekbaev, V. I. Korobov, Static and dynamic polarizability and the Stark and blackbody-radiation frequency shifts of the molecular hydrogen ions H_2^+, HD^+, and D_2^+, Phys. Rev. A 89 (2014) 052521. doi:10.1103/PhysRevA.89.052521. p. 71, 72, 75

[123] M. Schuh, F. Heiße, T. Eronen, J. Ketter, F. Köhler-Langes, S. Rau, T. Segal, W. Quint, S. Sturm, K. Blaum, Image charge shift in high-precision Penning traps, Phys. Rev. A 100 (2019) 023411. doi:10.1103/PhysRevA.100.023411. p. 71, 72

[124] M. Cheng, J. M. Brown, P. Rosmus, R. Linguerri, N. Komiha, E. G. Myers, Dipole moments and orientation polarizabilities of diatomic molecular ions for precision atomic mass measurement, Phys. Rev. A 75 (2007) 012502. doi:10.1103/PhysRevA.75.012502. p. 72

[125] S. Sasidharan, O. Bezrodnova, S. Rau, W. Quint, S. Sturm, K. Blaum, Penning-trap mass measurement of helium-4, Phys. Rev. Lett. 131 (2023) 093201. doi:10.1103/PhysRevLett.131.093201. p. 73

[126] F. Köhler, Bound-Electron g-Factor Measurements for the Determination of the Electron Mass and Isotope Shifts in Highly Charged Ions, Ph.D. thesis, Ruperto-Carola-University of Heidelberg, Germany (2015). doi:10.11588/heidok.00019184. p. 73, 74, 75

[127] J. Verdú, S. Djekić, S. Stahl, T. Valenzuela, M. Vogel, G. Werth, T. Beier, H.-J. Kluge, W. Quint, Electronic g factor of hydrogenlike oxygen $^{16}O^{7+}$, Phys. Rev. Lett. 92 (2004) 093002. doi:10.1103/PhysRevLett.92.093002. p. 74

[128] L. S. Brown, Geonium lineshape, Annals of Physics 159 (1) (1985) 62–98. doi:10.1016/0003-4916(85)90192-7. p. 74, 94

[129] S. Dickopf, High-precision Penning-trap measurements of the magnetic moments and hyperfine splitting in hydrogen-like beryllium-9, Ph.D. thesis, Ruperto-Carola-University of Heidelberg, Germany (2024). doi:10.11588/heidok.00035066. p. 74, 94

[130] D. Bakalov and S. Schiller, private communication. p. 75, 76, 86

[131] E. Colbourn, P. Bunker, Accurate theoretical vibration-rotation energies and transition moments for HD^+, HT^+, and DT^+, Journal of Molecular Spectroscopy 63 (2) (1976) 155–163. doi:10.1016/0022-2852(76)90001-1. p. 78, 86, 93, 95

[132] M. Hernández Vera, F. A. Gianturco, R. Wester, J. da Silva, H., O. Dulieu, S. Schiller, Rotationally inelastic collisions of H_2^+ ions with He buffer gas: Computing cross sections and rates, The Journal of Chemical Physics 146 (12) (2017) 124310. doi:10.1063/1.4978475. p. 92

[133] H. Jóźwiak, T. V. Tscherbul, P. Wcisło, Hyperfine and Zeeman interactions in ultracold collisions of molecular hydrogen with atomic lithium, The Journal of Chemical Physics 160 (2024) 094304. doi:10.1063/5.0193148. p. 92

[134] B. M. Latacz, M. Fleck, J. I. Jäger, G. Umbrazunas, B. P. Arndt, S. R. Erlewein, E. J. Wursten, J. A. Devlin, P. Micke, F. Abbass, D. Schweitzer, M. Wiesinger, C. Will, H. Yildiz, K. Blaum, Y. Matsuda, A. Mooser, C. Ospelkaus, C. Smorra, A. Soter, W. Quint, J. Walz, Y. Yamazaki, S. Ulmer, Orders of Magnitude Improved Cyclotron-Mode Cooling for Nondestructive Spin Quantum Transition Spectroscopy with Single Trapped Antiprotons, Phys. Rev. Lett. 133 (2024) 053201. doi:10.1103/PhysRevLett.133.053201. p. 96

[135] J. Eschner, G. Morigi, F. Schmidt-Kaler, R. Blatt, Laser cooling of trapped ions, J. Opt. Soc. Am. B 20 (5) (2003) 1003–1015. doi:10.1364/JOSAB.20.001003. p. 97

[136] M. Niemann, T. Meiners, J. Mielke, N. Pulido, J. Schaper, M. Borchert, J. Cornejo, A.-G. Paschke, G. Zarantonello, H. Hahn, T. Lang, C. Manzoni, M. Marangoni, G. Cerullo, U. Morgner, J.-A. Fenske, A. Bautista-Salvador, R. Lehnert, S. Ulmer, C. Ospelkaus, Cryogenic Penning-Trap Apparatus for Precision Experiments with Sympathetically Cooled (Anti)Protons, pp. 114–117. doi:10.1142/9789811213984_0029. p. 97

[137] Meiners, Teresa, Coenders, Julia A., Brombacher, Johannes, Niemann, Malte, Cornejo, Juan M., Ulmer, Stefan, Ospelkaus, Christian, Fast adiabatic transport of single laser-cooled $^{9}Be^{+}$ ions in a cryogenic Penning trap stack, Eur. Phys. J. Plus 139 (3) (2024) 262. doi:10.1140/epjp/s13360-024-04936-3. p. 97

[138] B. Tu, F. Hahne, I. Arapoglou, A. Egl, F. Heiße, M. Höcker, C. König, J. Morgner, T. Sailer, A. Weigel, R. Wolf, S. Sturm, Tank-Circuit Assisted Coupling Method for Sympathetic Laser Cooling, Advanced Quantum Technologies 4 (7) (2021) 2100029. doi:10.1002/qute.202100029. p. 98, 99, 107

[139] M. Bohman, V. Grunhofer, C. Smorra, M. Wiesinger, C. Will, M. J. Borchert, J. A. Devlin, S. Erlewein, M. Fleck, S. Gavranovic, J. Harrington, B. Latacz, A. Mooser, D. Popper, E. Wursten, K. Blaum, Y. Matsuda, C. Ospelkaus, W. Quint, J. Walz, S. Ulmer, BASE Collaboration, Sympathetic cooling of a trapped proton mediated by an LC circuit, Nature 596 (7873) (2021) 514–518. doi:10.1038/s41586-021-03784-w. p. 98

[140] C. Will, M. Wiesinger, P. Micke, H. Yildiz, T. Driscoll, S. Kommu, F. Abbass, B. P. Arndt, B. B. Bauer, S. Erlewein, M. Fleck, J. I. Jäger, B. M. Latacz, A. Mooser, D. Schweitzer, G. Umbrazunas, E. Wursten, K. Blaum, J. A. Devlin, C. Ospelkaus, W. Quint, A. Soter, J. Walz, C. Smorra, S. Ulmer, Image-current mediated sympathetic laser cooling of a single proton in a Penning trap down to 170 mK axial temperature (2023). arXiv:2310.10208. p. 98

[141] CERcuits, Kleinhoefstraat 6, 244O Geel, Belgium. [link].
URL https://cercuits.com/ p. 98

[142] F. von Busch, G. H. Dunn, Photodissociation of H_2^+ and D_2^+: Experiment, Phys. Rev. A 5 (1972) 1726–1743. doi:10.1103/PhysRevA.5.1726. p. 100

[143] Y. Weijun, R. Alheit, G. Werth, Vibrational population of H_2^+ after electroionization of thermal H_2, Zeitschrift für Physik D Atoms, Molecules and Clusters 28 (2) (1993) 87–88. doi:10.1007/BF01436971. p. 100

[144] W. Koot, W. van der Zande, D. de Bruijn, Rotational distribution of H_2^+ ions produced by 90 eV electron impact, Chemical Physics 115 (2) (1987) 297–305. doi:10.1016/0301-0104(87)80043-5. p. 100

[145] J. C. J. Koelemeij, B. Roth, S. Schiller, Blackbody thermometry with cold molecular ions and application to ion-based frequency standards, Phys. Rev. A 76 (2007) 023413. doi:10.1103/PhysRevA.76.023413. p. 100

[146] A. Wallach, Construction and testing of a pulsed valve for the supersonic expansion of molecular hydrogen (2022). p. 100

[147] G. H. Dunn, Photodissociation of H_2^+ and D_2^+: Theory, Phys. Rev. 172 (1968) 1–7. doi:10.1103/PhysRev.172.1. p. 100

[148] X. Urbain, B. Fabre, E. M. Staicu-Casagrande, N. de Ruette, V. M. Andrianarijaona, J. Jureta, J. H. Posthumus, A. Saenz, E. Baldit, C. Cornaggia, Intense-Laser-Field Ionization of Molecular Hydrogen in the Tunneling Regime and Its Effect on the Vibrational Excitation of H_2^+, Phys. Rev. Lett. 92 (2004) 163004. doi:10.1103/PhysRevLett.92.163004. p. 100

[149] P. Pérez, D. Banerjee, F. Biraben, D. Brook-Roberge, M. Charlton, P. Cladé, P. Comini, P. Crivelli, O. Dalkarov, P. Debu, A. Douillet, G. Dufour, P. Dupré, S. Eriksson, P. Froelich, P. Grandemange, S. Guellati, R. Guérout, J. M. Heinrich, P.-A. Hervieux, L. Hilico, A. Husson, P. Indelicato, S. Jonsell, J.-P. Karr, K. Khabarova, N. Kolachevsky, N. Kuroda, A. Lambrecht, A. M. M. Leite, L. Liszkay, D. Lunney, N. Madsen, G. Manfredi, B. Mansoulié, Y. Matsuda, A. Mohri, T. Mortensen, Y. Nagashima, V. Nesvizhevsky, F. Nez, C. Regenfus, J.-M. Rey, J.-M. Reymond, S. Reynaud, A. Rubbia, Y. Sacquin, F. Schmidt-Kaler, N. Sillitoe, M. Staszczak, C. I. Szabo-Foster, H. Torii, B. Vallage, M. Valdes, D. P. Van der Werf, A. Voronin, J. Walz, S. Wolf, S. Wronka, Y. Yamazaki, The GBAR antimatter gravity experiment, Hyperfine Interactions 233 (Aug 2015). doi:10.1007/s10751-015-1154-8. p. 101

[150] M. Ahmadi, B. X. R. Alves, C. J. Baker, W. Bertsche, E. Butler, A. Capra, C. Carruth, C. L. Cesar, M. Charlton, S. Cohen, R. Collister, S. Eriksson, A. Evans, N. Evetts, J. Fajans, T. Friesen, M. C. Fujiwara, D. R. Gill, A. Gutierrez, J. S. Hangst, W. N. Hardy, M. E. Hayden, C. A. Isaac, A. Ishida, M. A. Johnson, S. A. Jones, S. Jonsell, L. Kurchaninov, N. Madsen, M. Mathers, D. Maxwell, J. T. K. McKenna, S. Menary, J. M. Michan, T. Momose, J. J. Munich, P. Nolan, K. Olchanski, A. Olin, P. Pusa, C. Ø. Rasmussen, F. Robicheaux, R. L. Sacramento, M. Sameed, E. Sarid, D. M. Silveira, S. Stracka, G. Stutter, C. So, T. D. Tharp, J. E. Thompson, R. I. Thompson, D. P. van der Werf, J. S. Wurtele, Observation of the 1S–2S transition in trapped antihydrogen, Nature 541 (7638) (2017) 506–510. doi:10.1038/nature21040. p. 101

[151] T. Aumann, et al., PUMA, antiProton unstable matter annihilation, Eur. Phys. J. A 58 (2022) 88. doi:10.1140/epja/s10050-022-00713-x. p. 105

[152] C. Smorra, *et al.*, BASE-STEP: A transportable antiproton reservoir for fundamental interaction studies, Review of Scientific Instruments 94 (11) (2023) 113201. doi:10.1063/5.0155492. p. 105

[153] J. Karthein, S. M. Udrescu, S. B. Moroch, I. Belosevic, K. Blaum, A. Borschevsky, Y. Chamorro, D. DeMille, J. Dilling, R. F. Garcia Ruiz, N. R. Hutzler, L. F. Pašteka, R. Ringle, Electroweak Nuclear Properties from Single Molecular Ions in a Penning Trap, Phys. Rev. Lett. 133 (2024) 033003. doi:10.1103/PhysRevLett.133.033003. p. 106

[154] G. Arrowsmith-Kron, M. Athanasakis-Kaklamanakis, M. Au, J. Ballof, R. Berger, A. Borschevsky, A. A. Breier, F. Buchinger, D. Budker, L. Caldwell, C. Charles, N. Dattani, R. P. de Groote, D. DeMille, T. Dickel, J. Dobaczewski, C. E. Düllmann, E. Eliav, J. Engel, M. Fan, V. Flambaum, K. T. Flanagan, A. N. Gaiser, R. F. Garcia Ruiz, K. Gaul, T. F. Giesen, J. S. M. Ginges, A. Gottberg, G. Gwinner, R. Heinke, S. Hoekstra, J. D. Holt, N. R. Hutzler, A. Jayich, J. Karthein, K. G. Leach, K. W. Madison, S. Malbrunot-Ettenauer, T. Miyagi, I. D. Moore, S. Moroch, P. Navratil, W. Nazarewicz, G. Neyens, E. B. Norrgard, N. Nusgart, L. F. Pašteka, A. N Petrov, W. R. Plaß, R. A. Ready, M. Pascal Reiter, M. Reponen, S. Rothe, M. S. Safronova, C. Scheidenerger, A. Shindler, J. T. Singh, L. V. Skripnikov, A. V. Titov, S.-M. Udrescu, S. G. Wilkins, X. Yang, Opportunities for fundamental physics research with radioactive molecules, Reports on Progress in Physics 87 (8) (2024) 084301. doi:10.1088/1361-6633/ad1e39. p. 106

[155] Y. Liu, J. Schmidt, Z. Liu, D. R. Leibrandt, D. Leibfried, C. wen Chou, Quantum state tracking and control of a single molecular ion in a thermal environment, Science 385 (6710) (2024) 790–795. doi:10.1126/science.ado1001. p. 106

[156] T. Sailer, V. Debierre, Z. Harman, F. Heiße, C. König, J. Morgner, B. Tu, A. V. Volotka, C. H. Keitel, K. Blaum, S. Sturm, Measurement of the bound-electron g-factor difference in coupled ions, Nature 606 (7914) (2022) 479–483. doi:10.1038/s41586-022-04807-w. p. 107

[157] F. Heiße, M. Door, T. Sailer, P. Filianin, J. Herkenhoff, C. M. König, K. Kromer, D. Lange, J. Morgner, A. Rischka, C. Schweiger, B. Tu, Y. N. Novikov, S. Eliseev, S. Sturm, K. Blaum, High-precision determination of g factors and masses of $^{20}\mathrm{Ne}^{9+}$ and $^{22}\mathrm{Ne}^{9+}$, Phys. Rev. Lett. 131 (2023) 253002. doi:10.1103/PhysRevLett.131.253002. p. 107

[158] R. P. Feynman, R. B. Leighton, M. Sands, The Feynman Lectures on Physics, Addison-Wesley, 1965, last accessed: January 2025.
URL https://www.feynmanlectures.caltech.edu/ p. 109

[159] Spinoperators Easyspin (last accessed January 2025).
URL https://easyspin.org/documentation/spinoperators.html p. 110, 114

[160] I. Arapoglou, A. Egl, M. Höcker, T. Sailer, B. Tu, A. Weigel, R. Wolf, H. Cakir, V. A. Yerokhin, N. S. Oreshkina, V. A. Agababaev, A. V. Volotka, D. V. Zinenko, D. A. Glazov, Z. Harman, C. H. Keitel, S. Sturm, K. Blaum, g Factor of Boronlike Argon $^{40}\mathrm{Ar}^{13+}$, Phys. Rev. Lett. 122 (2019) 253001. doi:10.1103/PhysRevLett.122.253001. p. 115

Acknowledgments

Thank you to the many people who have supported me throughout the past years, both in and outside the world of physics.

Klaus, vielen Dank für die Möglichkeit in deiner Abteilung zu promovieren. Ich habe über die Jahre die Arbeitsatmosphäre in deiner Abteilung und deine Offenheit sehr zu schätzen gelernt. Danke, dass du immer erreichbar bist und auch immer bereit warst mich zu unterstützen. Deine Energie ist beeindruckend und motivierend.

Jeroen, thank you for accepting the role as my second referee.

Gabi, danke, dass du immer da bist, immer bereit bist zu helfen und immer eine Antwort auf alle möglichen organisatorischen Fragen hast!

Danke **Sven**, ich habe sehr viel von dir als Gruppenleiter gelernt in den letzten Jahren. Deine Begeisterung für Zusammenhänge in der Physik und darüber hinaus ist ansteckend und dein tiefes Verständnis hiervon und deine vielen Ideen haben mich motiviert. Vielen Dank für deine Geduld und die vielen ausführlichen und sehr hilfreichen Erklärungen!

Fabian und **Jonathan** danke für die jahrelange Zusammenarbeit seit Beginn meiner Zeit bei ALPHATRAP bis heute. Fabian, du hast mich an der Falle eingearbeitet und hast immer eine Antwort (mit mindestens einem Paper für mehr Details) bereit. Danke für die guten Gespräche und die Unterstützung! Jonathan, danke für die *großartige* Zeit und Unterhaltungen, die wir als Co-PhDs hatten! **Bingsheng** and **Matthew**, I enjoyed sharing an office with you at the start/end of my time at ALPHATRAP. I am thankful for the opportunity to work with PostDocs like you. Thank you, I learned a lot from you! **Tim**, ich bin sehr froh in den ersten Jahren meiner Zeit bei ALPHATRAP mit dir zusammen gearbeitet zu haben. Deine Freundschaft und dein Humor haben für mich mehr als nur einen kleinen Teil dazu beigetragen die Freude an der Arbeit zu finden und zu behalten. Thank you to all former and new group members during my time at ALPHATRAP: Fabian, Alex, Athulya, Kunal, Valentin, Alex, Anton, Simon, Luca and Jialin.

Danke an Prof. **Stephan Schiller** für die Kollaboration zu Wasserstoffmolekülionen. Das Ballett in der Wiener Staatsoper war unvergesslich. Danke an **Ulrich** für die Unterstützung und die schnellen Lösungen bei allen technischen Fragen. I would especially like to thank **Ivan** and **Victor** for the time together in the lab and the conversations on physics (and beyond) outside of the lab.

Thank you to the members of the other Penning trap groups at MPIK and Mainz: LSym, Pentatrap, μTex, ELCOTRAP, LIONTRAP, TRIGATRAP, g factor Mainz. I greatly appreciate the exchange of ideas, techniques and equipment and of course the fun times during lunch, after work, at the MATS days, and at conferences.

Furthermore, I would like to thank **José** and his group. Especially, thank you to the Cryptex team for the support when we calibrated the wavemeter with light from your frequency comb. Moreover, thank you to the XUV-comb team for sharing the GPS signal and for the openness to all changes we wanted to implement and the repeated trouble-shooting when we lost signal.

Danke an das CSR Team. Vor allem danke an **Holger** für die Infos und den Austausch zu Molekülen. Danke an **Manfred, Max, Elmar** und Team für die Unterstützung über die Jahre. Und vor allem auch für den nie leer werdenden Vorrat an Eis und Kaffee.

Vielen Dank an die Konstruktion unter Leitung von **Frank Müller** und die Werkstätten unter Leitung von **Torsten Spranz** und **Christian Kaiser**. Vor allem danke an **Yannick** für das Rendern der Bilder des experimentellen Aufbaus und die Geduld alle meine Wünsche schöner umzusetzen als ich es mir überhaupt vorstellen konnte. Sowie vielen Dank an die weitere Infrastruktur am Institut, die die Arbeit ermöglichen und vereinfachen (Elektronik, IT, ..).

Danke auch an das Nachbarinstitut EMBL, die Kantine und Cafeteria haben mich über die Jahre grandios versorgt.

Vielen Dank an alle des Turnvereins SGK. Der Sport und die Gemeinschaft mit euch gibt mir genau den Ausgleich den ich brauche. Thanks to my friends new and old for the fun over the past years. Danke, für die gemütlichen Stunden, jede Feier, jedes Festival, jeden Kletterurlaub, .. mit euch. Danke an meine WG, an alle mit denen ich über die Jahre zusammen gewohnt habe. Ihr wart mein Zuhause in den letzten Jahren.

Marvin du gehörst zu der Kategorie oben und auch bald zu der Kategorie unten ;). Danke dass du für mich da bist und für dein Verständnis. Danke dass du es schaffst mich zu beruhigen wenn ich zu schnell bin und mich zu pushen wenn ich zu langsam bin.

Last but not least, danke an meine Familie, vor allem an meine Eltern **Alex** und **Karin** und an meine Schwestern **Sarah** und **Sophia**. Danke, dass ihr da seid und mich so akzeptiert wie ich bin.